BONNER METEOROLOGISCHE ABHANDLUNGEN

Heft 86 (2018) (ISSN 0006-7156)
Herausgeber: Andreas Hense

Sebastian Knist

LAND-ATMOSPHERE INTERACTIONS IN MULTISCALE REGIONAL CLIMATE CHANGE SIMULATIONS OVER EUROPE

BONNER METEOROLOGISCHE ABHANDLUNGEN

Heft 86 (2018) (ISSN 0006-7156)
Herausgeber: Andreas Hense

Sebastian Knist

LAND-ATMOSPHERE INTERACTIONS IN MULTISCALE REGIONAL CLIMATE CHANGE SIMULATIONS OVER EUROPE

Land-atmosphere interactions in multiscale regional climate change simulations over Europe

Dissertation
zur
Erlangung des Doktorgrades (Dr. rer. nat.)
der
Mathematisch-Naturwissenschaftlichen Fakultät
der
Rheinischen Friedrich-Wilhelms-Universität Bonn

vorgelegt von
M.Sc. Sebastian Knist
aus
Düsseldorf

Bonn, März, 2018

Diese Arbeit ist die ungekürzte Fassung einer der Mathematisch-Naturwissenschaftlichen Fakultät der Rheinischen Friedrich-Wilhelms-Universität Bonn im Jahr 2018 vorgelegten Dissertation von Sebastian Knist aus Düsseldorf.

This paper is the unabridged version of a dissertation thesis submitted by Sebastian Knist born in Düsseldorf to the Faculty of Mathematical and Natural Sciences of the Rheinische Friedrich-Wilhelms-Universität Bonn in 2018.

Anschrift des Verfassers: Address of the author:

Sebastian Knist
Meteorologisches Institut der
Universität Bonn
Auf dem Hügel 20
D-53121 Bonn

1. Gutachter: Prof. Dr. Clemens Simmer, Rheinische Friedrich-Wilhelms-Universität Bonn
2. Gutachter: PD Dr. Silke Trömel, Rheinische Friedrich-Wilhelms-Universität Bonn

Tag der Promotion: 31. Juli 2018

Zusammenfassung

Wechselwirkungen zwischen der heterogenen Landoberfläche und der Atmosphäre spielen durch ihren Einfluss auf den Energie- und Wasserkreislauf eine fundamentale Rolle im Wetter- und Klimasystem. Globale Klimamodelle haben derzeit eine grobe horizontale Gitterauflösung in der Größenordnung von 100 km. Regionale Klimamodelle können durch ihre höhere Auflösung mesoskalige atmosphärische Prozesse besser auflösen und auch die heterogenen Landoberflächeneigenschaften realistischer abbilden. Dadurch können sie Merkmale des regionalen und lokalen Klimas detaillierter simulieren.
Ziel der vorliegenden Arbeit ist es, den Einfluss von Gitterauflösungen in regionalen Klimasimulationen in Bezug auf Land-Atmosphäre Wechselwirkungen und Niederschlag einschließlich der Niederschlagsextreme zu quantifizieren. Dazu werden mit dem regionalen Klimamodell WRF regionale Klimasimulationen in verschiedenen Auflösungen für das europäische Modellgebiet des Coordinated Regional Climate Downscaling Experiment (EURO-CORDEX) sowie für Mitteleuropa durchgeführt. Dabei findet ein Downscaling sowohl von ERA-Interim Reanalyse Daten als auch von Klimaprojektionen des globalen Klimamodells MPI-ESM-LR (RCP4.5) statt. Die Analyse dieser Simulationen setzt den Schwerpunkt auf Land-Atmosphäre Wechselwirkungen um ein besseres Verständnis der verschiedenskaligen Prozesse des Wasserkreislaufs und deren Sensitivitäten und Variabilitäten zu erlangen, sowohl unter den gegenwärtigen als auch unter den projizierten Klimabedingungen. Des Weiteren wird der Mehrwert von noch höher aufgelösten, konvektionserlaubenden Klimasimulationen, die eine der ersten in dieser Auflösung über Mitteleuropa für dekadische Zeitperioden darstellen, untersucht.

Die Stärke der Land-Atmosphäre Kopplung in Europa wird für ein Ensemble von ERA-Interim angetriebenen EURO-CORDEX Simulationen (1989-2008) untereinander und gegen Beobachtungsdaten verglichen. Dabei wird die Kopplungsstärke mittels der Korrelation von latentem und sensiblen Wärmefluss und mittels der Korrelation von latentem Wärmefluss und 2m Temperatur quantifiziert und mit Messungen des europäischen FLUXNET und Daten des Global Land Evaporation Amsterdam Model (GLEAM) verglichen. Die Simulationen stimmen größtenteils mit beiden Beobachtungsdatensätzen in den großskaligen Mustern überein, die durch starke Kopplung in Südeuropa und schwache Kopplung in Nordeuropa charakterisiert sind. In der Übergangszone zwischen beiden Kopplungsregimen in Mitteleuropa tendiert die Mehrheit der Modelle zur Überschätzung der Kopplungsstärke. Die Unterschiede zwischen den einzelnen Modellsimulationen lassen sich sowohl durch die verschiedenen von den Modellen verwendeten Landoberflächenmodelle als auch durch die jeweils unterschiedlich simulierten Witterungsbedingungen erklären, die aus den unterschiedlichen atmosphärischen Parametrisierungen resultieren.

Die Stärke der Land-Atmosphäre Kopplung in ERA-Interim angetriebenen WRF Simulationen mit 3 km und 12 km Gitterabstand über Mitteleuropa weist in beiden Auflösungen eine große Variabilität von Jahr zu Jahr auf und steht klar im Zusammenhang mit den Bodenfeuchtebedingungen in den jeweiligen Jahren. Die Kopplungsstärke unterscheidet sich deutlich für verschiedene Boden- und Vegetationstypen. Insgesamt ist die Kopplungsstärke in der 3 km im Vergleich zur 12 km Simulation stärker, was auf die geringere Niederschlagsmenge in der höheren Auflösung und dementsprechend geringere Bodenfeuchte zurückzuführen ist.
Die prognostizierte Klimaänderung für die Periode von 2071-2100 im Vergleich zu 1971-2000 basierend auf WRF Klimasimulationen für das EURO-CORDEX Gebiet in 0.44° Auflösung (Downscaling von MPI-ESM-LR, RCP4.5 Szenario, 1950-2100) weist eine Verstärkung der Land-Atmosphäre Kopplung in weiten Teilen West-, Mittel- und südlichen Osteuropas aufgrund der Verringerung der Bodenfeuchte in diesen Regionen auf. Regionen starker Kopplung zeigen dabei einen stärkeren Anstieg von Extremtemperaturen.

Zur Analyse des Mehrwerts von konvektionserlaubenden Klimasimulationen werden insgesamt neun Jahre ERA-Interim angetriebener WRF Simulationen mit 3 km und 12 km Gitterabstand über Mitteleuropa mit Stationsmessungen verglichen. Die höhere Auflösung zeigt eine deutlich bessere Reproduktion der stündlichen Niederschlagsverteilung sowie des mittleren Tagesgangs im Sommer. Die 12 km Simulation überschätzt insbesondere die leichten Niederschlagsintensitäten und unterschätzt Stark- und Extremniederschläge, die von der 3 km Simulation deutlich besser reproduziert werden. Die größten Unterschiede zwischen beiden Auflösungen treten in bergigen Regionen und im Sommer bei hoher konvektiver Aktivität auf. Der beobachtete Zusammenhang zwischen Temperatur und Extremniederschlag, der einen Anstieg von einer Skalierungsrate gemäß der Clausius-Clapeyron Gleichung (7% K^{-1}) zu einer super-adiabatischen Skalierungsrate aufweist, wird nur von der 3 km Simulation korrekt reproduziert.

Eine Sensitivitätsstudie zum Einfluss der Gitterauflösung verschiedener Bodeneigenschaften basierend auf fünf WRF Simulationen mit identischem Setup der Atmosphäre in 3 km Auflösung, aber verschiedenen Kombinationen von grob aufgelöster (12 km) Landnutzung, initialer Bodenfeuchte und Orographie für den Sommer 2003 zeigt, dass eine grob aufgelöste Orographie das Strömungsmuster signifikant beeinflusst. Die Glättung der Gebirgsrücken durch die gröbere Auflösung führt zu schwächer ausgeprägten Föhneffekten und mehr lokalem konvektiven Niederschlag. Der Effekt durch die gröbere Auflösung der Landnutzung ist vergleichsweise klein und eher auf die Änderungen der prozentualen Anteile der verschiedenen Landnutzungstypen durch die Aggregierung als auf die geringere Heterogenität zurückzuführen. Geringe Unterschiede in der Bodenfeuchte haben dagegen ein größeres Potential, den atmosphärischen Zustand signifikant zu beeinflussen.

Klimaprojektionen in 3 km und 12 km Auflösung über Mitteleuropa werden für zwei Zukunftsperioden Mitte (2038-2050) und Ende (2088-2100) des 21. Jahrhunderts durchgeführt und gegen eine Kontrollperiode (1993-2005) verglichen um die zukünftigen Änderungen der Niederschlagsstatistik zu quantifizieren. Beide Modellauflösungen simulieren eine leichte Abnahme der mittleren sommerlichen Niederschlagsmenge für beide Zukunftsperioden, während starke und extreme stündliche Niederschlagsmengen insgesamt zunehmen. Dieser Anstieg ist in den 3 km Simulationen stärker. Die Skalierungskurven von Temperatur und Extremniederschlag verschieben sich entlang der 7% K^{-1} Trajektorie zu höheren Maximalniederschlägen bei höheren Temperaturen.

Insgesamt bestärken die Ergebnisse dieser Arbeit den Mehrwert von konvektionserlaubenden Klimasimulationen, liefern neue Einblicke in die Land-Atmosphäre Wechselwirkungsprozesse und zeigen die Notwendigkeit, die Simulation der Land-Atmosphäre Kopplung in den Klimamodellen weiter zu verbessern.

Abstract

Interactions between the heterogenous land surface and the atmosphere play a fundamental role in the weather and climate system through their influence on the energy and water cycles. Global climate models (GCMs) currently have coarse horizontal grid resolutions in the order of 100 km. With their higher resolution regional climate models (RCMs) better resolve mesoscale processes in the atmosphere and better represent the heterogenous land surface properties. Thus, RCMs are able to provide more detailed characteristics of regional to local climate.
This thesis conducts regional climate simulations in multiple resolutions for the European domain of the Coordinated Regional Climate Downscaling Experiment (EURO-CORDEX) and a central European domain (3kmME) with the RCM WRF downscaling both ERA-Interim reanalysis and GCM MPI-ESM-LR (RCP4.5) climate change scenario data. The analysis focusses on land-atmosphere interactions to gain a better understanding of the regional water cycle components, the involved multi-scale processes, their sensitivities and variabilities both under present-day climate and future climate change conditions. Furthermore, the added value of the convection-permitting 3kmME simulations, being one of the first sets of decade-long convection-permitting regional climate simulations over Central Europe, is investigated.

A comparison of summertime land-atmosphere coupling strength is carried out for a subset of the ERA-Interim-driven EURO-CORDEX model ensemble (1989 to 2008). The coupling strength is quantified by the correlation between the surface sensible and the latent heat flux, and by the correlation between the latent heat flux and 2m temperature and compared to European FLUXNET observations and gridded observational Global Land Evaporation Amsterdam Model (GLEAM) data, respectively. The RCM simulations agree with both observational datasets in the large-scale pattern characterized by strong coupling in southern Europe and weak coupling in northern Europe. However, in the transition zone from strong to weak coupling covering large parts of central Europe the majority of the RCMs tend to overestimate the coupling strength in comparison to both observations. The RCM ensemble spread is caused by the different land surface models applied, and by the model-specific weather conditions resulting from different atmospheric parameterizations.
Investigation of land-atmosphere coupling strength in ERA-Interim driven WRF simulations in both 3 km and 12 km resolution for central Europe reveals large year-to-year variability related to the individual soil moisture conditions. Coupling strength largely differs for individual land use types. Forest compared to crop type reacts slower to drought conditions. Coupling is overall slightly stronger in the 3 km simulation, attributed to overall drier soils due to less precipitation.
The projected climate change based on a WRF 0.44° simulation downscaling GCM MPI-ESM-LR (RCP4.5) data alters the European land-atmosphere coupling regimes in summer. Due to increasingly drier soils, stronger coupling is simulated for large parts of western,

central and southern eastern Europe for the period 2071-2100 compared to 1971-2000. Areas of strongest future increase of extreme temperature coincide with strong coupling areas.

In order to analyse the added value of convection-permitting 3 km climate simulations, nine years of ERA-Interim driven simulations with the WRF RCM at 12 km and 3 km grid resolution over central Europe are evaluated against observations with a focus on sub-daily precipitation statistics and the relation between extreme precipitation and air temperature. A clear added value of the higher resolution simulation is found especially in the reproduction of the diurnal cycle and the hourly intensity distribution of precipitation. Too much light precipitation in the 12 km simulation results in a positive precipitation bias. Largest differences between both resolutions occur in mountainous regions and during the summer months with high convective activity. Moreover, the observed increase of the temperature–extreme precipitation scaling from the Clausius-Clapeyron (C-C) scaling rate of ~7% K^{-1} to a super-adiabatic scaling rate is reproduced only by the 3 km simulation.

The effect of land surface heterogeneity on the differences between 3 km and 12 km simulations is analysed based on five WRF simulations for JJA 2003, each with the same atmospheric setup in 3 km resolution but different combinations of 12 km resolution land use and soil type, initial soil moisture and orography. A coarser resolved orography significantly alters the flow over and around extensive mountain ridges like the Alps and impact the large-scale flow pattern. The smoothed mountain ridges result in weaker Föhn effects and in enhanced locally generated convective precipitation pattern peaking earlier in the afternoon. The effect of a coarser-resolved land use distribution is overall smaller and mainly related to changes in overall percentages of different land use types, rather than to the loss of heterogeneity in the surface pattern on the scale analysed here. Even small changes in soil moisture have a higher potential to affect the overall simulation results.

WRF climate simulations downscaling the MPI-ESM-LR data at 12 km and 3 km resolution for central Europe are analysed for three 12-year periods: a control, a mid-of-century and an end-of-century projection to quantify future changes in precipitation statistics based on both convection-permitting and convection-parameterized simulations. For both future scenarios both simulations suggest a slight decrease in mean summer precipitation and an increase in hourly heavy and extreme precipitation in large parts of central Europe. This increase is stronger in the 3 km runs. Temperature–extreme precipitation scaling curves in the future climate are projected to shift along the 7% K^{-1} trajectory to higher peak extreme precipitation values at higher temperatures while keeping their typical shape.

The results of this thesis clearly confirm the added value of convection-permitting climate simulations, provide further insights into land-atmosphere interaction processes and highlight the relevance of the RCMs ability to properly simulate coupling strength.

Contents

1 Introduction

1.1 Background and motivation

The Intergovernmental Panel on Climate Change (IPCC) 5th Assessment Report (IPCC, 2013) indicates a future increase of the climate system's variability, changes in the frequency and intensity of meteorological extreme events, an acceleration of the hydrological cycle and robust large-scale changes of the precipitation regime (e.g. decrease of summer-, increase of winter precipitation over Central Europe). Linked to this are modifications of the regional and local water balances (precipitation, evapotranspiration, etc.) with variable impacts on anthropogenic and natural systems, depending on their sensitivity (Goergen et al. 2010). Hence, there is a strong need for regional climate change information at the regional to local level (Giorgi et al. 2009), where adaptation measures eventually have to be implemented.

Regional climate downscaling

Global climate models (GCMs) are used to project the possible future evolution of the climate system as well as to improve the understanding of the climate system itself. They are numerical models built on a set of prognostic hydro- and thermodynamic partial differential equations and diagnostic equations that describe the governing dynamical and physical processes of the climate system (e.g., conservation of momentum, mass and energy conservation). The set of equations is discretized on a three-dimensional model grid using finite elements, finite differences or a spectral approach and are solved by numerical integration schemes. The dynamical processes in the atmosphere act at various spatial and temporal scales, ranging from the smallest turbulent eddies with a size of a few centimeters and a timescale of seconds to large-scale patterns oscillating on multi-annual time scales like the El Niño Southern Oscillation (ENSO) (Figure 1.1.a). Processes that are not resolved by the effective model resolution (at least four grid boxes) are calculated by parameterization schemes, e.g. for radiation, clouds, cumulus convection and turbulence. Due to the large number of data points and the high complexity of GCMs, their integration is computationally expensive. As they cover the whole globe, the resolution of their horizontal mesh is currently in the order of 100 km and they provide output at 6-hour intervals (Taylor et al. 2012b). Due to this coarse horizontal and temporal scale, GCMs are insufficient for reproducing many aspects of regional and local scale estimates of climate variability and change. Therefore, downscaling is needed to describe the local consequences of the global change, which can be done using empirical-statistical downscaling (ESD) or dynamical downscaling by means of regional climate models (RCMs). RCMs are applied

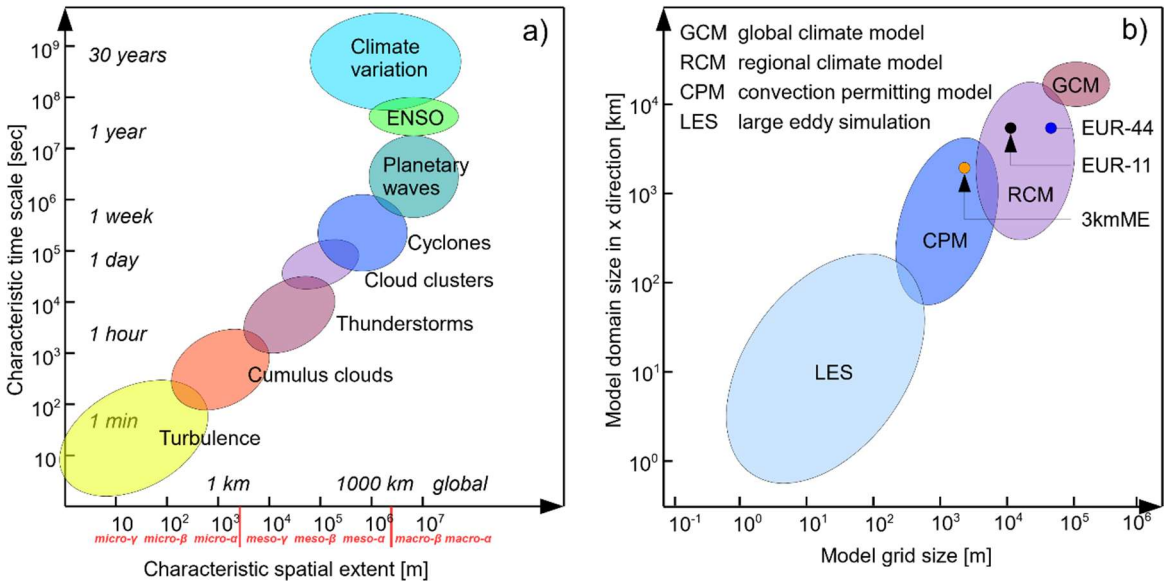

Figure 1.1: Characteristic spatial and temporal scales of different atmospheric processes (a) (following e.g. Orlanski, 1975), typical domain size and grid spacing of different atmospheric models including model domains used in this study (see Figure 2.1) (b).

over smaller (regional) domains using the GCM output data as lateral boundary conditions, thus the computational resources allow for finer horizontal grid spacings, typically in the range of 10 to 50 km (Figure 1.1.b). While such limited area models (LAMs) have been widely used in weather forecasting since the 1970s, their application for climate purposes started in the 1990s. With their higher resolution, RCMs better resolve mesoscale processes like mountain circulations and land-sea contrast effects (Figure 1.2). Thus, RCMs are able to provide more detailed characteristics of the regional to local climate. Still, high resolution climate change model runs remain challenging due to their high computational demand caused by the short time steps and their long runtime as well as the large data volumes involved.

Primary sources of uncertainties in RCM projections of the future climate are a combination of the emission scenarios (representative concentration pathways (RCP)), the GCM model configuration, its internal variability, the regional climate downscaling configuration, the internal variability of the RCM, the downscaling method itself as well as the geographic region (Giorgi 2005). However, by using an ensemble of several regional climate change projections from different RCMs driven by different GCMs, it is possible to derive bandwidths of possible changes and thereby also assess the uncertainty associated with the projected changes.

In the last decade, community efforts in RCM modelling have been organized e.g. in PRUDENCE (Christensen and Christensen 2007) and ENSEMBLES (Van der Linden and Mitchell J.F.B. 2009) for the European domain. With a joint experiment design, those model ensembles allow for an assessment of uncertainties in present and projected future

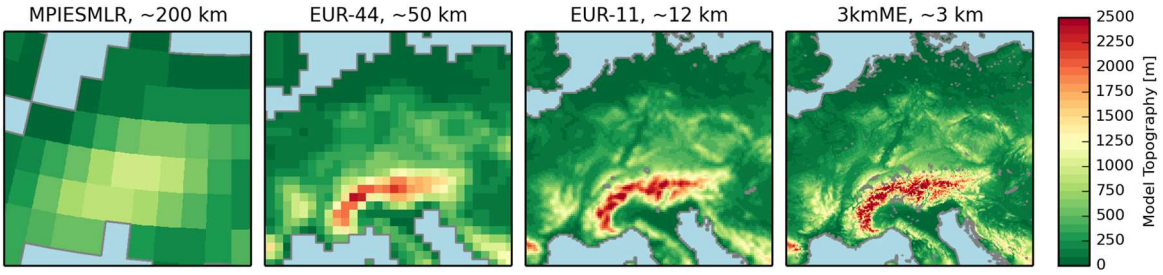

Figure 1.2: Land-sea distribution and topography of central Europe in different model resolutions.

climate as well as for model intercomparisons and evaluations. As part of the World Climate Research Program (WCRP) the Coordinated Regional Climate Downscaling Experiment (CORDEX) encompasses the latest of these RCM ensemble experiments and provides an unprecedented ensemble of state-of-the-art RCMs downscaling the Coupled Model Intercomparison Project Phase 5 (CMIP5, see Taylor et al. 2012b) global model results for different regions worldwide (Giorgi et al. 2009; Gutowski et al. 2016).

Convection-permitting modelling

Although RCMs at resolutions of about 10 km show substantial improvements over 50 km resolution (Prein et al. 2016a), uncertainties and deficits still remain in the representation of clouds, the diurnal cycle of summer convective precipitation, the intensity of extreme precipitation, especially over complex topography. The correct representation of sub-daily precipitation amounts is of high importance since extreme precipitation events, which often evolve over hourly time scales, can cause severe natural hazards like flash floods affecting urban areas and small river catchments. Such short-term events usually develop also over small space scales and are related to convective precipitation. Simulations with grid spacing of about 10 km, however, still require the parametrization of deep convection, which is considered as a major source for model errors and uncertainty, like shifted summer-time diurnal cycles and underestimates of intensity, frequency and spatial distribution of sub-daily precipitation (Brockhaus et al. 2008; Hohenegger et al. 2008; Hanel and Buishand 2010; Dirmeyer et al. 2012). Convection-permitting models (CPM) require grid sizes below 4 km to explicitly resolve deep convection without the need of a parameterization scheme (Prein et al. 2015).

While CPMs are commonly used in regional weather prediction since almost two decades, in regional climate modelling however, convection-permitting simulations are rare because of their high computational costs. They have so far been limited to small domain sizes (Knote and Heinemann 2010; Kendon et al. 2012; Prein et al. 2013; Fosser et al. 2015; Brisson et al. 2016) and/or seasonal simulations (Hohenegger et al. 2008; Langhans et al. 2013; Prein et al. 2013); simulations over Europe exceeding decadal time slices exist only for the Southern British Isles (Kendon et al. 2012), for a greater Alpine domain (Ban et

al. 2014), for Southwestern Germany (Fosser et al. 2015) and Belgium (Brisson et al. 2016). These limited simulations yielded already significant improvements for sub-daily precipitation statistics, for the representation of extreme precipitation events, for summer diurnal cycles of convective precipitation, and for the spatial structure of precipitation. A review paper on convection-permitting climate modelling by Prein et al. (2015) concludes, that the largest improvements are found for situations with dominant convective precipitation and over regions with heterogeneous land surface and complex topography.

Clausius-Clapeyron scaling of extreme precipitation events

With increasing near-surface air temperatures, precipitation events are expected to intensify by ~7% K^{-1} according to the Clausius-Clapeyron (C-C) relation for water vapor pressure (Trenberth et al. 2003). Observation based studies suggest that the increase of hourly precipitation extremes with temperature can exceed C-C scaling rates for daily mean temperatures above 12°C. This exceedance is most probably related to the release of latent heat in convective precipitation resulting in updrafts, which enhance moisture convergence (Lenderink and van Meijgaard 2008; Berg et al. 2013).

Many global and regional climate model simulations suggest an increase in daily extreme precipitation events with increasing temperature (IPCC 2013, Jacob et al. 2013). With the better representation of convective processes CPMs are potentially better suited to access changes in extreme precipitation in a future climate. So far, only few convection-permitting decade-long climate change mid or end-of-the-century simulations driven by GCM scenarios exist for European sub-domains (Kendon et al. 2014; Ban et al. 2015). Both Kendon et al. (2014) and Ban et al. (2015) found a decrease in future mean summer precipitation while sub-daily heavy precipitation substantially increases. Scaled by the mean temperature change, these increases exceed the C-C scaling rate in the UK (Kendon et al. 2014) but are consistent with the C-C relation over the Alps (Ban et al. 2015).

Land-atmosphere coupling

For a better understanding of the processes involved in the regional manifestation of climate change, land-atmosphere coupling is highly important (Seneviratne et al., 2010). Through the exchange of energy, mass and momentum at the earth's surface, land-atmosphere coupling affects boundary-layer evolution, convection and clouds, which in turn also affect for example precipitation intensity, as well as the intensity and duration of heat waves. Vice versa, atmospheric conditions directly and indirectly control the exchange processes. In general, land-atmosphere coupling strength can be defined as the degree to which the atmosphere responds to anomalies in the land-surface state (Koster et al. 2006). Multiple metrics have been defined for quantifying this coupling strength depending on the variables involved and the feedback processes addressed.

A key variable in the land-atmosphere coupling system is soil moisture, which controls to

a large extent the flux partitioning of sensible and latent heat (Seneviratne et al. 2010). Soil moisture-temperature feedback is strongest in transition zones between wet and dry climates. In a wet, energy-limited regime, soil moisture content is always sufficiently high, thus evapotranspiration is primarily limited by the state of the planetary boundary layer. In a dry, moisture-limited regime, the atmospheric moisture deficit cannot be entirely compensated by moisture supply from the land surface via evapotranspiration, i.e., the latent heat flux is constrained by the soil moisture content. The understanding of land-atmosphere coupling processes across multiple spatial and temporal scales has continuously improved through observations and modelling. Based on multi-model experiments of the Global Land-Atmosphere Coupling Experiment (GLACE) (Koster et al. 2006) have identified so-called "hot spot" regions of strong coupling at a global scale. On the local scale, land-atmosphere coupling has been investigated in the context of diurnal boundary-layer evolution (Santanello et al. 2009, 2013; Milovac et al. 2016) and cloud formation (Betts et al. 2015), all of them including observations. Effects of soil moisture-temperature coupling have been investigated on the climatological and daily time scale with positive feedback on the development of heat waves (Fischer et al. 2007; Miralles et al. 2012; Hirschi et al. 2014). Soil moisture-precipitation coupling shows positive and negative feedback mechanisms on global and local scales (Hohenegger et al. 2009; Taylor et al. 2012a; Froidevaux et al. 2014). (Guillod et al. 2013) reveal that this feedback not only depends on the amount of soil moisture, but also on its temporal and spatial distribution. This becomes also evident when applying RCMs at convection-permitting and non-convection-permitting model resolution; Hohenegger et al. (2009) show that the sign of the simulated soil moisture-precipitation feedback depends also on the applied convection parameterization. With the expected change in large-scale precipitation regimes simulated by global GCMs (IPCC 2013), land-atmosphere interactions will also change and lead to a shift of the transition zones between weak and strong coupling regimes (Seneviratne et al., 2006; Dirmeyer et al., 2014).

1.2 Research objectives and hypothesis

This study investigates land-atmosphere interactions in multiscale regional climate simulations in the context of the EURO-CORDEX project to gain a better understanding of the regional water cycle components, the involved multi-scale processes, and their sensitivities and variabilities both under present-day climate and future climate change conditions.

As part of the joint EURO-CORDEX analysis efforts, this study investigates land-atmosphere coupling in a subset of 16 RCM simulations from the EURO-CORDEX reanalysis-driven ensemble. Differences between individual RCMs are assumed to be

directly or indirectly related to the reproduction of the land-atmosphere coupling in these models. The focus is on the summer months June, July and August (JJA), when the land-atmosphere coupling is most relevant. In a projected warmer future climate and related large-scale changes of the precipitation regime, possible intensifications of coupling strengths and a shift of transition zones may influence future temperature extremes. These mechanisms are investigated for a WRF simulation downscaling a GCM RCP4.5 scenario simulation over the EURO-CORDEX domain.

Within this thesis one of the first sets of decade-long convection-permitting regional climate simulations with the WRF RCM over Central Europe (1440 km x 1368 km) is carried out, both for ERA-Interim reanalysis driven time slices and for climate change projections for mid (MOC) and end-of-the-century (EOC) driven by a GCM RCP4.5 scenario simulation. Sub-daily precipitation statistics and temperature-precipitation scaling are evaluated both for convection-permitting and coarser resolution simulations with parameterized convection in order to investigate the added value of the higher resolution. Furthermore, the convection-permitting future scenario simulations are investigated with respect to the relative change in precipitation statistics in MOC and EOC simulations and its relation to the mean temperature change. Extreme precipitation is expected to increase under warmer future climate conditions, whereby the scaling rate may differ for convection-permitting and coarser resolution simulations.

Finally, this thesis investigates the impact of the spatial scales of the patterns of land use, soil moisture and orography on convection-permitting RCM simulations in terms of atmospheric patterns and domain wide averages. To this goal, five 3 km grid size, convection-permitting seasonal simulations for central Europe are analysed, which are performed with different combinations of coarsely (12 km) resolved land surface property types. They allow to assess the impact of each individual land surface property on atmospheric flow, also in comparison to the driving 12 km simulation with parameterized convection.

1.3 Outline

Section 2.1 introduces the EURO-CORDEX RCM simulations used for the land-atmosphere coupling analysis. Section 2.2 provides an overview of the RCM simulations carried out for this thesis and introduces the WRF modelling framework. Observational datasets that have been used are presented in Section 2.3. Section 2.4 provides background information on methods to quantify land-atmosphere coupling and introduces the methods ultimately used in this study.

Chapter 3 shows the results of the land-atmosphere coupling analysis in the EURO-CORDEX evaluation ensemble. It includes an evaluation of the coupling-related variables soil moisture and latent and sensible heat flux as well as the analysis of land-atmosphere coupling based on two methods and a comparison of the results with coupling strengths derived from station observations and a gridded dataset. The analysis of land-atmosphere coupling in the ERA-Interim reanalysis-driven convection-permitting 3 km simulations is shown in Chapter 4. In Chapter 5 these 3 km simulations are compared against their parent 12 km simulations and evaluated against observations with a focus on the diurnal cycle, the intensity distribution of hourly precipitation, and the temperature-precipitation scaling. The effects of land surface inhomogeneity on convection-permitting simulations is investigated in Chapter 6. Chapter 7 presents the results of the climate change projections for the EURO-CORDEX domain in 0.44° resolution and for Middle Europe in 12 km and 3 km resolution.

Chapter 3 follows closely the contents in Knist et al. (2017) including all figures in this chapter. Results and figures of Section 5.2 to 5.6 as well as Section 7.5 and 7.6 have been published in Knist et al. (2018a). Contents of Section 6.2, 6.3 and 6.4 including all figures have been submitted for publication in Knist et al. (2018b).

2 Data and Methods

2.1 EURO-CORDEX

The first goal of this study is the production of regional climate control- and projection simulations with the RCM WRF (Weather Research and Forecasting Model) for Europe as a contribution to the CORDEX project. The main purpose of CORDEX is to dynamical downscale the different GCM control and projection runs of the Coupled Model Intercomparison Project Phase 5 (CMIP5) for 13 defined domains over all continents with a broad range of common RCMs[1]. Thus, the uncertainties due to varying GCM simulations, different greenhouse gas (GHG) emission scenarios, the natural climate variability, the downscaling method and the internal variability of the RCMs are captured. This leads to a broad range of possible changes in regional climate and thereby an assessment of uncertainty in addition to the ensemble mean of the projected change. Due to the agreement on a joint experiment design and data protocol, it facilitates data comparison and analysis. In order to fulfill the large computational effort to generate a large GCM-RCM combination matrix, several groups all over Europe coordinate in downscaling different GCMs with different RCMs[2].

As a first phase of CORDEX, ERA-Interim reanalysis driven RCM simulations have been carried out for the period from 1989 to 2008 in order to configure the different RCMs and evaluate the model results against observations. For the European domain (EURO-CORDEX) several joint evaluation studies have been performed based on ERA-Interim reanalysis-driven RCM simulations. Kotlarski et al. (2014) evaluated mean temperature and precipitation in the EURO-CORDEX evaluation ensemble from 1989 to 2008 and reported slight improvements compared to the ENSEMBLES simulations. In a study by Vautard et al. (2013) EURO-CORDEX RCMs showed an overall satisfying performance in the reproduction of heat waves, accompanied by a large ensemble spread. Both studies highlighted that RCM parameterizations have a strong influence on the model results. While some causalities for the differences in model results are shown, e.g., Vautard et al. (2013) point out sensitivity of very high near-surface air temperatures to microphysics and convections schemes, these studies recommend extended evaluation efforts for different model components and variables. For the subset of WRF simulations within the EURO-CORDEX ensemble Katragkou et al. (2015) evaluated short- and longwave radiation and cloud cover and their relation to temperature and precipitation biases. In an evaluation

[1] See www.cordex.org (last visited 20.01.2018)

[2] See http://www.euro-cordex.net (last visited 20.01.2018)

study on the added value of an increased spatial resolution on the reproduction of precipitation extremes in Prein et al. (2016a) show evidence, that the high-resolution 12 km simulations for the EURO-CORDEX model domain better reproduce mean and extreme precipitation than their coarser (50 km) counterparts. Casanueva et al. (2015) also show the added value of the high-resolution simulations regarding the spatial patterns.
A subset of the EURO-CORDEX RCM evaluation ensemble introduced in Section 2.2.4 provides the basis for the first part of this study: the analysis of land-atmosphere coupling in EURO-CORDEX evaluation experiments.

In the second phase, CMIP5 GCMs with different representative concentration pathways (RCP) scenarios are downscaled both for the control period from 1951 to 2005 and for the future scenario from 2006 to 2100 (Jacob et al. 2013). As contribution to EURO-CORDEX, dynamical downscaling of the Earth System Model of the Max Planck Institute in Hamburg (MPI-ESM-LR-r1, RCP4.5) for the whole period from 1951 to 2100 is carried out within this study.

2.1.1 The EURO-CORDEX domain

Figure 2.1 shows the EURO-CORDEX focus domain (colored topography). With a size of about 5000 × 5000 km^2 it covers the whole European continent including Iceland in the North-West, the Mediterranean and parts of North Africa in the South and the Black Sea in the East. The domain is defined in rotated geographical coordinates with a rotated North Pole located at 198°E 38.25°N. The rotated equator intersects the model domain so that the convergence of the meridians is minimal, and the coordinate system has a nearly Cartesian characteristic. The EURO-CORDEX simulations are carried out with two model grid sizes: The coarse 0.44° (~50 km) and the fine 0.11° (~12 km) mesh size (in the following named as EUR-44 and EUR-11), whereby each 16 EUR-11 grid cells perfectly fit into one EUR-44 grid cell. For the EURO-CORDEX focus domain that spans 106 (424) grid points in x-direction and 103 (412) grid points in y-direction in EUR-44 (EUR-11) resolution, the top-left corner grid point is defined at 315.86°E 60.21°N (331.79°E 21.67°N in rotated coordinates). Please note that for the EURO-CORDEX simulations the actual model domain is by a certain number of grid points at each side larger than the focus domain in order to cut out artificial effects at the lateral boundaries. In contrast to the EURO-CORDEX focus domain the actual model domain size is not defined and can be different for the individual RCM runs. For the WRF simulations performed within this study, the EUR-44 domain (red frame in Figure 2.1) spans 131 × 134 grid points and the EUR-11 domain (black frame) 436 × 448 grid points. For simplicity, the labels EUR-44 and EUR-

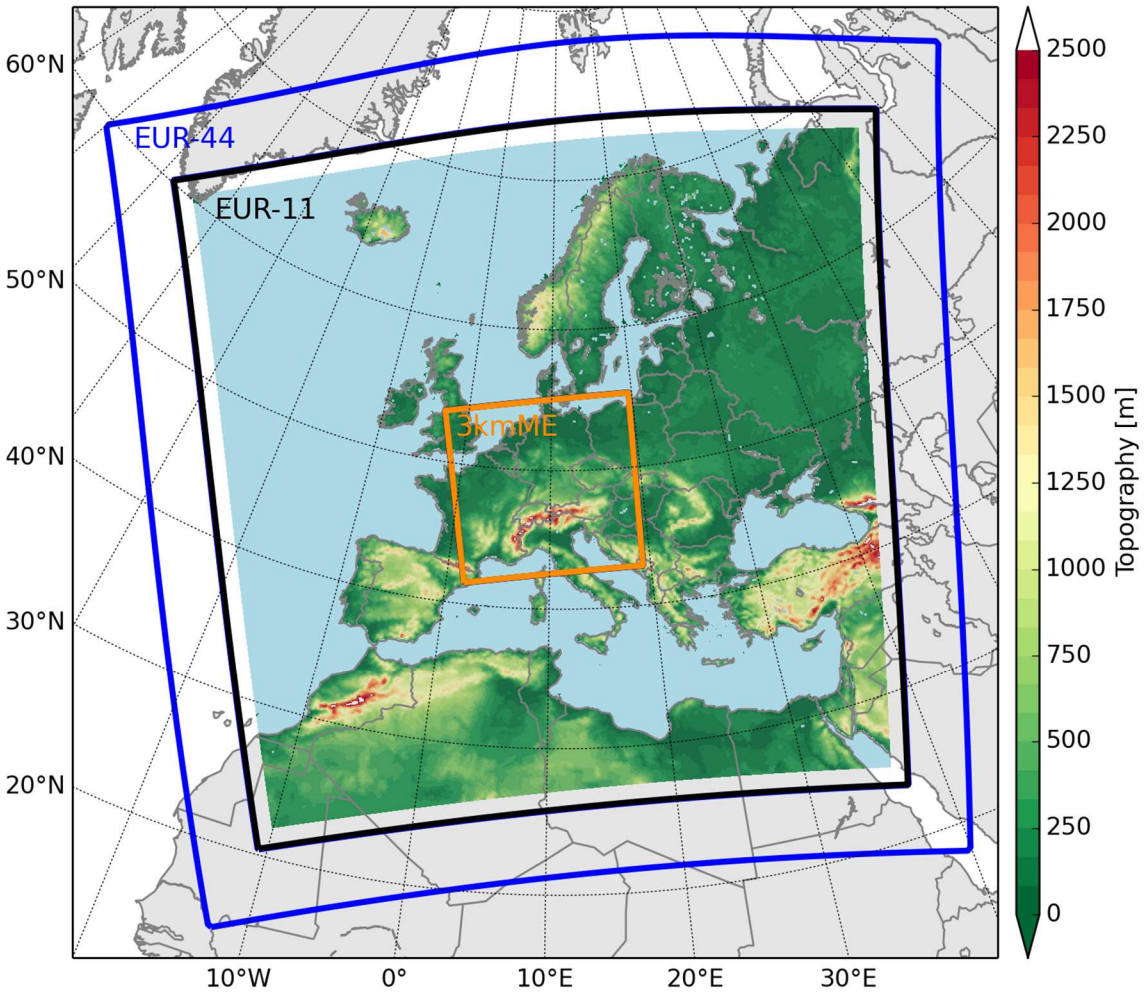

Figure 2.1: Model domains for EUR-44 (blue frame), EUR-11 (black frame) and 3kmME (orange frame) simulations. The coloured topography area indicates the EURO-CORDEX focus domain (see descriptions in the text).

11 refer both to the respective resolution as well as the respective domain throughout this study. The analysis is always done for the focus domain. A detailed description of the experiment design and model settings of the WRF simulations performed within this study is given in Section 2.2.

2.1.2 EURO-CORDEX RCM evaluation simulations

The land-atmosphere coupling analysis (Chapter 3) is based on parts of the EURO-CORDEX evaluation ensemble simulations that have been carried out by different groups participating in EURO-CORDEX (see Knist et al. 2017 and references therein). The evaluation simulations cover the time span from 1989 to 2008. To allow for model spinup, only data from 1990 onwards were used. The RCMs are driven by ERA-Interim reanalysis data at 0.75° resolution (Dee et al. 2011). Thus, the EURO-CORDEX simulations follow the observed large-scale weather conditions and can be compared with observations also

on significantly smaller than climatological time scales. The analysis is performed with the output of 16 RCMs including eight different WRF simulations as a subset of the EURO-CORDEX evaluation ensemble. Thirteen simulations were performed with EUR-44 and three with EUR-11 grid spacing. Table C.0.1 contains an overview of the simulations used in this study, whereby each RCM is identified by a unique abbreviation throughout the study. All WRF simulations use the land surface model (LSM) NOAH (Ek et al. 2003) and the boundary-layer scheme YSU (Hong et al. 2006), but different combinations of other atmospheric parametrization schemes. A detailed description of the different model setups is given in Vautard et al. (2013) and Katragkou et al. (2015). In addition to these main settings, the models also differ e.g. in the configuration of the lateral boundary relaxation zone around the EURO-CORDEX focus domain, the number of vertical levels, or interpolation settings for initial and static fields. These configurations can lead to larger ensemble spreads than for pure multi-physics ensembles (García-Díez et al. 2015). Thus, the ensemble analysed is an "ensemble of opportunity", which merely collects all simulations providing the required fields for the analysis. This also implies some inevitable restrictions when not all desirable parameters for this study were stored, such as upper soil moisture.

2.2 WRF RCM simulations

As mentioned above, RCM climate simulations for the WCRP EURO-CORDEX domain provide the basis for the analysis of land-atmosphere interactions at the continental scale. Furthermore, convection-permitting high-resolution climate simulations are carried out for a Central European domain. For all simulations downscaling both ERA-Interim Reanalysis and CMIP5 GCM MPI-ESM-LR (RCP4.5) data, the WRF model is used. The subsequent sections give a basic introduction of the model in general and a brief overview of the experiment designs and settings used for the several climate simulation runs. Detailed information about the WRF model is provided in the WRF documentation (Skamarock et al. 2008). An overview of all WRF simulations contributing to this study is given in Table 2.3.

2.2.1 The WRF model

The WRF model is a non-hydrostatic regional atmospheric model developed primarily at the National Center for Atmospheric Research (NCAR) and other US weather-related institutions with contributions from a worldwide user community. It can be used for a broad range of applications on different time and spatial scales both for idealized and real atmospheric simulations, e.g. ranging from large eddy simulation case studies to operational weather forecasts of national weather services as well as long-term regional climate

simulations. There are two dynamics solvers available whereof the Advanced Research WRF (ARW) is used in this study. It solves the unfiltered Euler equations on a 3-dimensional Arakawa C-grid. The time integration is done by a 3rd-order Runge-Kutta scheme with a smaller time step for acoustic and gravity wave modes. The horizontal grid is a rotated longitude-latitude grid. For the EURO-CORDEX grid, the rotated North Pole is located at 198°E 38.25°N, so that the equator intersects the model domain. For that reason, the convergence of the meridians is minimal, and the coordinate system has a nearly Cartesian characteristic. In vertical direction the model uses terrain-following coordinates based on dry hydrostatic pressure. To ensure a sufficient vertical resolution 50 vertical levels with a model top layer at 20 hPa are chosen for the model setup.

Because every regional model simulates just a part of the global atmosphere, it needs special lateral boundary conditions (LBC) provided by the driving global model. As a common method for limited area models WRF uses Davies-type LBC. This method uses a relaxation zone of an arbitrary number of grid points at the lateral boundary of the model domain where the values of the outer driving model are gradually fitted to the values of the interior model prognostic variables. In this model setup an exponential relaxation function for the width of ten grid points is used.

In most cases, the data of the global model is available in time steps of a few hours, in this case six hours. In order to provide boundary data for every time step of the inner model, the values are temporally interpolated to generate the lateral boundary values. Previously, data of the coarse outer model grid is spatially interpolated to the finer grid of the inner model. These interpolations are done by the WRF preprocessing system (WPS).

Since many physical processes in the atmosphere, like radiation, grid-scale precipitation, cumulus convection, turbulence, etc. have much smaller characteristic spatial scales than the model grid is able to resolve, these sub-grid scale processes have to be parameterized, i.e. they have to be derived from the grid scale prognostic variables. Thereby, the effective resolution of an atmospheric model is about seven times larger than the grid spacing (e.g. Skamarock 2004). For the WRF model, there are multiple schemes for the same processes available. The use of different combinations of parameterizations can have a significant influence on the simulation results. García-Díez (2014) found that a multi-physics ensemble of the WRF RCM can produce a similar spread as a multi-model ensemble within EURO-CORDEX and García-Díez et al. (2015) confirm that no parameterization combination performs best for all applications.

The following sections give an overview of the settings used for the WRF regional climate simulations each labeled by the same acronym used for publication and throughout this text.

2.2.2 The NOAH land surface model

The NOAH LSM (Chen and Dudhia 2001; Ek et al. 2003) is used for all WRF simulations within this study. It provides the lower boundary conditions for the atmospheric model and calculates the energy balance at the surface as well as fluxes of heat and water. These quantities result from plenty of complex sub-grid scale processes including not just the surface itself but also the subsurface soil. They are sensitively dependent on the spatially and temporally varying properties of the soil texture and vegetation.

At the early stage of numerical weather prediction models the LSM consisted of simple energy balance equations ignoring heat conduction into the soil and assumed a prescribed constant soil moisture. With the Bulk Model of Manabe (1969) the first model with spatial and temporal variation of soil moisture was developed but the vegetation was treated implicitly. Large improvement resulted from the explicit treatment of vegetation. In these so called "second generation LSMs" both soil and canopy interact with the atmosphere. That effects an improvement in the calculation of the latent heat flux since the evaporation from bare soil, water surfaces and plant canopy, and the transpiration through the stomata of the vegetation are calculated separately. With further development, the LSM included more and more complex biophysical, biochemical, hydrological and ecological processes, for example the explicit treatment of the carbon cycle that also improves the process of canopy transpiration related to photosynthesis.

In vertical direction NOAH LSM consists of four soil layers at 0-10 cm, 10-40 cm, 40-100 cm and 100-200 cm depth. Its hydrological physics is based on the diurnally dependent Penman potential evaporation approach (Mahrt and Ek 1984), the multilayer soil model (Mahrt and Pan 1984), and the primitive canopy model (Pan and Mahrt 1987). Soil moisture and soil temperature is calculated for each layer with maximum soil moisture limited to the individual soil type's pore volume. Evapotranspiration (ET) is expressed as the sum of direct evaporation from bare soil, water surface, canopy and sublimation from snow as well as the canopy transpiration via water uptake from roots in the soil is included. Direct bare soil evaporation is estimated from a simple linear method (Betts et al. 1997), and canopy surface evaporation is calculated from similar methods by Noilhan and Planton (1989). Vegetation transpiration is related to the complex process of photosynthesis when the stomata of the green leaves open for uptake and release of CO_2 and water vapor. The numerical measure for this is the canopy conductance. It is estimated by the formulation of Jacquemin and Noilhan (1990), representing the effects of solar radiation, air temperature, vapor pressure deficit and soil moisture. So, vegetation reacts sensitively to heat, dry air and dry soil stress and hence reduce transpiration.

2.2.3 Special settings for climate simulation

Because the simulated physical processes are the same for weather prediction and climate

projection, the model setup for a climate simulation does not differ much from a WRF weather prediction run. For global climate and weather models, the main difference lies in the questions, they seek to answer. Weather prediction models are mainly dependent on the initial conditions to achieve a most accurate forecast of the next days. Climate models are dependent on the boundary conditions like solar radiation, land use types and atmospheric composition of gases and aerosols that affect the way energy is absorbed or exchanged in the earth system. To capture the whole energy cycle also for the energy and mass transport processes on a long time scale, climate models consist of coupled atmospheric and ocean models. Also, a sea ice model is included to directly simulate the important ice-albedo feedback.

Since regional climate models do not simulate the whole earth system with an ocean and sea ice model included, the external forcing for change in the statistics of the climate within the model domain is mainly given by the lateral boundary values from the global climate model. In contrast to regional weather prediction runs, also sea surface temperature and sea-ice cover are variable lower boundary conditions prescribed by the driving global model. Thus, not just the annual cycle of these variables, but also its year-to-year change is forced to the RCM.
In addition to the changing external forcing given by the lateral and lower boundary conditions from the GCM, the radiative forcing of the increasing concentrations of greenhouse gases (RCP 4.5 in this case) is taken into account by the radiation scheme. A sensitivity test with one simulation using RCP4.5 gas concentrations and one using the 20^{th} century default reveals significant differences between both. The higher concentrations in RCP4.5 lead to increased downward longwave radiation at the land surface and thereby higher mean temperature.

Although exact initial conditions are less important for a long-term climate simulation it is suitable to start a model simulation with accurate initial values to reduce the spinup time of the model. Here, spinup means the adjustment of the modeled soil variables to their realistic values consistent to the respective soil type and atmospheric forcing.
The initial values for the WRF model run are provided by horizontally and vertically interpolated values of the GCM, which also applies to soil variables. This can cause inconsistencies because in most cases the LSM of the GCM differ from the RCM. First, due to their coarse spatial resolution, GCM data do not represent the heterogeneity of the RCM soil textures. Also, the definition of soil moisture or soil water content can differ. Despite skilled interpolation and conversion of units, the initial values for the WRF LSM may be inconsistent for many grid points of the model domain.
Compared to the time scales of the atmospheric processes, the soil variables react slowly to the atmospheric forcing. The deeper the soil layer, the longer is the spinup time for soil

moisture and soil temperature. Investigation of the spinup of the soil variables (by comparison of several runs with different dates of cold start) reveals that for regions with very less precipitation or a long period of frozen soil, it takes more than one annual cycle for the deep soil moisture to adjust.
To reduce the spinup of the soil layers, the initial soil moisture and soil temperature fields as well as the snow cover is either taken a former WRF climate simulation with the same resolution or at least a coarser WRF simulation, whenever it exists. Thus, at least the coarse soil moisture patterns are consistent and can adjust much faster on the local scale.

2.2.4 WRF EURO-CORDEX simulations

The first part of this study (Chapter 3) is based on RCM simulations of the previously described EURO-CORDEX domain which have been carried out by several partners of the EURO-CORDEX community. As part of this RCM ensemble, an ERA-Interim driven WRF simulation is used that has been carried out by Klaus Görgen. This simulation uses the WRF version 3.3.1 with the modified Kain-Fritsch deep convection scheme (Kain 2004), WSM 6-class cloud microphysics scheme (Hong and Lim 2006), CAM radiation scheme and YSU PBL scheme (Hong et al. 2006). In the following, this model configuration is labeled as WRF331A. Lateral boundary data is provided by 6-hourly ERA-Interim reanalysis data (0.75° grid) (Dee et al. 2011) for the simulation time span from 1989 to 2010.
The same model setup WRF331A has been used to dynamically downscale the global climate model data from MPI-ESM-LR (RCP4.5) for the control period from 1951 to 2005 and for the future scenario from 2006 to 2100. The GCM data is provided at 6-hourly time steps with 1.875° horizontal grid size. Unfortunately, these simulations could not be used for the analysis, since a software bug in the WRF model caused an erroneous pattern at the domain's lateral boundaries that evolves for long term transient simulations. A detailed description and analysis of this issue is given in the Appendix A.

Table 2.1: WRF parameterization setups in WRF331A and WRF361N.

Model ID	Radiation scheme	Convection scheme	Microphysics scheme	Boundary layer scheme	Land-surface model	Land use
WRF331A	CAM3.: (Collins et al. 2004)	Modified Kain-Fritsch: (Kain 2004)	WSM 6-class: (Hong and Lim 2006)	YSU: (Hong et al. 2006)	NOAH: (Ek et al. 2003)	IGBP-MODIS 30''
WRF361N	RRTMG: (Iacono et al. 2008)	Grell-Freitas: (Grell and Dévényi 2002)	WSM 5-class: (Hong et al. 2004)	YSU: (Hong et al. 2006)	NOAH: (Ek et al. 2003)	IGBP-MODIS 30''

A new EUR-44 simulation downscaling MPI-ESM-LR has been carried out with a patched WRF v3.6.1 and modified parametrization settings compared to WRF331A. This model

setup, in the following named as WRF361N, uses the Grell-Freitas convection scheme (Grell and Dévényi 2002), WSM-5 microphysics (Hong et al. 2004), RRTMG radiation (Iacono et al. 2008) and YSU PBL scheme (Hong et al. 2006). The decision results from several validation studies of WRF EURO-CORDEX evaluation simulations by Kotlarski et al. (2014), García-Díez et al. (2015) and Katragkou et al. (2015) as well as own tests. An overview of both WRF331A and WRF361N setups is shown in Table 2.1.

2.2.5 WRF convection-permitting climate simulations for Central Europe

The second part of this study (Chapters 5, 4 and 7.1) is based on convection-permitting regional climate simulations that are carried out for a Central European domain with 0.0275° (~3 km) grid spacing (480 × 456 grid points) in a one-way double nesting setup. The central European domain (in the following named as 3kmME) is nested into a pan-European 0.11° (~12 km, 448 × 436 grid points) domain slightly larger than the Euro-CORDEX focus domain (see Figure 2.1). For both domains the same model settings (WRF361N) and parametrizations are used, except for the Grell-Freitas convection scheme (Grell and Dévényi 2002) that is just used in the 12 km simulation and switched off in the 3 km simulation. The 3kmME domain is directly nested into the parent EUR-11 domain, i.e. both simulations run simultaneously, and boundary data is provided with every time step of the coarse simulation. Thus, both resolutions have almost identical atmospheric conditions at the boundary of the Central European (sub-)domain and the 3 km simulation does not suffer from coarse temporal interpolation of the boundary values. To allow for an analysis of the diurnal cycle and phenomena with short typical time scales (e.g. extreme precipitation events), output is written in hourly time steps.

Two experiments have been conducted both using the same model setup as described above. First, evaluation climate simulations have been carried out for three time slices from 1993 to 1995, 2002 to 2003 and 2010 to 2013. These time spans are chosen to cover most of the interannual variability in central Europe including both cold and hot climate events in central Europe, e.g. wet winter 1994, wet summer 2002 and dry and hot summer 2003. Lateral boundary data for the EUR-11 domain is provided by 6-hourly ERA-Interim reanalysis data (0.75° grid) (Dee et al. 2011). Each of the time slices run with a two month spinup starting in November of the previous year. Initial soil moisture, soil temperature and snow are taken from the former ERA-Interim driven 20-year WRF331A EUR-11 simulation. The results are discussed in Chapter 5.

For the second experiment, three each 12.5 yearlong simulations have been carried out that downscale global climate model data of the MPI-ESM-LR (same as downscaled for EUR-44) for a control time period (CTRL; 1993-2005) and mid-century (MOC; 2038-2050) and end-of-century (EOC; 2088-2100) future scenarios using an RCP4.5 greenhouse gas scenario

(see Section 7.5 and 7.6).

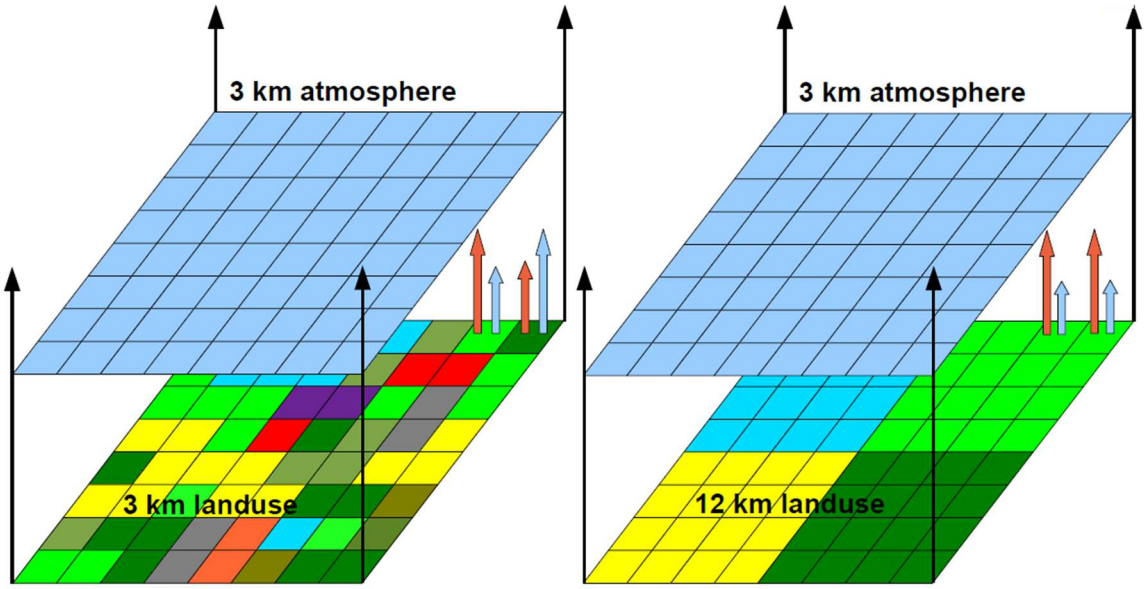

Figure 2.2: Experiment design of land surface sensitivity simulations on 3 km grid with original 3 km land use (left) and 12 km land use (right).

2.2.6 WRF sensitivity runs on land surface properties resolution

Chapter 6 investigates the resolution effect of individual land surface properties such as land use and soil type, orography and soil moisture.

For this sensitivity study, the same WRF/ARW model version and set up WRF361N as for the decadal convection-permitting simulations is used: The Central European domain 3kmME with 3 km grid spacing (480 × 456 grid points) is nested into the pan-European 12 km domain (EUR-11, 448 × 436 grid points). Five simulations have been run each with the same setup of the atmosphere in 3 km resolution but with different combinations of land surface properties in coarse 12 km resolution. Since the setup of the driving EUR-11 simulation is identical for all five simulations and there is no feedback from the inner 3kmME to the EUR-11 domain identical lateral boundary conditions are provided for the 3kmME domain. Thus, differences in the individual sensitivity runs only result from the different land surface properties as the horizontal grid as well as the atmospheric parametrizations are identical for all simulations. Lateral boundary data for the EUR-11 domain is provided by 6-hourly ERA-Interim reanalysis data (0.75° grid). The simulated time period covers the summer months (JJA) in 2003 that are characterized by both many convective precipitation events in June as well as a prominent dry and hot period in August. To separate the resolution effects of the individual land surface properties, five different setups have been prepared (Table 2.2). Since the soil type classification has a coarser than 3 km resolution, no additional simulations with 12 km soil type and e.g. 3 km land use have been run.

Table 2.2.: Resolution of land use, initial soil moisture and orography in each sensitivity simulation setup.

	Land use and soil type	Initial soil moisture	Orography
Setup A	12 km	12 km	12 km
Setup B	12 km	12 km	3 km
Setup C	12 km	3 km	3 km
Setup D	3 km	3 km	12 km
Setup REF	3 km	3 km	3 km

Setup of coarse land use and soil

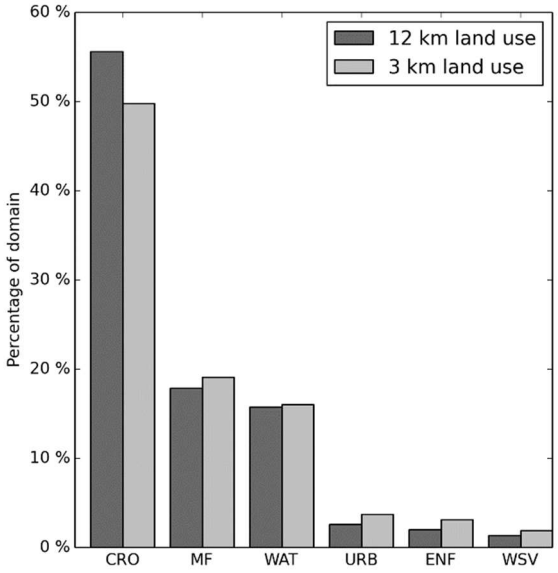

Figure 2.3.: Percentage of most frequent land use types in 3 km and 12 km resolution.

For all simulations, the WRF model and its land surface model NOAH is run with 3 km grid size. To get the desired coarse resolution of the land surface properties, the corresponding static parameters had to be changed. Within the WRF preprocessing system, the static parameters are created by the *geogrid.exe* program that interpolates the original static geographical data set (MODIS) onto the defined WRF grid. Once these static fields are defined, WRF and NOAH calculate the soil and surface variables based on these constant parameters throughout the simulation. Since the 3 km grid exactly fits into the driving 12 km grid, the land use and soil type related parameters have been taken from the EUR-11 wrfinput_d01 file and written to the original 3 km wrfinput_d02 file. Each 16 grid cells of the 3 km grid get the same value from one corresponding 12 km grid cell to get a coarsely resolved surface field in the 3 km simulation (Figure 2.2). Thereby, the percentages of individual land use types slightly change (Figure 2.3). It is important to note that the NOAH LSM does not use a mosaic approach but uses just the dominant land use type of one grid box. So, a single grid box doesn't take account of subgrid-scale

heterogeneity.

Setup of coarse orography

Since the orography of the land surface also determines the model's vertical grid levels, the manipulation of the orography is done one step earlier in the WRF preprocessing system. The 12 km orography is written to the 3 km geo_em_d02 preprocessing file that defines the horizontal grid and the land surface properties. Based on the new geo_em_d02 file, the preprocessing program *real.exe* is run again to interpolate the atmospheric input data onto the vertical model levels. While the interpolation of the coarse 12 km land use data onto the 3 km grid is done by nearest neighbor resampling, a distance weighted bilinear interpolation is used for the orography. For some grid cells, a nearest neighbor interpolation causes very steep slopes between the neighboring grid cells. Though a test simulation with this configuration runs numerically stable, unrealistic wind patterns evolve along the steep slopes. Therefore, the smoother bilinear interpolated orography is used for the simulations.

Setup of initial soil moisture

All simulations have been initialized with interpolated atmospheric variables from ERA-Interim. The soil temperature and soil moisture values as well as the snow variables have been taken from the former simulated EUR-11/3kmME evaluation run that started in November 2001. For the sensitivity runs with 12 km land use and soil type (setup A and B), the initial soil variables have been taken from the EUR-11 simulation and for those with 3 km land use and soil type from the 3kmME simulation (setup D and REF). It is important to note that in addition to the different horizontal pattern the overall mean soil moisture values are slightly different between the EUR-11 and 3kmME simulation, mainly due to different precipitation characteristics. For that reason, an additional setup C that uses 12 km land use and soil type (like setup B) is initialized with 3 km soil moisture from the 3kmME simulation.

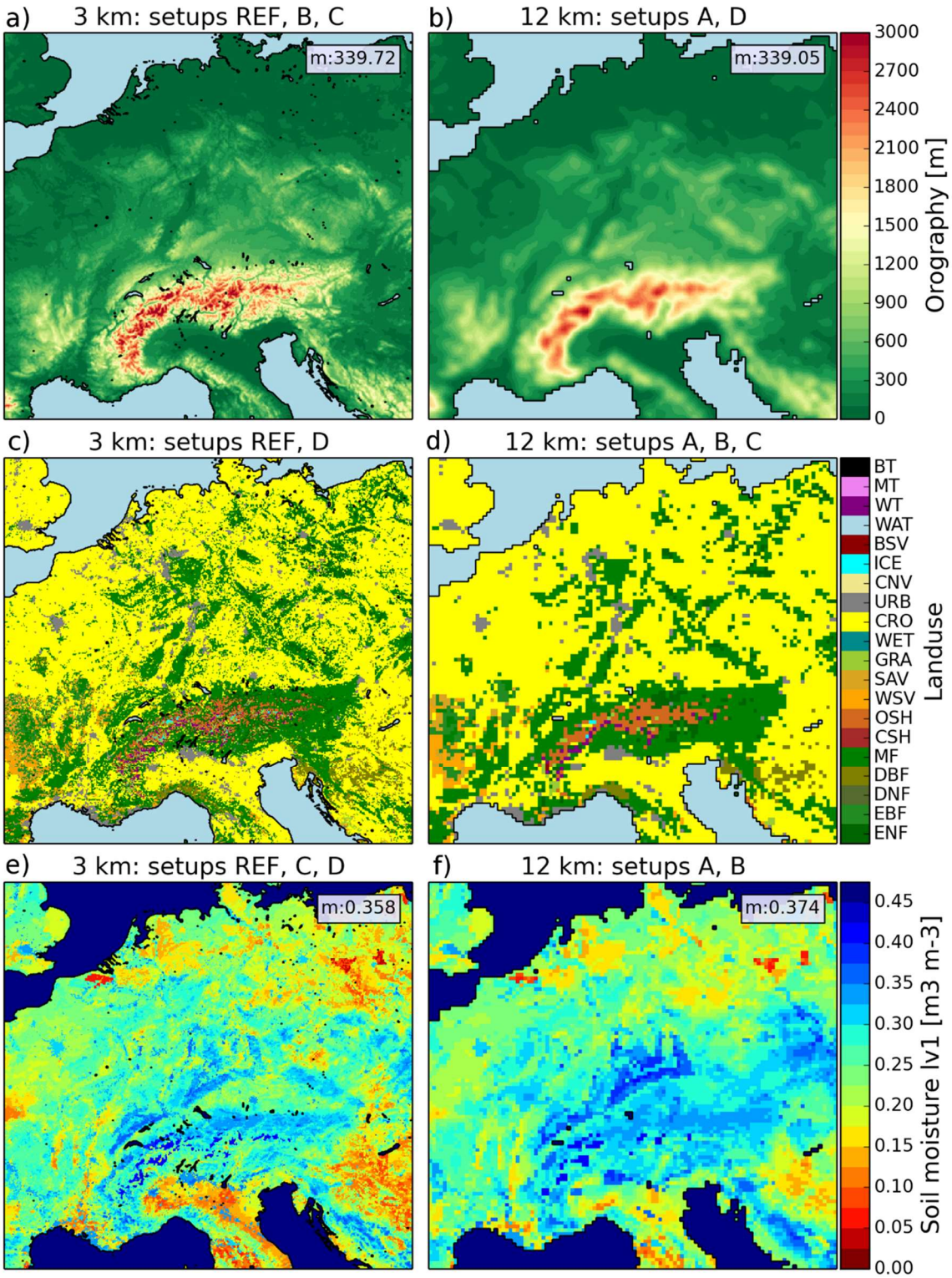

Figure 2.4.: Model orography (a, b), land use (c, d) and initial soil moisture (e, f) in 3 km (a, c, e) and 12 km resolution (b, d, f). Dominant land use types within the model domain are ENF: evergreen needleleaf forest; EBF: evergreen broadleaf forest; MF: mixed forest; WSV: wooded savanna; SAV: savanna; GRA: grasslands; WET: wetlands; CRO: cropland; URB: urban; ICE: snow or ice; BSV: barely/sparsely vegetated; WAT: water; WT: wooded tundra; MT: mixed tundra.

Table 2.3.: Overview of all WRF simulations contributing to this study.

Setup	Experiment	Forcing	Domain	Period	Out	Comment
						EURO-CORDEX evaluation runs
WRF331A	Evaluation	ERA-Interim	EUR-44	1989-2010	3hr	
WRF331A	Evaluation	ERA-Interim	EUR-11	1989-2010	3hr	
						Sensitivity study on bug at lateral boundary
WRF361N	Evaluation	ERA-Interim	EUR-44	1989-2008	3hr	without boundary patch, JUROPA2
WRF361N*	Evaluation	ERA-Interim	EUR-44	1989-2008	3hr	with boundary patch, JUROPA2
WRF361N*	Evaluation	ERA-Interim	EUR-44	1989-2008	3hr	with boundary patch, JURECA
WRF361N*	Evaluation	ERA-Interim	EUR-44	1989-2008	3hr	with boundary patch, JURECA, shifted initialization
						EURO-CORDEX CMIP5 GCM Downscaling
WRF361N	Historical	MPI-ESM-LR	EUR-44	1950-2005	3hr	Re-run of former WRF331A RCP4.5 run with new
WRF361N	RCP4.5	MPI-ESM-LR	EUR-44	2006-2100	3hr	WRF version, improved settings, boundary patch
						Convection-permitting evaluation runs for ME
WRF361N	Evaluation	ERA-Interim	EUR-11/ 3kmME	11/1992-12/1995	1hr	Direct 1-way-nesting of 3kmME into EUR-11
WRF361N	Evaluation	ERA-Interim	EUR-11/ 3kmME	11/2001-12/2003	1hr	
WRF361N	Evaluation	ERA-Interim	EUR-11/ 3kmME	11/2009-12/2013	1hr	
						Conv. perm. control and projection runs for ME
WRF361N	Historical	MPI-ESM-LR	EUR-11/ 3kmME	1993/07-12/2005	1hr	control time period (CTRL)
WRF361N	RCP4.5	MPI-ESM-LR	EUR-11/ 3kmME	2038/07-12/2050	1hr	near future projection, mid-of-century (MOC)
WRF361N	RCP4.5	MPI-ESM-LR	EUR-11/ 3kmME	2088/07-12/2100	1hr	far future projection, end-of-century (EOC)
						Sensitivity study on land surface resolution
WRF361N	Eval./Test	ERA-Interim	EUR-11/ 3kmME	06-08/2003	1hr	12 km land use/soil, 12 km initial sm, 12 km orog.
WRF361N	Eva./Test	ERA-Interim	EUR-11/ 3kmME	06-08/2003	1hr	3 km land use/soil, 3 km initial sm, 12 km orog.
WRF361N	Eval./Test	ERA-Interim	EUR-11/ 3kmME	06-08/2003	1hr	12 km land use/soil, 12 km initial sm, 3 km orog.
WRF361N	Eval./Test	ERA-Interim	EUR-11/ 3kmME	06-08/2003	1hr	12 km land use/soil, 3 km initial sm, 3 km orog.
WRF361N	Eval./Test	ERA-Interim	EUR-11/ 3kmME	06-08/2003	1hr	3 km land use/soil, 3 km initial sm, 3 km orog.
						Sensitivity study on influence of soil moisture
WRF361N	Eval./Test	ERA-Interim	EUR-11/ 3kmME	08/2003	1hr	Heat wave Aug 2003 with different soil moisture

2.2.7 General modelling framework and workflow

Downscaling of MPI-ESM-LR and ERA-Interim data requires several working steps including data retrieval, preprocessing, the actual model runs and data postprocessing. Major challenges for long term climate simulations are a long compute time as well as a large amount of data that accumulates for the different steps of processing. This requires supercomputing resources that allow for parallel computing and large data storage capacity as well as an efficient work- and data flow. The whole experiments are built on the infrastructure of the Juelich Supercomputing Center (JSC), in particular the supercomputer JUROPA, respectively its successor system JURECA[3].

For MPI-ESM-LR forcing data, additional steps of preprocessing are done before the GCM data can be used by the WRF preprocessing system (WPS). For that reason, additional tools have been developed including procedures of data conversion, interpolation, hydrostatic pressure calculation, etc. The actual preprocessing, i.e. the interpolation of the data onto the WRF model's grid and generation of the lateral forcing data files, is done by the WPS. Once the forcing data is produced the particular WRF simulations are started.
For the WPS and WRF model run control and data handling, a flexible and robust script system has been developed. It includes compilation, working directory structure, WPS and WRF simulation runs and a semi-automatic revision and documentation system. Thus, all model simulations are replicable regarding the stored environmental settings and the model settings itself given by the model's namelist.
The long runtime of the climate simulations requires restarts as the compute time of individual jobs on the supercomputer is limited. The EUR-44 simulations are restarted monthly, meaning the run-control script re-initiates itself after each successfully simulated month to restart the subsequent month. Thus, the output files exist in a well-manageable size. For the simultaneously running EUR-11/3kmME simulations that are much more computationally costly, restarts are done every five days and output is written in daily files each containing 24 hourly output times.
To make the model outputs compliant with the requirements of the CORDEX project and reduce the data volume, output data is postprocessed. This includes temporal aggregation, vertical interpolation on pressure levels, file-naming conventions, terms of meta-data, data formats, etc. For this purpose, a high-efficient postprocessing tool has been developed.

2.2.8 Computational resources of WRF on HPC Clusters

As mentioned above, all WRF simulations are performed on supercomputers JUROPA and JURECA at the Juelich Supercomputing Centre (JSC).

[3] http://www.fz-juelich.de/ias/jsc/EN/Expertise/Supercomputers (last visited 20.01.2018)

To assess the needed compute time for the long-term climate simulations and to find the optimum domain decomposition, the model code performance is analysed. Since the problem size defined by the domain size and the model time step is invariant a so-called strong scaling study is carried out. For each domain, WRF is run with a different number of central processing units (CPUs) and nodes and for the same simulated time of one month. Figure 2.5 exemplarily shows the scaling results for the EUR-11 domain on the JUROPA cluster. Starting with 32 CPUs as reference, the normalized speedup in wallclock runtime by stepwise doubling the number of CPUs is shown. Ideally, the speedup would be 100% per CPU doubling step, but with a larger number of sub-domains that run simultaneously on each CPU, the increasing communication reduces the overall speedup. The parallel efficiency (speedup ratio divided by ideal speedup) is still 65% for 256 CPUs. As the nested 3kmME domain has a similar number of grid points compared to the EUR-11 domain, the scaling behavior is similar for the simultaneously running EUR-11/3kmME simulation. Hence, these simulations are run using 256 CPUs on JUROPA (228 CPUs on JURECA). Wallclock time for one simulated month is approximately 24 h, whereby queueing time for submitted jobs on the supercomputers lead to actual much longer time to complete the simulations. For all simulations performed within these study (see Table 2.3), about 5 Million core hours compute time are used, and the data volume sums up to approximately 700 TB.

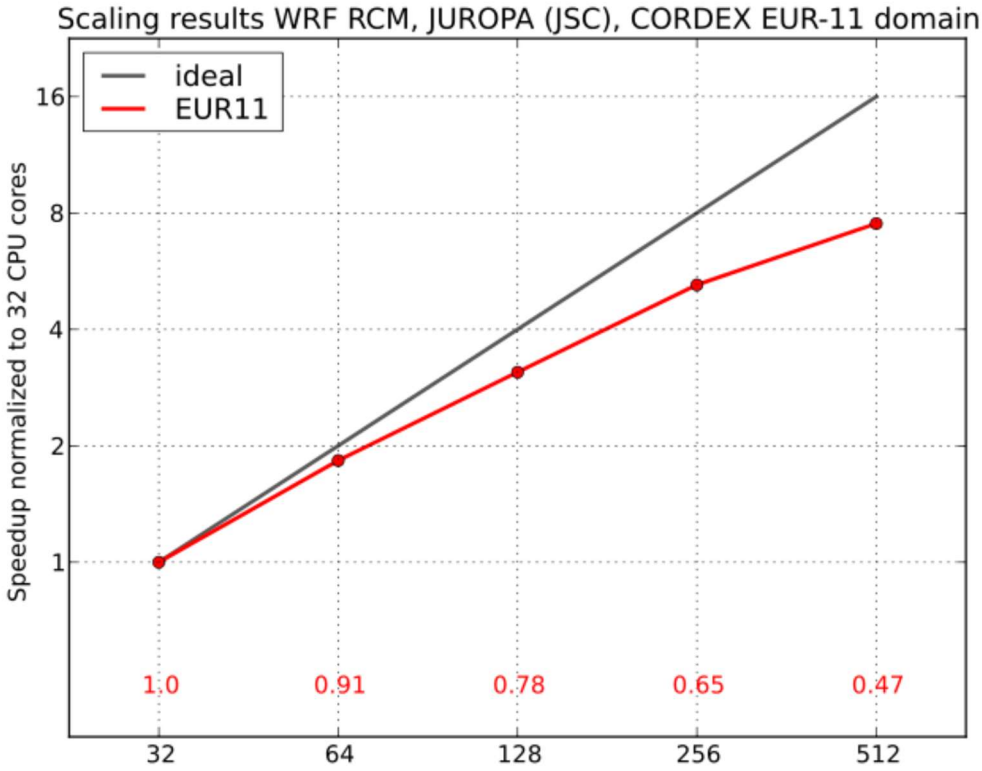

Figure 2.5: Scaling behaviour of WRF331A in climate mode on the JUROPA Linux cluster of JSC, strong scaling study for EUR-11 domain (448 × 436 × 50). Numbers given at the bottom are scaled parallel efficiencies (speedup ratio divided by ideal speedup).

2.3 Observational data

The following section introduces several observational datasets for the evaluation of several ERA-Interim driven RCM simulations. The first two (GLEAM and FLUXNET) are used for the analysis of land-atmosphere coupling in EURO-CORDEX RCM evaluation ensemble runs (Chapter 3). The station data of the national meteorological services in Germany and Switzerland are used for the analysis of precipitation statistics in the convection-permitting WRF simulations (Chapter 5).

2.3.1 GLEAM

For the evaluation of soil moisture and latent heat flux in the EURO-CORDEX evaluation ensemble as well as the coupling metric calculated from the correlation of latent heat flux and 2 m temperature (introduced in the next sub-section), the Global Land Evaporation Amsterdam Model (GLEAM) dataset version v3a (Martens et al. 2016) is used. It provides terrestrial evaporation and root zone soil moisture based on satellite-observed soil moisture through data assimilation of European Space Agency Climate Change Initiative soil moisture (ESA CCI SM) (Liu et al. 2011b; Wagner et al. 2012)), vegetation optical depth (Liu et al. 2011a) and snow water equivalents (Armstrong et al. 2005), ERA-Interim reanalysis air temperature and radiation, and the Multi-Source Weighted-Ensemble Precipitation (MSWEP) product (Beck et al. 2016). The daily data are provided on a global 0.25° grid and covers the period from 1980 to 2014. To ease the comparisons between the simulated and GLEAM data, both data are projected on to a rotated 0.22° latitude-longitude grid by nearest neighbour resampling. This grid has the same rotated pole (198.0; 39.25) as the EURO-CORDEX domain. For comparison with EUR-44 simulation data, the four points of the 0.22° grid fitting into one EUR-44 grid cell, are averaged. For the EUR-11 simulation data, a four-point RCM average is compared with the 0.22° grid GLEAM data. Only grid points defined as land points in both the RCM's and the satellite data's land masks are considered.

2.3.2 FLUXNET

Simulated latent and sensible heat fluxes of the EURO-CORDEX RCM evaluation runs are compared with the European FLUXNET[4] observations (Baldocchi et al. 2001). This data product contains pre-processed, quality-checked and instrument error-corrected observations from eddy covariance flux tower stations operated over central Europe with a highly variable data coverage from 1996 to 2007. FLUXNET point observations are

[4] See www.fluxdata.org

compared with RCM time series from the closest grid point. Only days for which all half-hourly values have a quality flag 0 or 1 (representing original or high quality gap filled data) and only months with a minimum of 20 high-quality days are taken into account. In total 42 stations meet these criteria with at least three years of high-quality data each; see Figure 3.7 for their geographic location. Since the simulations are driven by reanalysis data only at the lateral boundaries, the simulated weather conditions inside the RCM model domain on local and daily scales may differ considerably from the actual weather experienced at the FLUXNET stations. Hence, mean seasonal cycles are compared similar to e.g. Jaeger et al. (2009) are shown for four representative stations from contrasting climate regions and different vegetation types: Cabauw (the Netherlands), Las Majadas (Spain), Hyytiala (Finland), and Roccarespampani (Italy).

For the interpretation of the comparison, it is important to note that eddy covariance flux tower measurements can be systematically too low and that the energy balance is often not closed (Stoy et al. 2013; Wizemann et al. 2015). In order to assess this systematic error, a comparison of all energy balance components including ground heat flux and net radiation is needed. Under the assumption that the radiation measurement errors are much smaller than the turbulent flux measurement errors, the net radiation is considered as a reference and the systematic underestimation of the observed heat fluxes is estimated to range from 0% to 40% for each of the 42 stations. For all but one station, the sum of the three surface fluxes is 30% to 35% lower than the net radiation. Analogous to Jaeger et al. (2009), the residual is assumed to be caused by equally underestimated turbulent fluxes and thus added to the latent and sensible heat flux following the Bowen ratio. In reality, however, the residual depends on terrain, surface properties and the condition of the atmospheric boundary layer and thus a correct Bowen ratio is just an assumption (Ingwersen et al. 2011; Wizemann et al. 2015).

2.3.3 Rain gauge station data

Two national station datasets that provide hourly data are used for the evaluation of the ERA-Interim driven WRF EUR-11 and 3kmME simulations (see results in Chapter 5). 1014 rain gauge stations in Germany provided by the Deutscher Wetterdienst[5] (DWD) and 80 stations in Switzerland from the MeteoSwiss ANETZ[6] (automatic monitoring network) are used. The location of the stations is shown in Figure 1.1, whereby the color indicates different height ranges. All Swiss stations cover the complete evaluation time span and about 80% of the German stations provide data for at least seven years. Temperature observations are collected for all Swiss stations and most of the German stations (594).

[5] ftp://ftp-cdc.dwd.de/pub/CDC/observations_germany/climate/hourly/precipitation/historical

[6] https://gate.meteoswiss.ch/idaweb/login.do

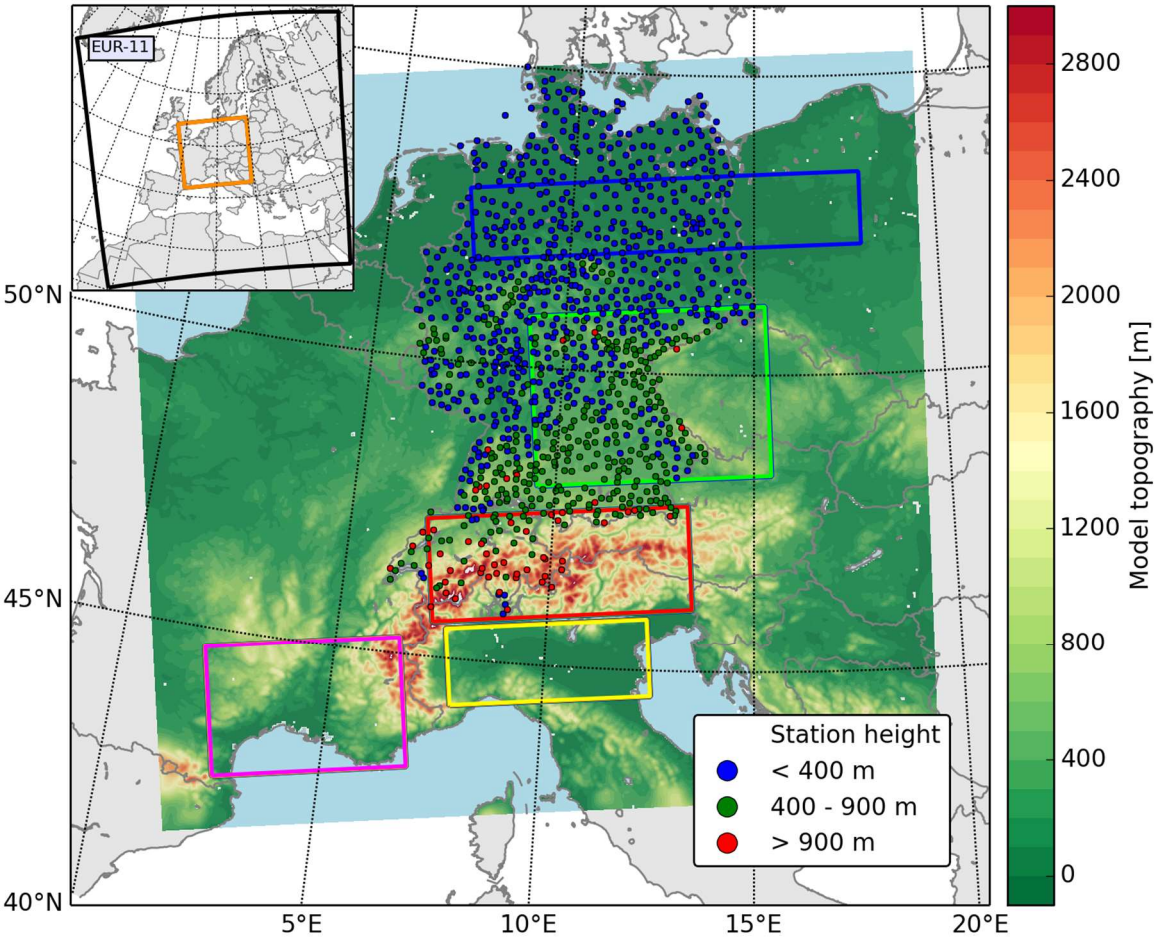

Figure 2.6: Central European model domain (3 km grid size) nested into EURO-CORDEX domain (12 km grid size, EUR-11) as shown in small map upper left. Dots show rain gauge stations for different altitude ranges (blue: <400 m, green: 400-900 m, red: >900 m). Colored boxes indicate different analysis regions (blue: Lowlands, green: Uplands, red: Alpine, yellow: Northern Italy, pink: Southern France).

2.4 Land-atmosphere coupling metrics

In general, land-atmosphere coupling strength can be defined as the degree to which the atmosphere responds to anomalies in the land-surface state (Koster et al. 2006). Depending on the region and the climate, the land surface can amplify or dampen exchange fluxes and feedbacks associated with interactions between the land and the atmosphere (Lorenz et al. 2015). In this context, coupling strength is an important integrative diagnostic for the exchange processes between the land-surface and the atmosphere and can strongly affect climate and climate extremes.

Several metrics have been defined for quantifying this coupling strength depending on the variables involved and the feedback processes addressed, e.g. by Seneviratne et al. (2006), Dirmeyer (2011), Miralles et al. (2012) and Decker et al. (2015). The methods can be separated in two major groups addressing either soil moisture–temperature or soil moisture–precipitation feedback processes, albeit not all methods necessarily use the soil moisture variable in their formulas. In the following, several metrics to quantify soil-moisture temperature coupling strength are presented, also including those methods ultimately used in this study as not all are suitable for our purpose. This listing is not intended to be exhaustive but gives a short overview of the diversity in metrics and applications. Further metrics addressing soil moisture–precipitation coupling have been investigated but have not been suitable either for the available data or the particular European climate zones.

Koster et al. (2004, 2006) presented the first model-intercomparison study focused on land–atmosphere coupling: the Global Land–Atmosphere Coupling Experiment (GLACE-1), where the coupling strength was quantified for a single boreal summer. The GLACE-1 coupling measure Ω_X measures (Koster et al. 2006) was estimated for two ensembles of GCM simulations. The first is a write ensemble, where soil moisture is calculated interactively and is different in every ensemble member (ensemble W). Soil moisture is written out at every time step from one ensemble member (W1). In the second ensemble (ensemble R), soil moisture is identical in every ensemble member; the data from W1 is read back into the model and substitutes the soil moisture calculation. 16 members are run for each of the write ensembles and read ensembles as described in Koster et al. (2006). The measure

$$\Omega_X = \frac{16\sigma_{\hat{X}}^2 - \sigma_X^2}{15\sigma_X^2} \tag{1}$$

with σ_X^2 being the intraensemble variance of the atmospheric quantity X (e.g. temperature or precipitation) and $\sigma_{\hat{X}}^2$ being the corresponding variance of the ensemble mean time series.

In GLACE-1, this measure quantifies sub-seasonal soil moisture–atmosphere coupling, that is, for ensemble simulations with 16 members that are run over a season only. First, six-day means or totals (means for temperatures, totals for precipitation) are calculated from every simulation. The variable σ_X^2 is calculated as the variance across six-day means or totals from the whole ensemble. Next, the ensemble mean time series is calculated that is then used to obtain $\sigma_{\bar{X}}^2$ variance of the ensemble mean. The variable $\Delta\Omega_X$ can then be calculated based on the two different variances as

$$\Delta\Omega_X = \Omega_X(R) - \Omega_X(W) \tag{2}$$

Seneviratne et al. (2006) proposed alternative $\Omega_{X,G}$ and $\Delta\Omega_{X,G}$ coupling measures in analogy to the GLACE-1 measures to assess the impact of soil moisture–climate coupling on longer time scales. These measures are computed using multiyear simulations instead of ensemble simulations for a single year (or season), with one simulation being fully interactive and the other simulation using prescribed climatological soil moisture (i.e., removing the interannual variability of soil moisture). The variable $\Omega_{X,G}$ assesses the degree of interannual and intraseasonal similarity in each experiment (Seneviratne et al. 2006):

$$\Omega_{X,G} = \frac{N\sigma_{\bar{X}}^2 - \sigma_X^2}{(N-1)\sigma_X^2} \tag{3}$$

with N being the number of years $\Omega_{X,G}$ is calculated across. The variable $\sigma_{\bar{X}}^2$ is the variance calculated from the N-year climatology, analogous to Ω_X, where it is calculated from the ensemble mean. The variable σ_X^2 is calculated from N times 14 six-day means in each season and thereby includes both the interannual as well as the intraseasonal variability. The difference between $\Omega_{X,G}$ from the control run and from the uncoupled experiment with the prescribed climatological seasonal soil moisture cycle gives the coupling measure $\Delta\Omega_{X,G}$. Hence, as noted by Seneviratne et al. (2006), $\Omega_{X,G}$ represents the extent to which the removal of interannual variability of soil moisture increases intraseasonal and interannual similarity (or decreases variability).

Though these GLACE coupling measures provide fundamental benchmark for identifying 'hot spot' regions of strong coupling, they are based on a special experiment design of computationally expensive ensemble simulations and cannot be applied to standard GCM/RCM output or evaluated against observations.

Many methods are based on correlations between characteristic variables connected to surface exchange processes. They address in particular the soil moisture–temperature feedback process and allow for a diagnosis of energy limited and soil moisture limited regimes.

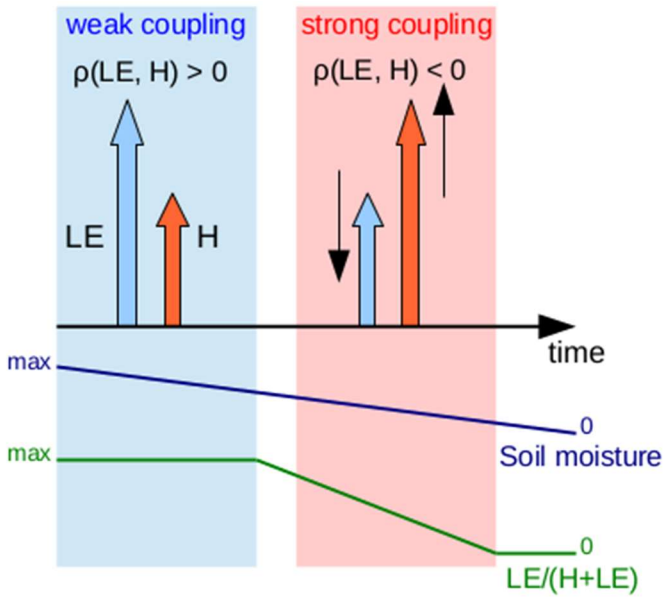

Figure 2.7: Definition of coupling regimes by use of the correlation of latent (LE) and sensible (H) heat flux.

One coupling metric is the correlation ρ between the sensible heat H and latent heat flux LE as both variables are the components of the surface energy balance, which compete for the redistribution of net surface radiation energy into other energy forms:

$$\rho(LE, H) \tag{4}$$

For energy limited regions soil moisture is available in sufficient amounts. In this case, land surface temperature also dictates near-surface atmospheric humidity resulting in concordant near-surface moisture and temperature gradients and a positive correlation between both fluxes (Figure 2.7). For water-limited regions, however, soil moisture limits evapotranspiration and thus also near-surface atmospheric humidity and its gradient, while temperature gradients and sensible heat fluxes may still increase in response to increasing radiation. Since latent heat fluxes in turn further reduce soil moisture, correlations between the two fluxes become smaller or even negative. In this case even small changes in soil moisture affect the near-surface atmosphere profoundly. Figure 2.8 shows exemplarily the H-LE-correlation based on daily mean values for the JJA summer seasons in 2002 and 2003 for the ERA-Interim driven EUR-44 WRF simulation. Contrasting patterns appear for central and western Europe: In 2003 negative correlations indicate strong coupling related to anomalous warm and dry conditions, which culminated in the well-known western European heat wave in August. In contrast, the summer season of 2002 is characterized by rather wet conditions giving rise to positive turbulent flux correlations in this region. Regarding the noisy pattern in Northern Africa, please note that the H-LE correlation based metric is only meaningful in regions where evapotranspiration is reasonably large.

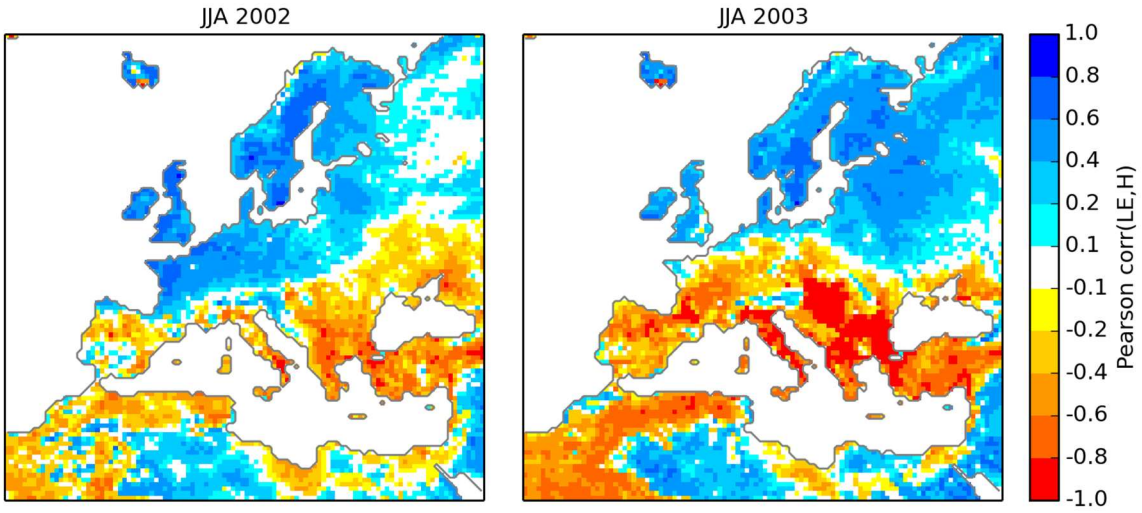

Figure 2.8: Correlation of daily mean latent and sensible heat flux for summer (JJA) (left) 2002 and (right) 2003 based on the ERA-Interim driven WRF EUR-44 simulation.

Other correlations, such as air temperature correlated to latent heat flux or net radiation correlated to latent heat flux as defined by Seneviratne et al. (2006), are also considered as a useful land-atmosphere coupling metrics:

$$\rho(LE, T) \tag{5}$$

$$\rho(LE, R_n) \tag{6}$$

Miralles et al. (2012) defined an observationally based soil moisture–temperature coupling measure Π based on long-term correlations as

$$\Pi = \rho(H, T) - \rho(H_p, T) \tag{7}$$

where ρ is the Pearson's correlation coefficient, H is the sensible heat flux and H_p is calculated using net radiation R_n and an estimate of the potential latent heat flux LE_p such that $H_p = R_n - LE_p$. The potential latent heat flux LE_p is the latent heat flux that would occur if a sufficient water source was available and is estimated in Miralles et al. (2012) by following an approach by Priestley and Taylor (1972).

Dirmeyer (2011) and Dirmeyer et al. (2014) split land–atmosphere coupling into two pathways: a terrestrial segment linking the state of the land to the surface fluxes and an atmospheric segment linking the surface fluxes to the state of the atmosphere. The first leg indicates the potential of the land surface to influence the atmosphere, so it is a necessary but not sufficient condition (Dirmeyer 2011). The second leg then adds the influence from the surface fluxes on the atmospheric state to the full land–atmosphere feedback. The terrestrial first leg can be the influence from any land surface variable A (e.g. soil moisture) on any surface flux B (latent or sensible heat flux):

$$I_{A,B} = \sigma(A)\beta(A,B) \tag{8}$$

where $\sigma(A)$ is the standard deviation of A and $\beta(A,B)$ the slope of the linear regression of A and B. In the same way, the second leg $I_{B,C}$ is calculated for the surface flux B and an atmospheric variable C (e.g. temperature or lifting condensation level). The full two-legged index is then derived by adding the second leg to the first leg:

$$I_{A,C} = \sigma(A)\beta(A,B)\beta(B,C) \tag{9}$$

All of the metrics mentioned above need time series of the individual variables with a certain length to provide significant results. In general, they can be applied to different temporal scales and can be based on daily to seasonal averages. However, interpretation and direct comparison of coupling strength has to be done with care when different temporal averages are used. The coupling metrics are not able to assess instantaneous or at least daily coupling strength. Furthermore, some metrics are not well-suited for a direct comparison of different RCMs and/or observations, when individual variables of the metric are derived differently (e.g. the calculation of the potential evaporation or differing depths of soil layers and saturation levels for soil moisture).
In general, there is no unique way to define land atmosphere coupling strength and since different metrics address individual processes in the complex land-atmosphere feedback system they can show different results. Also a direct comparison of different coupling metrics is hampered since the value ranges and units differ and the definition of "strong" and "weak" may not be consistent. Lorenz et al. (2015) suggest that specific coupling experiments like GLACE are required to scale the different measures for each particular climate model.

Within this study, in the land-atmosphere coupling analysis in Section 3.4, the intercomparison of the EURO-CORDEX RCM ensemble is first based on H-LE-correlations calculated from 10-day mean values over the summer seasons of the full period 1990-2008. This H-LE-correlation is the diagnostic that is used to access coupling strength in comparison to the FLUXNET station data. Furthermore, the correlation of evaporative fraction (LE / H+LE) and total soil moisture is used for the RCM intercomparison of the link between soil moisture and flux partitioning. As a further coupling metric, the correlation of latent heat flux (LE) and 2 m air temperature (T) based on 10-daily mean summer (JJA) values of the period from 1990 to 2008 is used as a coupling metric, also in order to evaluate the RCM results against the values calculated from the GLEAM evaporation and ERA-Interim 2 m air temperature. Using ERA-Interim air temperatures seems most suitable since these temperature data are also used as forcing data for GLEAM. While both metrics describe

the soil moisture-temperature coupling process, the H-LE-correlation indicates the process of changing flux partitioning at the surface, the LE-T-correlation describes the second step of the feedback pathway into the atmosphere.

For the land-atmosphere coupling analysis of the ERA-Interim driven EUR11/3kmME WRF simulations (see Section 4.2), the H-LE-correlation and the coupling index $I_{SM,LE}$ between soil moisture and latent heat flux are used as coupling measures.

3 Land-atmosphere coupling in EURO-CORDEX evaluation simulations

3.1 Introduction

This chapter investigates the land-atmosphere coupling in a subset of 16 RCM simulations from the ERA-Interim driven EURO-CORDEX ensemble over the period from 1990 to 2008 (see Section 2.1.2)[7]. Previous evaluation studies focussing on temperature and precipitation reveal large differences between the individual RCM simulations (Vautard et al. 2013; Kotlarski et al. 2014; Katragkou et al. 2015). These differences may be either directly or indirectly related to the reproduction of the land-atmosphere coupling in these models. The focus is on soil moisture-temperature feedbacks during the summer months of June, July and August, when the land-atmosphere coupling is most relevant.

First, the reanalysis-driven simulations are particularly evaluated with respect to soil moisture, latent and sensible heat flux, which have not been examined in previous EURO-CORDEX evaluation studies. Model output for soil moisture and surface fluxes is compared to a satellite-based root zone soil moisture dataset (Section 3.2) and with turbulent heat fluxes derived from FLUXNET flux tower measurements (Section 3.3), respectively. An adequate reproduction of these variables is mandatory for a realistic coupling strength simulation.

In Section 3.4, two coupling strength metrics, based on the correlation of the simulated surface sensible and latent heat fluxes as well as latent heat flux and air temperature, are then applied to the simulations and compared to station observations from FLUXNET and gridded dataset GLEAM, respectively. The results are summarized and discussed in Section 3.5.

3.2 Evaluation of soil moisture

The different LSMs in the RCMs analysed have very different soil characteristics; thus, a direct comparison of the available total (i.e. vertically integrated) soil moisture is not meaningful. Especially, the differing depths of the soil layers and the saturation levels related to soil porosity, make a grid point-wise comparison of the total soil moisture amounts of the individual models difficult. Despite exhibiting different mean total soil moisture amounts, the RCMs are expected to reproduce typical intra- as well as interannual variability for different regions in Europe.

[7] This chapter follows closely the contents in Knist et al. (2017) including all figures.

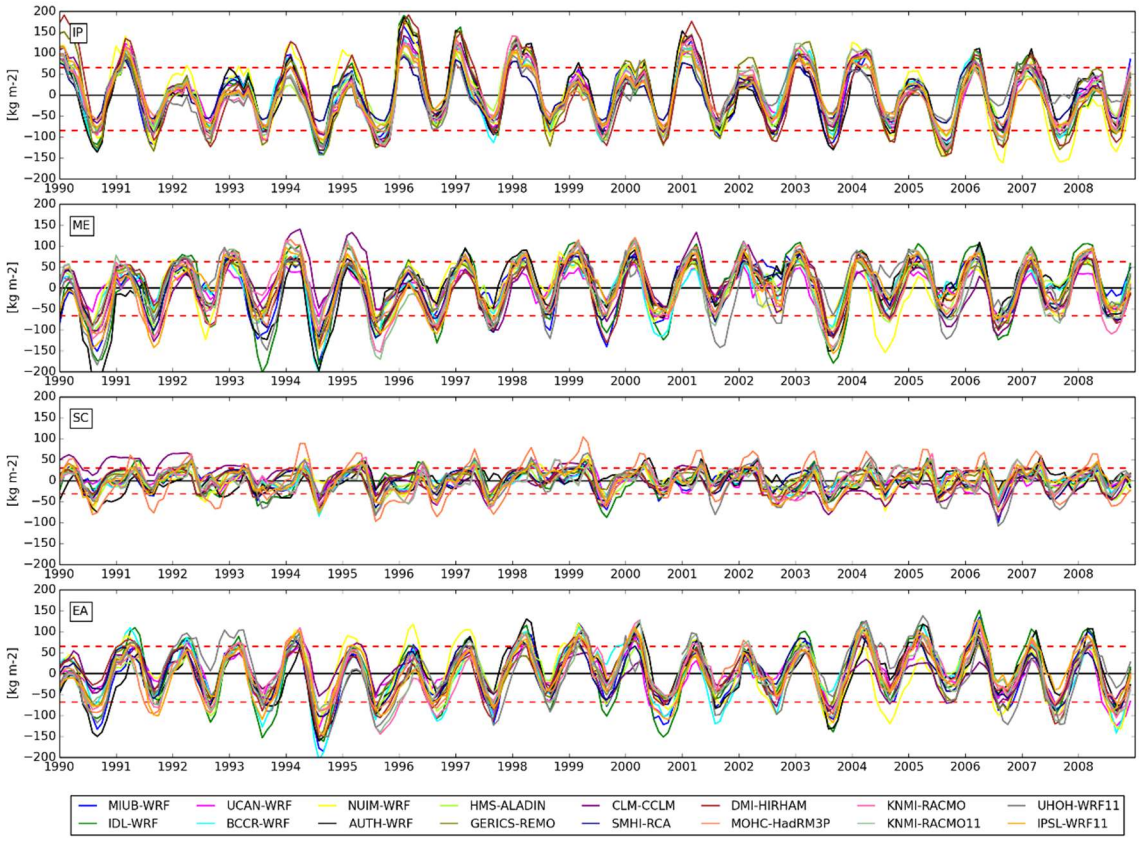

Figure 3.1.: Time series of total (vertically integrated) soil moisture anomalies (individual RCM mean 1990–2008 subtracted) averaged for PRUDENCE regions Iberian Peninsula, middle Europe, Scandinavia, and eastern Europe (see location in Figure C.0.15. Red dashed lines indicate the ensemble mean annual minimum and maximum values averaged for the whole time span.

Though the different soil characteristics still affect the potential maximum dynamic range (min minus max) of the models, subtraction of the individual RCM's long-term mean from total soil moisture monthly means allows for a comparison of the annual cycle and representation of wet and dry anomalies in individual years and regions (Figure 3.1). For all regions, all RCMs' soil moisture time series show a clear annual cycle. The average maximum soil moisture is reached in March and the minimum in September with overall agreement between the RCMs and slight interannual variability in timing. In the southern European regions, the minimum is reached a few weeks later. The mean range between yearly minimum and maximum multi-model mean (indicated by the red dashed lines) is dependent on the soil characteristics and the climate conditions.

With a precipitation maximum during winter and high demand for evapotranspiration during the dry summer months, the Iberian Peninsula shows the largest mean range with 140 kg m-2, compared to also well pronounced amplitudes of 120 kg m^{-2} and 110 kg m^{-2} in eastern and central Europe. In Scandinavia the range is much smaller, the annual cycle is less pronounced and the individual RCM simulations are less correlated to each other when the annual cycle is removed. The weaker annual cycle is related to overall wet conditions

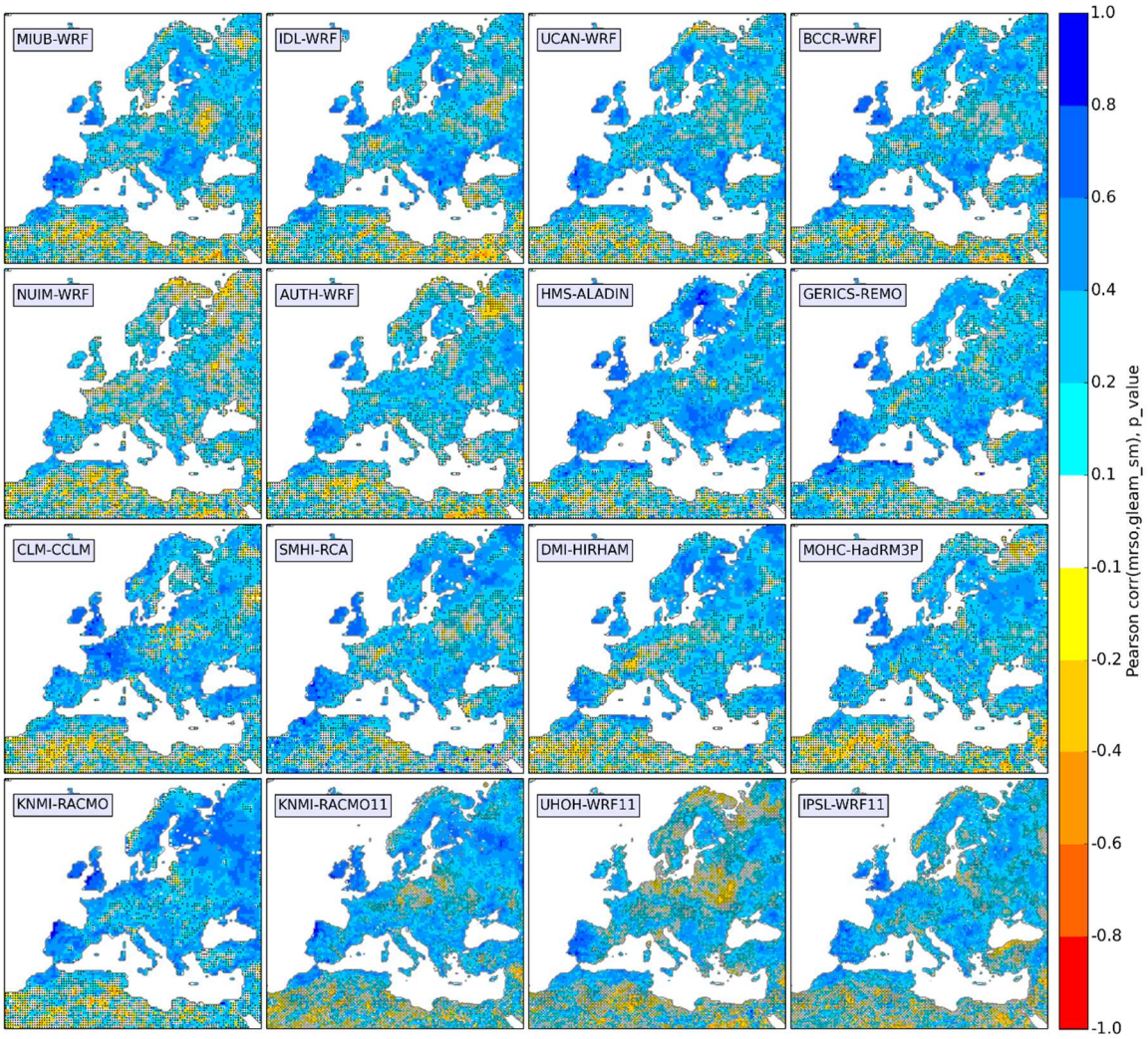

Figure 3.2: Correlation of GLEAM volumetric near-root zone soil moisture and vertically integrated total soil moisture in individual RCM simulations (monthly means subtracted by individual RCM's long-term monthly means, JJA, 1990 to 2008, dotted where correlation is below 5% significance level).

throughout the year and a smaller amount of evapotranspiration in this energy-limited high latitude region. Here, the differences in the annual cycle between the RCMs most likely result from effects of snow cover and frozen soils. For all regions, a distinct inter-annual variability is evident, both for the maxima and minima as well as for the seasons in between. The variability of the minima is larger than the maxima in those regions where the winter is wet enough to reach near saturation conditions frequently, as seen e.g. in central Europe (standard deviation of ensemble mean yearly minima is 24.1 kg m^{-2} versus 14.8 kg m^{-2} for the maxima). For the Iberian Peninsula also soil moisture maxima during winter show a larger inter-annual variability (here, the standard deviation of the minima is 13.9 kg m^{-2} versus 32.3 kg m^{-2} of the maxima). Despite some outliers for some models and years, the RCMs show overall good agreement in simulating the soil moisture

differences between individual years; anomalously wet and dry seasons are captured quite consistently, e.g. the wet conditions during the summer 2002 in central Europe and the very dry summer in 2003 or the wet year 1996 in the Iberian Peninsula region.

So far, the RCMs intra- and interannual variation in vertically integrated total soil moisture have been intercompared amongst each other. In the following, the RCMs ability to reproduce the GLEAM soil moisture (with assimilated ESA CCI satellite based soil moisture) patterns for Europe is investigated. The comparison of the RCMs total soil moisture to the GLEAM root zone soil moisture is restricted to the correlation of summertime monthly means for JJA over the period from 1990 to 2008 (Figure 3.2). Since the soil moisture typically follows an annual cycle that per se leads to a positive correlation, consequently the individual RCM's mean annual cycle is subtracted so that the correlation is based on monthly anomalies from the individual long term monthly means. Overall, the RCMs show significant positive correlation with the GLEAM soil moisture for large parts of Europe. Except for the pluvious Moroccan-Algerian Atlas region, there is no significant correlation for Northern Africa due to the very dry summer conditions and hence small soil moisture variations. The comparison shows regional differences for the individual RCMs correlation to GLEAM soil moisture. While in some regions e.g. the Iberian Peninsula and the British Isles, a positive correlation prevails, in other regions, e.g. Poland and Ukraine the RCMs predominantly do not show a significant correlation with GLEAM. Although RCMs like KNMI-RACMO, HMS-ALADIN and IPSL-WRF have larger areas of positive correlation with the GLEAM soil moisture, no single RCM is outperforming the others across the domain. Even though the WRF RCMs feature the same LSM, there is no WRF-specific soil moisture pattern. For example, the MIUB-WRF and IDL-WRF simulations show a high correlation in southeastern Europe while the NIUM-WRF and AUTH-WRF simulation are not significantly correlated with the GLEAM soil moisture in this region. For northeastern Europe the KNMI-RACMO simulations show the largest agreement with the GLEAM data. Comparing both resolutions (EUR-44 and EUR-11) the large-scale pattern is similar; differences remain on the local scale. When all months of the other seasons are taken into account the patterns are similar, however, the correlation is generally slightly higher (data not shown).

In general, areas of uncorrelated RCM to GLEAM soil moisture may exist for multiple reasons, both from the models and data point of view: differences in soil and vegetation parameterization, unrepresented lateral soil moisture flow and irrigation as well as internal variability of weather patterns in the individual RCM runs. The latter may explain the higher correlations in western parts of Europe, where the weather patterns possibly agree better and the internal variability is smaller due to the closer distance to the western lateral

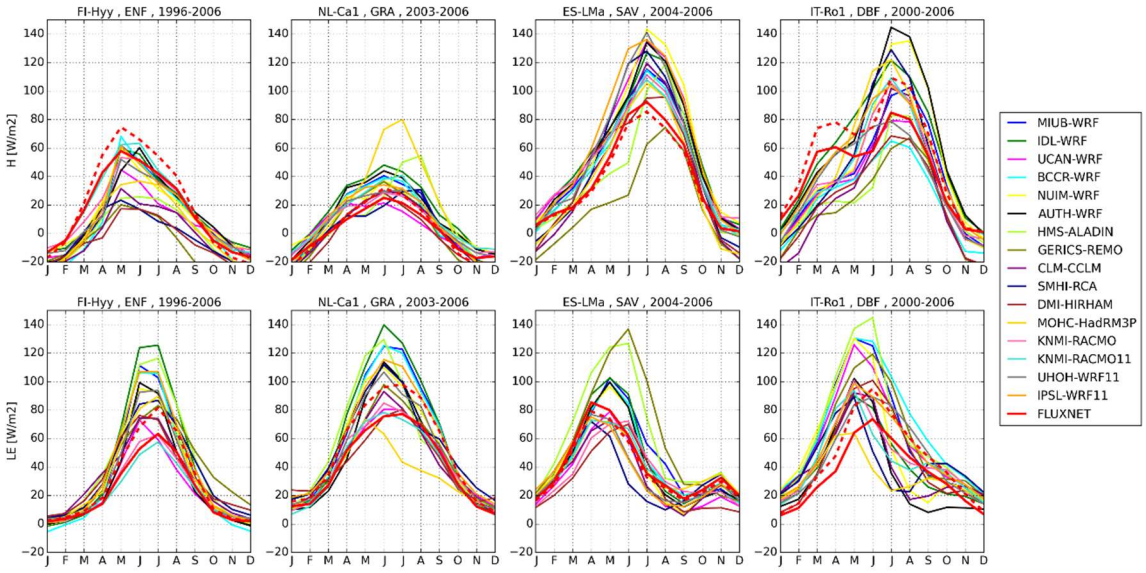

Figure 3.3: Mean annual cycles of monthly mean of (top row) sensible and (bottom row) latent heat flux at four representative FLUXNET stations (thick red line) and derived from the closest model grid points. The red dashed line indicates an estimated correction of the flux tower measurement bias by adding the residual of the energy balance according to the Bowen ratio (assuming net radiation and ground heat flux to be correct). Only years with high-quality FLUXNET data are included. Stations from left to right are Hyytiala (Finland) with evergreen needleleaf forest (years 1997–2006), Cabauw (Netherlands) with grassland (years 2003–2006), Las Majadas (Spain) with savanna (years 2004–2006), and Roccarespampani-1 (Italy) with deciduous broadleaf forest (years 2000–2006).

boundary and prevailing westerlies. This would need some further investigation.

Unfortunately, it is not possible to directly intercompare absolute values of total soil moisture or to determine biases for the different RCM's LSMs. In different models (and also for same models but different soil texture and vegetation type) the same amounts of soil moisture may be an indication of energy limited conditions in one and soil moisture limited conditions in another model. The impact on the flux partitioning however is decisive for the coupling to the atmosphere, which will be investigated in the following sections. To this point the RCMs have shown reasonably well reproduction of the 1990-2008 soil moisture interannual and intraseasonal variability.

3.3 Evaluation of surface fluxes

The following section investigates the RCMs representation of both latent and sensible heat flux. Mean seasonal cycles of latent and sensible heat flux simulated by the 16 member EURO-CORDEX ensemble are compared for four FLUXNET stations representative for different climate zones (Figure 3.3). Both data sets are averaged over the subset of years for which high quality FLUXNET data are available.

The typical soil moisture related partitioning between latent and sensible heat as captured

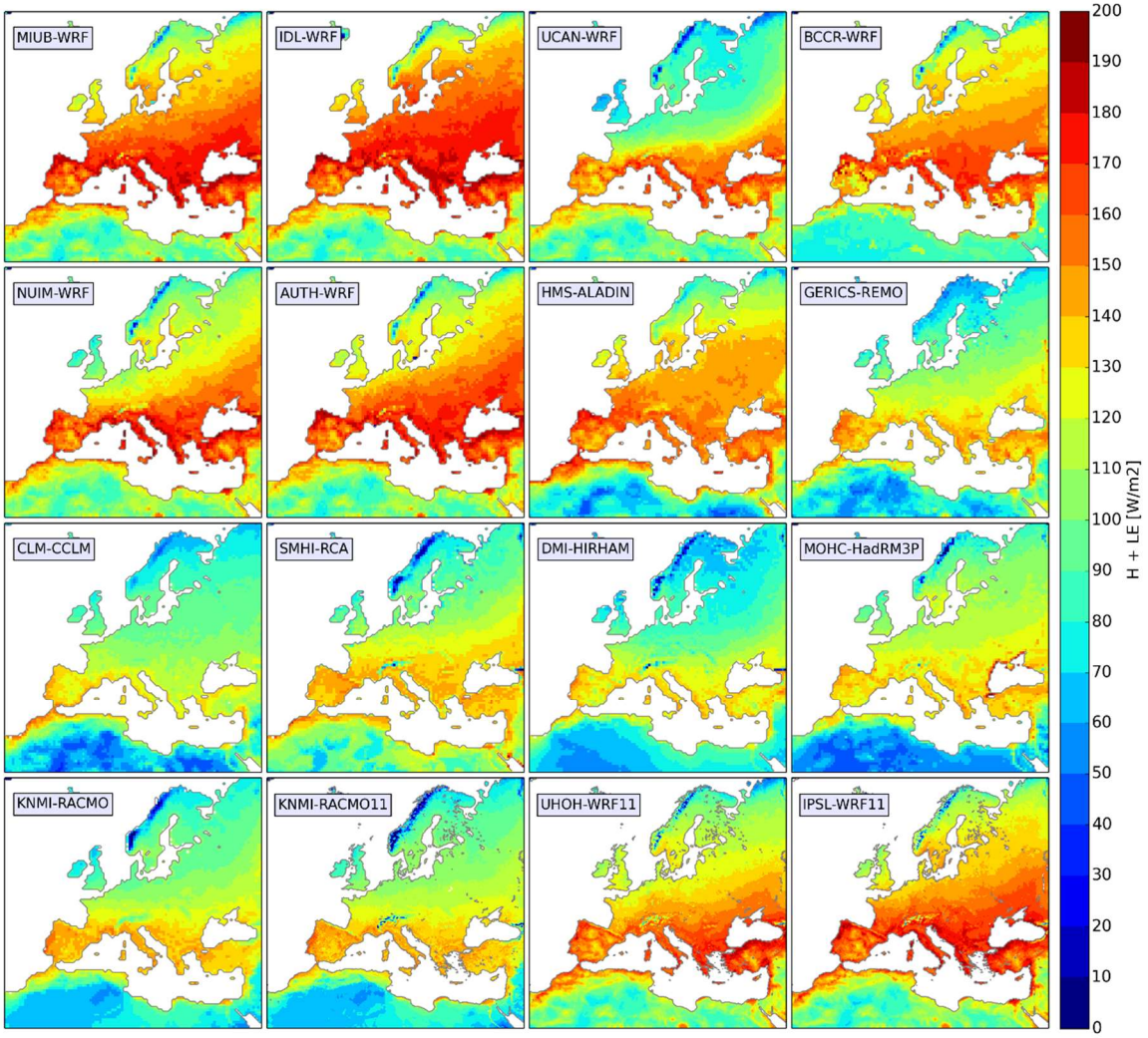

Figure 3.4: Spatial distribution of the summer (JJA) mean sum of latent and sensible heat flux, between 1990 and 2008. The averages were computed over the complete time span including nighttime values, which explains the comparatively low maxima.

by the FLUXNET observations is reproduced by the RCM ensemble. For example, in the Netherlands, where conditions with high soil moisture prevail, latent heat fluxes on average exceed sensible heat fluxes, whereas in Spain the sensible heat flux dominates in summer due to soil moisture limitation while latent heat flux is highest in spring. Individual model simulations, however, may differ substantially from the FLUXNET observations and show larger differences for some locations (see e.g. the comparison at station IT-Ro1). Such differences can be related to different land use types at the station and in the model, which stresses the sensitivity of flux partitioning to surface characteristics. Model runs at the higher EUR-11 resolution better represent surface heterogeneities, but the 12 km $\times$ 12 km grid cells are still much larger than the typical footprint of a flux tower station. Moreover, even results from individual model runs with exactly the same surface type differ owing to differences in atmospheric conditions that may evolve in response to internal model variability, especially in net radiation and soil moisture, a key variable for flux partitioning.

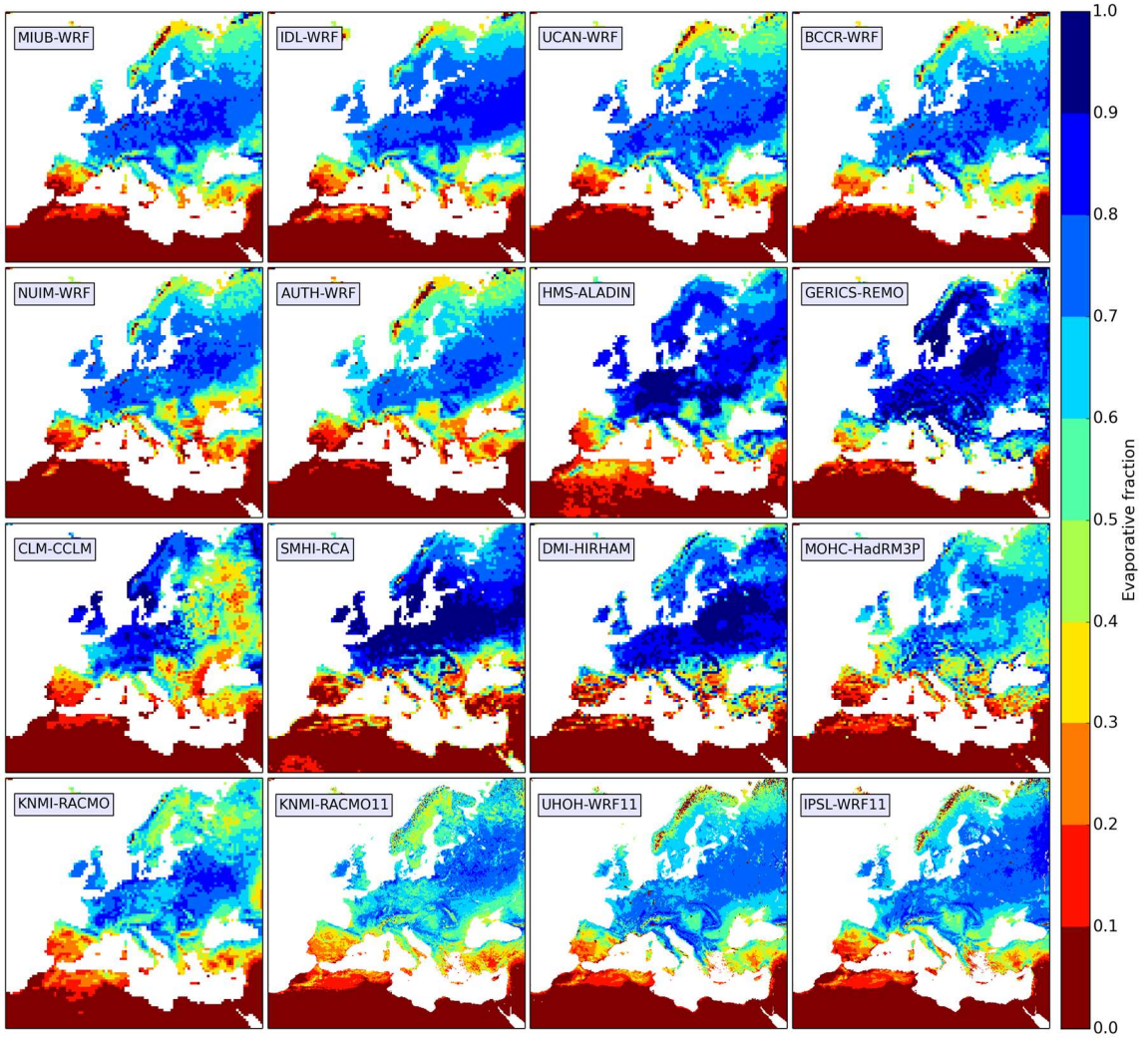

Figure 3.5: Summer (JJA) mean of the evaporative fraction (latent heat flux divided by the sum of latent and sensible heat flux) for the years 1990 to 2008.

Despite these limitations, the FLUXNET data product is the only data set that allows for such a direct evaluation of the model fluxes.

While the expected seasonal cycle is the dominant feature, both in the observations and in the RCM simulations, the maxima produced by the individual RCMs differ substantially, e.g. up to 40-80 W m-2 in summer both for H and LE. Since the WRF RCMs use the same LSM and mostly the same surface type, the variation between the runs must be attributed to different climate states generated due to the different atmospheric parameterizations.

The effects of the differences in the simulated net radiation are obvious by comparing the sum of the summertime (JJA) turbulent surface fluxes for the EURO-CORDEX domain (Figure 3.4). As already seen for the model grid points near FLUXNET stations (Figure 3.3) also this domain-wide comparison depicts systematic differences between particular RCMs. For example the UCAN-WRF underestimates both surface heat fluxes resulting from very low net radiation, which mostly result from reduced incoming solar radiation caused by relatively high cloud cover as shown by Katragkou et al. (2015).

Most RCMs simulate the expected climate-related patterns in flux partitioning expressed by the mean evaporative fraction in Figure 3.5: dry summer climates show low evaporative fractions e.g. in the Mediterranean region, while over wetter central and northeastern Europe latent heat fluxes exceed sensible heat fluxes.
For some regions, however, differences between the ensemble members can be large. For example, HIRHAM, RCA and ALADIN simulate very high evaporative fractions (reaching up to five times higher latent than sensible heat flux) for central, northern and eastern Europe. The different WRF simulations in turn show relatively low evaporative fractions over Scandinavia especially in the mountainous regions, which can be explained by the land cover type "barren tundra" in their common NOAH LSM and not by different climate conditions. In the WRF simulations also the grid points classified as "urban" stick out with almost zero evapotranspiration. Especially in the Mediterranean the models differ also in the spatial distribution of variability, which is most probably also a result of different land surface parametrizations. For the eight WRF model simulations the differences only result from diverging climate conditions due to the distinctly different sets of atmospheric parameterizations, dynamics settings, or slightly different initial conditions. For these runs, differences in flux partitioning are consistent with differences in near-surface soil moisture. The relatively dry conditions simulated by AUTH-WRF and NUIM-WRF for southeastern Europe contrast clearly with the wetter UHOH-WRF simulation. The connection between soil moisture and flux partitioning is given in the next section.

3.4 Land-atmosphere coupling analysis

3.4.1 EURO-CORDEX ensemble comparison to FLUXNET

The distinctly different seasonal cycles of latent versus sensible heat flux for different climate regions (Figure 3.3) suggest their correlation as an indication of coupling strength as introduced in Chapter 2.4. The correlation of latent and sensible heat is based on non-overlapping 10-day means over the summer season (JJA) over the years 1990 to 2008 and calculated for each individual RCM (Figure 3.6).
For all RCMs, weak coupling (positive correlation) prevails over northern Europe while strong coupling (negative correlation) dominates southern and southeastern Europe. This finding roughly coincides with regions attributed with strong coupling in Seneviratne et al. (2006), Fischer et al. (2007) and Miralles et al. (2012). For central Europe, the location of the transition zone from one regime to the other differs considerably between some RCMs. Especially UCAN-WRF and DMI-HIRHAM locate the transition zone further to the south

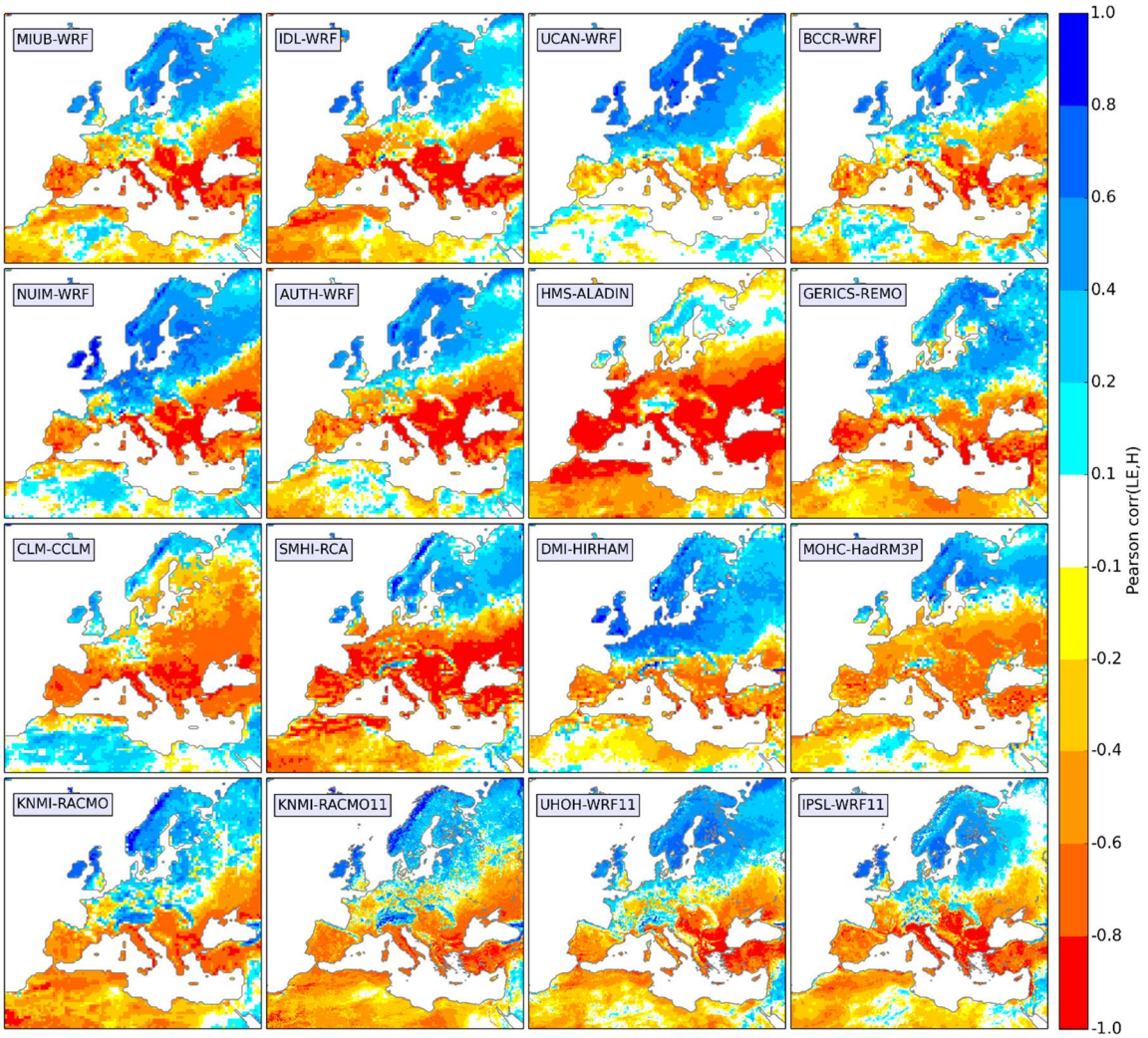

Figure 3.6: Correlation of summer (JJA) 10-day averages of latent and sensible heat flux for the years 1990 to 2008.

compared to the other RCMs while CLM-CCLM and HMS-ALADIN show strong coupling over a larger area which even reaches Scandinavia and Russia. For the other seasons (data not shown) coupling is much weaker than in summer. For Northern Africa the results have to be interpreted with care, since the H-LE-correlation is not meaningful in regions with very low evapotranspiration.

On the regional scale, much of the spatial heterogeneity in coupling strength can be related to orography, respectively its influences of more precipitation, more cloud cover and colder temperatures. The Carpathians, Alps and Pyrenees display substantially weaker coupling strength compared to the surrounding flatter terrain.

There are many possible reasons for the differences in the RCM runs that cannot be clearly separated from each other. On the one hand, the different climate model states (e.g. seen in the parameters precipitation, net radiation, etc.) evolving in the individual model runs due to different atmospheric parametrizations and other settings have a major influence on the coupling strength. This influence is clearly seen for the individual WRF simulations

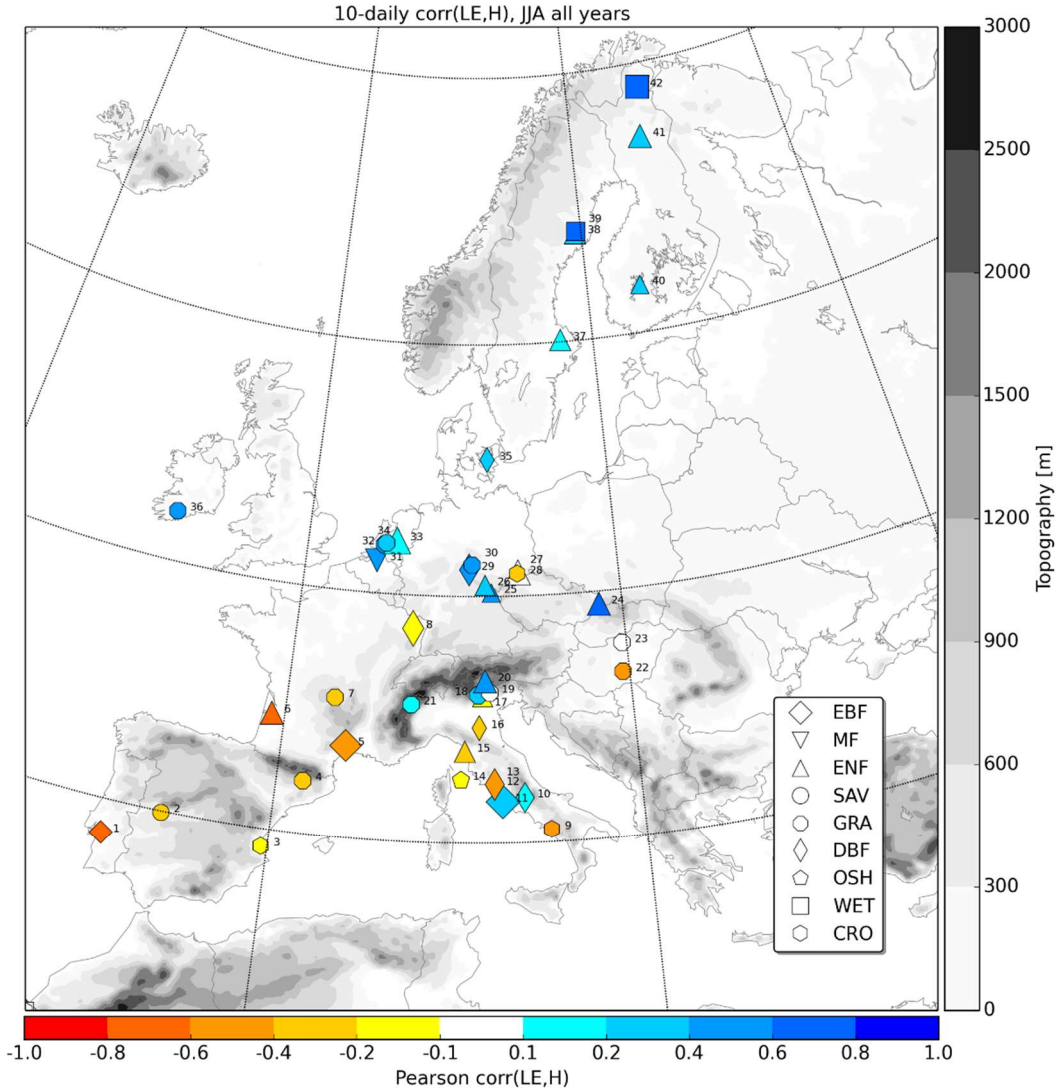

Figure 3.7: Correlations of 10 day mean observed summertime (JJA) latent and sensible heat flux for all available years at the FLUXNET stations. Only days for which all half-hourly values have a quality flag 0 or 1 (original data or high-quality gap filled) are taken into account, and only months with a minimum of 20 high-quality days. Symbols indicate the vegetation type at the station. The larger the size of the symbol the more high-quality data are available. Numbers refer to the individual stations as shown in Figure 3.8.

(same LSM and PBL scheme) that show differences in mean precipitation, radiation and temperature (Katragkou et al. 2015). The relatively weak coupling produced by UCAN-WRF compared to the other WRF versions is caused by the reduced net radiation compared to the other WRF simulations. On the other hand, the individual RCM's LSM characteristics and the parametrization of the land surface (vegetation type, soil type, etc.) decisively affect the coupling strength, too. The coupling strength is thereby a useful integrative metric which may help to explain differences observed in other parameters or phenomena. For example, if the models fail to correctly represent coupling strength, it is also highly likely that they over- or underestimate heat waves (Vautard et al. 2013).

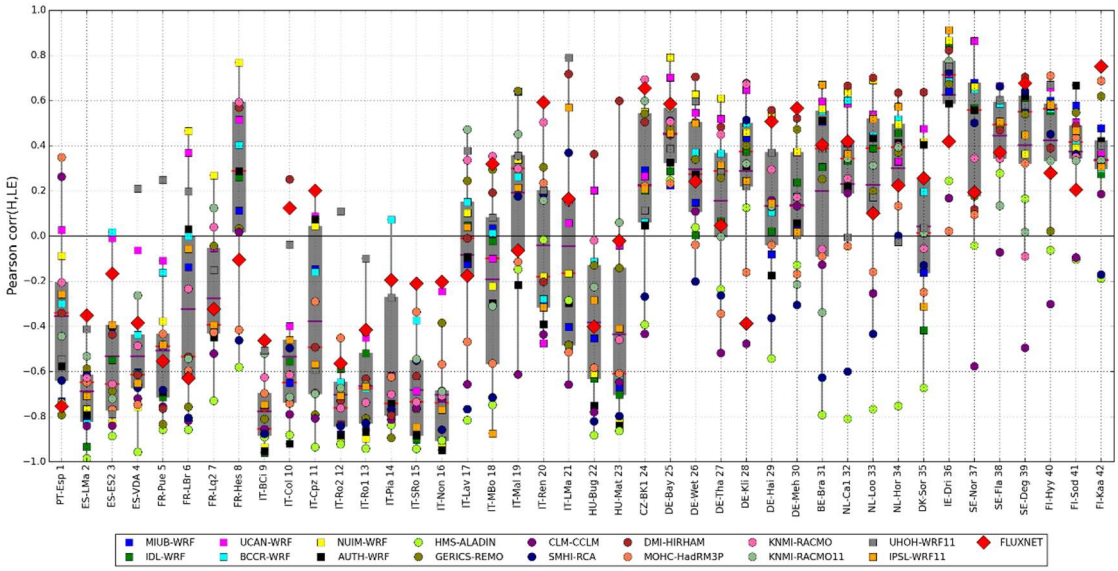

Figure 3.8.: Correlations of 10-daily mean observed summertime (JJA) latent and sensible heat flux for all available years at the FLUXNET stations (big red diamonds); the numbers on the x axis correspond to the station labeling in Figure 3.7. Small colored dots (and squares for WRF RCMs) indicate the H-LE correlation values of the individual RCMs at the nearest grid point to a FLUXNET station. The calculation is based on the same time spans for which observation data are available. Boxplots indicate the quantile range (gray), the medians (red line), and the means (purple line) of the RCM ensemble for each station. Stations are ordered geographically from south to north along the x axis.

Though this is no complete proof of causality, the intercomparison of summertime extreme temperatures (90th percentile) shows that those RCMs that show a stronger (weaker) than average coupling predominantly simulate higher (lower) than average extreme temperatures (data not shown).

The coupling analysis above is now applied to the FLUXNET observations for an evaluation of the RCMs. Figure 3.7 displays the correlation of 10-day averages of summertime (JJA) latent and sensible heat fluxes for several of the 42 FLUXNET stations. Only months with at least 20 days of high quality data are used and only stations with at least three years of data are shown. Because measurement time periods differ for the displayed stations, differences between nearby located stations may partly result from different weather conditions during the different time periods covered. The observations show mainly negative (positive) correlations indicating strong (weak) coupling in southern (northern) parts of Europe and are thus in rough accordance with the RCM results.

A direct comparison of the 42 FLUXNET stations to the RCMs is provided in Figure 3.8. Here, the same H-LE-correlation values as in Figure 3.7 are shown, together with derived coupling strength metric from the individual RCMs. In contrast to Figure 3.6, the correlation from the RCMs is based on the time span for which FLUXNET observations are available. Again, a large diversity within the RCM ensemble is seen for many locations. Outliers, like the overall stronger coupling in the HMS-ALADIN run and the CLM-CCLM

run for northern Europe are obvious, as well as the weaker coupling in DMI-HIRHAM, UCAN-WRF and NUIM-WRF for most stations in central Europe. A comparison with the FLUXNET data reveals that the observations are within the quantile range of the RCMs for 16 out of 42 stations. However, regarding the sign of the correlation reflecting strong or weak coupling regime, the median of the RCMs and the FLUXNET observation agree for 80% of the stations. The number of stations where the observed H-LE-correlation is above the 75 percentile of the RCMs (i.e., RCMs show a stronger coupling than observed) exceeds the number of stations where the RCM's coupling strength is weaker than the observed coupling strength (20 compared to 6). Also regarding the RCM ensemble means for each station, the observed FLUXNET coupling strength in terms of H-LE-correlations appears slightly weaker than for the RCM simulations (26 out of 42 stations).

As the stations are not equally distributed in space, it is possible that they might favor certain conditions with a similar coupling strength in locations with multiple stations and therefore reduce the representativeness of the observations. Besides variable local climate conditions the vegetation types (indicated by the symbols shape in Figure 3.7 impact coupling strength: In the Netherland's FLUXNET stations e.g., the correlations are higher over grassland (NL-Ca1 and NL-Hor) than over forest (NL-Loo). To corroborate such relations, however, the number of stations in similar climatic regions is unfortunately too sparse.

3.4.2 EURO-CORDEX ensemble comparison to GLEAM

In addition to the correlation of latent and sensible heat flux, the following section investigates two process steps of the soil moisture-temperature coupling; first the connection of soil moisture to flux partitioning and second the connection of flux partitioning to atmospheric temperature which is defined as the second coupling metric that is applied in this study. The connection between soil moisture and flux partitioning is indicated by the correlation of the 10-day averaged summertime (JJA) evaporative fraction (ratio of latent heat to the sum of sensible and latent heat flux) and total (i.e. vertically integrated) soil moisture (Figure 3.9). As decreasing (increasing) soil moisture leads to a decrease (increase) of the evaporative fraction, positive correlations are found over most of Europe in all model runs. Exceptions are the northern parts of Scandinavia and Russia

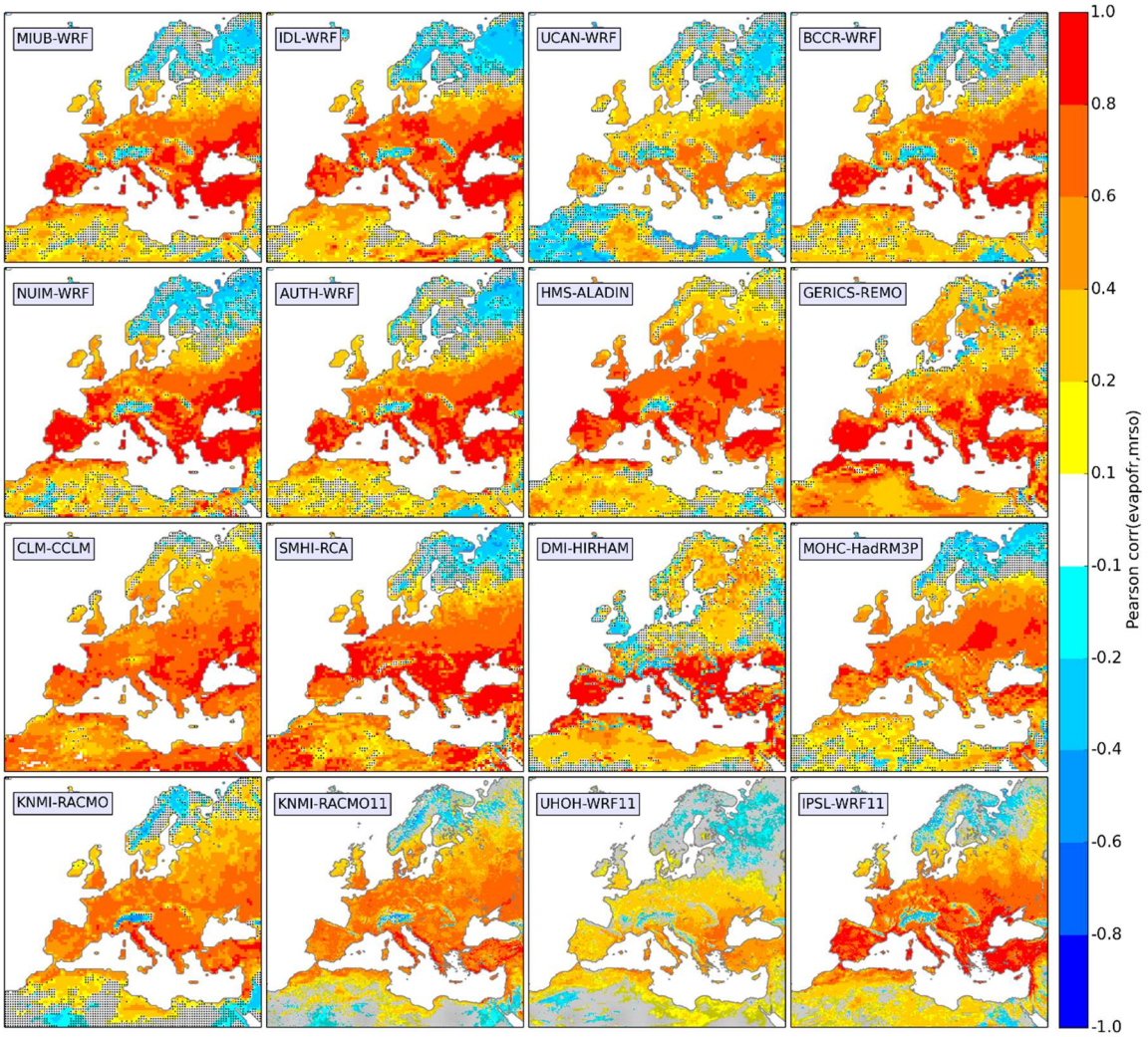

Figure 3.9: Correlation between 10 day averages of total soil moisture and the evaporative fraction computed for the summers between 1990 and 2008 (dotted where correlation is below 5% significance level).

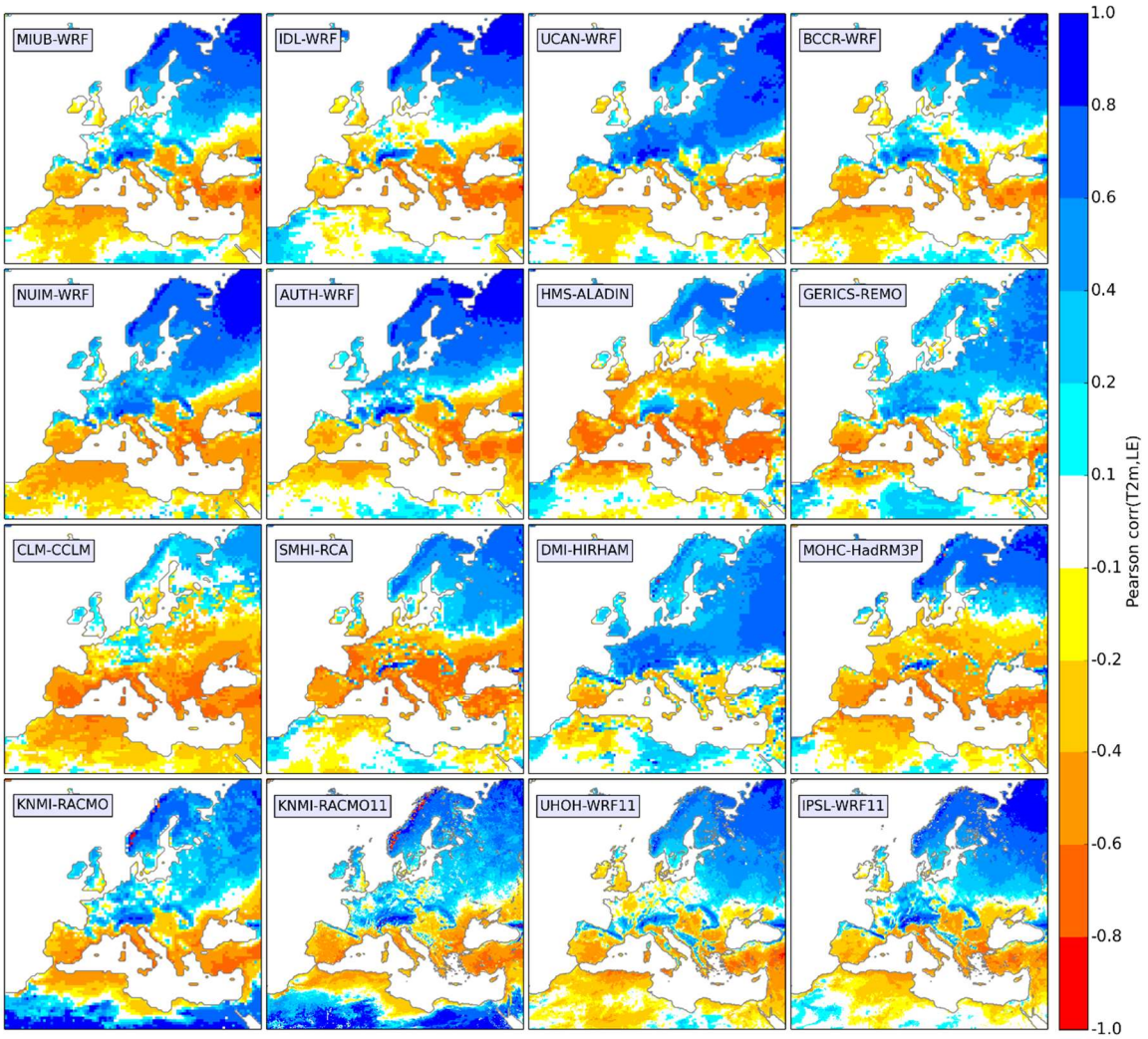

Figure 3.10: Correlation of summer (JJA) 10 day averages of latent heat flux and air temperature (2 m) for the years 1990 to 2008.

and over the Alps, where the WRF runs, MOHC-HadRM3P and SMHI-RCA show no or even negative correlations. This behaviour can most likely be attributed to a delayed thawing of frozen soil layers. When only the uppermost soil layer moisture is used (as possible for the WRF simulations), the correlation with the evaporative fraction is also positive. The noisy pattern in northern Africa relates to the very dry conditions in summer with latent heat flux close to zero and soil moisture at its minimum. While all models show similar results for Europe, the DMI-HIRHAM model differently shows patterns of uncorrelated or even slightly negative correlations for the British Isles and parts of central and eastern Europe. Since both evaporative fraction and soil moisture are quite high in these regions it is assumed to be an energy limited regime where a small decrease in soil moisture does not much affect the flux partitioning.

The correlation of 10-daily averages of latent heat flux and 2 m air temperature is shown in Figure 3.10 for the 16 RCM simulations. The comparison of the individual RCMs gives

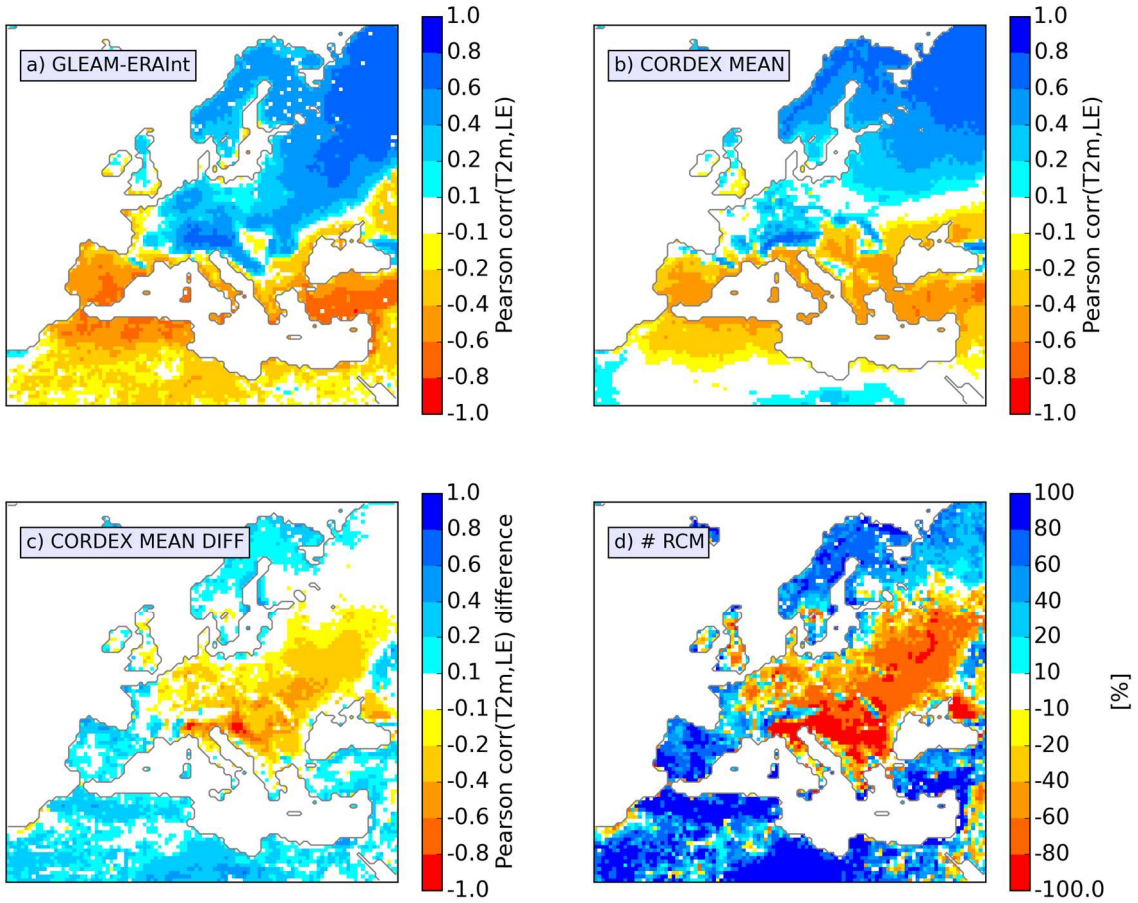

Figure 3.11: (a) Correlation of latent heat flux and air temperature (2 m) for GLEAM (LE) and ERA-Interim (T), (b) for the ensemble mean of Figure 3.10, and (c) for the difference of (a) minus (b). (d) Percentage of RCMs that simulate stronger (red) or weaker (blue) coupling strength than GLEAM-ERAInt.

a similar picture as the H-LE-correlation in Figure 3.6 in the way that stronger than ensemble average coupling (e.g. HMS-ALADIN, CLM-CCLM, SMHI-RCA and MOHC-HadRM3P) as well as weaker coupling (e.g. UCAN-WRF, DMI-HIRHAM) is identified for the same RCM simulations. Again, all simulations show a clear north-south-pattern with strong coupling in southern Europe and weak coupling in northern Europe. Overall, the LE-T-correlation is slightly weaker than the H-LE-correlation signal and the transition zone from positive to negative correlation is located further to the south. The first can be explained by the fact that LE-T-correlation describes one step further in the land-atmosphere coupling process chain of changing soil moisture leading to changing fluxes leading to changing temperature and that local temperature changes are also largely affected by advection. This fact also suggests that different coupling metrics cannot be directly compared in terms of absolute values even if it is a correlation based metric ranging from -1 to 1.

With the GLEAM dataset for evaporation and the ERA-Interim reanalysis for 2 m

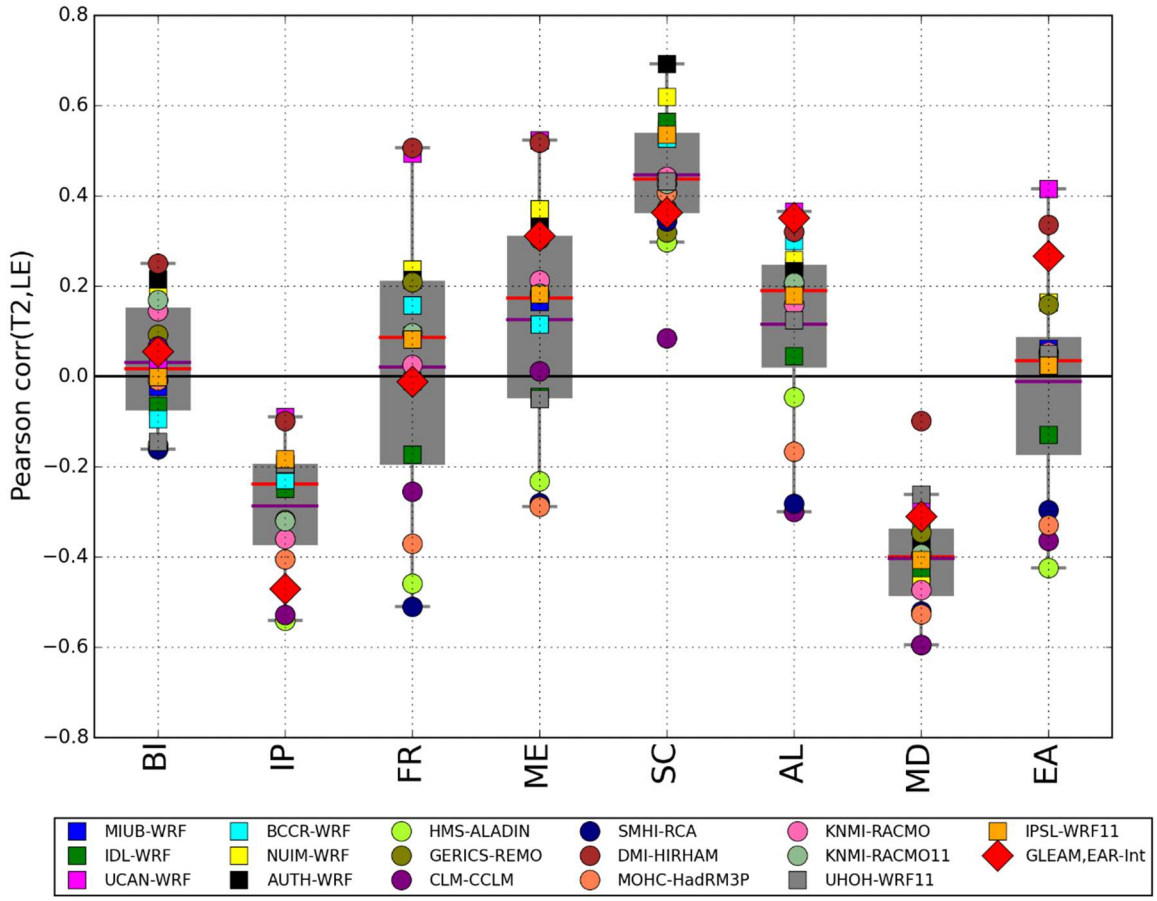

Figure 3.12: Correlations of 10-daily mean summertime (JJA) latent heat flux and air temperature for the years 1990–2008 averaged for different PRUDENCE regions. Boxplots indicate the quantile range (gray), the medians (red line), and the means (purple line) of the RCM ensemble for each region. The big red diamonds show the LE-T correlation of GLEAM-ERAInt.

temperature a gridded observation-based reference for the LE-T-correlation coupling metric is given in Figure 3.11. The averaged coupling strength of the 16 RCM ensemble is in overall good agreement with the observation-based pattern as both indicate strong coupling (negative correlations) for the Iberian Peninsula, Italy, south-eastern Europe and parts of France and weak coupling (positive correlations) for Scandinavia and north-eastern Europe. The related difference plot shows that the ensemble mean coupling strength is stronger for large parts of central and eastern Europe and slightly weaker for the Iberian Peninsula and northern Scandinavia. Also, grid point wise counting the number of RCMs that simulate stronger coupling than GLAEM-ERAInt (red (blue) colors indicate more (less) than half of the ensemble) gives a similar picture.

The direct comparison of the individual RCMs and the GLEAM-ERAint LE-T-correlation for the individual PRUDENCE regions is displayed in Figure 3.12. While a majority of RCMs agree with the GLEAM-ERAint correlation sign for all regions, the ensemble spread as expected from Figure 3.10 is quite large especially for France, Middle Europe, the Alpine

domain and eastern Europe. For those regions, where coupling is either clearly weak (Scandinavia) or strong (Iberian Peninsula, Mediterranean) the RCMs differ less. In line with the maps in Figure 3.12 more than 75% of RCMs overestimate the observation-based coupling strength for Middle Europe, the Alpine domain, the Mediterranean and eastern Europe. They predominantly show less strong coupling for the Iberian Peninsula, whereby all RCMs and the observation-based reference indicate negative LE-T-correlation in this region. Compared to the individual station grid points in Figure 3.8 the RCM spread is less pronounced which mainly results from spatial averaging. The comparison to the GLEAM data product leads to more confidence in the FLUXNET based analysis (Section 4.1): there is a tendency of the RCMs to overestimate coupling strength, albeit this does not apply to all regions. Please note, that this is also based on the assumption, that the GLEAM-ERAint is the perfect benchmark. Though both GLEAM and ERA-Interim are well established and thoroughly evaluated datasets, they are also based on models that may have the same constraints in the ability of simulating the soil and land surface processes correctly. Still, it can be considered as a most fair reference for the purpose of this study.

3.5 Summary and conclusion

The individual models generally agree on the large-scale patterns corresponding to the European climate zones, but regionally the spread of results can be large. The RCMs' total soil moisture time series averaged over the PRUDENCE regions show clear annual cycles with largest amplitudes in southern Europe and also reasonable inter-annual variability according to the weather conditions in the individual years. For the majority of the RCMs the soil moisture is positively correlated with GLEAM soil moisture for large parts of Europe, strongest for the Iberian Peninsula and the British Isles, but less correlated for parts of eastern Europe.

The expected flux partitioning following the European climate regions is fairly well reproduced by the RCM ensemble and also in accordance with representative FLUXNET observations. The partially large ensemble spread can most probably be attributed to differing LSM parametrizations including assumptions concerning vegetation and soil type distributions. A benchmarking intercomparison by Best et al. (2015) revealed that LSMs still have deficits in the correct representation of the fluxes and do not appropriately use the information available in the atmospheric forcing data.

For the EURO-CORDEX RCM simulations the diversity in the simulated fluxes partly results from different sets of atmospheric parametrizations, which impact the simulated regional weather conditions. This influence can be inferred from a sub-set of WRF simulations which use the same LSM: some members produce regionally higher overall

surface energy fluxes due to higher solar radiation caused by less cloudiness in response to different convection and microphysics parameterizations. Multiple feedbacks between land surface and atmospheric processes result in differences in e.g. mean 2 m air temperature and total precipitation (as analysed in other evaluation studies (Kotlarski et al. 2014; Katragkou et al. 2015)). These differences, however, depend on many model parameters and cannot be directly or exclusively linked with coupling properties of the individual RCMs.

The land-atmosphere coupling strength is investigated both in observations and simulations via two integrative metrics based on the correlation between sensible and latent heat fluxes and the correlation of latent heat flux and 2 m air temperature, respectively, which describe the strength of soil moisture related feedback processes. A major advantage of these methods is its easy applicability to both standard RCM output, on which we had to rely in this study, based on an ensemble-of-opportunity, and to the FLUXNET observations (for H-LE-correlation) as well as to the gridded GLEAM-ERAInt observation-based data (LE-T-correlation).

The coupling-strength analysis of the EURO-CORDEX simulations based on H-LE-correlation for the summer months (JJA) over the period 1990 to 2008 revealed strong coupling in southern Europe and weak coupling in northern Europe for all members of a multi-model ensemble in overall agreement with the FLUXNET measurements. In the transition zone over large parts of central Europe between these coupling regimes the RCMs diverge and show a wide range of coupling strengths. There is a tendency towards a stronger coupling in the RCMs with reference to the FLUXNET observations, but the relatively small number of sufficiently long and high-quality observation time series for many regions limits the confidence of that conclusion.

The comparison of the LE-T-correlation derived from the RCM results and from the gridded GLEAM-ERAInt reference, however, corroborates the statement, that the majority of RCMs overestimates the coupling strength for large parts of Europe. This is consistent with evaluation studies on global models that reveal an overestimation of land-atmosphere coupling in the mid-latitudes (Sippel et al. 2016) and parts of the U.S. (Merrifield and Xie 2016).

Both metrics agree in attributing stronger and weaker coupling strength than average to individual RCMs. While both show the typical north-south pattern for Europe the transition from positive to negative correlation is slightly shifted to the south for the LE-T-correlation metric. Overall the detected regions for strong coupling in southern Europe agree with previous studies based on global models (Koster et al. 2006; Dirmeyer 2011), regional models (Seneviratne et al. 2006; Jaeger et al. 2009) as well as observations (Miralles et al. 2012) for a similar time span but using different experiment designs and coupling metrics. The results also support the suggestion by Lorenz et al. (2015) that the coupling strength derived from different metrics may provide similar information although

they cannot be directly compared in their absolute values unless appropriately scaled. Consistent, but inevitably computationally expensive GLACE-type experiments like by Koster et al. (2006), Seneviratne et al. (2006) or Hirsch et al. (2014) for all RCMs would allow for a more robust assessment of coupling strength than possibly with the ensemble-of-opportunity at hand. Nevertheless, the relatively simple correlation based coupling metrics are suitable for an intercomparison of different RCM runs. The coupling metrics provide additional information for the explanation of differences seen in e.g. extreme temperatures that show positive biases for the more strongly coupled RCMs. Finer model resolutions generate additional small-scale heterogeneities in coupling strength, but these seem not to affect the large-scale coupling patterns. In order to corroborate this statement, however, a larger number of direct comparisons of EUR-11 and EUR-44 simulations with the same RCM are required.

The strength of land-atmosphere coupling varies across seasons and regions and it is expected to become stronger in the context of a warming climate, especially in locations where this feedback plays an important role (Seneviratne et al. 2006; Dirmeyer et al. 2014). In Section 7.2 and 7.3 the change of land-atmosphere coupling pattern under an RCP4.5 future scenario is investigated for the MPI-ESM-LR driven EUR-44 WRF simulation.

4 Land-atmosphere coupling in WRF EUR11/3kmME evaluation simulations

4.1 Introduction

The analysis of land-atmosphere coupling in the EURO-CORDEX RCM ensemble revealed a large variability in coupling strength in different RCM simulations. Central Europe has been identified as a transition zone between weak and strong coupling. The comparison of coarse EUR-44 and fine EUR-11 resolution showed that finer model resolutions generate additional small-scale heterogeneities in coupling strength, but these do not seem to affect the large-scale coupling patterns. This section further investigates the influence of higher resolution on the coupling strength based on the ERA-Interim driven EUR-11/3km evaluation runs (see Section 2.2.5). The setup enables a direct comparison of coupling strength in the 3 km and 12 km run. Furthermore, the interannual variability of coupling strength in Central Europe is investigated as the simulated time span fairly represents the variability of the Central European weather conditions including both wet and dry years. In addition to the correlation-based coupling metrics further methods for quantifying coupling strength are applied.

4.2 Comparison of coupling strength in individual summer seasons

Coupling strength defined as the correlation of daily mean latent and sensible heat flux for each of the simulated years (just JJA summer season) in the 3 km resolution run shows large interannual variability (Figure 4.1). The year-to-year changes in coupling strength are consistent with the respective weather conditions in the individual years and correlate with the local year-to-year soil moisture changes (Figure C.0.1). In summer 2002, coupling strength is weak since soil moisture conditions are wet enough to limit evapotranspiration just by incoming radiation energy. In the dry and warm summer 2003, limited soil moisture conditions are indicated by an overall strong coupling, except for the Alpine region, which indicates weak coupling for all simulated years. Generally dry and sunny regions in summer, like southern France, northern Italy and the Balkan region, favor strong coupling conditions.

Applying the coupling index after Dirmeyer (2011) defined as the product of standard deviation of soil moisture and linear regression of soil moisture and latent heat flux identifies similar patterns for strong and weak coupling in the individual years (Figure 4.2). As discussed in Section 2.4, a direct quantitative comparison of both coupling strength

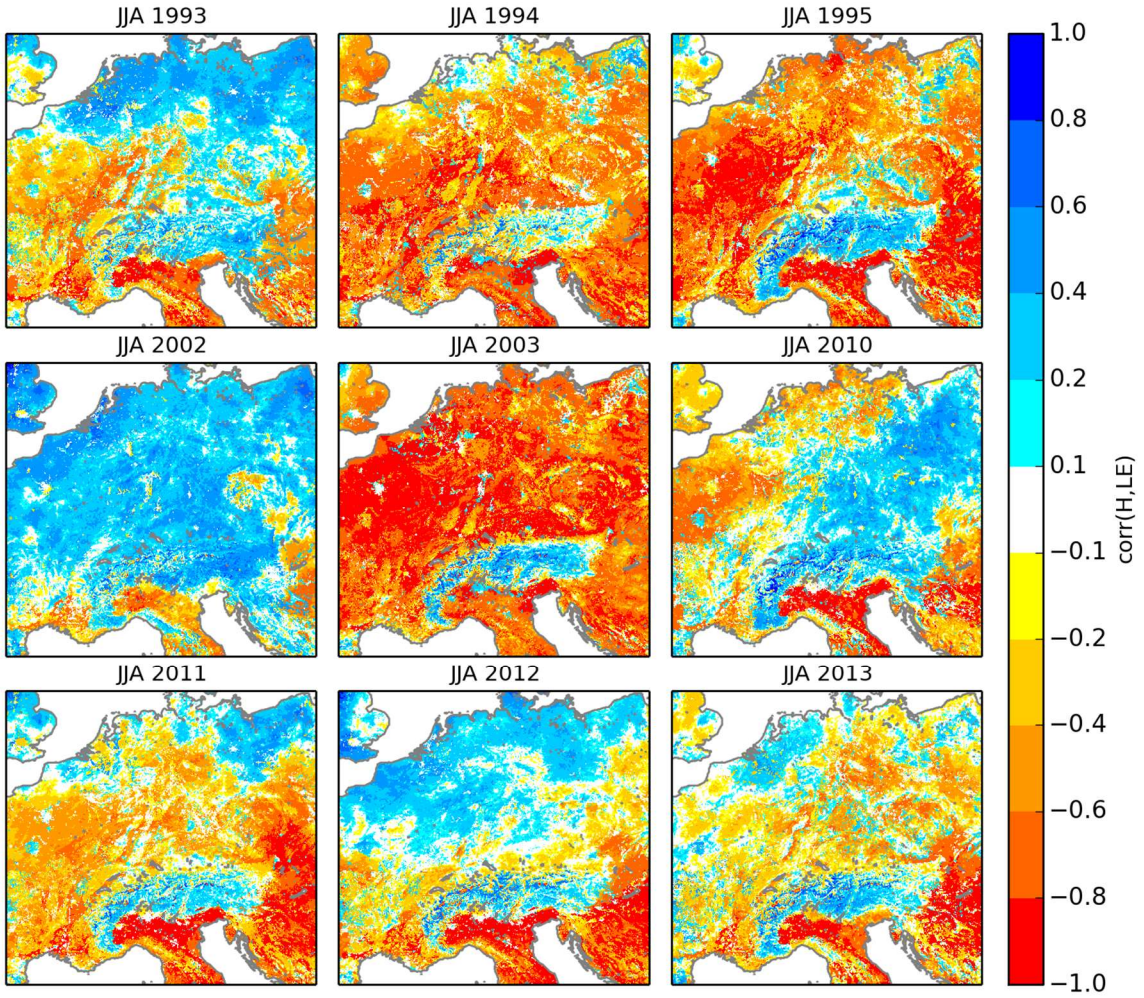

Figure 4.1: Correlation of summer (JJA) daily averages of latent and sensible heat flux for nine individual years 1993-1995, 2002-2003, 2010-2013 in the ERA-Interim driven WRF3 simulation.

metrics is not useful as scales and units differ. However, consistent regions of strong and weak coupling manifest for both metrics.

Both metrics reveal a strong heterogeneity in the coupling pattern consistent with the heterogeneous land use (see land use types in Figure 2.4c). There is a clear influence of land use type on coupling strength owing to the different characteristics for evapotranspiration, flux partitioning, albedo and roughness length. Urban grid points stick out with weak or neutral coupling as they are by model design decoupled to soil moisture. In forested areas, coupling strength is much weaker than in neighboring cropland areas.

To investigate the different coupling characteristics, soil moisture time series of all averaged crop vs. all averaged mixed forest grid points for the two seasons 2002 and 2003 are compared (Figure 4.4). For both land use types, an expectable seasonal cycle with maximum soil moisture in winter and minimum soil moisture at the end of summer is simulated. The variability is larger in the upper soil layers and larger for crop than forest type land use both on daily and seasonal time scales. In the dry summer 2003, a stronger and earlier

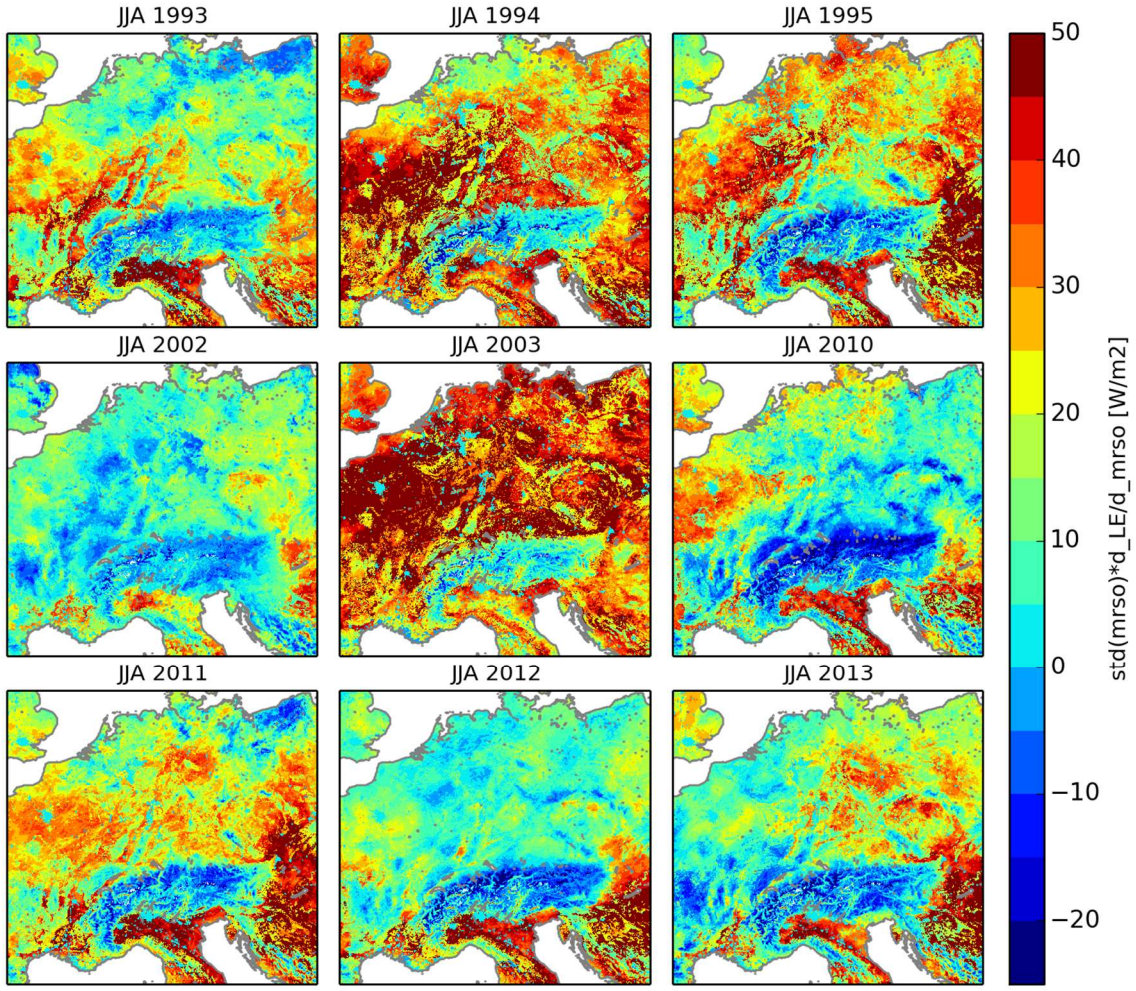

Figure 4.2: Coupling index $I_{SM,LE}$ for nine individual summer seasons (JJA) 1993-1995, 2002-2003, 2010-2013 in the ERA-Interim driven WRF3 simulation. Red (blue) colours indicates strong (weak) coupling.

decrease for crop type area soil moisture (just upper 3 levels) is seen. In forested grid points the soil moisture deficit evolves slower and reaches its minimum a few weeks later. Unlike for forest type, the 4th (lower most) soil layer at crop type land use is decoupled from the other layers in summer as it is not reached by roots and soil moisture remains nearly constant. Please note that also soil type sensitively influences the absolute value as well as the temporal evolution of soil moisture depending on the soil's porosity and permeability. However, also separated for different soil types, the comparison of soil moisture evolution at forest and crop type grid points shows similar results.

The non-linear connection between soil moisture and flux portioning is seen in the contrasting seasonal cycles of latent and sensible heat flux for spatially averaged crop and forest land use type grid points (Figure 4.3). In 2002, both crop and forest latent heat flux follow a harmonic seasonal cycle according to the incoming net radiation. The evaporative fraction increases in summer (to 0.65-0.75) and is typically little higher over crop than over forest land use type. In 2003, the evolution is clearly different. While the increase of latent

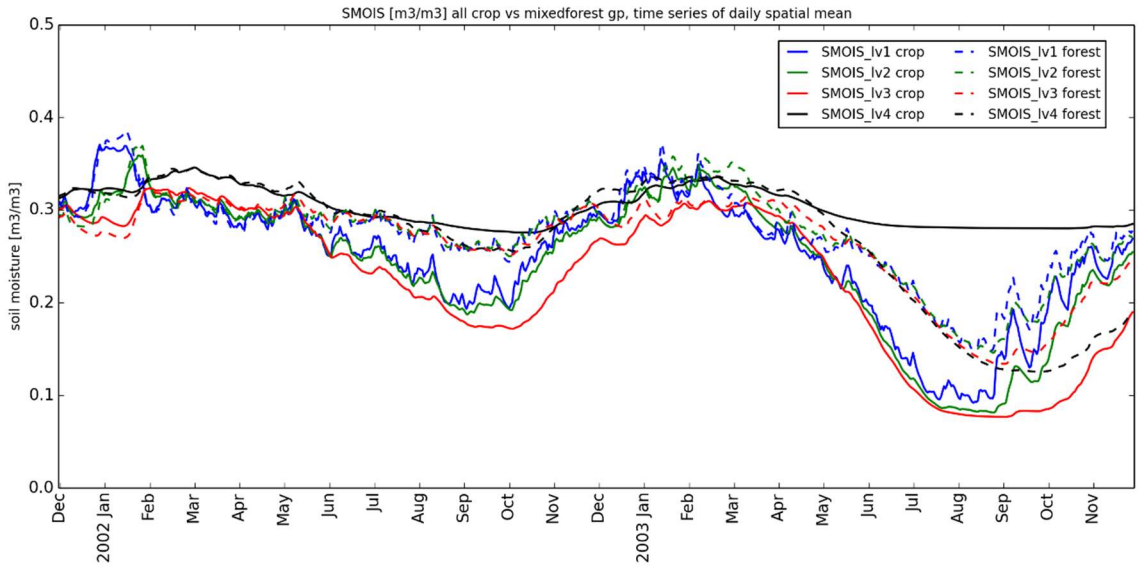

Figure 4.4: Time series of soil moisture from December 1st 2001 to December 1st 2003 in ERA-Interim driven WRF 3 km simulation averaged over all crop land use type grid cells (solid lines) and all mixed forest land use type grid cells (dashed lines) in four soil layer depths (blue: 0-10 cm, green: 10-40 cm, red: 40-100 cm, black: 100-200 cm).

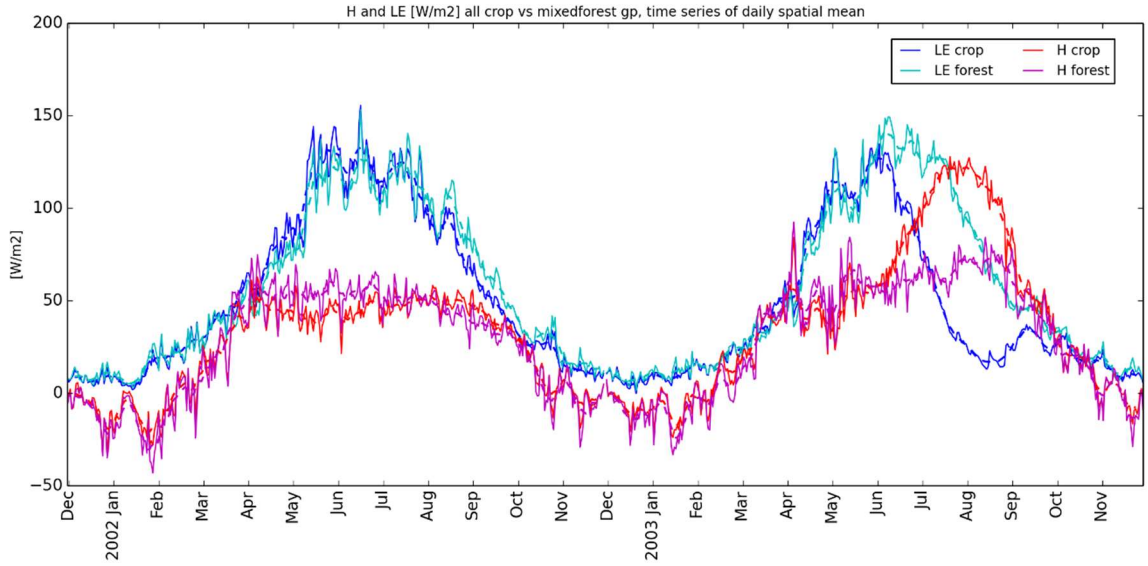

Figure 4.3: Time series of latent (blue and cyan) and sensible (red and purple) heat flux from December 1st 2001 to December 1st 2003 in ERA-Interim driven WRF 3 km simulation averaged over all crop land use type grid cells (blue and red) and all mixed forest land use type grid cells (cyan and purple).

heat flux is similar in spring, evapotranspiration at crop land use strongly decreases in summer accompanied by an according increase of sensible heat flux. This anticorrelation of the fluxes indicating strong coupling in Figure 4.1 is also seen for forest area, but less strong. The decrease of latent heat flux starts later, and the evaporative fraction does not fall below 0.4. Unlike crop, where the root zone just covers the upper three soil layers (with 10 cm, 30 cm and 60 cm thickness), forest roots additionally reach the soil moisture storage

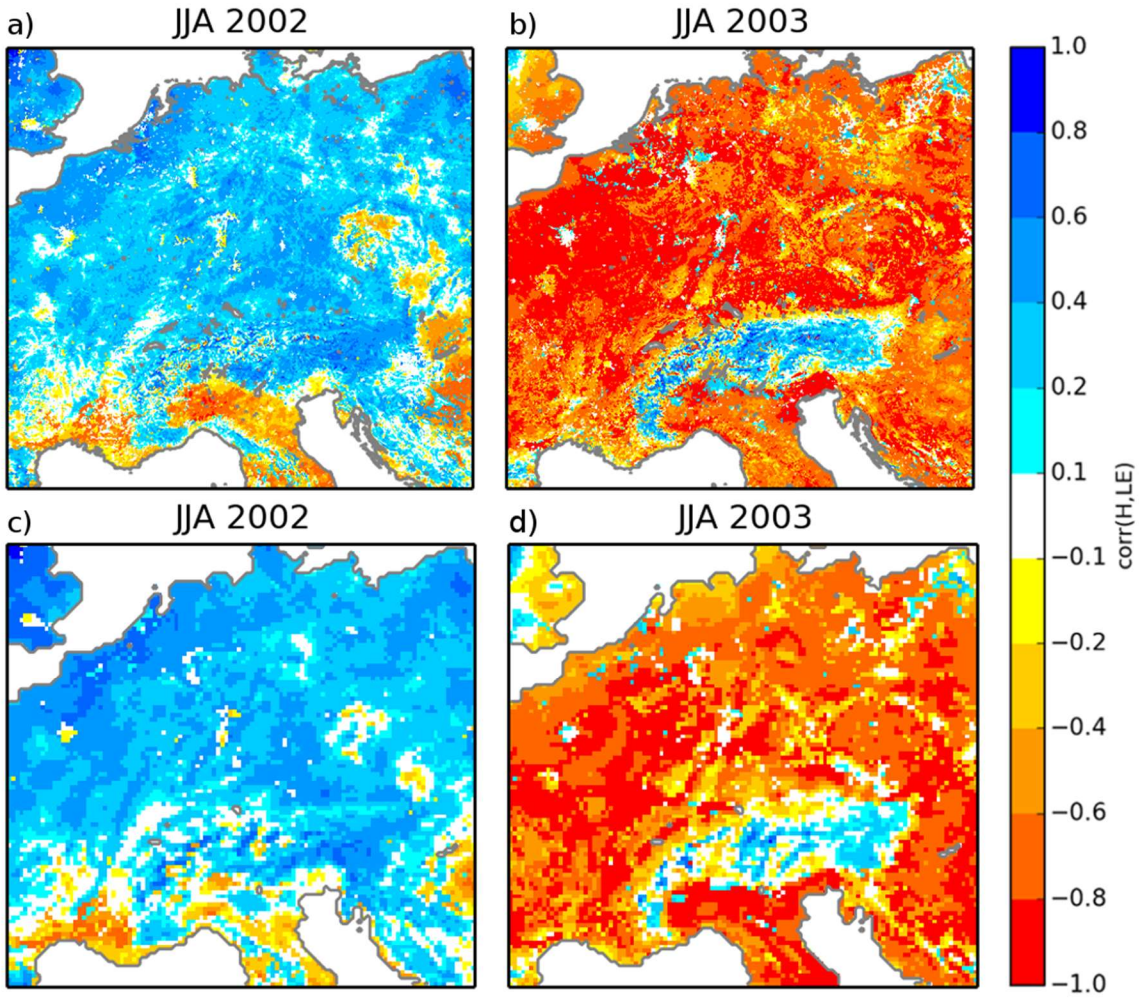

Figure 4.5: Correlation of summer (JJA) daily averages of latent and sensible heat flux in 2002 (a, c) and 2003 (b, d) in the ERA-Interim driven WRF3 (a, b) and WRF12 (c, d) simulation.

of the deepest soil layer (100 cm thickness). Hence, with the absence of precipitation, transpiration reducing drought stress conditions are reached later for forest vegetation.

Strong coupling conditions potentially facilitate the evolution of extreme temperatures. While specific large-scale atmospheric conditions, like advection of warm air masses, persistent high pressure systems and associated clear sky conditions, are necessary for heat build-up, land-atmosphere coupling plays an important role for the evolution of heat waves (as e.g. shown by Fischer et al. (2007), Miralles et al. (2012, 2014), Teuling et al. (2013)). For all nine simulated summer seasons, the coupling strength pattern indicates a significant spatial correlation (0.55 on average) with the difference of mean daily maximum temperature and mean temperature (see Figure C.0.2). Except for urban grid points, the local year-to-year changes in coupling strength correspond with the changes in mean daily maximum temperature.

Comparison of the 12 km and the 3 km resolution run shows an overall stronger coupling in the high resolution run for all individual years and both coupling metrics (exemplarily shown for 2002 and 2003 in Figure 4.5, see Figure C.0.4 and Figure C.0.5 in Appendix C

for all individual years). Like in the 3 km resolution, the coupling pattern is related to the land use, hence it is less heterogeneous in the coarser resolution. The overall slightly weaker coupling in the WRF12 run is most probably not directly owing to the coarser resolution of the land surface but more likely resulting from the wetter conditions in the WRF12 run (Figure C.0.3). As shown in Chapter 5, the 12 km resolution with parameterized convection produces more low intensity, high-frequency and large spread precipitation, less runoff and hence more soil moisture, which overall leads to a lower coupling strength.
The connections between soil moisture anomaly, coupling strength and maximum temperature manifest also for WRF12, both in comparison of individual years and regions as well as in comparison to WRF3. So, lower mean and maximum temperatures as well as smaller difference between both temperatures in WRF12 compared to WRF3 are consistent with the weaker coupling in large parts of the domain (Figure C.0.6). The impact of the surface resolution and the heterogeneity of land use properties is further investigated in Chapter 8.

4.3 Soil moisture sensitivity during heatwave 2003

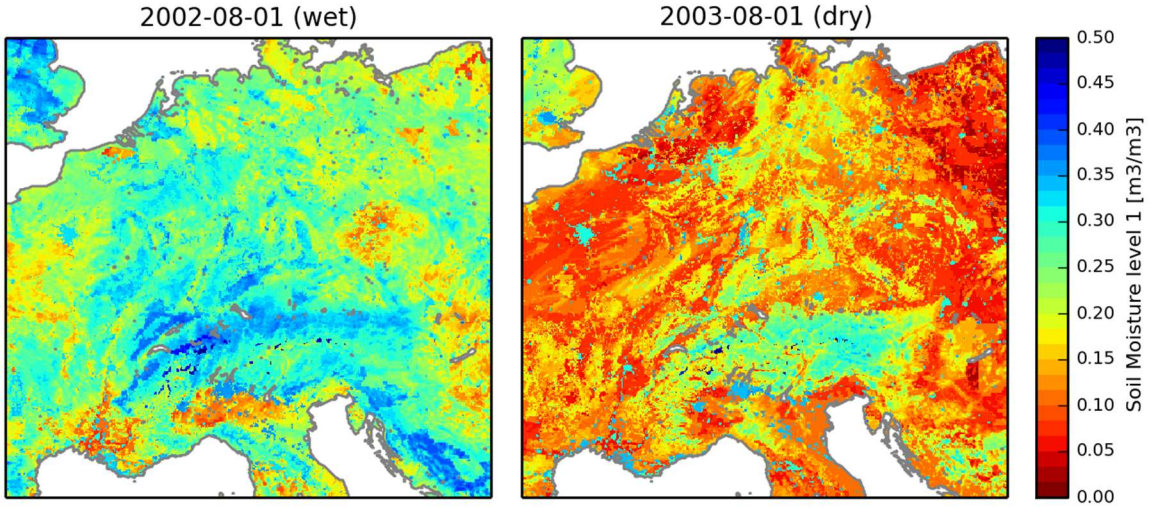

Figure 4.6: Upper level soil moisture in 2002-08-01 (left) and 2003-08-01 (right).

In order to investigate to which extent soil moisture can influence atmospheric conditions in the WRF model a simple sensitivity experiment has been set up for the 3kmME domain. For the experiment, the hottest phase of the Central European heat wave in August 2003 is simulated (1^{st} to 5^{th} of August). It is characterized by strong negative soil moisture anomalies, a persistent anticyclonic circulation, almost clear sky conditions and consequently high temperature anomalies (Schär et al 2004). In contrast, though not fully saturated, soil moisture conditions in August 2002 have been much wetter (see Figure 4.5). The experiment seeks to answer the question how much the heat anomaly in 2003 could have been reduced, if the wet soil moisture conditions from August 2002 existed in August

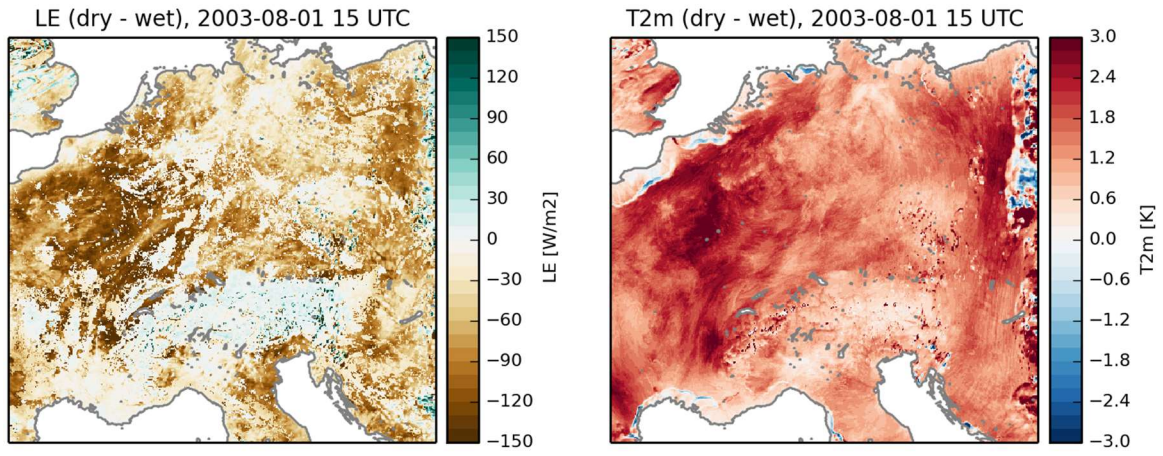

2003.

Therefore, two simulations both restarted from the ERA-Interim driven EUR-11/3kmME simulation (started in November 2001) at 2003-08-01 0 UTC have been carried out with the WRF EUR-11/3kmME nesting setup: one simulation with the original dry soil in August 2003 and one with the wet soil moisture values taken from August 2002 for all four model surface layers. The initial atmospheric conditions as well as the lateral boundary conditions for the 3kmME domain are identical for both simulations, so that any differences solely result from the initial soil conditions.

The comparison of both runs reveals a strong evaporative cooling effect in the wet run that

Figure 4.7: Difference of latent heat flux (left) and 2m temperature (right) in wet minus dry simulation at 2003-08-01 15 UTC (after 15 hours simulation time).

evolves rapidly after sunrise on the first day. Figure 4.7 shows the situation at 15 UTC. Marked differences in latent heat flux between both simulations occur for large parts of the domain reaching up to 150 W/m2 more latent heat flux in the wet run. Heterogeneity

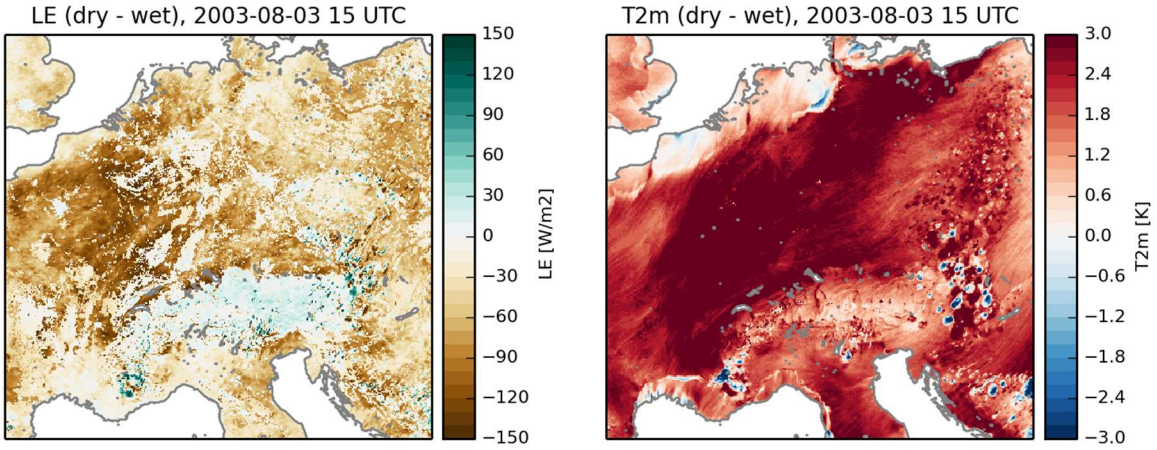

Figure 4.8: Difference of latent heat flux (left) and 2m temperature (right) in wet minus dry simulation at 2003-08-03 15 UTC (after 63 hours simulation time).

is caused by different land use types. Regions with small differences either result from

urban areas where latent heat flux is zero or from mainly forested areas where latent heat flux is equally high in both simulations. Here, soil moisture is still sufficient for evapotranspiration as soil moisture is also taken up by roots in deeper soil layers. Differences in latent heat flux potentially also result from different net radiation, but except for some clouds near the eastern and north-western boundary almost clear sky conditions dominate for the whole domain in both simulations. The reduced evaporative cooling in the dry simulation leads to overall higher temperatures compared to the wet run reaching up to +3 K for parts of France consistent with the largest differences in latent heat flux. Near the coast line, especially at the North Sea and the French Mediterranean coast, the temperature difference is much smaller. This can be explained by a strong sea breeze that evolves during daytime and reduces the local heating effect. The overall stronger heating-up of the land surface in the dry simulation and thereby stronger buildup of a low-level heat low leads to slightly stronger onshore winds that push the cold sea air further to the land's interior. This results in a line of colder temperatures in the dry run ca. 50 km away from the coast.

Since the large-scale circulation is quasi-stationary and no exchange of the central European air mass is taking place the stronger heating-up of the boundary layer in the dry run further intensifies in the following days. The lack of evaporative cooling in the dry run leads to widespread 3-4 K higher temperatures after three days (Figure 4.8). Besides the direct local effect on the near surface variables, the drier soil moisture conditions influence the large-scale circulation by producing a stronger heat low and enhanced ridging of the midtroposphere (Figure 4.9).

Although the present modelling experiment represents an extreme situation, it reveals the positive feedback mechanism between soil moisture, large-scale circulation, and temperature. Other experimental studies on the evolution of the 2003 European heat wave indicate that without soil moisture anomalies, the heat anomalies could have been reduced by 40% (Fischer et al 2007).

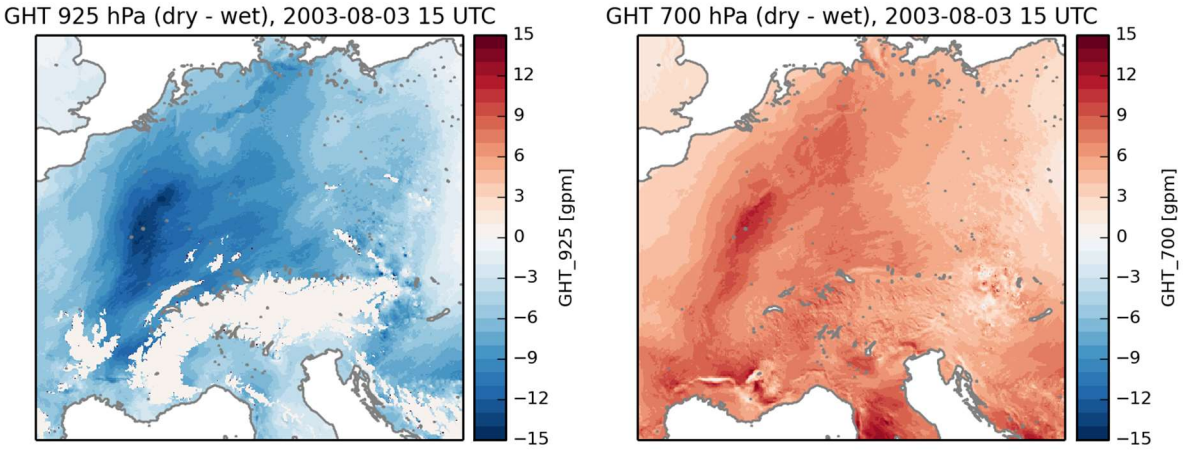

Figure 4.9: Difference of 925 hPa geopotential height (left) and 700 hPa geopotential height (right) in wet minus dry simulation at 2003-08-03 15 UTC (after 63 hours simulation time).

5 Validation of precipitation statistics in convection-permitting WRF climate simulations

5.1 Introduction

In this chapter, the ERA-Interim reanalysis driven EUR-11/3kmME time slice simulations (see Section 2.2.5) are compared against station observations with a focus on the diurnal cycle, the intensity distribution of hourly precipitation, and the temperature-precipitation scaling both for convection-permitting and coarser resolution simulations with parameterized convection[8].

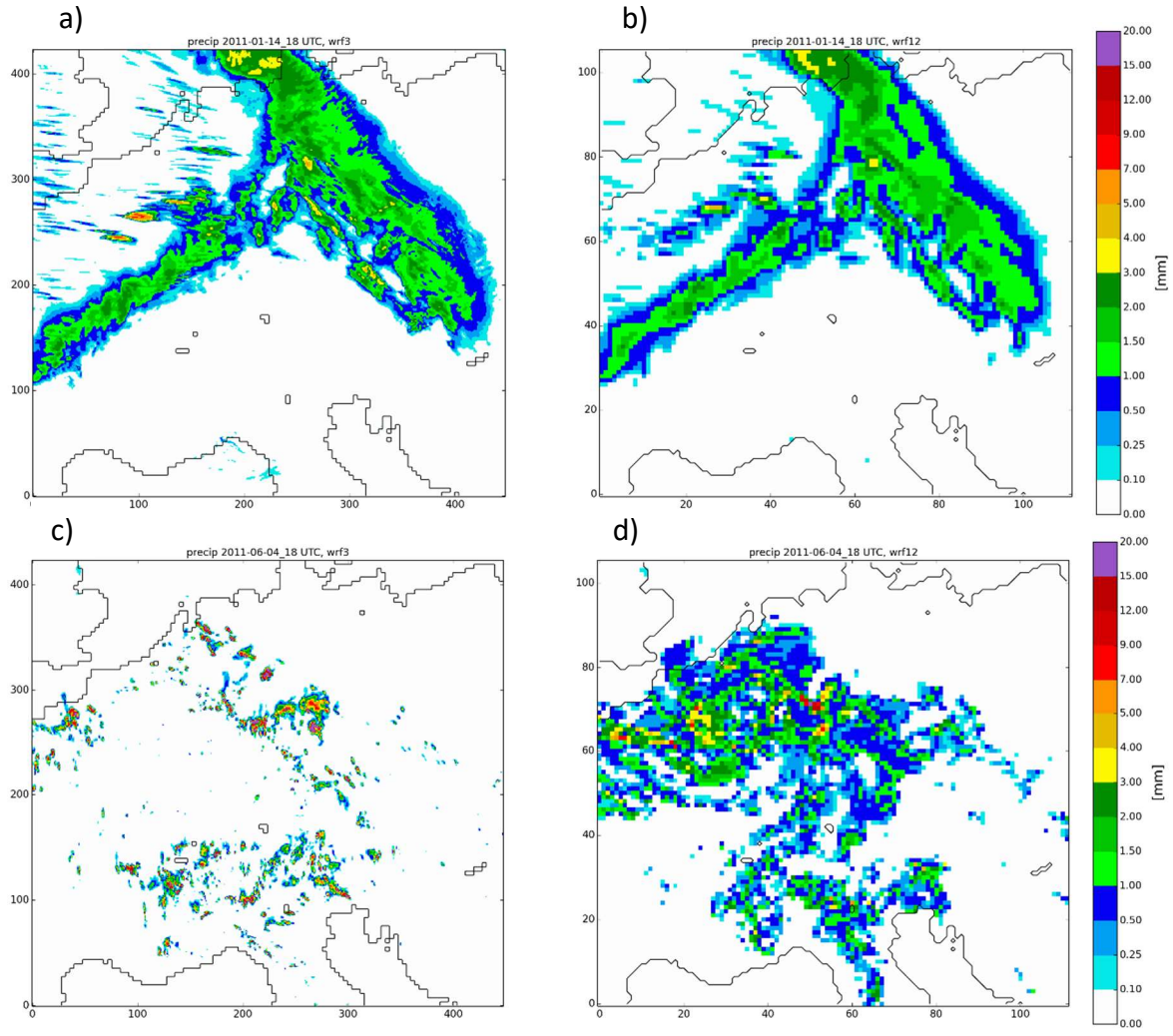

Figure 5.1: Example for typical precipitation pattern (1h sum) in winter (a, b: passing frontal system in 2011-01-14 18 UTC) and in summer (c, d: convective precipitation in 2011-06-04 18 UTC) in 3 km (a, c) and 12 km (c, d) WRF361N simulation.

[8] Results and figures of Section 4.2 to 4.6 have been published in Knist et al. (2018a).

The major differences between 12 km resolution and convection-permitting 3 km resolution manifest in the precipitation characteristics, both in the spatial and intensity distribution as well as in the temporal evolution. Though the focus of this analysis is not on the spatial distribution, Figure 5.1 gives an example how both simulations typically differ in their precipitation patterns. Taken as a snapshot from the ERA-Interim driven longterm simulation (Figure 5.1.a, b) shows the hourly precipitation sum of a passing frontal system over Central Europe in winter (2011-01-14 18 UTC). While the large-scale pattern of the warm and cold front as well as the overall intensity of the dominantly stratiform precipitation is quite similar in both simulations, intensity differences are seen on the local scale. Local higher precipitation intensity is seen in the 3 km simulation, especially for the post frontal convective cells.

Larger differences evolve in summer (Figure 5.1.c, d), when convective processes play a major role. The snapshot at 2011-06-04 18 UTC shows a typical situation of a day with strong convective activity. The 3 km simulation shows many separate convective cells with a diameter of 10-70 km and high precipitation intensity. In contrast, the precipitation areas are much more widespread with lower intensity in the 12 km simulation. There are also embedded grid cells with high precipitation intensity, but less strong compared to the 3 km simulation, even when the 3 km data is averaged over 12 km grid boxes. Though the exact location of the convective cells cannot be expected to match observed precipitation due to internal variability in this free running long-term simulation, the overall pattern in the 3 km simulation is much more realistic.

As suggested by a so far limited number of previous long-term convection permitting climate simulations (e.g. Kendon et al. 2012; Ban et al. 2014; Fosser et al. 2015; Prein et al. 2015; Leutwyler et al. 2016), significant improvements in sub-daily precipitation statistics, the representation of extreme precipitation events, summer diurnal cycles of convective precipitation, and the spatial structure of precipitation are expected for the 3 km simulation compared to the 12 km simulation. The analysis intercompares results for different regions. Largest improvements are expected over regions with complex topography.

5.2 Methods

Two national station datasets of DWD (1024 stations) and MeteoSwiss (80 stations) (see Section 2.3.3) that provide hourly data are used for the evaluation of the ERA-Interim driven WRF EUR-11 and 3kmME simulations.

For the comparison RCM data is extracted from the grid point closest to each observation station. For the comparison of 3 km (WRF3) and 12 km (WRF12) model data, the WRF3 fields are averaged to the WRF12 fields via conservative remapping (Jones 1999) resulting

in WRF3_12 fields that conserve the integral of precipitation over the domain.
Metrics are computed for all grids, for which at least one station is available and then averaged over all stations as well as selected altitude ranges (see station location in Figure 2.6). For the intensity distributions spatial averaging results from pooling of all stations and respective grid points. Precipitation percentiles are calculated based on all hours, including dry hours; thus, percentiles are not affected by different numbers of wet hours. This approach differs from other studies assessing heavy precipitation trends using percentiles relative to wet hours (e.g. defined as hours > 0.1 mm); thus indices cannot be directly compared and may produce misleading results if the percentage of wet hours changes (Schär et al. 2016).
The analysis also focusses on the scaling of extreme precipitation with temperature and compares the scaling with the Clausius-Clapeyron scaling which predicts ~7% K^{-1}. C-C-scaling assumes that in a warming climate extreme precipitation will further increase with the same rate (Allen and Ingram 2002; Trenberth et al. 2003). The scaling is calculated from daily mean 2 m air temperatures and the daily maximum hourly precipitation following the method first applied by (Lenderink and van Meijgaard 2008): for each station or model grid, daily maximum hourly precipitation over the investigated period is attributed to the daily mean temperature over the same period sorted into 1 degree bins. To account for different station and grid surface altitudes, temperature is extrapolated to sea level by assuming a lapse rate of 0.0065 Km^{-1}. For each temperature bin with a sample size larger than 100, the 99th percentile of the precipitation values ($P99_{dmax}$) is calculated. The $P99_{dmax}$ values are then averaged over the stations or grid areas in the particular analysis region.

5.3 Mean diurnal cycle of precipitation

Daytime land surface heating during summer leads to a diurnal cycle in convective processes and the ensuing evolution of clouds and precipitation. The mean diurnal precipitation cycles in both 12 km and 3 km WRF simulations are compared with the station data over Germany and Switzerland (Figure 5.2). The diurnal cycles of grid cells nearest to the station locations are averaged for the summer months (JJA) of the simulation time period. The results for the 3 km simulation, both the original 3 km grid data (WRF3, yellow) and their 12 km averages (WRF3_12, red) differ only marginally for all stations (Figure 5.2a) and also for the individual altitude ranges (Figure 5.2b-d) while clear differences are obvious between coarse and high-resolution runs and the observations. The amplitude of the diurnal cycles from the WRF simulations is larger and shifted to earlier times by about 3 (WRF3) and 4 (WRF12) hours compared to the observations, which peak at 18 UTC. While the night-time precipitation amount in WRF12 better

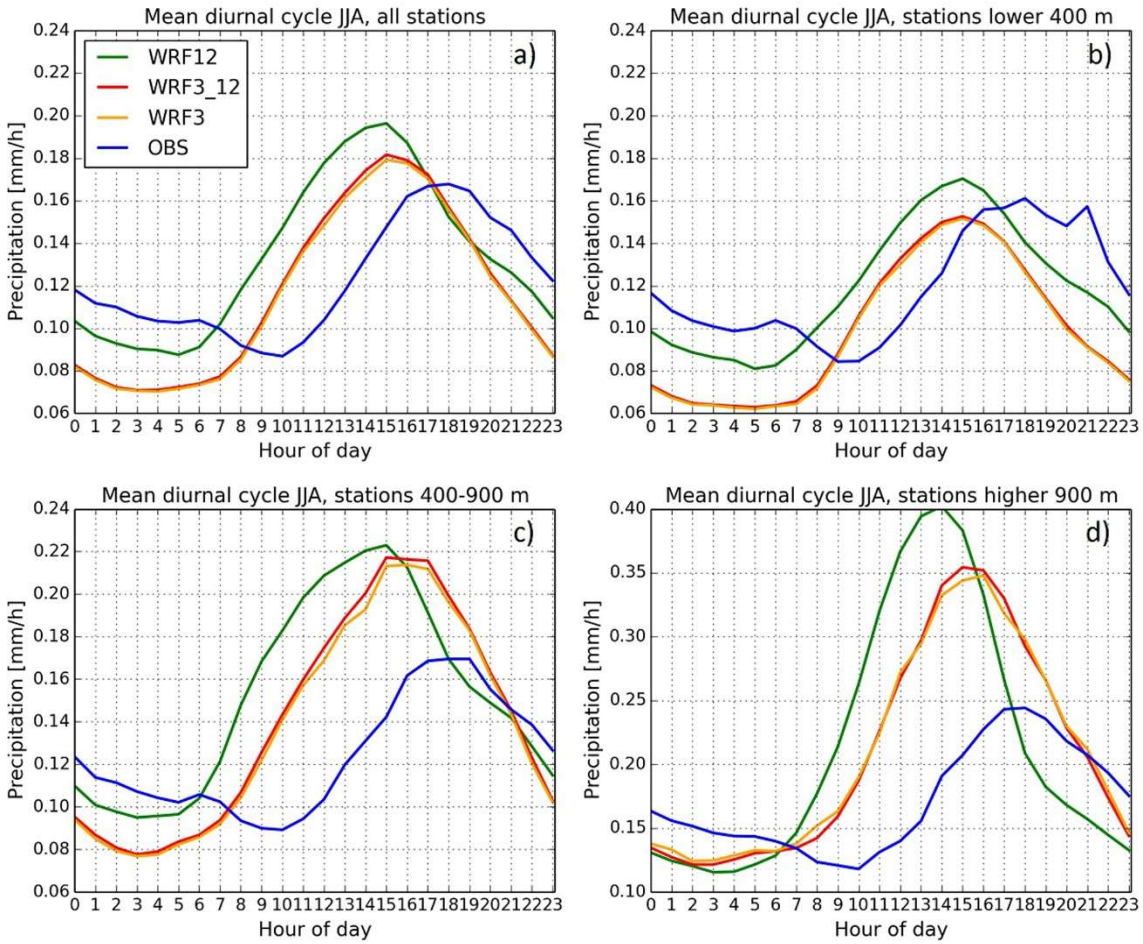

Figure 5.2: Mean diurnal cycle of summer (JJA) precipitation based on all rain gauge stations (blue lines) (a), lowland stations (<400 m) (b), uplands stations (400-900 m) (c) and Alpine stations (> 900 m) (d). Green lines indicate the ERA-Interim driven 12 km WRF simulation (WRF12), yellow lines the 3 km simulation (WRF3) and red lines the 3 km results interpolated on 12 km grid (WRF3_12). For each station the nearest model grid point is taken into account.

matches the observations (WRF3 clearly underestimates), the amplitudes and phasing during daytime is better simulated by WRF3, except for the low altitude stations (Figure 5.2b). Overall, WRF12 results in larger mean precipitation than WRF3, and both overestimate average precipitation, except for the lowlands (Figure 5.2a).

Results slightly differ for regions at different altitudes (compare Figure 5.2 a, b and c). The height ranges < 400 m is mainly located in Northern Germany, 400-900 m in the central and southern German Uplands, and > 900 m in the Alpine region (see Figure 2.6 for the station locations). For stations < 400 m the phases of the diurnal cycles from WRF3_12 and WRF3 are quite similar with WRF12 showing roughly 10-20% more precipitation than WRF3; both underestimate night-time precipitation compared to stations. While the timing of the peak is delayed by about 3 hours in both simulations, the daily maximum precipitation differs by only 5% from the observations. For upland stations (Figure 5.2c, d) there is a phase shift of 1-2 hours between both simulations with WRF3 closer to the observations. Both simulations clearly overestimate amplitude and mean

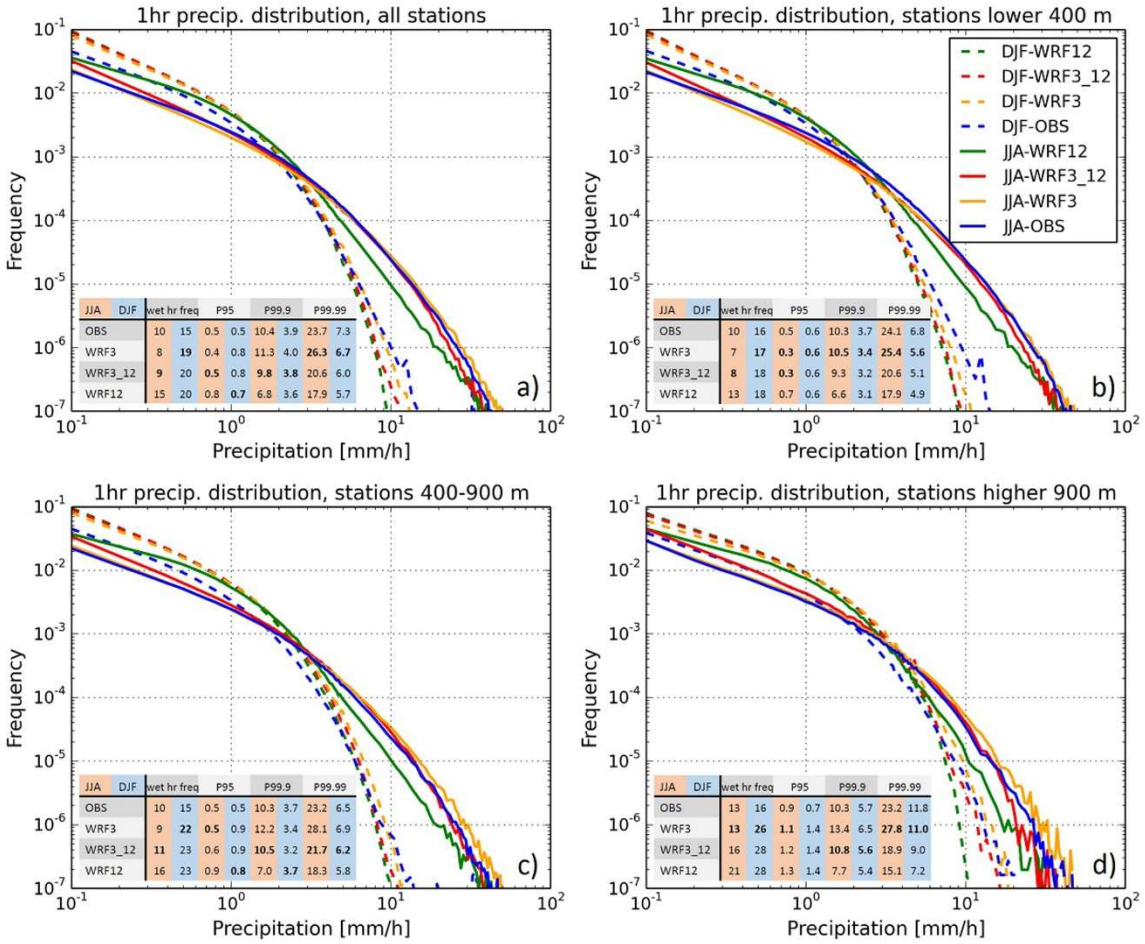

Figure 5.3: Intensity distribution of hourly precipitation based on all rain gauge stations (blue lines) (a), lowland stations (<400 m) (b), uplands stations (400-900 m) (c) and Alpine stations (> 900 m) (d). Green lines indicate the ERA-Interim driven 12 km WRF simulation (WRF12), yellow lines the 3 km simulation (WRF3) and red lines the 3 km results interpolated on 12 km grid (WRF3_12). For each station the nearest model grid point is taken into account. Solid lines show results for summer (JJA), dashed lines for winter (DJF). Tables show the wet hour frequency in% and 95th, 99.9th and 99.99th hourly precipitation percentiles in mm, whereby bold printed values are closest to the observation.

daytime precipitation, especially for the Alpine region. While night-time precipitation amounts are similar a much too large maximum of 0.40 mm/h is reached already at 14 UTC by WRF12 compared to 0.35 mm/h at 15 UTC in WRF3 and 0.25 mm/h at 17 UTC in the observations.

Overall, both the timing and peak are slightly better reproduced by the convection-permitting WRF3 simulation, but compared to studies by Kendon et al. (2012) and Ban et al. (2014), the improvement by the higher resolution runs are less pronounced. This is in agreement with Prein et al. (2013), who found that the improvement of precipitation diurnal cycle by convection-permitting models over coarser-scale runs are model-dependent with WRF simulations showing the smallest differences.

5.4 Hourly precipitation intensity

During winter time (DJF, dashed lines, Figure 5.3a) low and medium hourly precipitation intensities have similar occurrences between WRF12 and WRF3/WRF3_12 but are more frequent compared to the observations; accordingly the occurrence of heavy precipitation (> 6 mm/h, 99.99th percentile) is underestimated especially by WRF12 (Figure 5.3a). Differences between both resolutions are larger during the summer months (JJA, solid lines, Figure 5.3a). The larger precipitation amounts by WRF12 are produced by a much higher occurrence of light and medium precipitation, which overcompensates the underestimated occurrence of heavy and extreme precipitation. Overall, WRF3/WRF3_12 results better fit the observations as also indicated by the percentage of wet hours and the 95th, 99.9th and 99.99th percentiles of hourly precipitation including dry hours (see tables in Figure 5.3). For very high hourly precipitation sums (> 10 mm/h) WRF3 data even slightly exceeds the observations.

Similar behavior is seen for all height ranges (Figure 5.3a-c): overestimation of light and moderate precipitation in WRF12 in summer and in both simulations in winter, underestimation of heavy precipitation in WRF12, overall much better reproduction of heavy precipitation in WRF3_12 and WRF3, especially in summer. In winter, when convection is less frequent, the largest difference between both resolutions occurs for the Alpine region, where heavy precipitation events are better represented in WRF3. In summer, heavy precipitation in mountainous regions is slightly overestimated as also reported in previous studies in this region (Langhans et al. 2013; Prein et al. 2013; Ban et al. 2014). The overall better reproduction of hourly precipitation intensity distributions confirms findings in other convection-permitting climate simulations (Kendon et al. 2012; Ban et al. 2014; Fosser et al. 2015; Brisson et al. 2016).

5.5 Temperature–extreme precipitation scaling

Figure 5.4 compares the simulated and observed temperature-extreme precipitation scaling rates by plotting the 99th percentile of the daily maximum hourly precipitation (P99dmax) as a function of daily mean temperature extrapolated to mean sea level for all stations (Figure 5.4a) and separated for different height ranges (Figure 5.4b-d). Overall, both model simulations agree with the observations in the C-C scaling of 7% K^{-1} (indicated by the gray dashed lines) for the temperature range from 0°C to 11°C. From 11°C to 22°C WRF3_12 follows the stronger (super-adiabatic) T-P99 scaling (~10% K^{-1}) of the observations, which is not reproduced by WRF12. This finding is consistent with the differences found in the precipitation intensity distributions between both resolutions and observations in summer compared to winter (Figure 5.3).

For temperatures above 22°C, the scaling reverses to lower $P99_{dmax}$ values in both simulations and observations, indicating the transition to a dry regime where high temperatures are accompanied with limited moisture supply. For even higher temperatures the relation becomes uncertain due to the low number of occurrences.

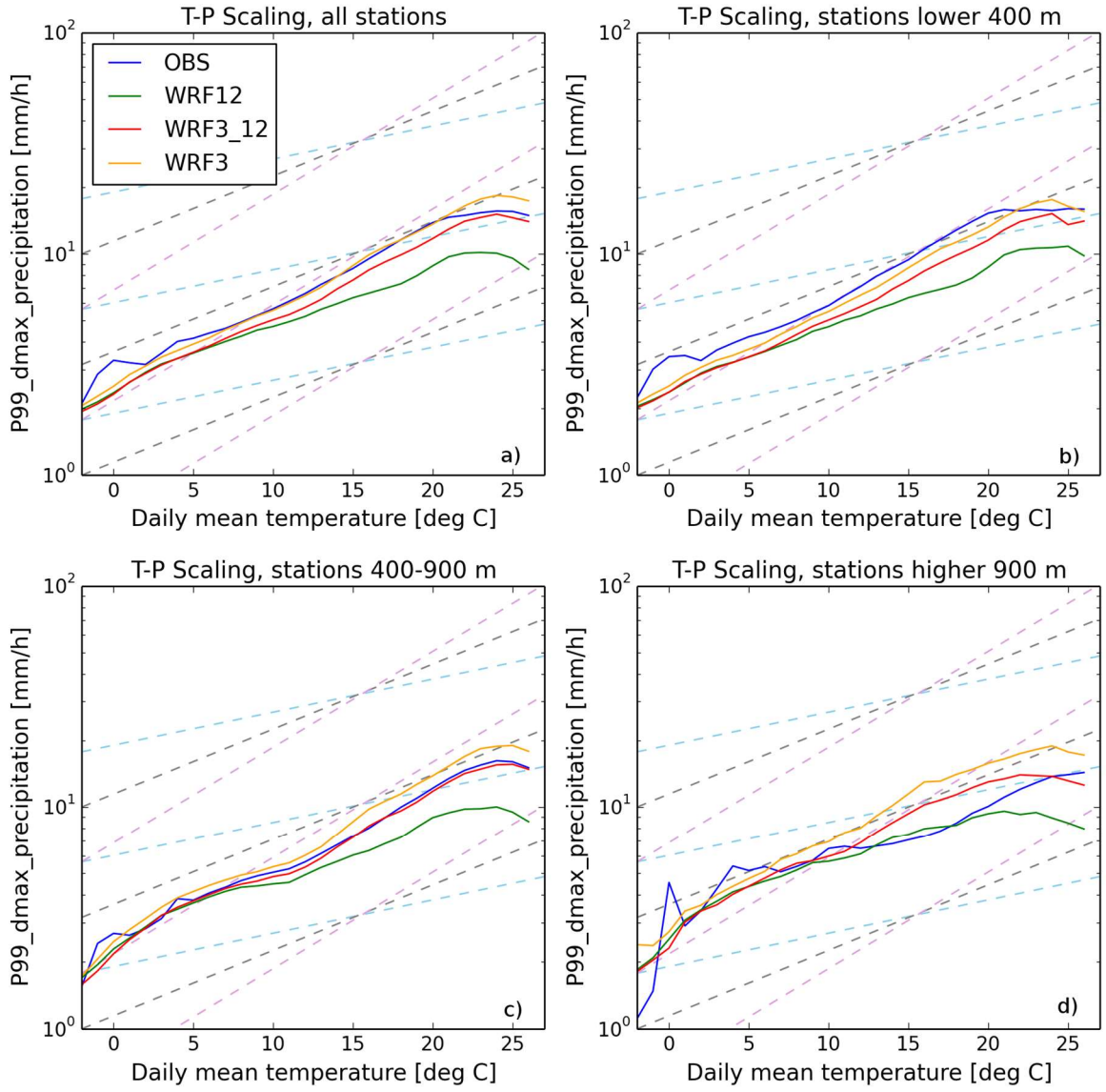

Figure 5.4: Temperature–extreme precipitation scaling in the ERA-Interim driven WRF12 (green), WRF3_12 (red) and WRF3 (yellow) compared to station observations (blue) based on all stations (a), on lowland stations (< 400 m) (b), on uplands stations (400-900 m) (c) and lower right on Alpine stations (> 900 m) (d). For each grid point nearest to a station daily maximum hourly precipitation is discretized into one-degree bins of daily mean temperature. To account for different altitudes, temperature is extrapolated to sea level by assuming a lapse rate of 0.0065 Km^{-1} first. For each temperature bin with a sample size larger than 50 the 99th percentile of the precipitation values (P99dmax) is calculated and averaged over all stations. Light blue, grey and pink dashed lines indicate a scaling of 3.5% K^{-1}, 7% K^{-1} and 10.5% K^{-1} (according 0.5, 1 and 1.5 times C-C scaling rate), respectively.

The scaling curves for WRF3 have a similar shape as WRF3_12 but are shifted to overall slightly higher precipitation. Overall, the scaling rates are slightly stronger in WRF3 (+0,2% K^{-1}). However, this effect of regridding from WRF3 to WRF3_12 is relatively small compared to the difference between WRF3_12 to WRF12. In line with the intensity distributions (Figure 5.3), the scaling curves of WRF3 are closest to the observations for lowland stations, but slightly overestimate the extreme precipitation for uplands (400-900 m) and Alpine stations (>900 m). WRF3_12 fits the observed super-adiabatic scaling rates for temperatures above 12°C best for the uplands stations (400-900 m). For lowlands stations, the simulated P99dmax values are somewhat lower than in the observations. For the Alpine region, scaling curves from simulations and observations are less homogeneous and scaling rates are overall slightly weaker than for lowlands and uplands. Besides topography related effects like forced ascending and differential heating at mountain slopes also artefacts due to the – now much larger – extrapolation of temperature to mean sea level may play a role. Overall, however, our results are in line with e.g. Lenderink and van Meijgaard (2008) and Ban et al. (2014).

The comparison is now extended on the temperature-extreme precipitation scaling (T-P99dmax) between the 12 km and 3 km simulations to the whole model area to extend the range of climate conditions, albeit at the expense of missing observations (Figure 5.5). Thus, spatial averages over all grid points are compared without the restriction of available observations. The scaling curves for the Lowland and Upland regions (blue and green curves in Figure 5.5a) largely resemble the respective curves shown in Figure 5.4 since most of the stations are located in these areas. Both show C-C scaling in the temperature range from 0°C to 10°C, increasing to super-adiabatic scaling in WRF3_12 for 10°C to 22°C and a drop for higher temperatures. In southern France and northern Italy (pink and yellow curves in Figure 5.5b) the drop of $P99_{dmax}$ already starts at about 17°C, which is most probably related to dry and hot summer conditions but insufficient precipitable water to generate strong precipitation. The convection-permitting runs (WRF3_12, solid lines) generate overall higher $P99_{dmax}$ values in all analysis regions than the coarse resolution runs (WRF12, dashed lines). Differences are small from 0°C to 10°C., but WRF12 is completely missing the increase in scaling rate for higher temperatures. Since the curves differ between the regions, temperature must be just one factor in the complex extreme precipitation generation process. While higher precipitation values can be expected for regions with steep orography (like the Alps), the higher $P99_{dmax}$ values for the same temperatures in southern France and northern Italy compared to the other regions must result from other local (thermo-)dynamic conditions (local wind systems, advection of moist air masses from the Mediterranean Sea, atmospheric stability).

The regionally different scaling curves result in a slightly flatter scaling rate for the whole domain average (black line, Figure 5.5a) and also largely mask the increase to a super-adiabatic scaling rate for warmer temperatures. Prein et al. (2016) also found regionally

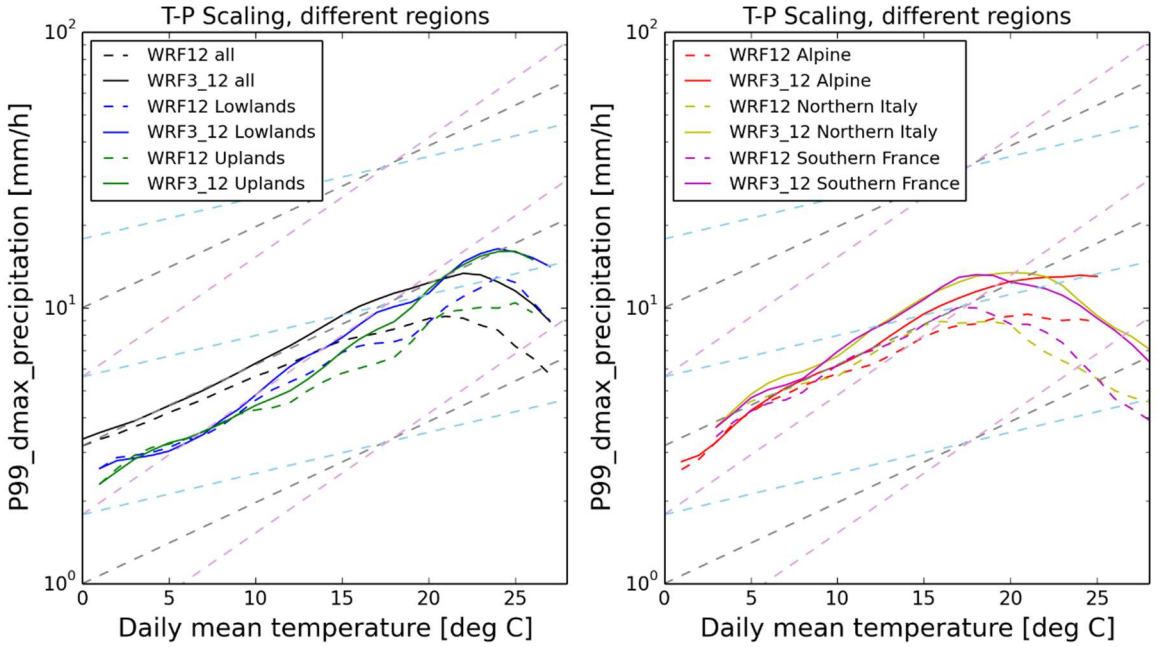

Figure 5.5: Temperature–extreme precipitation scaling in the ERA-Interim driven WRF12 (dashed) and WRF3_12 (solid) for different analysis regions. a) all domain grid points (black), lowlands (blue), uplands (green); b) Alpine (red), southern France (yellow) and northern Italy (purple), see Figure 2.6 for the definition of the analysis regions. For each grid point in a region daily maximum hourly precipitation is discretized into one-degree bins of daily mean temperature with one degree overlap. To account for different altitudes, temperature is extrapolated to sea level by assuming a lapse rate of 0.0065 Km^{-1} first. For each temperature bin with a sample size larger than 100 the 99th percentile of the precipitation values ($P99_{dmax}$) is calculated and averaged over all grid points. Grey dashed lines indicate a scaling of 7% K^{-1} according to the Clausius-Clapeyron relation.

different scaling curves over the U.S.A. and identified moisture as a limiting factor for extreme precipitation at high temperatures. For Central Europe the regional climate is less diverse, but the impact on the scaling curves is still detectable. Obviously, the interpretation and comparison of scaling curves, averaged over regions with varying topography has to be done with care. Averaging over different grid point or station heights without height corrections on the near-surface temperature and accordingly different near surface temperatures always leads to flatter scaling curves.

5.6 Summary and conclusion

The results for 12 km and 3 km resolution clearly differ for summer in structure, diurnal cycle and mean precipitation amount. In winter, differences are smaller and mostly related to orography. The comparison of 9-year ERA-Interim-driven simulations against rain gauges in Germany and Switzerland show, that the 3 km simulations better reproduce observed hourly precipitation intensity distributions. Too frequent light precipitation results in a wet bias in both simulations, which is however reduced in the 3 km resolutions

runs in summer. The frequencies of heavy and extreme hourly precipitation are underestimated in the 12 km runs and much better captured in the 3 km runs, although extreme precipitation events are overestimated in mountainous regions, which might also result from observation uncertainties (Ban et al. 2014). While the 3 km runs also better represent the diurnal cycle of precipitation, the improvement in phase and amplitude in the convection-permitting simulation is less compared to other studies (e.g. Kendon et al. 2012; Ban et al. 2014; Fosser et al. 2015). Largest differences between both resolutions, also when compared to observations, are found in mountainous regions, where onset and daily maximum are simulated too early and too strong, respectively, especially in the 12 km simulation. This is consistent with findings by Langhans et al. (2013) and Prein et al. (2013). They however suggest that the poor performance of the coarse simulation is caused by the convection scheme rather than by the unresolved small-scale topography. An investigation of this issue will be part of the sensitivity study in Chapter 6. Overall, results are in line with findings on convection-permitting climate simulations summarized by (Prein et al. 2015) and confirm the added value of convection-permitting climate simulations.

Also, the observed scaling of extreme precipitation ($P99_{dmax}$) with daily mean temperature is better reproduced by the convection-permitting simulations. The 12 km simulations miss the observed increase from a C-C scaling rate (~7% K^{-1}) to a super-adiabatic scaling rate (~ 10% K^{-1}) at temperatures above 11°C in accordance with the underestimation of the frequency of summer heavy and extreme precipitation events. The stronger scaling rate, related to dominant convective precipitation in this temperature range (Berg et al. 2013), is better captured by the explicit simulation of convection in WRF3. However, both simulations reproduce the observed drop of scaling rates at high temperatures caused by moisture limited conditions. Scaling-rate curves differ between sub-regions like, e.g., an earlier drop of the scaling rate in southern France and northern Italy.

With the better representation of the precipitation intensity distribution and the temperature–extreme precipitation scaling, convection-permitting simulations are potentially also better suited for assessing changes of precipitation statistics in the projected future climate. The expected increase of extreme precipitation under warmer future climate conditions is investigated and compared for both 3 km and 12 km resolution in Section 7.5 and 7.6.

6 Effects of land surface inhomogeneity on convection-permitting WRF simulations

6.1 Introduction

The comparison of the WRF evaluation simulations for Central Europe with 12 km and 3 km grid size revealed an added value of the higher resolution, especially for precipitation statistics. So far, it is not clear, whether the differences between both simulations mainly result from better resolving of atmospheric processes in the 3 km simulation, especially the explicit simulation of the deep convection, or how much the higher resolution of the heterogenous land surface and its effect on the atmospheric processes contribute to the results.

Furthermore, the impact of a better resolved land surface can be separated into effects of land use heterogeneity and of orography. Land use types may differ largely in albedo, roughness length, leaf area index, etc., which impact the surface radiation and energy balances and the turbulent transport of momentum, heat and water vapor to the atmosphere. As seen in the previous chapter, clear local differences in land-atmosphere coupling related to different land use types exist for WRF3 and WRF12.

Dependent on the scale and contrast of its heterogeneity, land use patterns may induce sensible heat flux patterns, that generate circulations on scales ranging from the turbulent scale that affect the state of the atmospheric boundary layer up to organized mesoscale circulations similar to the land-sea breeze effect (Giorgi and Avissar 1997; Avissar and Schmidt 1998).

In the following, the impact of the spatial scales of the patterns of land use, soil moisture and orography on convection-permitting RCM simulations in terms of atmospheric patterns and domain wide averages is investigated. To this goal, five 3 km grid size, convection-permitting seasonal simulations for central Europe are performed, each with different combinations of coarsely (12 km) resolved land surface property types (see Section 2.2.6). This allows to assess the impact of each land surface property on atmosphere flow, also in comparison to the driving 12 km simulation with parametrized convection. The simulations cover the summer season (JJA) 2003 as this season was characterized by strong land-atmosphere coupling conditions (see Section 4.2). It had mainly convective precipitation events in June and July as well as longer dry and hot periods in July peaking in a severe heat wave in the first half of August.

The results are compared for several variables, first with a focus on seasonal means and similarities in the horizontal difference patterns, and second for their temporal evolution.[9]

[9] Results and figures of Section 6.2 to 6.4 have been submitted for publication in Knist et al.

6.2 Surface properties impacts on the evolution of atmospheric states

In this section the mean differences of state variables between the reference run REF with all land surface characteristics resolved at 3 km and the results of setups with all (A) or part (B, C and D) of the land surface properties resolved at 12 km are analysed (see Table 2.2). As there are at least two setups that have one land surface property in coarse resolution in common, similarities in their difference patterns to the REF run allows to separate their individual impacts. Furthermore, the temporal dynamics of the difference patterns between the different setups for different variables based on the evolution of ten-daily means are investigated. This analysis is based on the hypothesis, that some difference patterns may depend on the weather conditions and large-scale flow and that similarities in the patterns are consistent throughout the simulated time period.

6.2.1 Latent and sensible heat fluxes

Summer 2003 in central Europe was anomalous warm and dry and culminated in a severe heat wave beginning of August. The domain spatial mean upper-level soil moisture continuously decreased in the reference simulation from 0.35 m^3/m^3 beginning of June to 0.27 m^3/m^3 end of August (Figure 6.1, leftmost column). While latent heat flux dominates the turbulent fluxes in June, the system underwent a transition from energy limited to soil moisture limited conditions, accompanied with a strong decrease of latent heat flux and an increase in sensible heat flux till the end of August (Figure 6.2 and Figure 6.3, leftmost column). The horizontal patterns of latent and sensible heat flux are very heterogeneous due to their dependence on soil moisture, land use, and soil type. For example, urban areas are clearly identified by high sensible heat fluxes and very low latent heat fluxes. High latent heat fluxes and low sensible heat fluxes are simulated for the forested areas in the German uplands and central France as well as in the Alpine foothills. For the lower mostly cropland areas, sensible heat fluxes exceed latent heat fluxes, especially in the Po valley and the southern parts of the domain. Soil moisture limited conditions are reached much faster in areas with crop land use type while forested areas sustain a high evaporative fraction until August.

Differences in turbulent fluxes between the reference and the different setup occur instantly for coarse land use simulations (setups A, B and C) at grid points that changed their land use type with respect to the original 3 km reference run (Figure 6.2 and Figure 6.3, second row). Besides the noisy pattern with alternating positive and negative differences on the

(2018b).

local scale, the setups A and B simulate for large areas higher mean latent and lower mean sensible heat fluxes. These differences related to the slightly wetter initial soil moisture conditions of the 12 km resolution (Figure 6.1), which lead to 5.4 W/m² higher (4.1 W/m² lower) domain average latent (sensible) heat fluxes for JJA 2003. Interestingly, the excess in latent (and deficit in sensible heat) fluxes in setups A and B peak in mid-July and not in June when the soil moisture difference is largest. This results from the non-linear relationship between soil moisture and latent heat flux: the transition from the energy-limited state (when soil moisture does not impact evapotranspiration) to the soil moisture-limited state (when evapotranspiration decreases with decreasing soil moisture) is reached earlier in the initially drier REF simulation than in the initially moister A and B setups. Until the end of August differences decrease as latent heat flux is low in all simulations.
For setup C with an initial soil moisture identical to REF, strong differences mainly occur just for grid points with different land use types caused by the different resolution of the land use type maps. The domain mean latent heat flux for setup C is consistently lower than for setups A and B, but 3-4 W/m² higher compared to the REF run because of the slightly different percentages of land use types (see Figure 2.3 and Figure 2.4). Separating time series of daily latent heat flux differences averaged over different groups of grid points that undergo a land use change from REF to setup C illustrates the individual contribution to the mean latent heat flux difference between both setups (Figure 6.4). The initially higher domain average latent heat flux in setup C mainly results from the surplus of grid points with land use type crop that are urban (low evapotranspiration) in REF compared to the opposite transition. A similar effect holds for land use changes from mixed forest in REF to crop in setup C and vice versa: in June crop grid points typically evapotranspirate more than mixed forest land use grid points, which reverses with the drying of the soil conditions in July and August. The slightly different fluxes between setup C and REF even for the same land use types at the beginning of the simulation relate to differences in mean vegetation fraction between the 3 km and 12 km resolution setups.
For setup D (like REF but coarse orography) initially only small differences compared to REF occur. The then evolving noisy difference pattern is mainly related to the evolution of local differences in soil moisture generated by the differently evolving precipitation. Overall, the differences in turbulent fluxes between all setups versus the REF simulation are dominantly related to the flux partitioning and less to differences in incoming solar radiation (that are discussed in the next section).

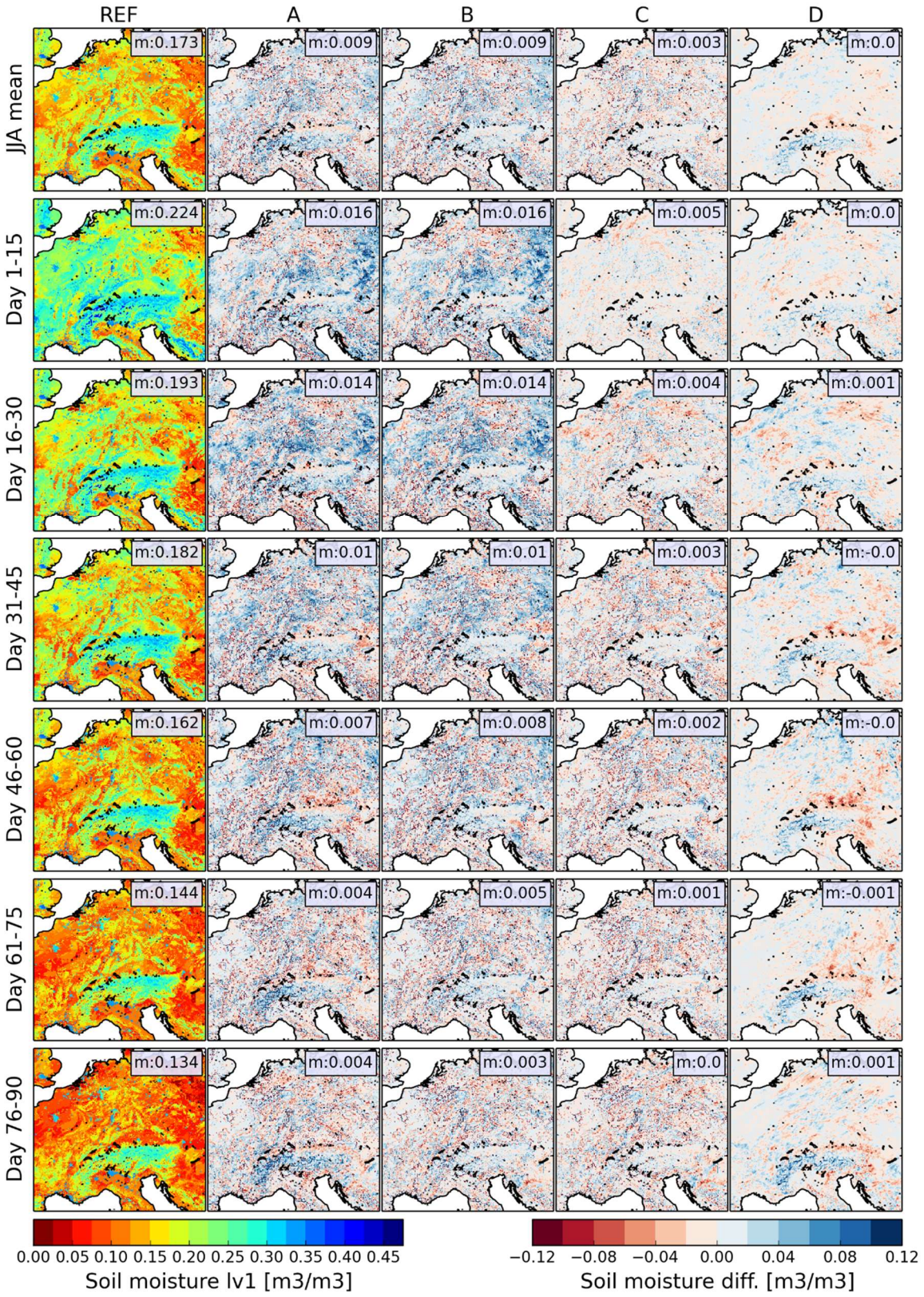

Figure 6.1: Spatial distribution of upper-level soil moisture (JJA mean, first row) and its temporal evolution (15-daily means, second to last row) in the REF simulation (first column) and in the setups A to D (second to fifth column) displayed as difference to REF. Domain averages and differences are shown in the upper right corner.

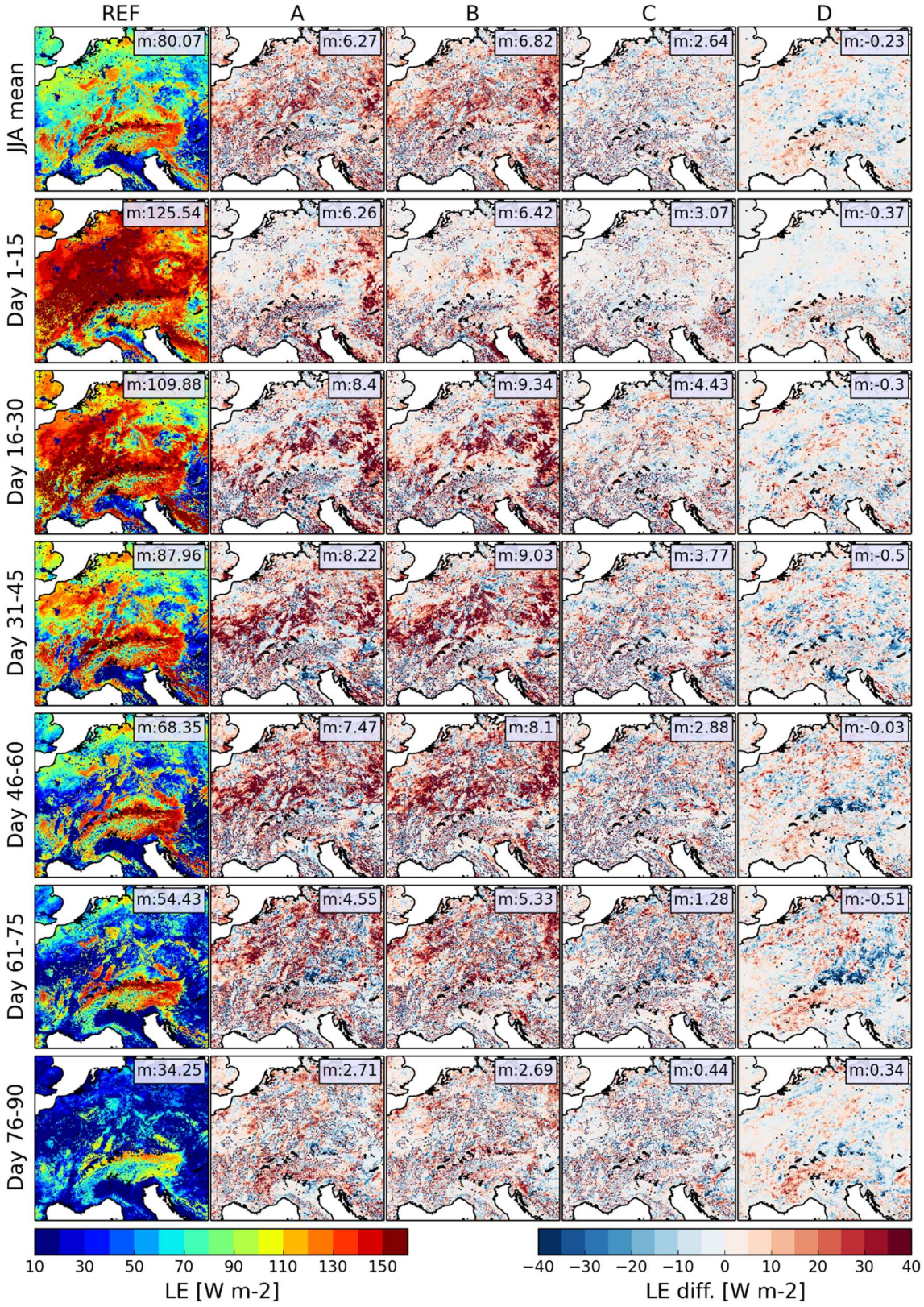

Figure 6.2: Spatial distribution of latent heat flux (JJA mean, first row) and its temporal evolution (15-daily means, second to last row) in the REF simulation (first column) and in the individual setups A to D (second to fifth column) as difference to REF. Domain averages are shown in the upper right corner.

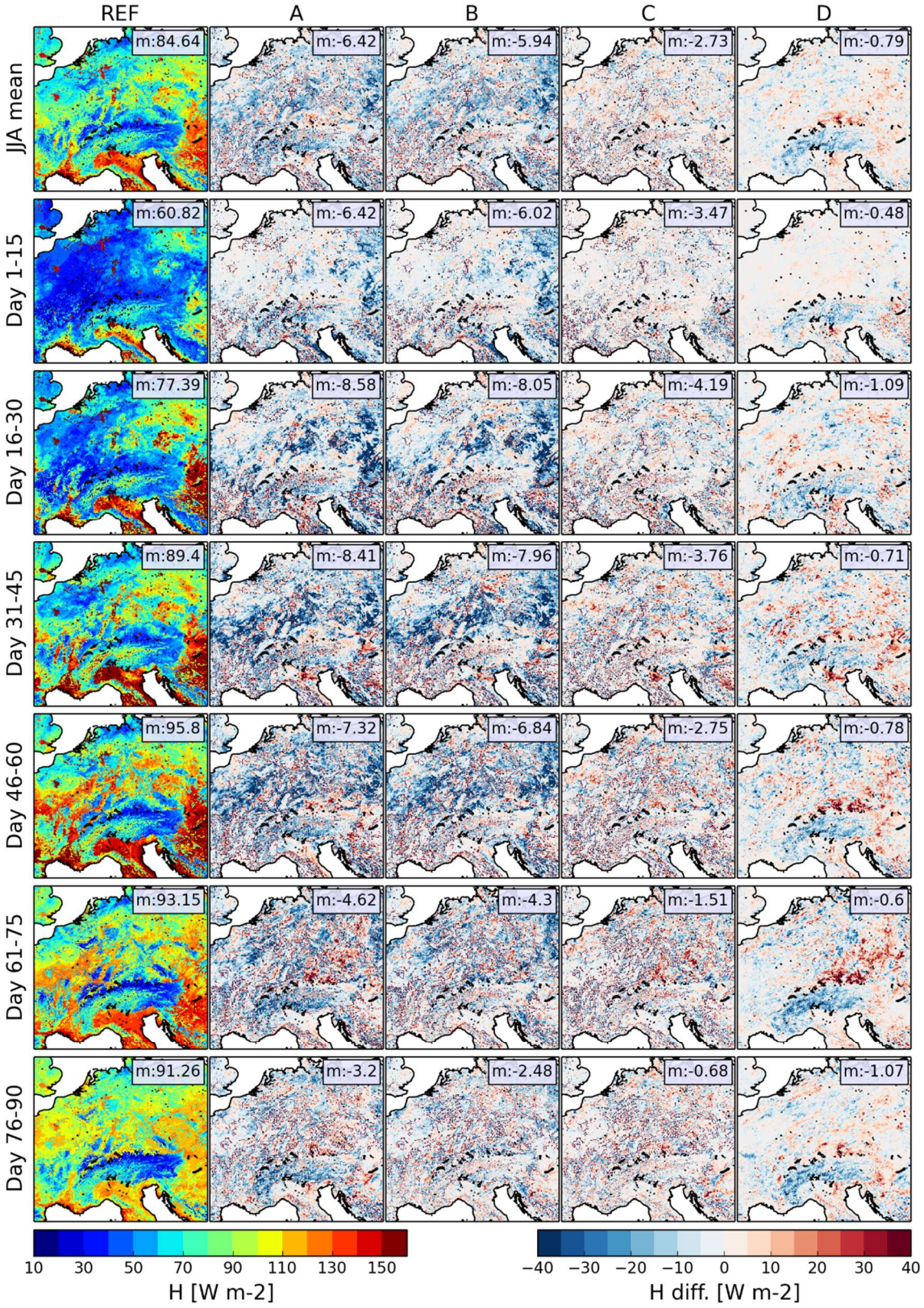

Figure 6.3: Spatial distribution of sensible heat flux (JJA mean, first row) and its temporal evolution (15-daily means, second to last row) in the REF simulation (first column) and in the individual setups A to D (second to fifth column) as difference to REF. Domain averages are shown in the upper right corner.

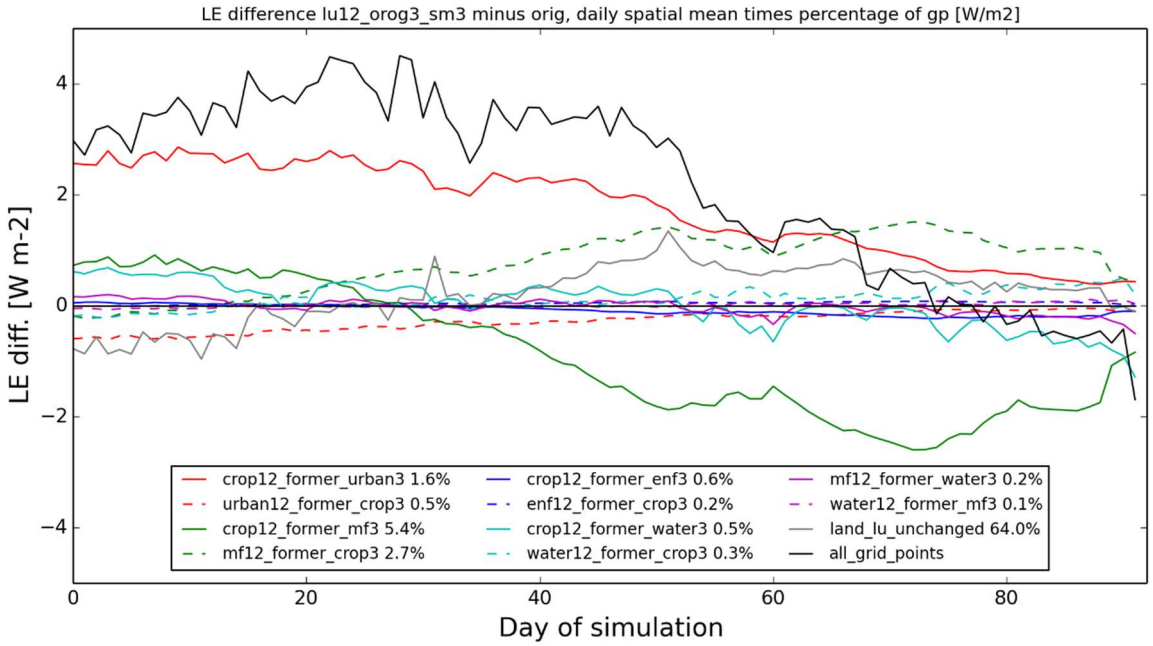

Figure 6.4: Time series of spatially averaged daily mean latent heat flux differences between Setup C and REF for different groups of land use types that undergo a land use change from REF (3 km) to Setup C (12 km). The spatial averages are multiplied by the percentage of grid points of each group so that their individual contribution to the whole domain average difference (black line) is shown.

6.2.2 Short wave radiation

Incoming shortwave radiation (SW_d) dominates the variability of surface net radiation, which is the main driver of the turbulent fluxes, and is inversely related to daytime cloudiness. Since there is no direct dependency of SW_d on land surface properties differences between the setups are by a factor of four smaller (Figure 6.5). Due to the complex non-linear land-atmosphere feedback processes, systematic difference patterns can be hardly identified also because of the random internal variability generated during the evolution of the individual runs. Nevertheless, some similarities show up between the difference maps for the different setups.

The largest similarity in the difference patterns – also in terms of spatial correlation coefficient (see Table 6.1) – are observed for the setups with the same coarse orography (A and D). As already seen for the mean values over the whole time series less shortwave radiation reaches the surface over the Alpine ridge because of the consistently higher convective activity. Other regional patterns only sporadically show up indicating a dependency on weather conditions.

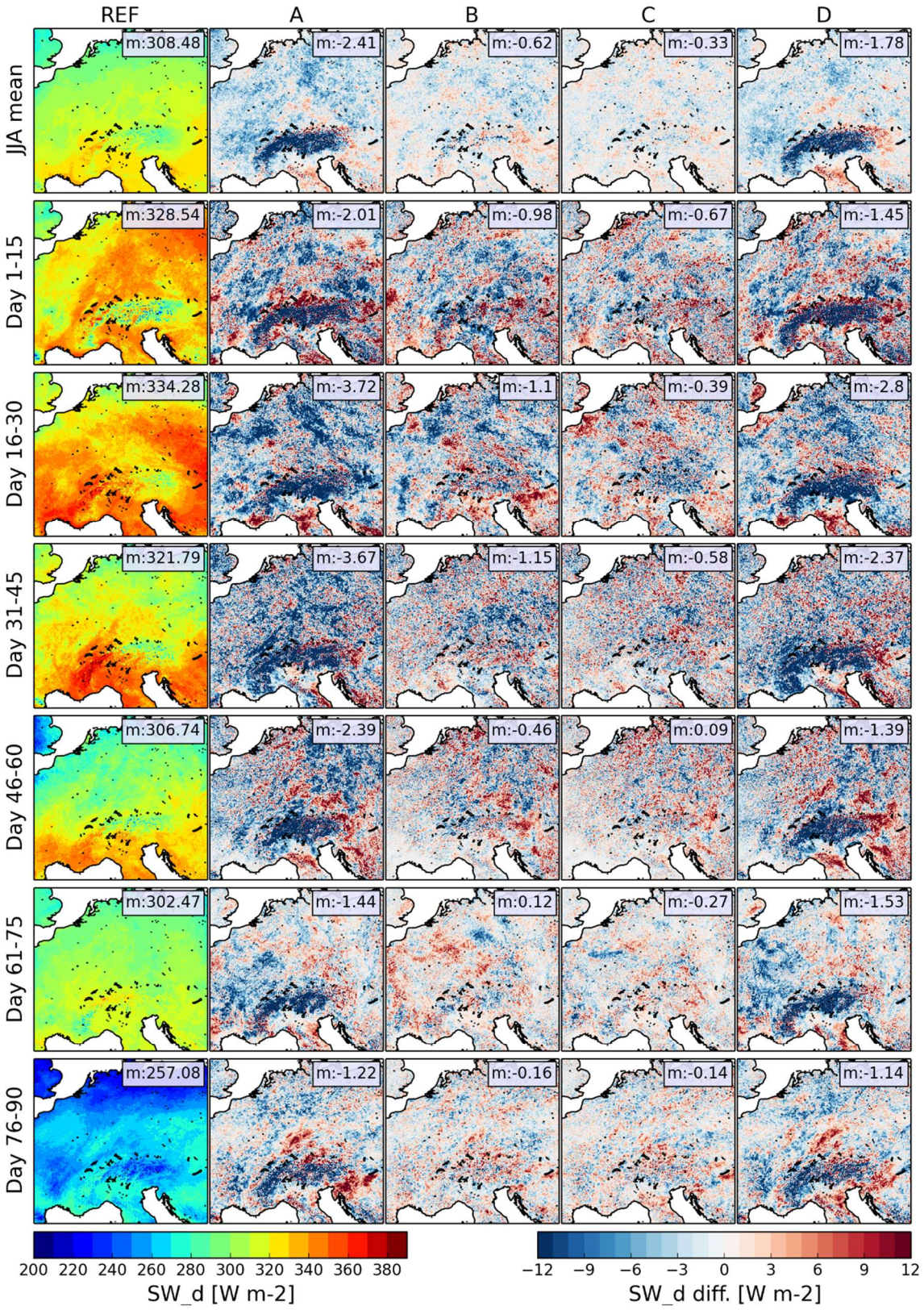

Figure 6.5: Spatial distribution of incoming shortwave radiation (JJA mean, first row) and its temporal evolution (15-daily means, second to last row) in the REF simulation (first column) and in the individual setups A to D (second to fifth column) as difference to REF. Domain averages are shown in the upper right corner.

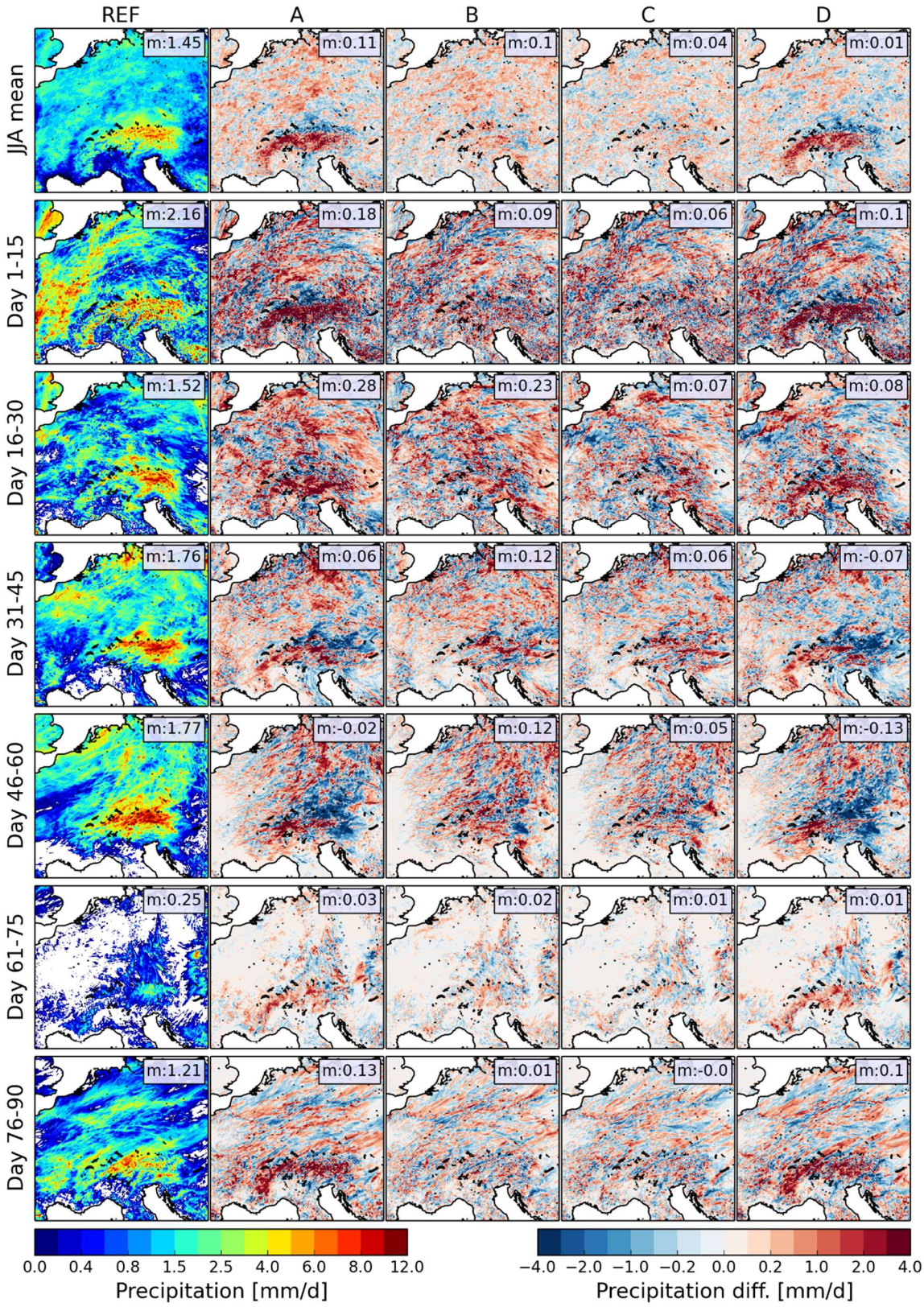

Figure 6.6: Spatial distribution of precipitation (JJA mean, first row) and its temporal evolution (15-daily sums, second to last row) in the REF simulation (first column) and in the individual setups A to D (second to fifth column) as difference to REF. Domain averages are shown in the upper right corner.

Setups B and C, which differ from REF by their coarse land use type resolution, show only scattered differences in incoming solar radiation, which mostly cancel each other in the mean. Setup B, which additionally differs from REF by an initially slightly wetter soil, generates somewhat less incoming overall shortwave radiation, thus more cloudiness. The same difference is seen between the two setups with coarse orography but different initial soil moisture, A and D. These differences most likely result from the overall higher evapotranspiration and thus more clouds in the moister setups A and B. This causality is corroborated by the anti-correlated temporal evolution of the difference in average shortwave radiation and latent heat flux except for setup D, which suggests that in this case, the differences are dominantly caused by different flow pattern due to the coarse orography. The difference patterns for setups B and C show despite the noisy structure some similarities on the regional scale (average daily correlation 0.49) that suggest a systematic impact of the coarsely resolved land use. For setups that have one surface property in common highest spatial correlation is seen between setup A and D (same 12 km orography). Consistently, lowest correlation between setups that differ in just one surface property occurs for setup A and B (different orography).

Table 6.1: Mean spatial correlation between different setups' daily difference patterns to the REF simulation for short wave radiation and precipitation.

	B vs. D	C vs. D	A vs. C	A vs. B	B vs. C	A vs. D	A vs. (B+D)
identical	-	sm3	lu12	lu12,sm12	lu12,or3	or12	lu12,sm12,or12
SW_d	0.29	0.30	0.34	0.40	0.49	0.69	0.70
precip	0.36	0.37	0.37	0.39	0.48	0.61	0.62

6.2.3 Precipitation

Precipitation in JJA 2003 is characterized by high amounts in the central and eastern Alps and in the central German uplands (Figure 6.6, left column). The noisy pattern with large variability on the local scale results from single convective events, whose tracks also cause lines of high precipitation amounts as seen for example in northern Germany and over the North Sea. Since the location of single convective cells and its evolution is mostly random also the difference pattern of the individual setup runs with respect to the REF simulation is mostly noisy. However, there are similarities in the pattern. Consistent with the results for incoming shortwave radiation, more precipitation is observed in the setups with less shortwave radiation (more clouds). E.g. setups A and D with the coarse orography are consistently wetter throughout the simulated months over the Alpine ridge where up to 30% more precipitation is simulated for JJA 2003. Difference patterns in other regions are more heterogenous and vary with time, while some similarities exist between setups with coarsely resolved land surface properties. Like shortwave radiation, setups A and D are

correlated highest (0.61) followed by setups B and C (0.48). Again, positive and negative differences mostly chancel out and lead to overall precipitation differences <10% with the higher initial soil moistures leading to higher precipitation for all 15-daily domain averages. Setups A and B (coarse land use and higher initial soil moisture) lead to about 7% more mean precipitation compared to their counterparts D and REF, respectively, with the same topography resolution. Setups C and REF, which only differ in the resolution of land use and soil type, only differ by 3% in mean precipitation with the higher values for REF with its higher resolved land use distribution.

6.2.4 CAPE and 850 hPa level patterns

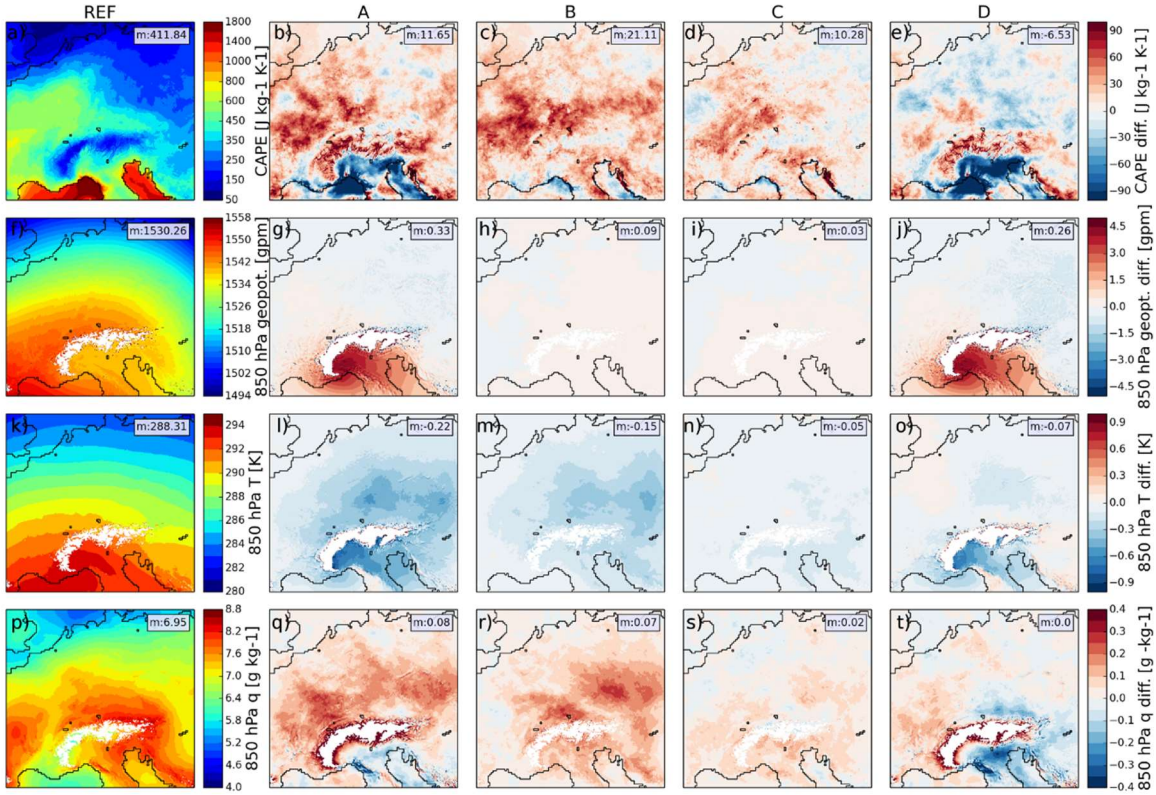

Figure 6.7: Spatial distribution of the summer (JJA) 2003 mean CAPE (a-e), geopotential height of the 850 hPa level (f-j), temperature at 850 hPa (k-o) and specific humidity in 850 hPa (p-t) in the REF simulation (a, f, k, p) and in the individual setups A to D as difference to REF. Domain averages are shown in the upper right corner.

Summer precipitation is mostly convective; thus, differences in precipitation should also be visible in the convective available potential energy (CAPE, Figure 6.7a-e). High CAPE not necessarily results in stronger precipitation on average but only the potential for strong convective events. The runs with coarse land use (setups A, B and C) show slightly higher overall CAPE, while the runs with coarse orography (setups A and D) simulate lower CAPE compared to their respective counterparts. Moreover, the coarse topography runs (setups A and D) result in consistently lower CAPE south of the Alps, which most probably

results from different flow patterns over and around the Alpine ridge with the smoothed orography (Figure 6.7f-j) as detailed below.
The coarsely resolved orography (setups A and D) influences the flow pattern in 850 hPa over the whole period much stronger than highly resolved setups B and C (Figure 6.7f-j). The strongest differences occur south of the Alps. On any occurrence of north-westerly flows towards the Alps (which is the case for most of the simulated period), lee-cyclogenesis results in lower surface pressure and the 850 hPa geopotential height, which is however weaker in the coarse topography setups A and D (Figure 6.7g and j). A possible reason is the overall lower height of the main Alpine ridge in the smoothed 12 km orography, which leads to a weaker Föhn effect resulting in slightly lower temperatures at the downwind side and less precipitation at the windward side of the mountains. The rest of the domain does not exhibit significant differences in geopotential and flow pattern between the different setups. Runs with coarsely resolved land use but highly resolved orography (setups B and C) do not differ much in mean 850 hPa height compared to REF, thus topography dominates the observed changes in flow pattern. In general, all strong local temperature differences between setups with coarse and fine resolved land use vanish above the boundary layer and no effect of land use heterogeneity is seen at 850 hPa (Figure 6.7k-o). The overall slightly colder 850 hPa mean temperature (0.1-0.5 K) in setups A and B are likely related to the overall higher sensible heat flux and less evaporative cooling due to slightly wetter initial soil in those setups (see Figure 6.2 and Figure 6.3). This is consistent with difference patterns of 850 hPa specific humidity that is slightly higher in setups A and B compared to REF (Figure 6.7p-t). Again, the strong heterogeneity at the surface completely vanishes at the 850 hPa level.

6.3 Mean diurnal cycle of orographic precipitation

Besides the larger scale difference pattern caused by the different flow pattern the coarsely resolved orography also results in overall more precipitation and clouds especially over the Alps. The mostly convective summer precipitation follows a pronounced mean diurnal cycle with maximum precipitation in the afternoon. While night-time precipitation amounts are quite similar the coarse orography runs simulate higher (+40%) and earlier (-1 hr) afternoon maxima compared to REF (Figure 6.8). The mean hourly precipitation patterns suggest, that the coarse orography facilitates the initiation and evolution of more organized, longer lasting, and larger convective cells. The higher convective activity corresponds with higher mean CAPE values reached in these runs.

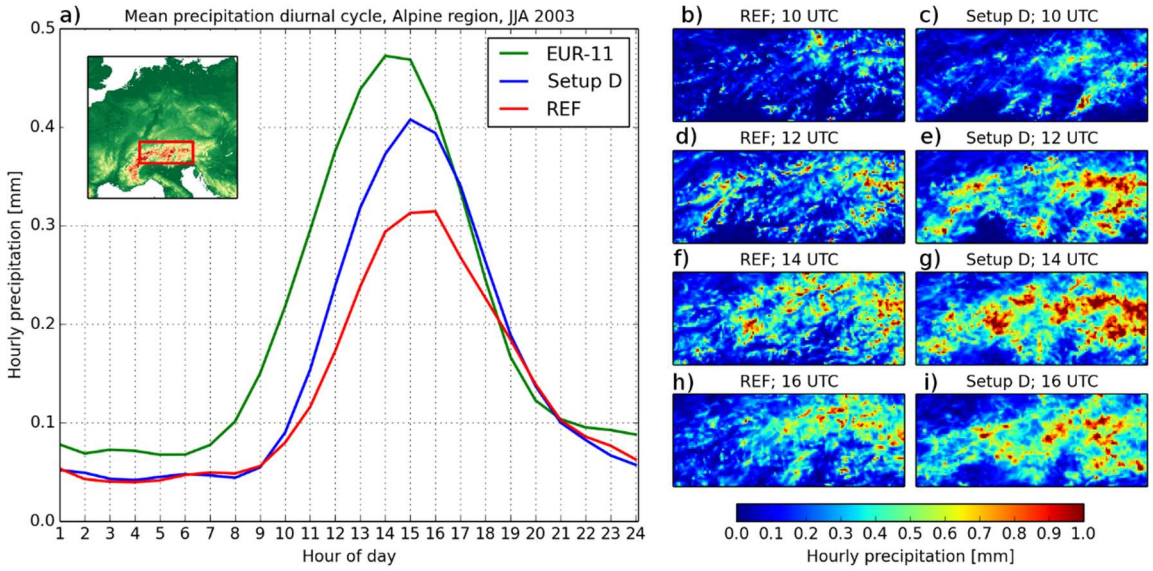

Figure 6.8: Mean diurnal cycle of precipitation in the Alpine region (red box in upper left corner) in setup D, REF and EUR-11 (a) and spatial distribution of mean hourly precipitation at 10, 12, 14 and 16 UTC in REF (b, d, f, h) and setup D (c, e, g, i).

6.4 Discussion and conclusion

The five WRF simulations for JJA 2003, each with the same atmospheric setup in 3 km resolution but different combinations of coarsely resolved (12 km) land use and soil type, initial soil moisture and orography, indicate that a coarser resolved orography significantly alters the flow over and around extensive mountain ridges like the Alps and impact the large-scale flow pattern. The smoothed mountain ridges result in weaker Föhn effects and in enhanced locally generated convective precipitation pattern peaking earlier in the afternoon.

The latter result is at variance with other studies, which suggest lower precipitation over smoothed orography (e.g. Smith et al. 2015). These seemingly conflicting results can likely be attributed to the character of precipitation, which was mostly convective in our summer study and predominantly stratiform in the winter cases analysed in Smith et al. (2015). Also, Prein et al. (2013) identified only small differences in simulated convective summer precipitation over the eastern Alpine region between with 3 km and 12 km orography runs. They concluded that the typically positive precipitation bias in convection-parameterized simulations mainly results from the parameterization scheme and the less resolved atmospheric dynamics rather than from the coarsely resolved orography.

The results from Section 6.3 do not confirm this conclusion. The mean diurnal cycle of precipitation over the Alpine region in the REF, setup D and the driving EUR-11 simulation suggests that the much higher precipitation amount in EUR-11 (+80%) is at

least partly attributed to the coarsely resolved orography that leads to an increase of 40% in setup D compared to the REF simulation. The steeper slopes and higher differences between valleys and peaks in the 3 km orography may initialize stronger vertical wind speeds and lift air more easily to the levels of condensation and free convection, which would suggest overall less convective precipitation with coarser orography contrary to our results where the smoothed orography seems to facilitate the initiation and evolution of more organized and overall larger convective cells that last longer. This reasoning is also consistent with the higher mean CAPE values observed for the simulations with smooth orography.

Besides of local effects on near-surface variables caused by inevitably differing land use types, the loss of heterogeneity in coarsely-resolved land use type maps going from 3 km to 12 km resolution does not systematically affect atmospheric flow, temperature or precipitation pattern. However, domain average differences in latent heat flux (about +3% between setup C and REF) and consequently differences mean cloudiness and precipitation (about +3%) may result from the slightly changing percentages of land use types upon aggregation. No clear differences in the hourly precipitation intensity distribution and its mean diurnal cycle are however observed (no shown). Positive spatial correlations between precipitation and shortwave difference patterns of setups with coarse land use also suggest a non-random effect on the cloud formation. However, additional perturbed ensemble simulations with each setup would be necessary to better assess systematic influences on the pattern.

The initial soil moisture more strongly alters the regional scale atmospheric patterns compared to the scale of the land use type heterogeneity. In our setup, the overall higher (+2.3% domain average) initial soil moisture taken from EUR-11 climate runs (setup A and B) compared to the 3kmME climate runs (setups REF, C, and D) lead to systematic differences in domain averaged latent and sensible heat flux and consequently also in cloudiness and precipitation in the order of 6 to 8% domain average. The impact of soil moisture differences clearly depends on the weather conditions and is largest for transitions from energy to soil moisture limited land-atmosphere coupling regimes, that widely occurred for the simulated season. In line with previous studies and results from Chapters 3 and 4 the experiment highlights the sensitivity of land-atmosphere coupling to soil moisture dynamics in particular for this anomalous dry summer 2003 (Fischer et al. 2007; Seneviratne et al. 2010; Keune et al. 2016) and confirms a contrasting response of different land use types (e.g. crop and forest) to heat wave conditions (Teuling et al. 2010).

In summary, when decreasing the spatial resolution of individual land surface properties, orography has the largest impact on the overall simulation results as it alters the flow over and around mountain ridges and largely influences the local precipitation pattern and intensity over regions with complex orography. The effect of a coarser-resolved land use maps is overall smaller and mainly related to changes in overall percentages of different

land use types, rather than to the loss of heterogeneity in the surface pattern on the scale analysed here. Even small changes in soil moisture (both spatial averages and local differences) have a higher potential to affect the overall simulation results, although this might also depend on the particular land surface model used. Overall, differences caused by coarsely resolved land surface properties are much smaller compared to differences between simulations with 3 km and 12 km grid spacings of the atmosphere (Ban et al 2014, Kendon et al. 2012, Prein et al 2013).

This study does not cover all potential combinations of resolution changes in the three land surface properties. A setup with only the initial soil moisture at coarse resolution could be considered. Potential effects can, however, be inferred from comparisons between setups B and C. Also missing are setups with coarse orography and land use and 3 km initial soil moisture, and with coarse orography and soil moisture and 3 km land use. Also a setup, where the percentages of coarse and original land use are made identical could be considered. To assess differences solely caused by internal variability, ensemble runs for each setup would be helpful.

7 Climate change projection simulations

7.1 Introduction

This chapter presents the results of the EUR-44 as well as the EUR-11/3kmME climate change projections downscaling the GCM MPI-ESM-LR-r1 RCP4.5 data. The analysis of the EUR-44 simulation focusses on the climate change signal for temperature and precipitation in relation to the driving GCM (Section 7.2). Furthermore, the projected change of the coupling strength pattern and related effects are investigated (Section 7.3). The expected change of precipitation statistics in the projected warmer future climate is compared for the convection-permitting 3 km simulation and the 12 km simulation (Section 7.5). Sections 7.4 and 7.6 furthermore investigate the projected temperature–extreme precipitation scaling in the EUR-44 and EUR-11/3kmME runs, respectively[10].

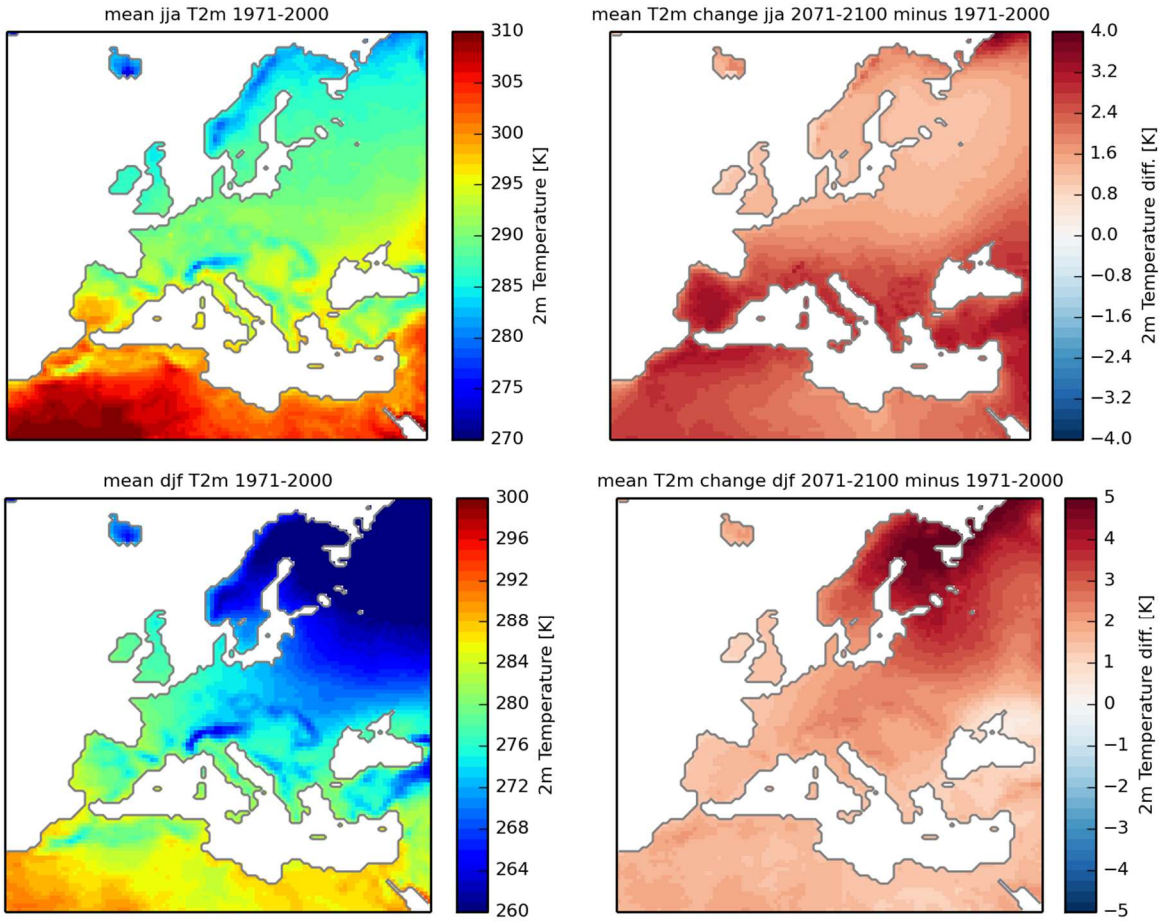

Figure 7.1: Mean 2m temperature in the control period (1971-2000, left) and its relative change in the far future (2071-2100, right) in the MPI-ESM-LR driven EUR-44 simulation in summer (top) and winter (bottom).

[10] Results and figures of Section 7.5 and 7.6 have been published in Knist et al. (2018a)

7.2 Climate change signal in EUR-44 compared to driving GCM

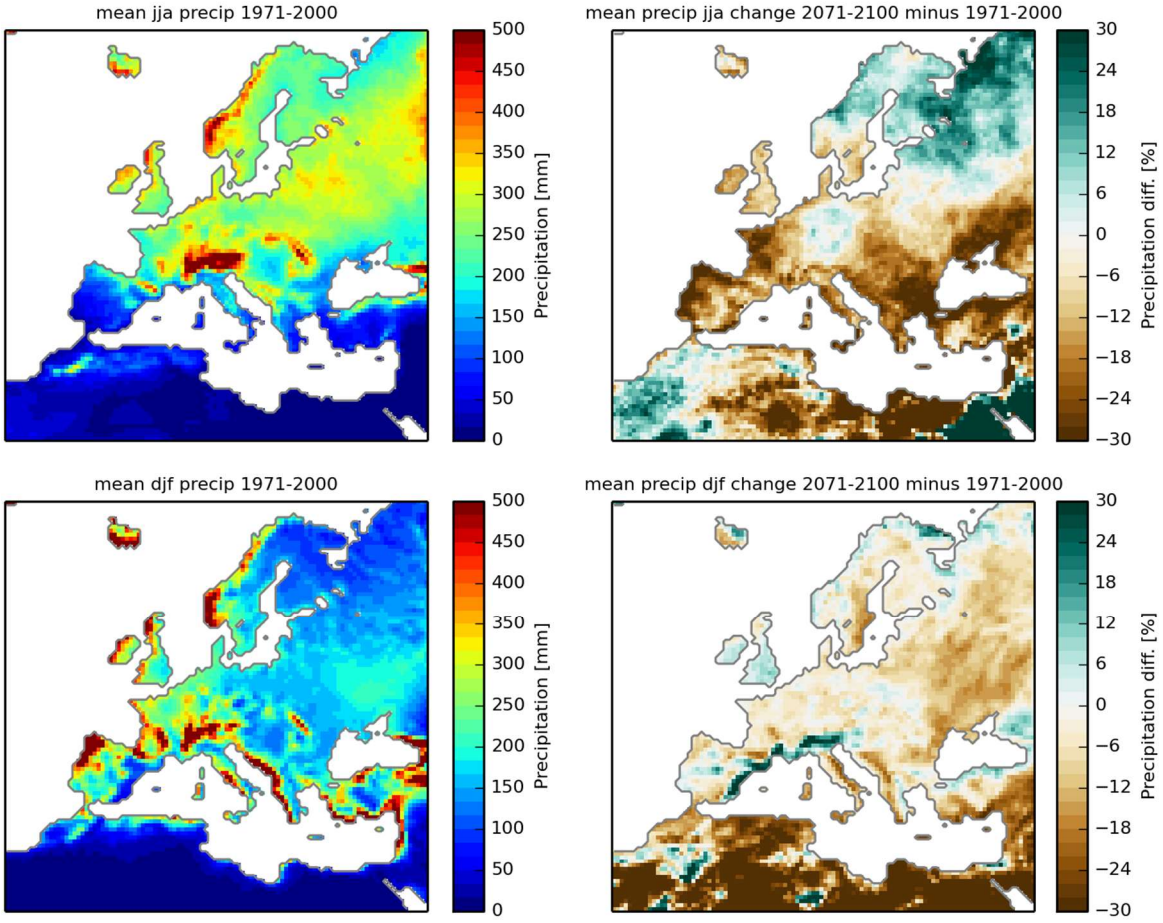

Figure 7.2: Mean seasonal precipitation sum in the control period (1971-2000, left) and its relative change in the far future (2071-2100, right) in the MPI-ESM-LR driven EUR-44 simulation in summer (top) and winter (bottom).

The EUR-44 simulation downscaling the GCM MPI-ESM-LR RCP4.5 data projects an overall future increase in mean 2m temperature in Europe (period 2071 to 2100 compared to the control period 1971 to 2000, Figure 7.1). Warming is projected all over the EURO-CORDEX domain and for all seasons. In summer, strongest temperature change up to 3.5 K is seen for the Mediterranean region, while the increase for north-western Russia and Scandinavia is about 1 to 1.5 K (Figure 7.1b). In contrast, strong warming (3-5 K) is projected for north-western Europe in winter, while the rest of the continent shows a less strong temperature increase (1-2 K) (Figure 7.1d).

For mean precipitation, the future changes are more heterogenous (Figure 7.2). In summer, there is a contrasting pattern with 10-30% less precipitation in southern and western Europe and 5-20% more precipitation in northern Scandinavia and Russia. In winter,

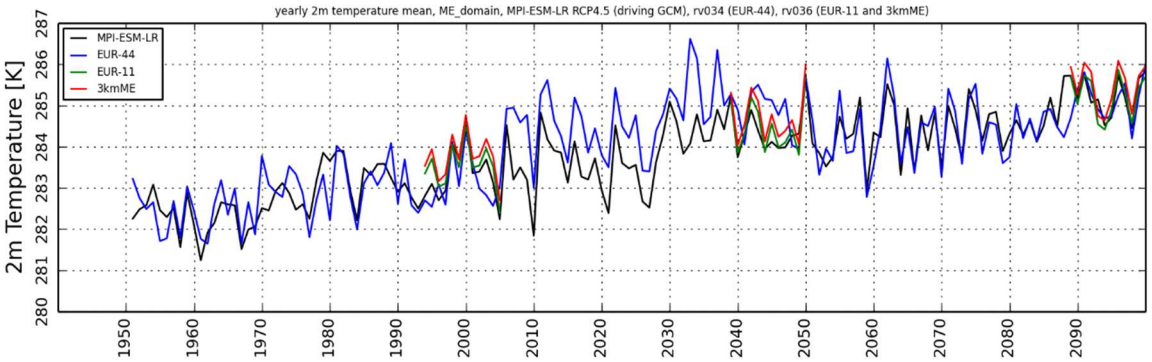

Figure 7.3. Time series of annual mean 2m temperature spatially averaged over the 3kmME domain in the driving GCM MPI-ESM-LR (black), the WRF EUR-44 (blue), EUR-11 (green) and 3kmME (red) simulation.

slightly less precipitation (5-10%) is simulated for most regions in Europe, while especially the Mediterranean coastal regions in Spain and France and the southern Alpine region show an increase of about 30%.

The large-scale precipitation change patterns are in line with the driving GCM for summer (see Figure C.0.8 in Appendix). However, differences become apparent on the regional scale, especially in or near mountainous regions. In winter, the change patterns of the GCM show an increase of mean precipitation (10-20%) for Sweden, Finland and northwestern Russia in contrast to the EUR-44 simulation indicating a slight decrease in this area. A comparison of the time series of EUR-44 and MPIESM for this area's mean precipitation in winter reveals a trend to increasing differences between both (see Figure C.0.8 in Appendix). However, the annual variability is similar and both time series are correlated also for far future. The continuously drying trend is exclusively seen for the north-eastern part of the domain as e.g. the time series for ME are not drifting apart. The 2071-2100 vs. 1971-2000 change in mean sea-level pressure pattern are similar in EUR-44 and MPI-ESM-LR. Both show higher mean pressure over central eastern Europe and lower mean pressure over the north-eastern corner of the domain. However, a slightly stronger south-westerly pressure gradient over Scandinavia and north-western Russia in combination with higher ridge of the Scandinavian Mountains in the EUR-44 resolution and the resulting stronger Föhn effects may cause the drier conditions in EUR-44 in winter.

The comparison of the time series from 1950 to 2100 for the middle European domain reveals the warming trend (Figure 7.3). This trend as well as a strong interannual variability is in line with the driving GCM. A high correlation (0.73) between both time series indicates a good agreement in the large-scale flow patterns. Differences in the year-to-year variation result from internal variability in the EUR-44 simulation. However, for the period from 2006 to 2050, a constant shift of about 1 K higher temperature in the EUR-44 simulation becomes apparent both compared to the GCM and the EUR-44 periods from 1950

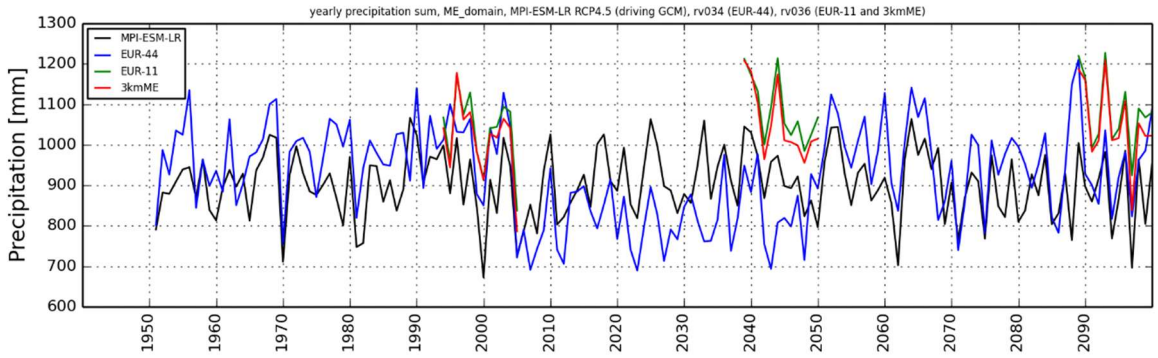

Figure 7.4: Time series of annual precipitation sum spatially averaged over the 3kmME domain in the driving GCM MPI-ESM-LR (black), the WRF EUR-44 (blue), EUR-11 (WRF12, green) and 3kmME (WRF3, red) simulation.

to 2005 and 2050 to 2100. Investigation of the radiation balance reveals increased shortwave radiation (+5 W/m²) for the period from 2006 to 2050 that is not seen in the GCM data (see Figure C.0.9 in the Appendix). Longwave radiation reasonably increases in line with the increasing RCP4.5 greenhouse gas concentrations and the driving GCM (Figure C.0.10). The higher mean shortwave radiation results from about 6% less cloud cover in the period 2006 to 2050 compared to the previous and subsequent periods. Consistently, less mean precipitation (10-20%) is simulated (Figure C.0.11). While the mean annual precipitation in EUR-44 mostly exceeds mean precipitation amounts in MPI-ESM-LR for the periods 1950 to 2005 and 2051 to 2100 it is constantly lower for 2006 to 2050. Comparison of the periods' mean cloud cover patterns over the whole domain indicates the largest negative difference for central Europe and smaller or positive differences for the surrounding areas (Figure C.0.12). This pattern is consistent with and potentially results from a higher mean sea-level pressure (+3-4 hPa) in central Europe and lower mean sea-level pressure (-2 hPa) near the northwestern domain boundary in 2006-2050 compared to both 1950-2005 and 2051-2100 (Figure C.0.13). Though the relation between cloud cover and mean sea level pressure is non-linear and the daily and seasonal variability is large, the process of descending air masses in high pressure systems and the consequent warming and drying causally relates the patterns of mean cloud cover and mean sea level pressure. Yet, the question remains what causes these systematic differences in the mean flow pattern during this certain time period as they are not visible in the driving GCM data (Figure C.0.14). In general, changes in the model settings may cause large differences in the overall simulation results. However, here, identical settings have been used throughout the simulation. Intense investigation of all components of the modelling system finally reveals slight systematic differences in the boundary data for pressure and other 3D variables over mountainous areas that result from a different way of vertical interpolation of boundary data in the WPS. Largest differences occur at the northwestern boundary where the EUR-44 domain cuts the Greenland topography. The differences are in the order of 2-6 hPa over a

few grid points at the northern boundary, however, they evolve in the model domain and seem to have a systematic influence on the cyclogenesis process near Greenland that drives the large-scale weather patterns in Europe. Though it was not planned by experiment design, it highlights the remarkable teleconnection of a slight disturbance in boundary data at some grid points on the domain wide flow pattern that can cause mean temperature and precipitation changes in the order of a significant climate change signal in some regions.

Time series of annual mean precipitation and annual mean temperature for the 3kmME domain in the 12 km (WRF12) and 3 km resolution (WRF3) control (CTRL), mid-of-century (MOC) and end-of-century (EOC) projection runs (green and red lines in Figure 7.3 and Figure 7.4) are in line with the time series of the driving GCM and a consistent year-to-year variability is indicated by a high correlation between both. Mean 2m temperature in WRF3 is about 0.2 K higher compared to WRF12 throughout the simulated years and both slightly exceed mean temperature in MPI-ESM-LR. In the following section, projected future changes in MOC and EOC are analysed relative to CTRL. It is important to note that the simulated time periods are shorter than climate time periods of 30 years and are affected by decadal variability, i.e. a decadal period may be by chance warmer or colder than the surrounding 30-year mean. As indicated by the time series for temperature and precipitation, the means of CTRL, MOC and EOC are neither significantly warmer/colder or drier/wetter than the surrounding 30-year means. However, within the typical 30-year control (1971-2000), near future (2021-2050) and far future (2071-2100) periods, the respective last decade is the warmest, which is in line with the overall warming trend. So, the relative changes from 1993-2005 to 2038-2050 (2088-2100) are similar to 1971-2000 to 2021-2050 (2071-2100).

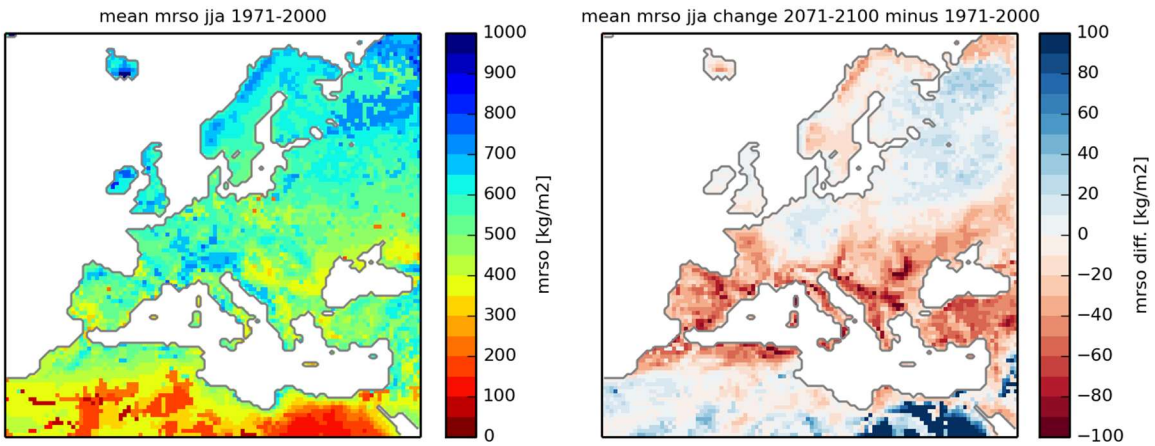

Figure 7.5: Mean summer (JJA) total soil moisture in the control period (1971-2000, left) and its relative change in the far future (2071-2100, right) in the MPI-ESM-LR driven EUR-44 simulation.
.

7.3 Change of land-atmosphere coupling in EUR-44

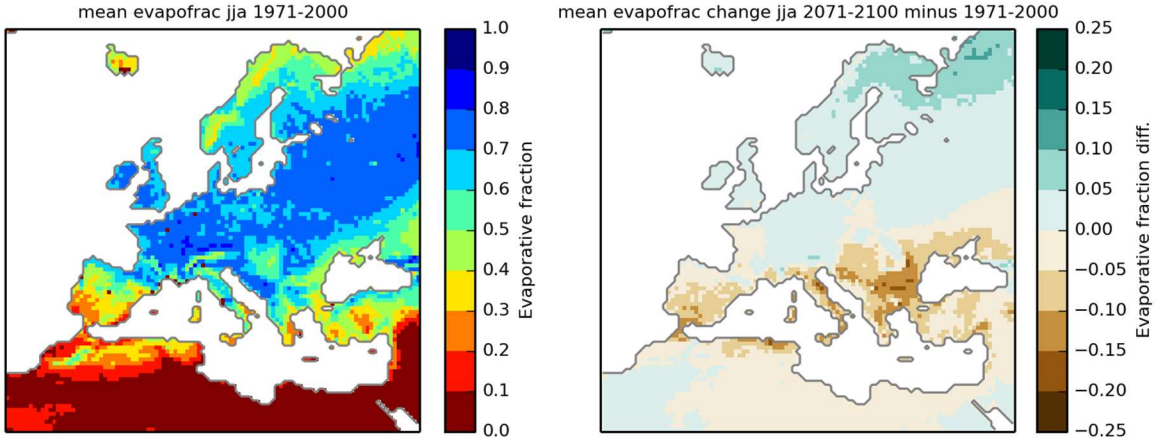

Figure 7.6.: Mean summer (JJA) evaporative fraction in the control period (1971-2000, left) and its relative change in the far future (2071-2100, right) in the MPI-ESM-LR driven EUR-44 simulation.

The projected future change in mean precipitation is expected to change the mean soil moisture patterns in summer which is in turn a decisive parameter for flux partitioning and land-atmosphere coupling. Especially in the Mediterranean region and large parts of south-eastern Europe less mean precipitation in summer (and already in spring) leads to less mean soil moisture (vertically integrated) in these areas. Slightly wetter soils are simulated for central Europe and large parts of north-eastern Europe (Figure 7.5). As revealed by the ERA-Interim driven EURO-CORDEX evaluation simulations (Section 3.4.2) there is a high correlation between soil moisture and evaporative fraction. Hence, lower in mean evaporative fraction in 2071-2100 is simulated for the drier Mediterranean areas while a slight increase is seen for central and north-eastern parts of Europe. However, evaporation is already near potential evaporation in these areas so that a surplus of soil

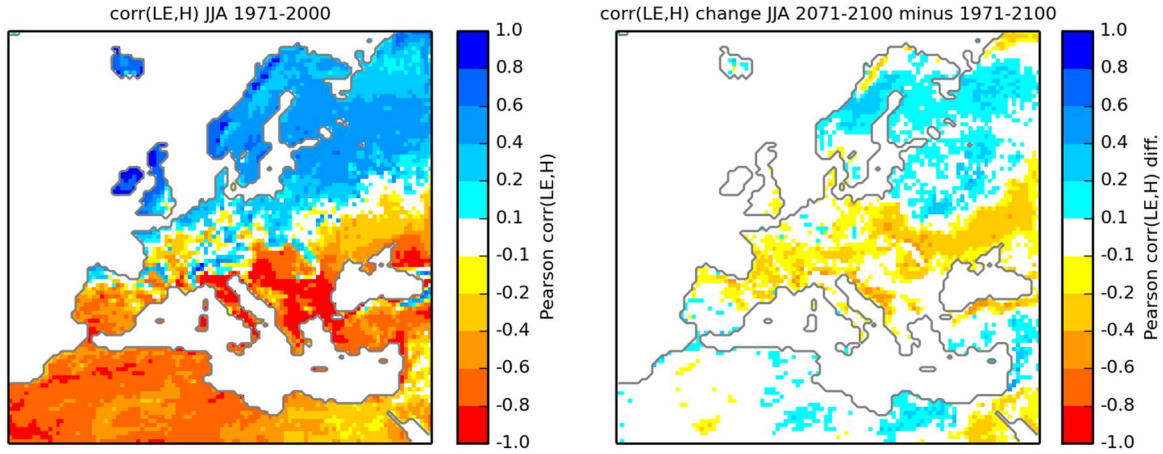

Figure 7.7: Mean summer (JJA) daily correlation of latent and sensible heat flux in the control period (1971-2000, left) and its relative change in the far future (2071-2100, right) in the MPI-ESM-LR driven EUR-44 simulation.

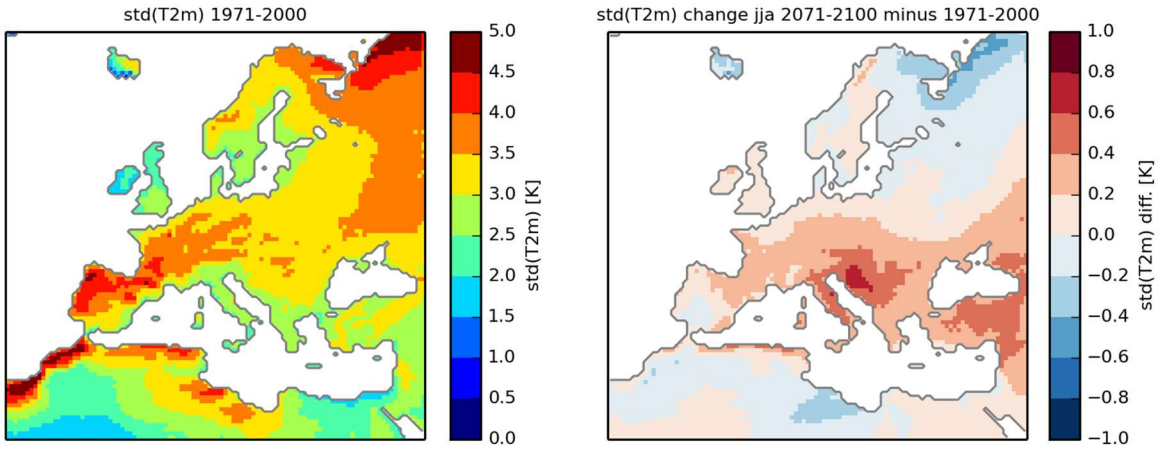

Figure 7.8: Standard deviation of daily 2m temperature (seasonal cycle removed) in summer (JJA) in the control period (1971-2000, left) and its relative change in the far future (2071-2100, right) in the MPI-ESM-LR driven EUR-44 simulation.

moisture does not much effect flux partitioning. In northern parts of Scandinavia and Russia, less soil moisture in the future is accompanied by a slight increase in evaporative fraction. This behaviour was also observed for the ERA-Interim driven WRF simulations and can most likely be attributed to a delayed thawing of frozen soil layers.

The change of soil moisture patterns in the projected future is accompanied by a change in land-atmosphere coupling indicated by the correlation of 10-daily mean latent and sensible heat flux (Figure 7.5). The control period 1971-2000 reveals a similar N-S pattern like in the ERA-Interim driven WRF331A simulation with strong (weak) coupling in southern (northern) Europe and a transition zone in central and eastern Europe. In the far future time period, stronger coupling is simulated for large parts of France, southern central Europe, the Balkan region, Ukraine and southern Russia. A change to weaker coupling is seen for large parts of Scandinavia and north-eastern Europe. Comparison of Figure 7.5 and Figure 7.7 indicate that soil moisture changes affect changes in coupling strength largest in the transition zone, whereby drier (wetter) conditions lead to stronger (weaker) coupling. In eastern Europe, the contrasting future change pattern of more soil moisture in the North and less soil moisture in South results in sharpening of the transition zone between weak and strong coupling in this region. In regions where either coupling is already very strong (like in south-eastern Europe) or evaporative fraction is already very low (like in southern Spain and northern Africa) a future decrease in soil moisture has little impact on the coupling strength.

Though this is no complete proof of causality, a future increase of summertime standard deviation of daily temperature (Figure 7.8) is largest in southern Europe where land-atmosphere coupling is strong. In line with that, strongest increase of extreme temperature (99th percentile) within overall warming is projected for these areas (Figure 7.9). Though

local temperature is largely affected by dynamic processes (advection of warm and cold air masses, warming descending air masses, etc.), strong local land-atmosphere coupling favours temperature increase in case of high net radiation, hence evolution of heat waves.

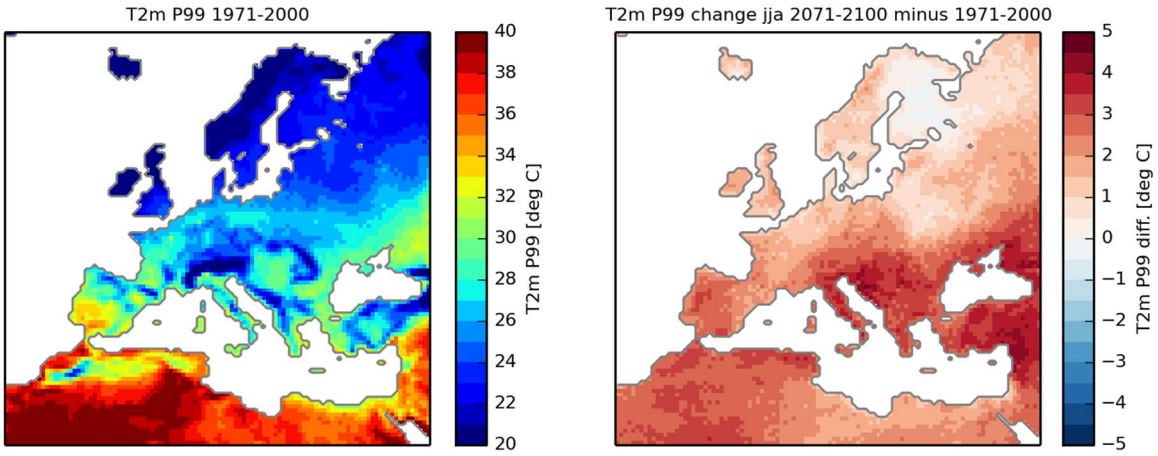

Figure 7.9: Extreme 2m temperature (P99) in summer (JJA) in the control period (1971-2000, left) and its relative change in the far future (2071-2100, right) in the MPI-ESM-LR driven EUR-44 simulation.

7.4 Projected temperature–extreme precipitation scaling in EUR-44

In the following, temperature–extreme precipitation scaling curves averaged for several PRUDENCE regions are compared for the 30-year control time period from 1971 to 2000 and the far future from 2071 to 2100 in the EUR-44 simulation (Figure 7.10). Different to the T-P99$_{dmax}$ scaling curves for the EUR-11/3kmME simulations with hourly precipitation data, here, the scaling is based on daily maximum 3-hourly precipitation sorted into 1-degree daily mean temperature bins.

In line with the scaling curves in different regions within the 3kmME domain (Section 5.5), the scaling curves for the individual PRUDENCE regions each have a characteristic shape depending on the climate conditions. Over the British Isles, middle Europe, France and Scandinavia P99$_{dmax}$ precipitation monotonically increases with temperature up to 20-22°C. The average scaling rate is lower than C-C-scaling (~5% K^{-1}) and, like in the 12 km resolution, does not increase to super-adiabatic scaling for temperatures above 11°C. For temperatures above 20°C in France and middle Europe, the curves drop to negative scaling rates. In southern European regions, e.g. the Iberian Peninsula, Mediterranean region as well as in eastern Europe, the scaling curves are overall flatter (~5% K^{-1} for IP, ~3% K^{-1} for EA and 2% K^{-1} for MD) before they drop to negative scaling rates. The peak temperature of the highest P99$_{dmax}$ precipitation is lower for the Iberian Peninsula (~12°C) compared to the other regions.

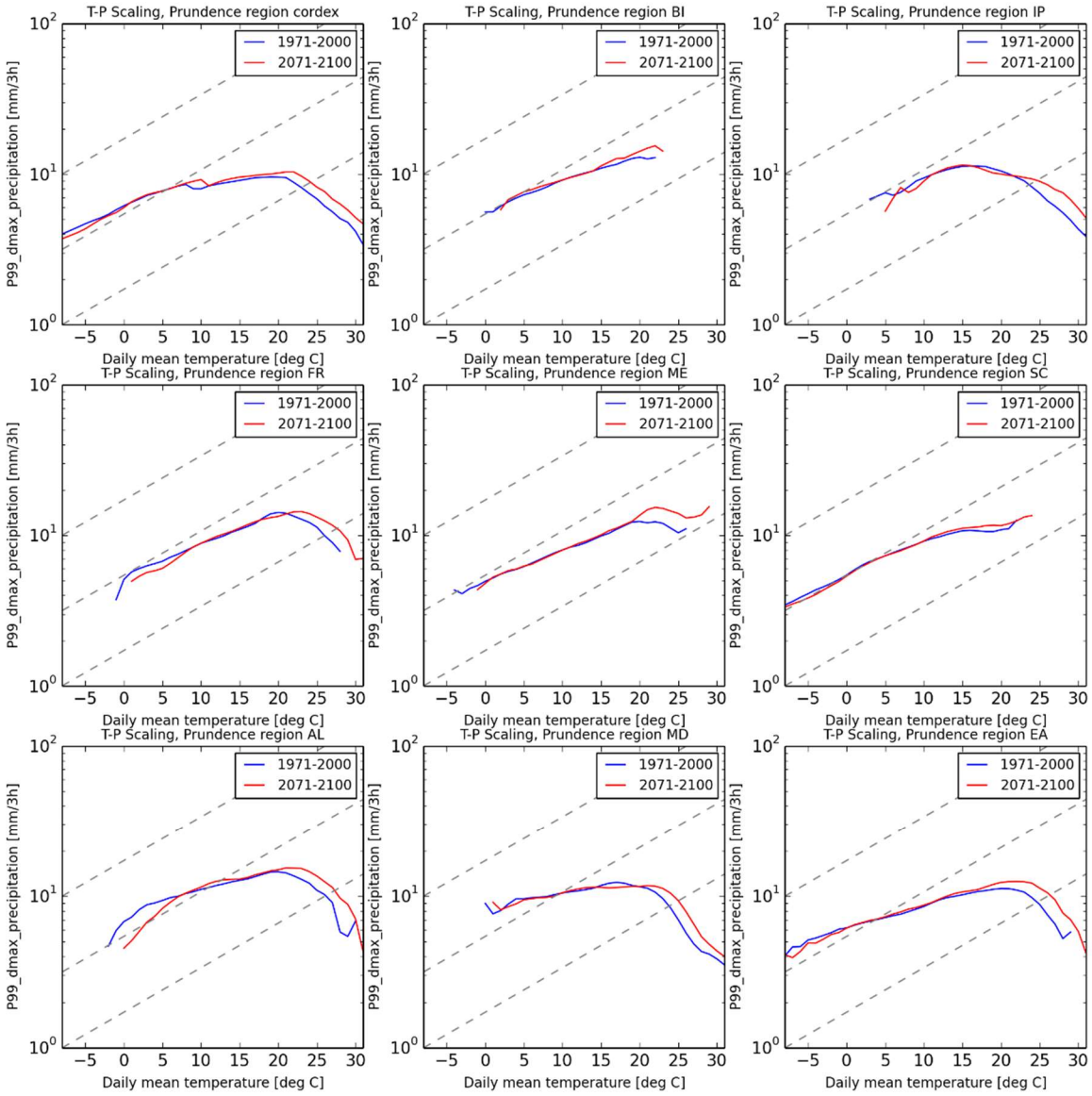

Figure 7.10: Temperature–extreme precipitation scaling in the MPI-ESM-LR driven EUR-44 simulation for 1971-2000 (blue) and 2071-2100 (red) averaged over the whole domain (upper left) and individual PRUDENCE regions (see location in Figure C.0.15. For each grid point in the particular analysis region daily maximum 3-hourly precipitation is discretized into one-degree bins of daily mean temperature. To account for different altitudes, temperature is extrapolated to sea level by assuming a lapse rate of 0.0065 K m^{-1} first. For each temperature bin with a sample size larger than 50 the 99th percentile of the precipitation values ($P99_{dmax}$) is calculated and averaged over all stations. Grey dashed lines indicate a scaling of 7% K^{-1} according to the Clausius-Clapeyron relation.

In the projected future climate (2071-2100), the scaling curves are shifted to higher peak temperatures while keeping their individual shapes. Accordingly, the drop to negative scaling rates starts at higher temperatures. The shift on the temperature axes is roughly in the range of the projected mean temperature change (+2-3 °C). On the precipitation axes the curves are not shifted (to overall higher $P99_{dmax}$ values) according to C-C scaling in general and seem to follow the individual scaling rates for the temperature range below

the peak temperature.

As discussed in the Section 5.5, flattening or dropping of the scaling curves is probably related to limited moisture conditions accompanied at this high temperature range. Accordingly, the scaling of latent heat flux with temperature at days with $P99_{dmax}$ precipitation also reveals a drop at high temperatures (Figure C.0.16) related to limited soil moisture conditions (Figure C.0.17). However, dropping of latent heat flux starts at higher temperatures compared to the respective peak temperatures for extreme precipitation.

7.5 Projected changes in mean and heavy precipitation in high resolution runs

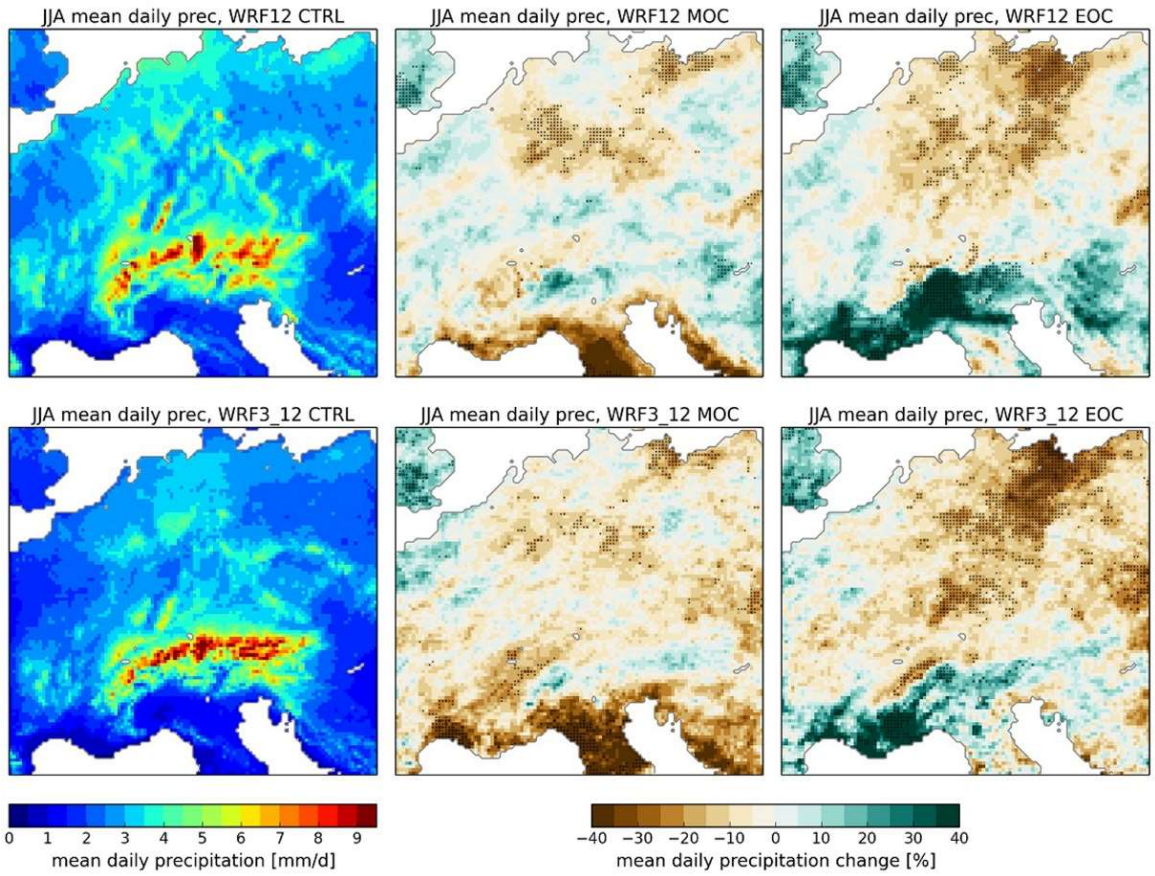

Figure 7.11: Summer (JJA) mean precipitation [mm/d] in the CTRL simulation time period (left) and its relative change in MOC (middle) and EOC (right) for WRF12 (upper row) and WRF3_12 (lower row). Dots highlight significant changes (0.05 level).

With the better representation of the precipitation intensity distribution (as revealed in Chapter 5) CPMs are potentially also better suited to access changes in extreme precipitation in the future climate. This section investigates projected future precipitation statistics from the down-scaled MPI-ESM-LR GCM runs forced by a RCP4.5 scenario. Changes

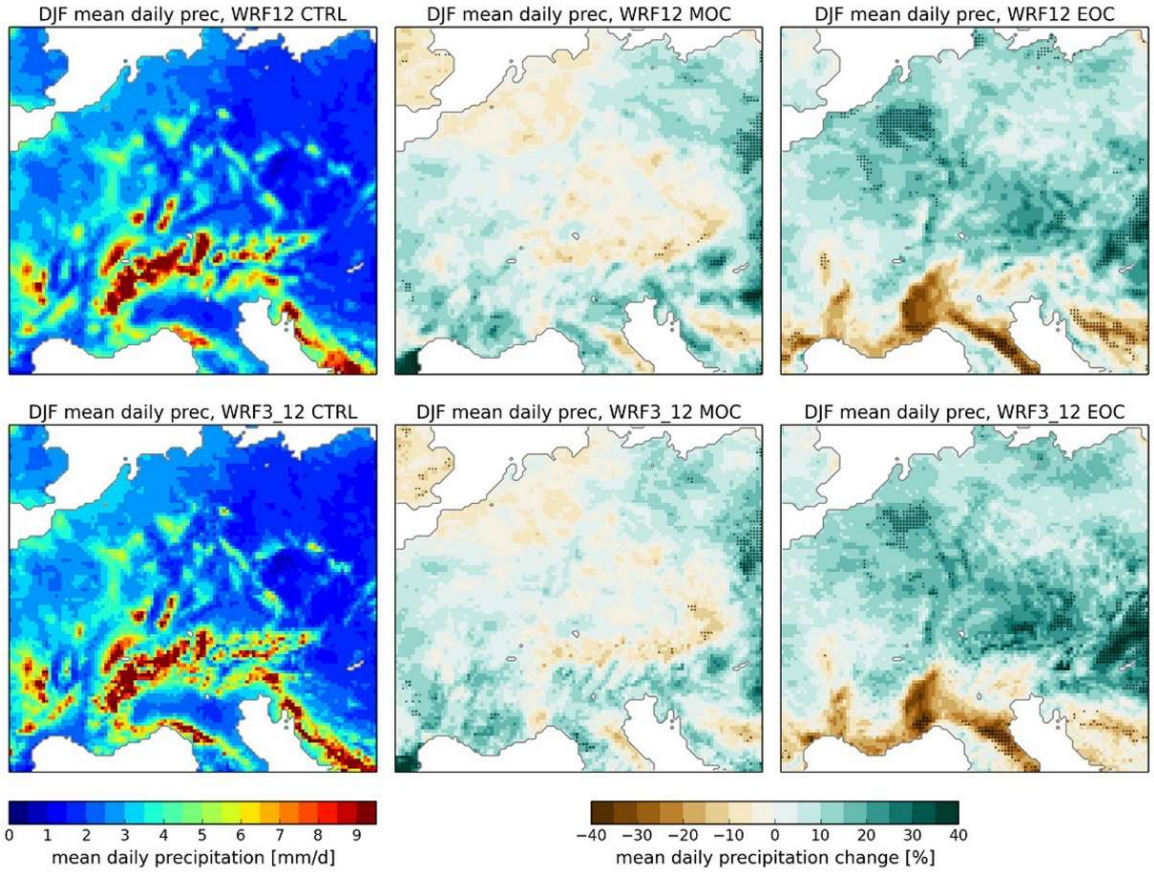

Figure 7.12: Winter (DJF) mean precipitation [mm/d] in the CTRL simulation time period (left) and its relative change in MOC (middle) and EOC (right) for WRF12 (upper row) and WRF3_12 (lower row). Dots highlight significant changes (0.05 level).

with respect to the control time period (CTRL) from 1993 to 2005 are analysed for the mid-of-the-century (MOC) period from 2038 to 2050 and the end-of-the-century (EOC) period from 2088 to 2100 both for the 3 km convection-resolving runs (WRF3_12) and its driving 12 km resolution (WRF12) simulation.

Consistent with the re-analysis driven evaluation simulations, WRF12 overall generates more precipitation compared to WRF3_12 for the control period in summer (JJA) (Figure 7.11, left subplots); both simulate reasonable spatial distributions with highest precipitation amounts over the uplands and Alpine mountain ranges and dry conditions in southern France and northern Italy. For the near and the far future both WRF12 and WRF3_12 largely agree in the predicted coarse scale precipitation change pattern (Figure 7.11, middle and right subplots). Both simulate 15-40% less precipitation for the Mediterranean region for MOC; the convection-permitting run in addition indicates overall less precipitation for Central Europe. For end-of-century (EOC) both simulations project 10-30% drier conditions over Germany and Poland but 15-40% more precipitation over southern France and northern Italy. However, changes are significant for only 21% of grid points given the range

of the inter-annual variability. Prominent, however, is the much stronger and more widely-spread increase of predicted precipitation south of the Alps in the WRF12 simulations. The overall trend to drier conditions is slightly stronger in WRF3_12; the domain-averaged difference of mean precipitation between WRF12 (wetter) and WRF3_12 (drier) increases from 16% in CTRL to 20% in MOC and 22% in EOC.

Differences between WRF12 and WRF3_12 are generally smaller in winter (DJF, Figure 7.12). Except for local differences in mountainous regions the spatial distribution and the mean precipitation is similar, both for the CTRL time period and the projected changes. For MOC both simulate 10-20% more precipitation for some parts of France and Germany while drier conditions are projected for the eastern Alpine region and parts of Czech Republic. Relative changes are overall stronger for EOC with a 15-40% decrease in mean precipitation for the Mediterranean region and a 10-30% increase for large parts of Central Europe north of the Alps. Again, for most grid points the changes are not indicated significant.

The large-scale precipitation changes are similar to the driving GCM (not shown), especially the drier (wetter) pattern north (south) of the Alps in EOC winter and the drier

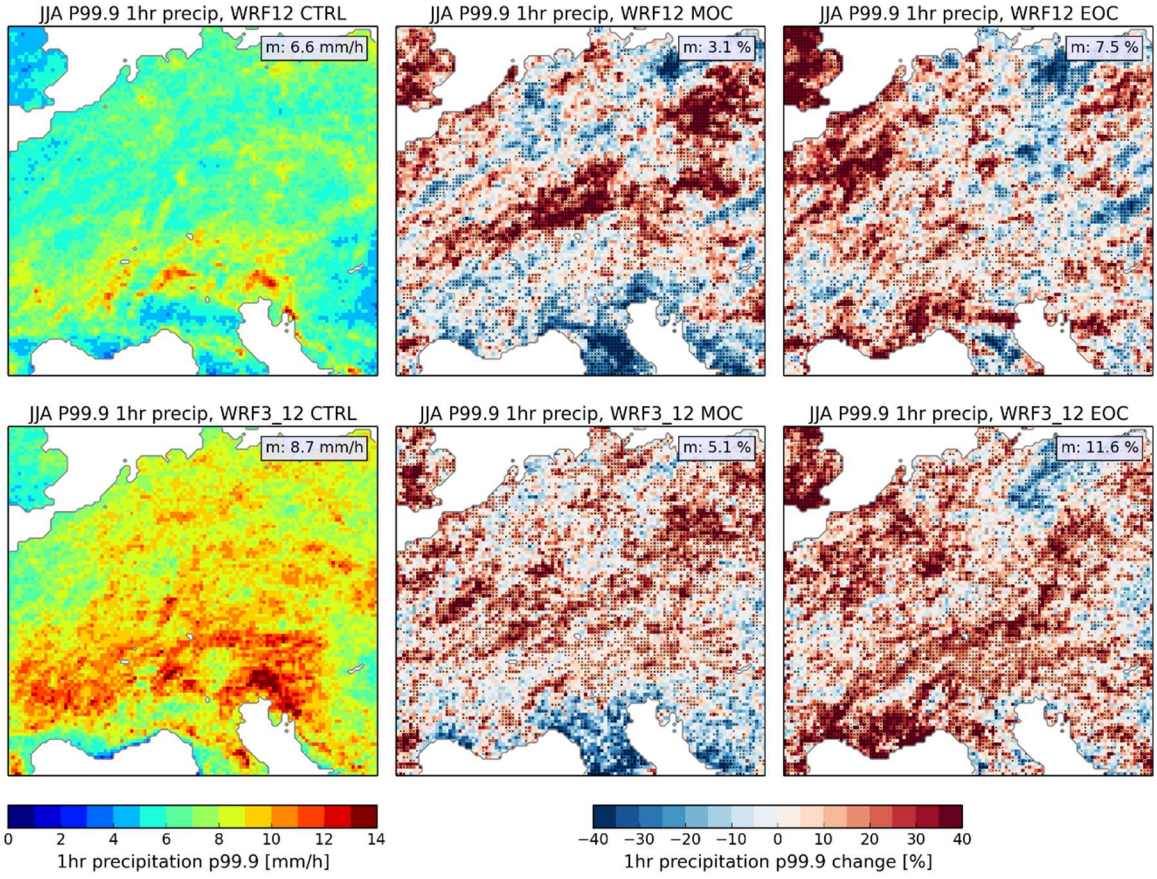

simulation time period (left) and its relative change in MOC (middle) and EOC (right) for the WRF12 (upper row) and WRF3_12 (lower row). Dots highlight significant changes (0.05 level)

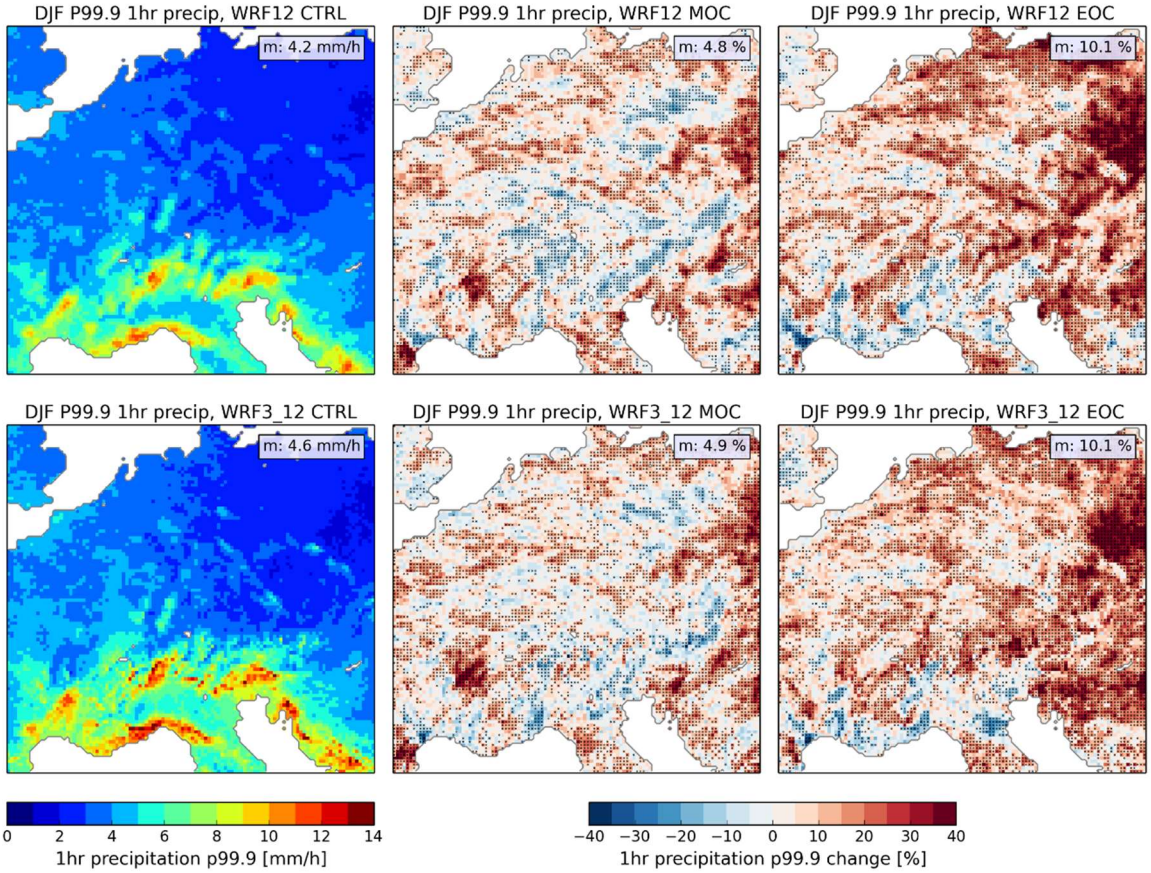

Figure 7.14: Hourly extreme precipitation sums (99.9th percentile) in winter (DJF) in CTRL simulation time period (left) and its relative change in MOC (middle) and EOC (right) for the WRF12 (upper row) and WRF3_12 (lower row). Dots highlight significant changes (0.05 level)

Mediterranean region in summer. However, the strong increase for summer precipitation in EOC in southern France and southern Alpine region is less prominent in the GCM simulation. Projected domain average precipitation decreases in summer (-5% for MOC and -10% for EOC) are slightly stronger in the GCM simulation. In winter the projected mean precipitation change is similarly small in the GCM and WRF simulations.
The spatially averaged near-surface summer 2 m air temperature is on average 0.5 K higher in WRF3_12 CTRL and its increase for MOC (+1.3 K) and EOC (+1.9 K) by 0.1 K stronger compared to WRF12 (not shown). This is consistent with the slightly drier conditions and lower cloud cover in WRF3 in summer leading to a stronger radiation energy input. The temperature increase in the driving GCM is slightly stronger (+1.5 K for MOC, +2.3 K for EOC). Mean temperature changes in winter (+1 K for MOC, +2.2 K for EOC) are almost identical between WRF12 and WRF3_12 and similar to the driving GCM.

Summertime extreme precipitation (99.9th percentile) during the control period is considerably stronger in the convection-permitting simulations (Figure 7.13, left sub-plots) in agreement with the validation results. Unlike for mean precipitation, both simulations

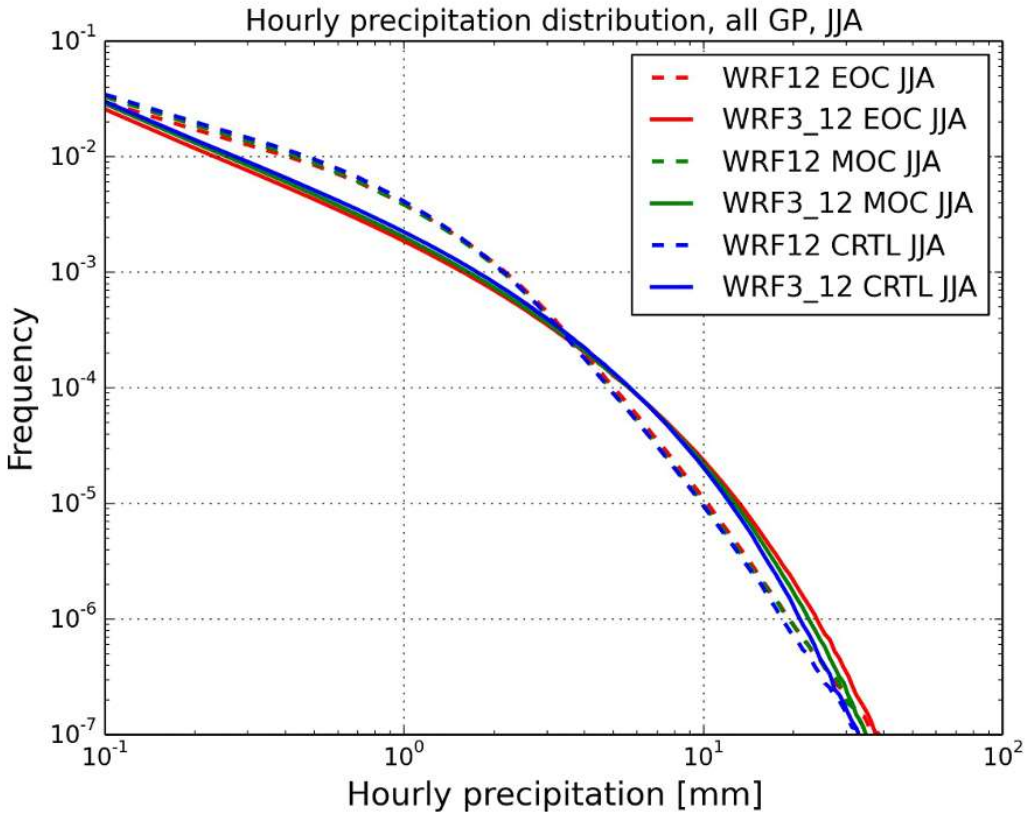

Figure 7.15: Intensity distribution of hourly precipitation in summer (JJA) taking all domain grid points into account. WRF12 is indicated by dashed lines and WRF3_12 by solid lines. Colors indicate the 12-year simulation time periods CTRL (blue), MOC (green) and EOC (red).

indicate an increase in extreme precipitation for MOC (+5% domain average in WRF3_12, +3% in WRF12) and EOC (+12% for WRF3_12, +8% for WRF12). The noisy change pattern in MOC and EOC reflects the internal variability in these free simulations caused by these isolated and usually very local events. The regional stronger increase in southern France and south western UK is accompanied by an increase in mean precipitation in these areas (see Figure 7.11).

In winter, both WRF3_12 and WRF12 show a similar increase in P99.9 of 5% on average for MOC and 10% for EOC (Figure 7.14). The pattern is overall slightly more homogeneous compared to the summer months and also more consistent in both resolutions including significant increases of extreme precipitation especially in eastern Europe. In southern France and northern Italy, the decrease in EOC mean precipitation (see Figure 7.12) seems to manifest itself also in extreme precipitation.

The intensity distribution of hourly precipitation sums for CTRL, MOC and EOC differ between WRF12 and WRF3_12 (Figure 7.15) with more light and moderate precipitation in WRF12 and more heavy precipitation in WRF3_12. This difference intensifies in MOC

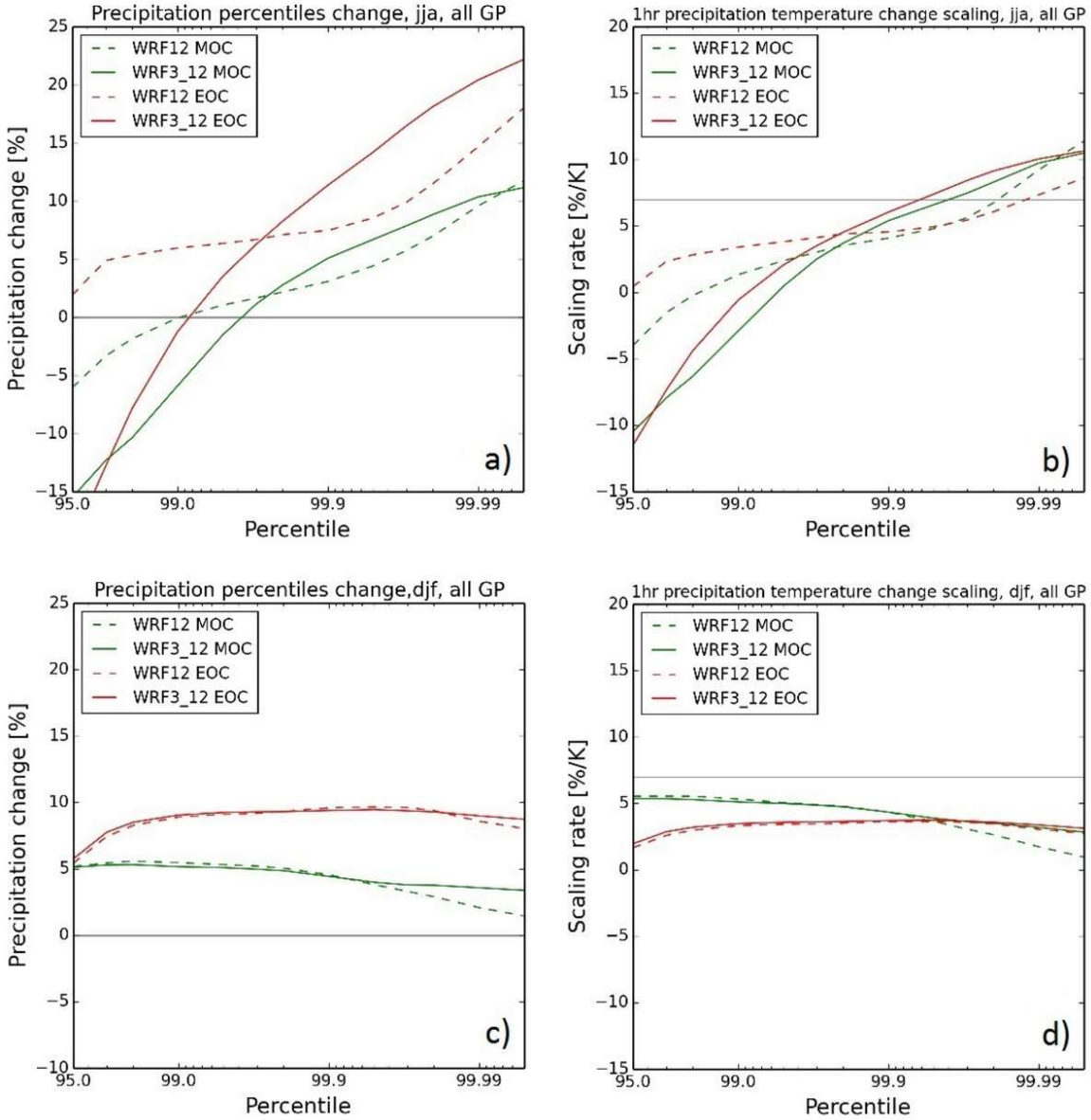

Figure 7.16: a, c Percentage change of hourly precipitation percentiles in MOC (green) and EOC (red) as difference to CTRL for both WRF12 (dashed) and WRF3_12 (solid) based on the spatial average of all grid point relative changes for summer (a) and winter (c). **b, d** Scaling rate of percentage change of hourly precipitation percentiles normalized by local mean temperature change in MOC (green) and EOC (red) as difference to CTRL based on the spatial average of all grid point relative scaling rates for summer (b) and winter (d)

and EOC; while light and moderate precipitation further decrease in WRF12 and WRF3_12, the increase in heavy precipitation is stronger in WRF3_12.

This behavior is also confirmed by the domain averaged percentage change of hourly precipitation percentiles for MOC and EOC with respect to CTRL (Figure 7.16a) in summer. For MOC, WRF12 and WRF3_12 simulate an increase for percentiles higher than 99.5 and 99.7, respectively, of up to +10% while the lower percentiles are reduced. For

EOC,
WRF3_12 increases faster to higher positive changes reaching +20% for the 99.99th percentile. The decrease in mean precipitation (Figure 7.11) is caused by less light and moderate hourly precipitation rates below the 99th percentile. In WRF12 the trend to stronger future increase for higher percentiles is less pronounced.
The WRF3 simulations for summer reach the C-C scaling rate of 7% K^{-1} for MOC (EOC) at the 99.94th (99.95th) percentile, for WRF12 around the 99.98th percentile (Figure 7.16b); both simulations show a super-adiabatic scaling exceeding 10% K^{-1} above the 99.99th percentile.
Both simulations agree in the future change in heavy and extreme precipitation in winter; both show an increase of 5% (9%) for MOC (EOC) for the percentile range from 98th to 99.98th (Figure 7.16c). Unlike in summer the scaling rates remain below 5% K^{-1} and are projected to even decrease for extreme precipitation percentiles (Figure 7.16).

7.6 Projected temperature–extreme precipitation scaling in high resolution runs

For all time slices, current (CTRL), mid- (MOC) and end-of-century (EOC) 12 km and 3 km resolution runs yield constant scaling rates for the temperature range from 2°C to 18°C (Figure 7.17). While WRF3_12 shows a C-C scaling of 7% K^{-1}, the scaling rate in WRF12 is slightly smaller (~5.7% K^{-1}), which is consistent with the results from the evaluation period as is the drop to negative scaling rates for high temperatures. For MOC and EOC the scaling curves are shifted to higher temperatures approximately parallel to the 7% K^{-1} scaling line; thus, the drop of the scaling rate due to the transition to moisture limited regimes starts at higher temperatures and accordingly higher P99dmax precipitation, i.e. the projected warming must be accompanied by an overall increase in moisture. This is in good agreement with results by Prein et al. (2016) for the contiguous US.
The shift of the scaling curves parallel to the C-C scaling lines, while keeping their individual shapes for the future climate, is also found for the individual climate sub-regions (Figure 7.17b-f). For lowlands and uplands, the increase to super-adiabatic scaling starts in the convection-permitting runs above 10°C while the 12 km runs stick with a monotonic 7% K^{-1} also for higher temperatures. For northern Italy the T-P99dmax scaling for the 3 km runs during is slightly below 7% K^{-1} for temperatures up to 16 °C, then increases to super-adiabatic scaling until 20°C in the control period, where it drops to negative scaling rates; for MOC and EOC this drop shifts to 21°C and 22°C, respectively. For southern France results are similar, but the shapes of the scaling curves are less coherent for the different time slices probably due to the small subdomain and larger variability.
Consistent with the evaluation results, scaling curves for WRF12 are overall flatter for all

sub-regions and miss a transition to super-adiabatic scaling. But the shift of the scaling curves in warmer climates (MOC, EOC) with higher temperatures and stronger peak precipitation is also apparent. The shift does, however, not as clearly follow the C-C scaling trajectory like the 3 km runs. When averaged over the whole domain (Figure 7.17a) the shift follows a lower than C-C-scaling rate, while the results for the sub-regions are too noisy due to the small shifts.

It is important to note that already for the moderate warming signal in the RCP4.5 scenario used here (about 1.5 K in MOC and about 2 K in EOC) compared to RCP8.5 scenarios used in other studies with warmings of 4-5 K (e.g. in Kendon et al. 2014; Ban et al. 2015; Prein et al. 2016), extreme precipitation clearly increases in our WRF simulations.

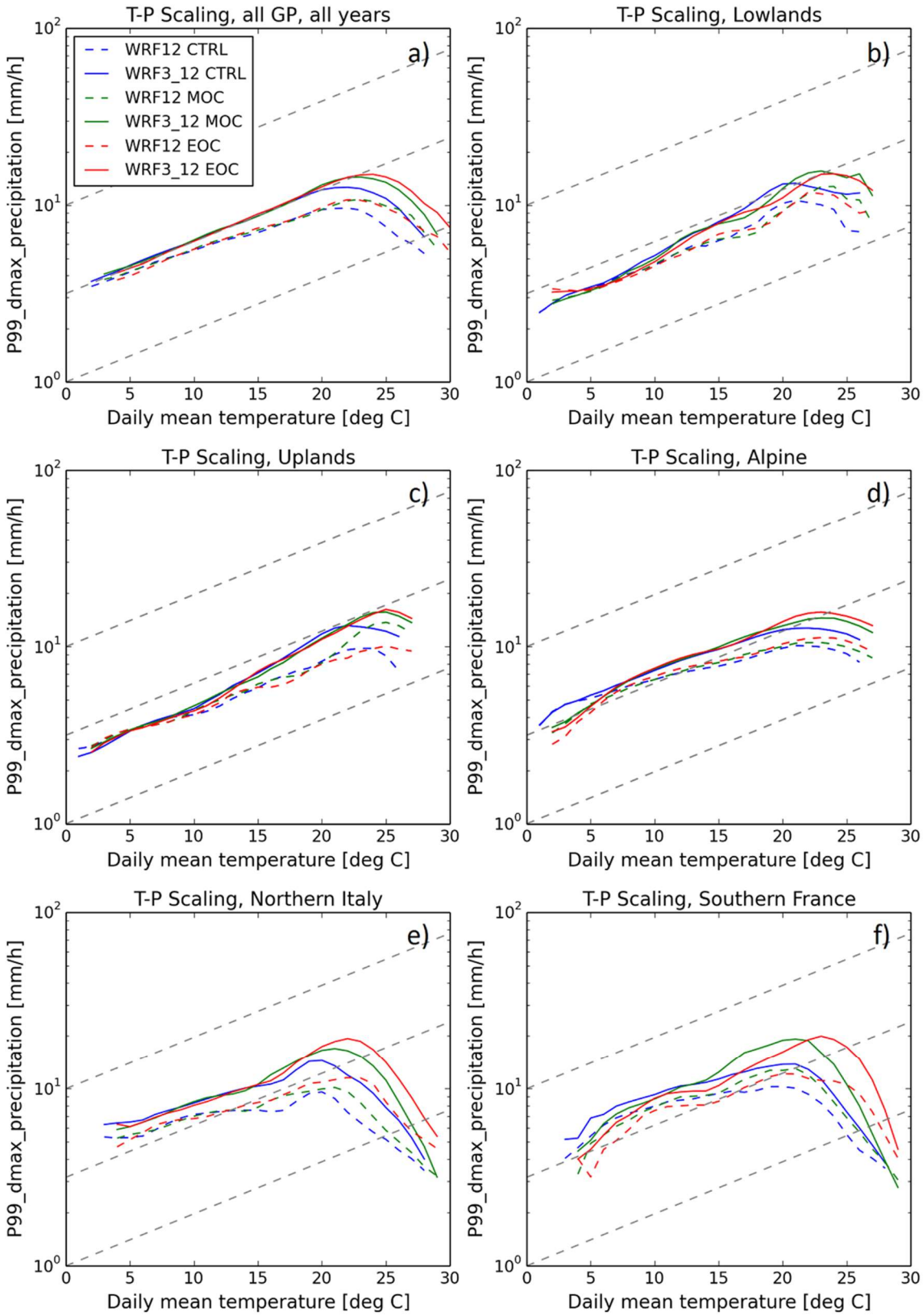

Figure 7.17: Temperature–extreme precipitation scaling in WRF12 (dashed) and WRF3_12 (solid) for simulation time period CTRL (blue), MOC (green) and EOC (red) for different regions. For each grid point daily maximum hourly precipitation is discretized into one-degree bins of daily mean temperature. To account for different altitudes, temperature is extrapolated to sea level by assuming a lapse rate of 0.0065 Km^{-1} first. For each temperature bin with a sample size larger than 100 the 99^{th} percentile of the precipitation values ($P99_{dmax}$) is calculated and averaged over all grid points in the particular region.

8 Summary and outlook

We performed and analysed regional climate simulations in multiple resolutions for the EURO-CORDEX domain (EUR-44, EUR-11) and a central European domain (3kmME) with the WRF RCM downscaling both ERA-Interim reanalysis and GCM MPI-ESM-LR (RCP4.5) climate change scenario data.
The analysis focussed on land-atmosphere interactions to improve our understanding of the regional water cycle components, the involved multi-scale processes, their variabilities and sensitivities to model resolution both under present-day climate and future climate change conditions. Also the added value of a higher model resolution was investigated, in particular the convection-permitting 3kmME simulations that constitute one of their first kind performed over a decade with the WRF RCM over Central Europe.

Land-atmosphere coupling analysis
The land-atmosphere coupling strength is investigated in a subset of the ERA-Interim driven EURO-CORDEX RCM ensemble. Two integrative metrics are used, one based on the correlation between sensible and latent heat fluxes which is compared to FLUXNET observation, and the other based on the correlation of latent heat flux and 2 m air temperature which is compared to gridded GLEAM-ERAInt observation-based data.

- For both coupling metrics, the EURO-CORDEX RCM simulations reveal strong coupling in southern Europe and weak coupling in northern Europe in overall agreement with the observations. However, in the transition zone between both regimes over large parts of central Europe, the RCMs diverge and show a wide range of coupling strengths.
- The majority of RCMs tends to overestimate the coupling strength for large parts of Europe when compared to both FLUXNET observations and gridded GLEAM-ERAInt reference. This is consistent with evaluation studies on global models that reveal an overestimation of land-atmosphere coupling in the mid-latitudes (Sippel et al. 2016) and parts of the U.S. (Merrifield and Xie 2016).
- The partially large ensemble spread can most probably be attributed to differing LSM parametrizations including assumed vegetation and soil type distributions. However, the diversity in simulated soil moisture and surface fluxes - and hence the coupling strength - is not solely attributed to the LSMs but partly results from different atmospheric parametrizations, which impact the simulated regional weather conditions.
- Coupling strength derived from different metrics may provide similar information although they cannot be directly compared in their absolute values unless appropriately scaled. Consistent, but inevitably computationally expensive

GLACE-type experiments like by Koster et al. (2006), Seneviratne et al. (2006) or Hirsch et al. (2014) for all RCMs would allow for a more robust assessment of coupling strength than possibly with the ensemble-of-opportunity at hand. Nevertheless, the relatively simple correlation based coupling metrics are suitable for an intercomparison of different RCM runs.

- Though differences in e.g. mean 2 m air temperature and total precipitation (as analysed in other evaluation studies (Kotlarski et al. 2014; Katragkou et al. 2015)) depend on many model parameters and cannot be exclusively linked with coupling properties of the individual RCMs, the coupling metrics provide additional information for the explanation of differences seen in e.g. extreme temperatures that show positive biases for the more strongly coupled RCMs.
- The land-atmosphere coupling strength based on two coupling metrics in 3 km and 12 km simulations for central Europe vary strongly from year-to-year due to different soil moisture conditions. The coupling strength largely differs for individual land use types; forests responds slower to drought conditions than crop. Regions and seasons of strong coupling correlate with extreme temperatures. The overall stronger coupling in the 3 km compared to 12 km simulations is attributed to the overall drier conditions in summer in the 3 km simulations.

Land atmosphere coupling under climate change conditions

An EUR-44 simulation downscaling the GCM MPI-ESM-LR (RCP4.5 scenario) has been carried out to assess the climate change signal for temperature and precipitation in relation to the driving GCM and to investigate the projected change of the coupling strength patterns in Europe.

- The projected future climate reveals an overall increase of the mean 2m-temperature in the range of 2-4 K for the period 2071-2100 compared to 1971-2000. The large-scale precipitation change patterns (less summer precipitation in southern and western Europe, more precipitation in north-eastern Europe) are in line with the results from the driving GCM, however, differences become apparent on the regional scale, especially in or near mountainous regions.
- The projected climate change alters the land-atmosphere coupling regimes in summer. Due to increasingly drier soil conditions, stronger coupling is simulated for large parts of France, southern central Europe and southern eastern Europe. A decrease in coupling strength is projected for large parts of Scandinavia and north-eastern Europe because of wetter soils. In regions where either coupling is already very strong (like in south-eastern Europe) or the evaporative fraction is already very low (like in southern Spain and northern Africa) a future decrease in soil moisture has little impact on the coupling strength.

- The strongest future increase of extreme temperature exceeding the mean temperature change is simulated in the strong coupling areas.

As the future projection is based on a single RCM simulation downscaling a single GCM with a RCP 4.5 scenario, the results provide just one possible scenario for the regional future climate. For the assessment of uncertainty in the future coupling regimes and its impact on phenomena like heat waves, further studies with the whole EURO-CORDEX ensemble are required. As the evaluation of coupling strength in the EURO-CORDEX RCMs suggests, the large ensemble spread, especially for the transition zone in between southern and northern Europe, can be also expected for the future scenario runs and may affect the diversity in the projected increase of extreme temperature in these areas.

The results encourage the further development of LSMs in order to improve their ability to properly simulate coupling strength. Besides a more sophisticated representation of plants and their ability to adjust to environmental conditions, the simulation of the full hydrological cycle including the dynamic groundwater flow is recommended. Fully coupled soil-vegetation-atmosphere models, which show a significant impact of the groundwater representation on land surface-atmosphere processes (Rahman et al. 2015; Keune et al. 2016), may reduce the uncertainty in climate simulations.

Added value of convection-permitting simulations

The added value of convection-permitting climate simulations is investigated based on nine years of ERA-Interim driven EUR-11/3kmME simulations are evaluated against rain gauges in Germany and Switzerland with a focus on the diurnal cycle, frequency distribution of rainfall and the relation between extreme precipitation and near-surface air temperature.

- The results reveal a clear added value of the higher resolution for the sub-daily time scale by an improved reproduction of the diurnal cycle and the hourly intensity distribution of precipitation in summer. In winter, differences are smaller and mostly related to orography.
- Too frequent light precipitation results in a wet bias in both simulations, which is however reduced in the 3 km resolutions runs in summer. The frequencies of heavy and extreme hourly precipitation are underestimated in the 12 km runs and much better captured in the 3 km runs, although extreme precipitation events are overestimated in mountainous regions.
- The improvement in phase and amplitude of the diurnal cycle in the convection-permitting simulation is, however, less pronounced when compared to other studies (e.g. Kendon et al. 2012; Ban et al. 2014; Fosser et al. 2015).
- The largest differences between the results obtained with both resolutions and observations, are found in mountainous regions.
- The convection-permitting simulations better reproduce the observed scaling of

extreme precipitation ($P99_{dmax}$) with daily near-surface mean temperature. The 12 km simulations miss the observed increase from a C-C scaling rate (~7% K^{-1}) to a super-adiabatic scaling rate (~10% K^{-1}) at temperatures above 11°C in accordance with the underestimation of the frequency of summer heavy and extreme precipitation events. The stronger scaling rate which relates to dominant convective precipitation in this temperature range (Berg et al. 2013), is better captured by the explicit simulation of convection. Both simulations reproduce the observed drop of scaling rates at high temperatures caused by moisture limited conditions. The scaling-rate curves differ between sub-regions like, e.g., an earlier drop of the scaling rate in southern France and northern Italy.

Effect of land surface heterogeneity

The effect of land surface heterogeneity on the differences between 3 km and 12 km simulations is analysed based on five WRF simulations for JJA 2003, each with the same atmospheric setup in 3 km resolution but different combinations of 12 km resolution land use and soil type, initial soil moisture and orography.

- A coarser resolved orography has the largest impact on the overall simulation results as it alters the flow over and around mountain ridges and largely influences local precipitation pattern and intensity over complex orography.
- Coarser-resolved land use maps have a smaller effect, which is mainly related to resolution-dependent changes in overall percentages of land use types, rather than to the loss of surface heterogeneity on the scales analysed here.
- Even small changes in soil moisture (both spatial averages and local differences) have a higher potential to affect atmospheric patterns, although this might also depend on the particular land surface model used.
- An additional sensitivity study shows, that widespread large differences in soil moisture as e.g. seen between the wet summer 2002 and the dry summer 2003 may cause temperature differences in the range of 3-4 K and impact large scale circulation.
- Overall, differences caused by coarsely resolved land surface properties are much smaller compared to differences between simulations with 3 km and 12 km grid spacings of the atmosphere.

Future change in precipitation statistics

EUR-11/3kmME simulations downscaling GCM MPI-ESM-LR (RCP4.5) have been carried out for mid-of-the-century (MOC, 2038-2050) and end-of-the-century (EOC, 2088-2100). These are compared with the control run (CTRL, 1993-2005) to quantify future changes in precipitation statistics based on both convection-permitting and convection-parameterized simulations.

- Slight decreases of mean summer precipitation over central Europe are suggested for MOC and EOC, respectively, while heavy and extreme hourly precipitation intensities increase in particular for the higher percentiles. The latter tendency is stronger in the 3 km simulations leading to larger differences between the frequency-intensity distributions with progressing climate change.
- Super-adiabatic scaling (>7% K^{-1}) is found for extreme hourly precipitation above the 99.95th percentile in line with similar studies for the UK (Kendon et al. 2014) but larger for the Alpine region as found by Ban et al. (2015) who did not find super-adiabatic intensity increases. Differences might result from different models, resolutions and regions considered.
- Temperature–extreme precipitation scaling curves in the present and the future climate shift to higher temperatures and higher peak extreme precipitation for several sub-regions of the 3kmME domain in MOC and EOC approximately following a 7% K^{-1} (C-C) trajectory while keeping the typical shape of the individual scaling curves with a drop of scaling rates.
- Scaling curves in different PRUDENCE regions in the EUR-44 simulation depend on climate conditions and the moisture availability that hampers extreme precipitation at high temperatures. Compared to the convection-permitting 3 km simulation, the scaling rates are overall smaller for the 12km simulations. An increase of hourly extreme precipitation with temperature can be only assessed by simulations at convection-permitting resolution. GCM and RCM simulations with coarse resolution and parameterized convection are by design not well-suited to project future extreme precipitation changes at sub-daily time scale.

Overall, this thesis finds the clear added value of convection-permitting climate simulations. As long-term convection-permitting climate simulations are still rare, and results may be restricted to individual model configurations, resolutions and different domains, more coordinated efforts to produce convection-permitting model runs are needed. Defining common experiments and standards for data output and model evaluation will help to investigate uncertainties in a systematic way. A recently launched project under the auspices of the CORDEX Flagship Pilot Studies program aims to build the first-of-its-kind ensemble of convection-permitting climate simulations to investigate present and future convective processes and related extremes over Europe and the Mediterranean (Coppola et al. 2017). There are still challenges such as the large computational demands and big model output data volume. New computer architectures and by running models mainly on accelerators (e.g., graphical processing units (GPUs)) can lead to significant speedups and enable CPMs to run on larger domains and longer periods (Leutwyler et al. 2016). Added value of CPMs in areas beyond precipitation, including processes such as local wind systems, snowpack dynamics and hydrology, land–atmosphere coupling,

evapotranspiration, and the representation of clouds and radiation should be further explored (Prein et al. 2017). Therefore, high-quality and high-resolution observational datasets are needed, also to re-assess and adjust RCM parameterizations at convection-permitting scale.

Finally, these new CPM data products may be used in the future for impact assessments by local decision makers for their risk management and adaptation strategies since CPMs approach the scale at which real world planning decisions are made.

Appendix

A. Effect of WRF lateral boundary forcing treatment in climate simulations

This section discusses a bug-related unphysical artifact originating at the lateral boundary that has been detected during the analysis of the long-term WRF331A EUR-44 runs. Since it has a non-neglectable effect on the inner model domain, it was highly recommended to be solved before starting further long-term WRF simulations. In collaboration with other international experienced WRF RCM modelling groups from the USA, France, Spain, and Austria, which could also identify this artefact in their simulations, a comprehensive error report was prepared for the WRF developers at the National Center for Atmospheric Research (NCAR, USA). A solution has been jointly found and has finally been fixed. In the following, the problem and its solution will be briefly described. Furthermore, an analysis of simulations with a corrected and non-corrected model version is presented, which provides insights about the influence of lateral boundary disturbances on regional climate simulations.

In several long-term transient regional climate simulations with WRF v3.3.1, v3.5.1 and v3.6.0 (those that have been tested) using different setups, compute machines, forcing data, and compilers an accumulating unphysical artefacts evolved along the lateral boundaries after some time (~10^5 time steps, a few months for a 60-seconds time step). The artefact is most pronounced at the outermost grid points (specified zone), but it is also seen in the relaxation zone and it advected into the interior of the model domain. The results are stripe-like patterns in the interior of the domain that ultimately stem from the artefacts along the boundaries. The artefact evolves in the uppermost model layers first and later on extends to lower levels. Several variables (P, T, U, V, W, QV) are affected, while the artefact is most clearly seen in pressure perturbation and wind velocity (see Figure A.0.1). Since the effect accumulates slowly but continuously, it more and more affects also the inner model domain.

The artefacts resulted from the way boundary data is adjusted with every model time step at the outermost domain grid cells (so-called specified zone). In the WRF modules *solve_em* and *module_bc* data is read from the *wrfbdy* file that includes the interpolated values from the driving coarser GCM or reanalysis data. Instead of replacing the values in the specified zone by the absolute values, tendencies with associated rounding inaccuracies have been added to the values of the previous time step. Hence, the inaccuracy can grow

with every time step. However, it takes a large number of time steps (~10^5), until the effect is visible in the simulations. This issue was fixed by using the absolute values for the specified zone. The changes are implemented in WRF since version 3.7.0 and in a patched version 3.6.1 that is used for the simulations within this study (WRF361N).
Several questions arose for the simulations that have been carried out with the non-corrected WRF version:

- Does the artefact influence the climate (change) signal in long (transient) WRF/ARW climate mode simulations?
- Does this have an effect on the simulations with WRF done within the WCRP CORDEX and EURO-CORDEX context?
- Is there a systematic difference between two model simulations with / without the bug fix? Or, are the potential and expected differences just random? What is the magnitude of these differences?

To investigate the influence of the artefact on longterm simulations, two 20-yearlong ERA-Interim driven EUR-44 simulations, one patched and one unpatched WRF361N version, have been carried out and compared for mean temperature and precipitation.
The results show overall just slight differences in mean 2m temperature (+/- 0.2K) and precipitation (+/- 5%) (Figure A.0.2). The time series of annual precipitation and temperature show slight differences from year to year but are not increasing with time (Figure A.0.3). Surprisingly, the first year shows the largest differences, although the differences at the lateral boundary due to the artefact grow with time. Large differences between both runs, that start with identical initial conditions, are seen after the first three months (Figure A.0.4). Though they are initially caused by the disturbance at the lateral model forcing by the unpatched model version, the differences do not seem to be process-related and mostly result from internal variability in both runs. A comparison of two simulations with identical setup (patched version) but shifted by a one-day in the starting time reveals differences in the same order of magnitude for mean values.

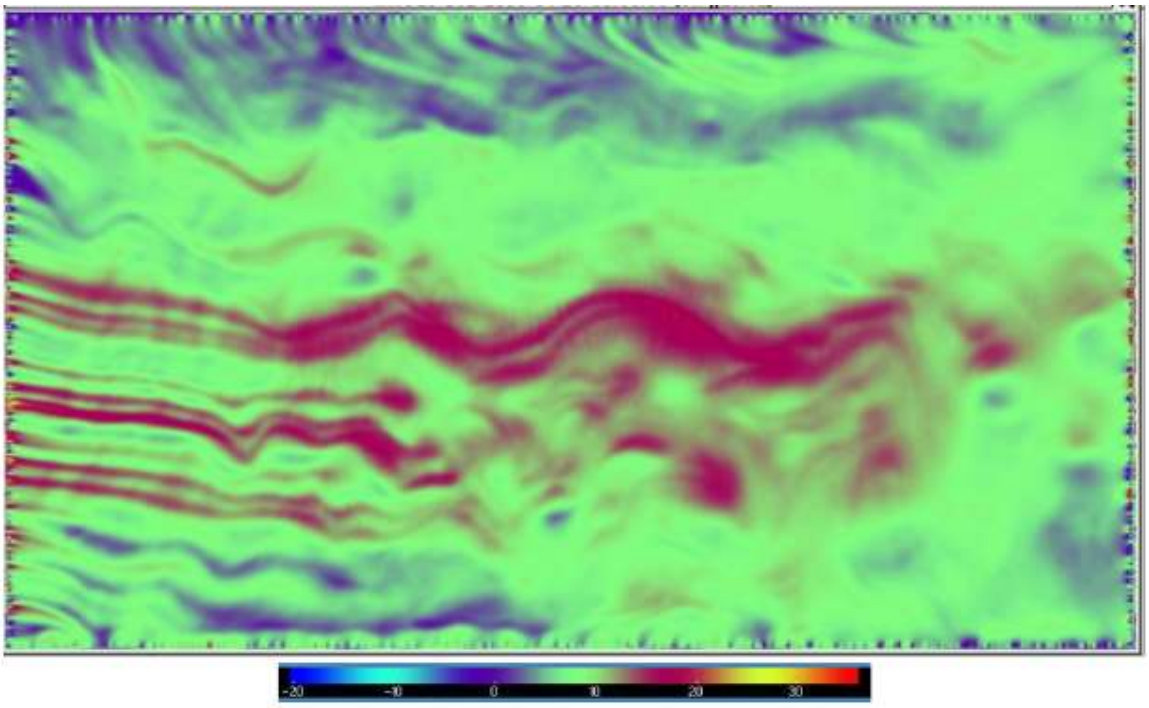

Figure A.0.1: U-wind [m/s] in uppermost layer in 3 km one-way nested WRF simulation after 16 months of simulation. Unphysical pattern at the lateral boundary leads to "stripes" advecting into the model domain.

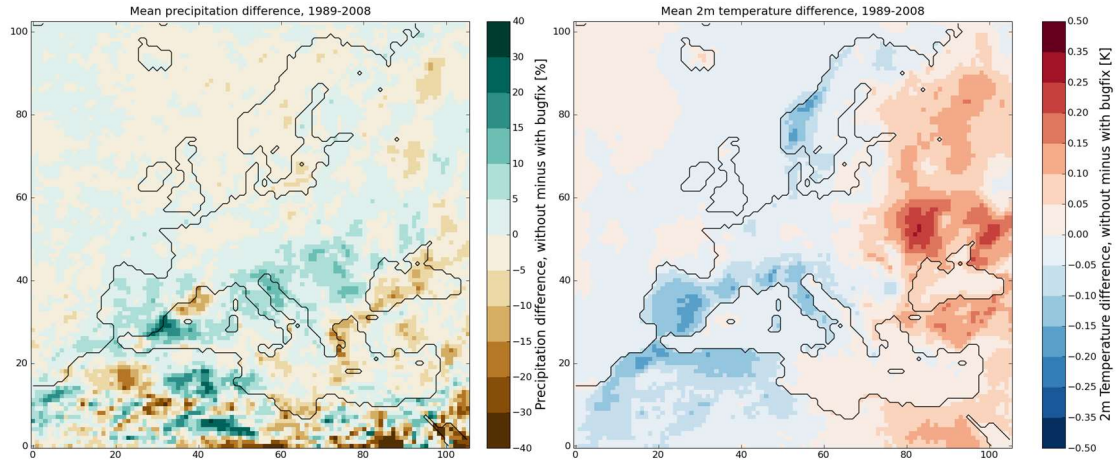

Figure A.0.2: Mean precipitation and mean temperature difference between two ERA-Interim driven EUR-44 simulations from 1989 to 2008, one with boundary error fixed and one unfixed.

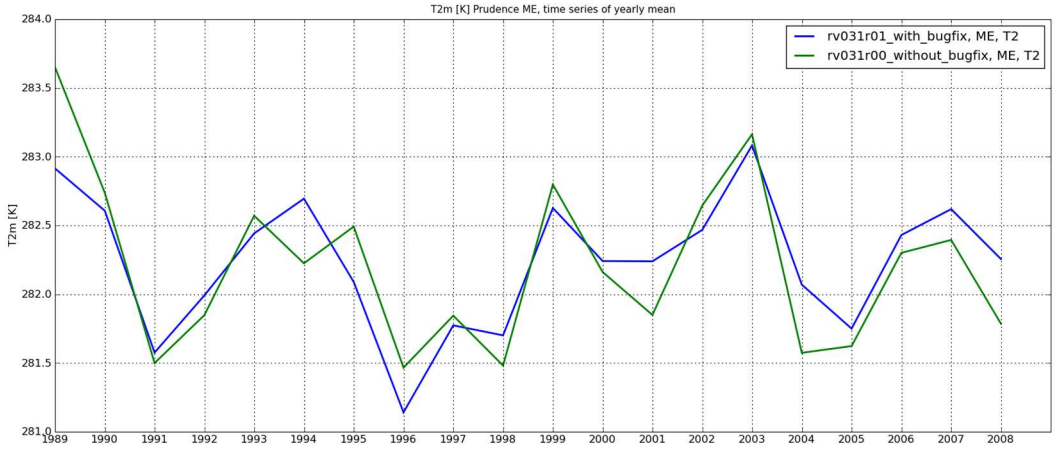

Figure A.0.3: Time series of annual mean 2m temperature in Middle Europe in WRF simulation with (blue) and without (green) fixed boundary error.

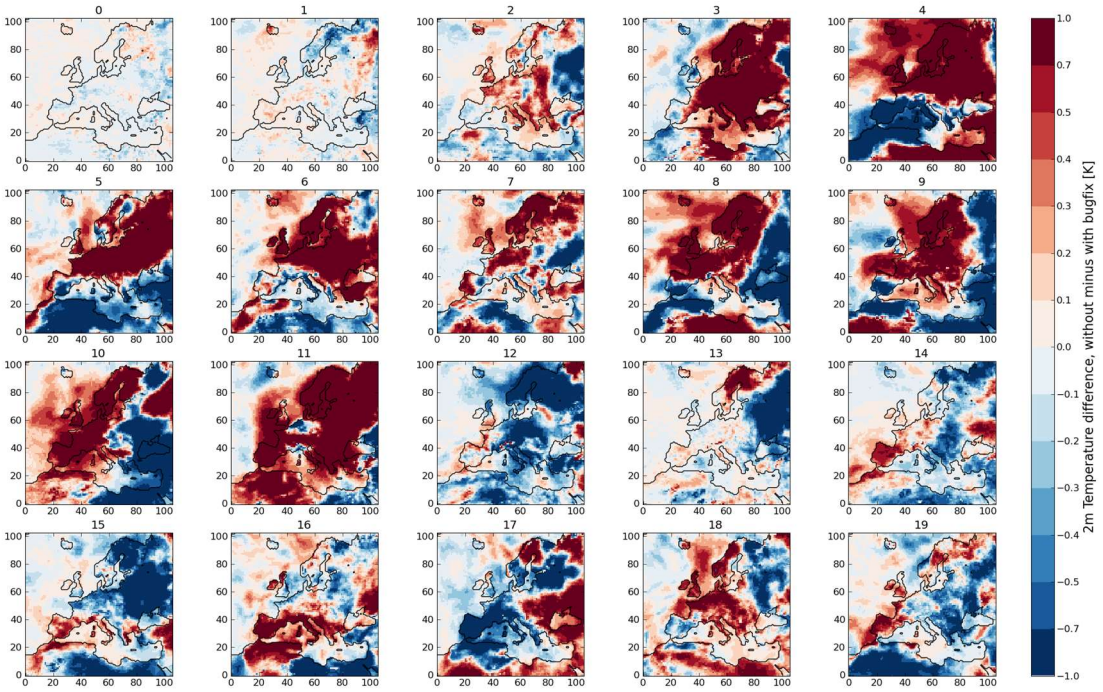

Figure A.0.4: Difference of monthly mean 2m temperature between two EUR-44 WRF simulations, one with fixed and one with unfixed boundary error, for the first 20 months of simulation. Larger differences occur after three months but remain in the range of internal variability.

B. LARSIM simulations

To investigate the potential added value of a higher resolution (3 km compared to 12 km) of the atmospheric model output on the performance of a hydrological model, the ERA-Interim driven EUR-11/3kmME data is used to drive the Large Area Runoff Simulation Model (LARSIM) (Ludwig et al., 2006). LARSIM is a conceptional distributed water balance model that considers interception, evapotranspiration, snow accumulation, snow compaction and snow melt, soil water storage as well as storage and lateral transport in streams and lakes (Figure B.0.1). The model raster elements include ground level, slope, land use, field capacity and stream geometry. It reproduces the real stream network by calculative intersection of the digital stream network and the model raster.

LARSIM has a 5 km grid that covers several central European river catchments (Figure B.0.1). Here, two one-year simulations are carried out for the upper Danube catchment from 2012-07-01 to 2013-07-01: one with meteorological input data (here: daily precipitation and temperature) from the 12 km EUR-11 and one from the convection-permitting 3 km WRF361N simulation. The WRF data is regridded on the 5 km LARSIM grid via conservative remapping (Jones 1999). The results for both input data resolutions are compared for time series of streamflow at several gauging stations (see Figure B-3). The streamflow has an increased variability and overall higher peaks for 3 km resolution input data, especially in small river catchments. For large river catchments, the results for both input resolutions are very similar. The results reflect the differences in mean precipitation and intensity distribution between the 3 km and the 12 km WRF simulation. Higher peak stream flows for 3 km input result from higher heavy precipitation in the 3 km WRF simulations in the northern Alps. This is mainly caused by the steeper orography in the 3 km resolution, and thereby stronger forced ascending of air mass in case of a northerly wind component towards the Alps. In small river catchments local heavy precipitation events that cause high streamflow are better represented in the convection-permitting 3 km simulation. Due to a better representation of complex terrain the location of orographic precipitation is potentially better simulated by the 3 km WRF run. As orography often defines watersheds this leads to a more accurate distribution of precipitation into the right river catchments. For larger catchments the local intensity differences between 3 km and 12 km input data become less apparent as the streamflow accumulates over a larger area and local spikes are smoothed out.

Still, further investigation is needed for longer streamflow time series and other river catchments.

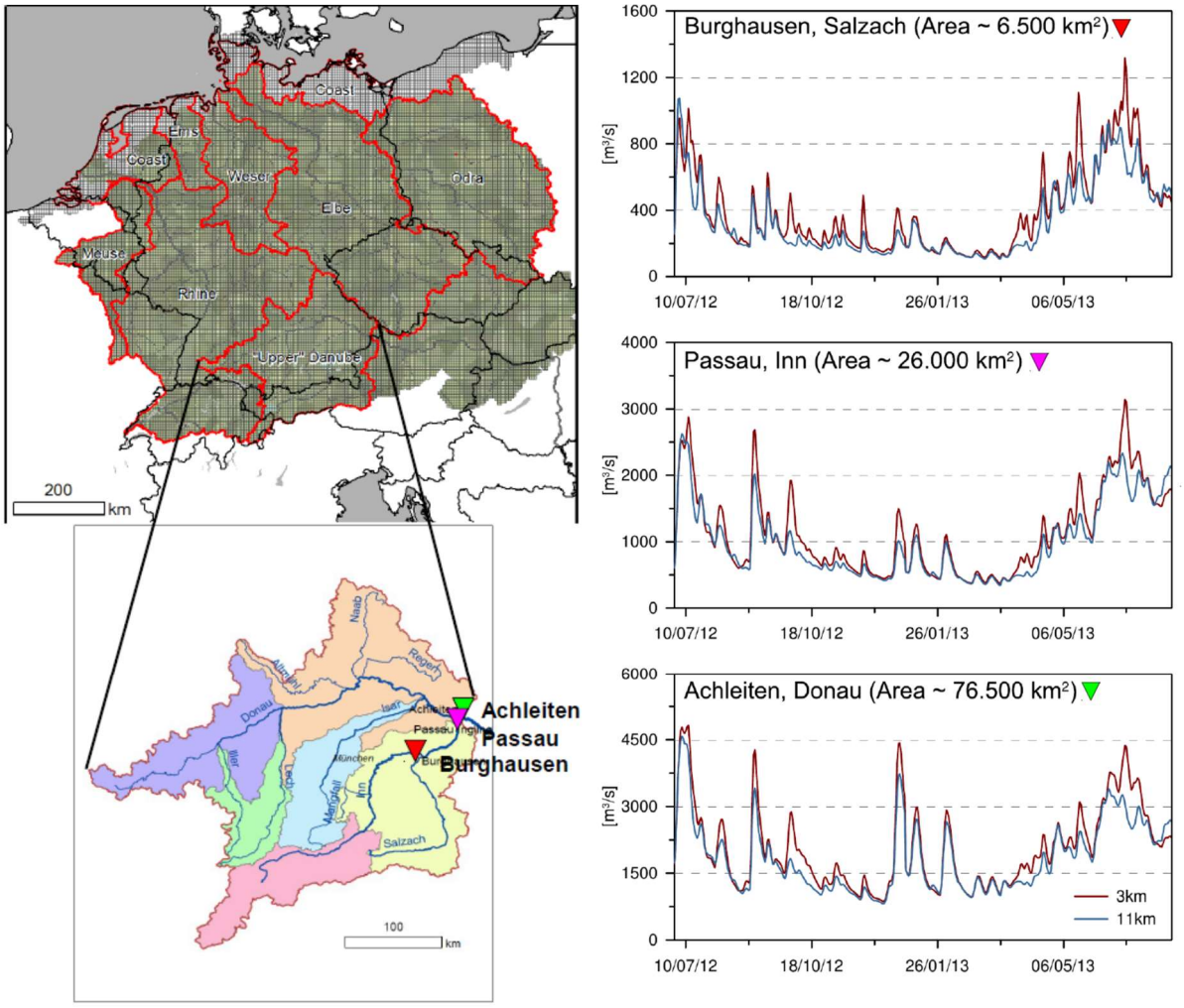

Figure B.0.1: LARSIM grid for several Middle European river catchments and upper Danube catchment (left). LARSIM streamflow for several gauging stations, WRF 12 km (blue) vs. 3 km (red) input (right).

C. Additional analyses

The following figures provide additional information for the analysis of land-atmosphere coupling in EUR-11/3kmME evaluation simulations in Section 4.2 (Figure C.0.1 to Figure C.0.6) and the analysis of EUR-44 climate change projection simulation in Sections 7.2 to 7.4 (Figure C.0.7 to Figure C.0.17).

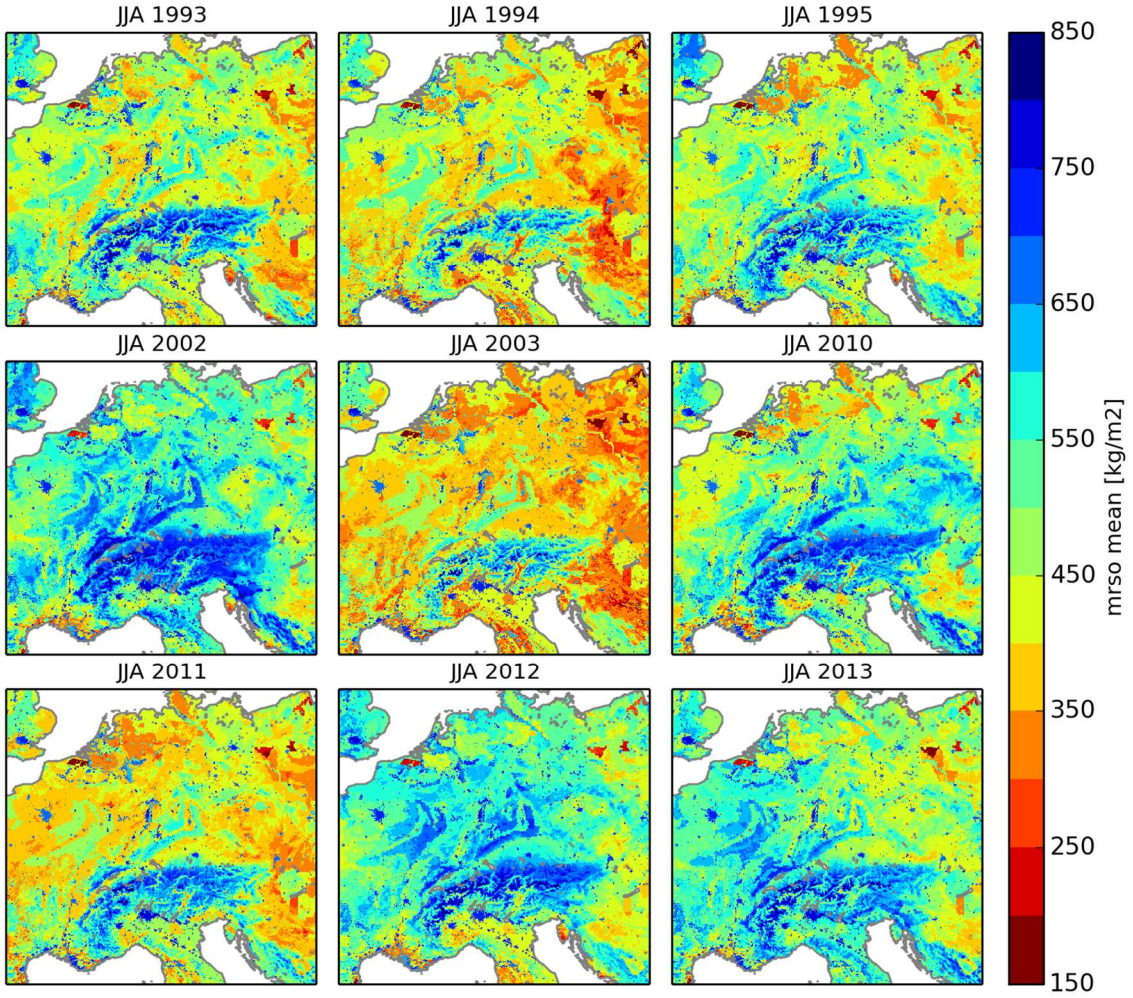

Figure C.0.1: Mean total soil moisture in summer (JJA) of nine individual years 1993-1995, 2002-2003, 2010-2013 in the ERA-Interim driven WRF3 simulation.

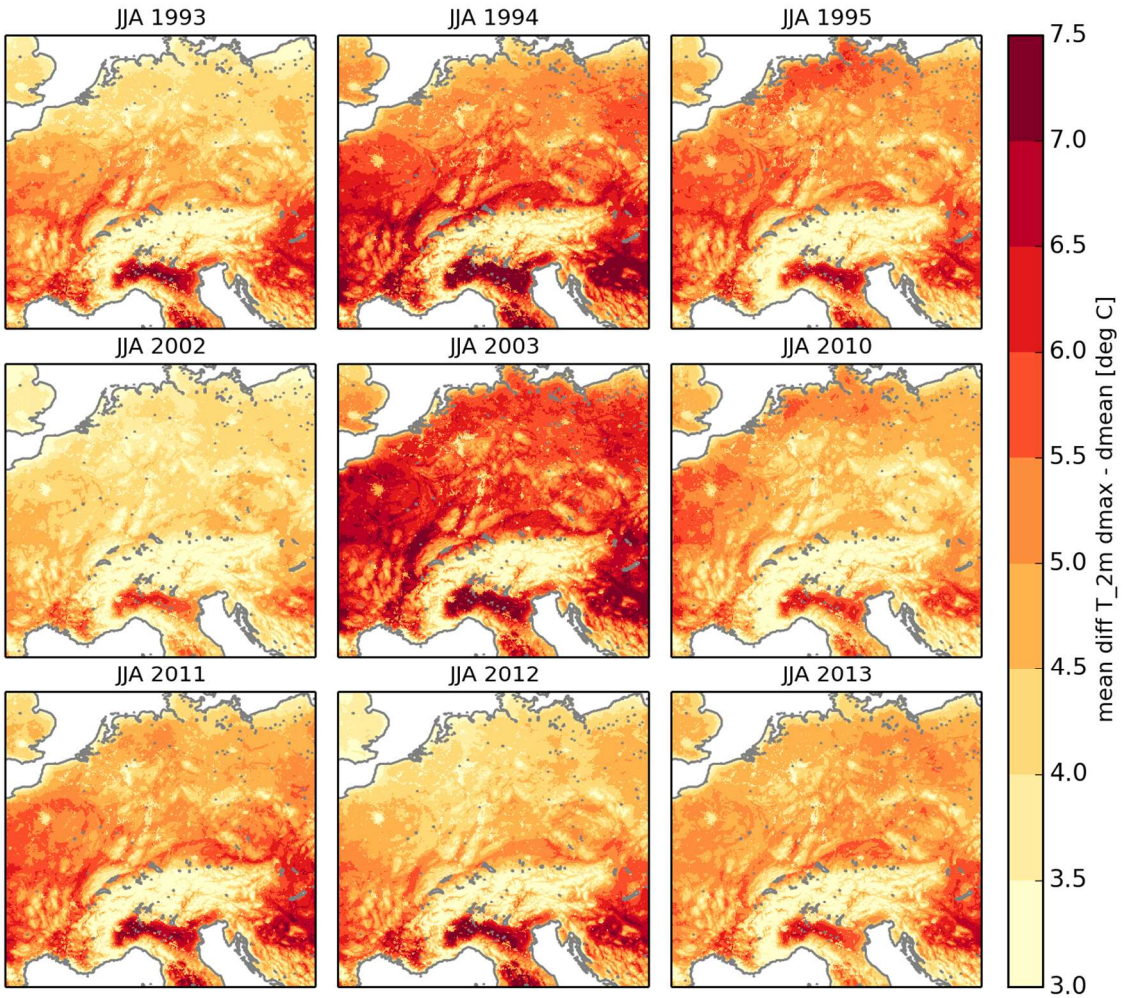

Figure C.0.2: Difference of daily maximum temperature minus mean temperature in summer (JJA) of nine individual years 1993-1995, 2002-2003, 2010-2013 in the ERA-Interim driven WRF3 simulation.

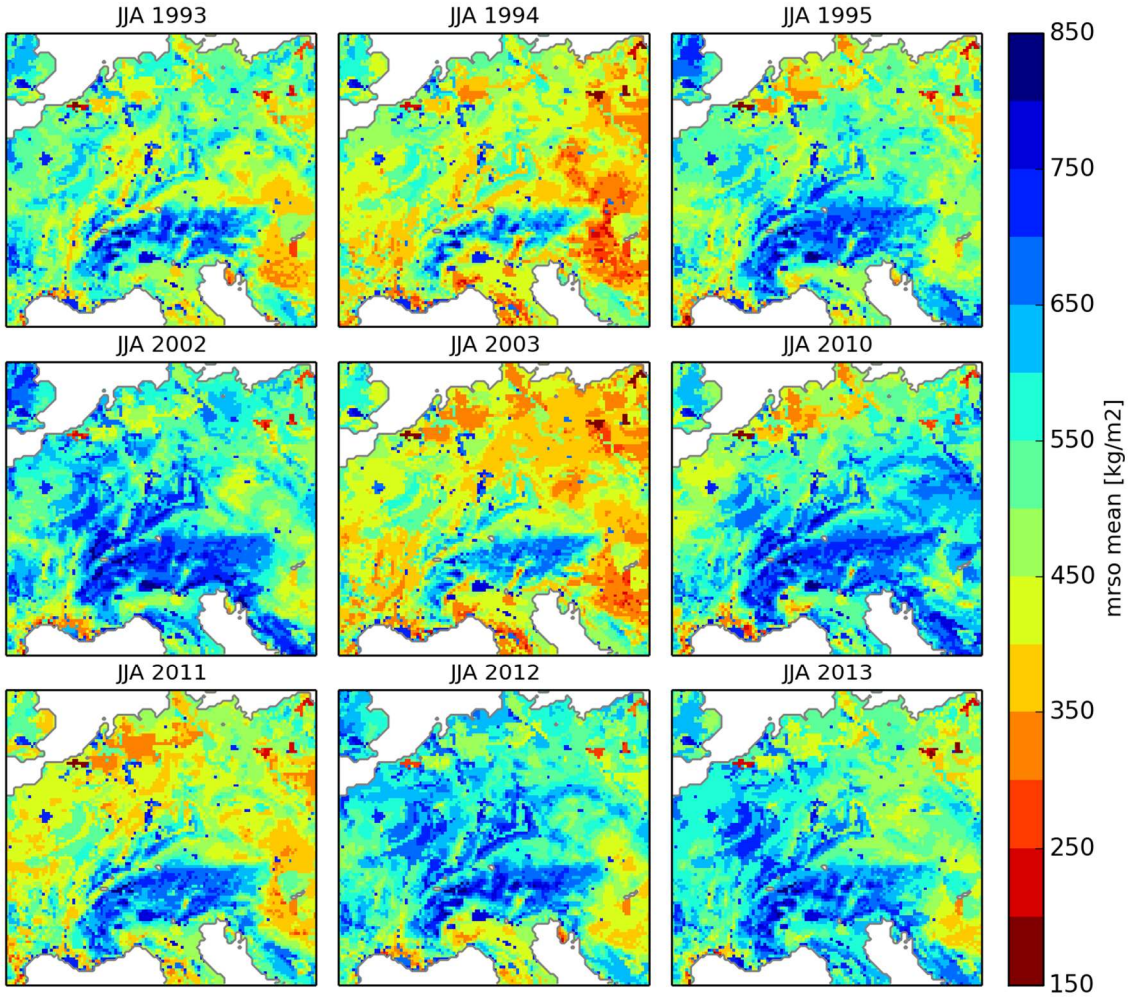

Figure C.0.3: Mean total soil moisture in summer (JJA) of nine individual years 1993-1995, 2002-2003, 2010-2013 in the ERA-Interim driven WRF12 simulation.

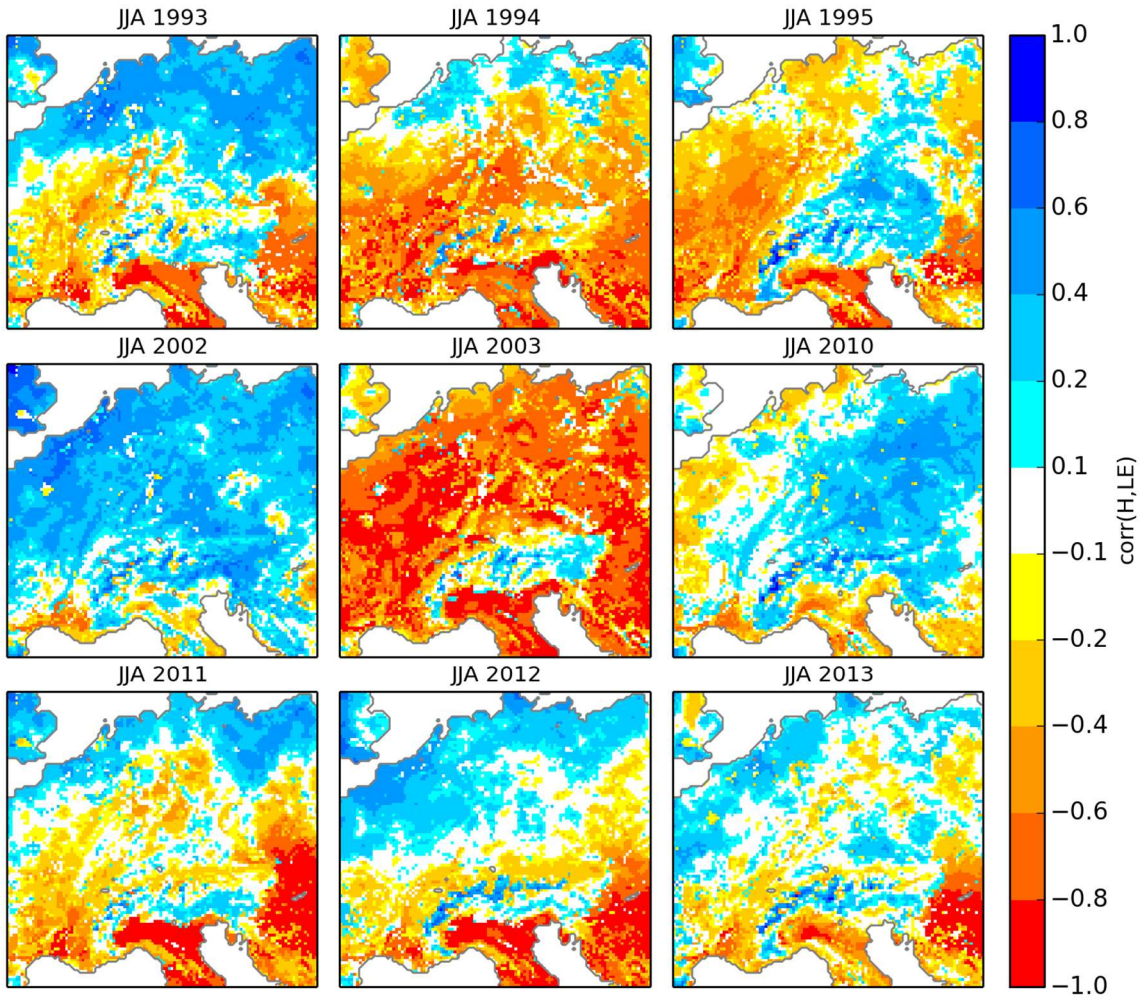

Figure C.0.4: Correlation of summer (JJA) daily averages of latent and sensible heat flux for nine individual years 1993-1995, 2002-2003, 2010-2013 in the ERA-Interim driven WRF12 simulation.

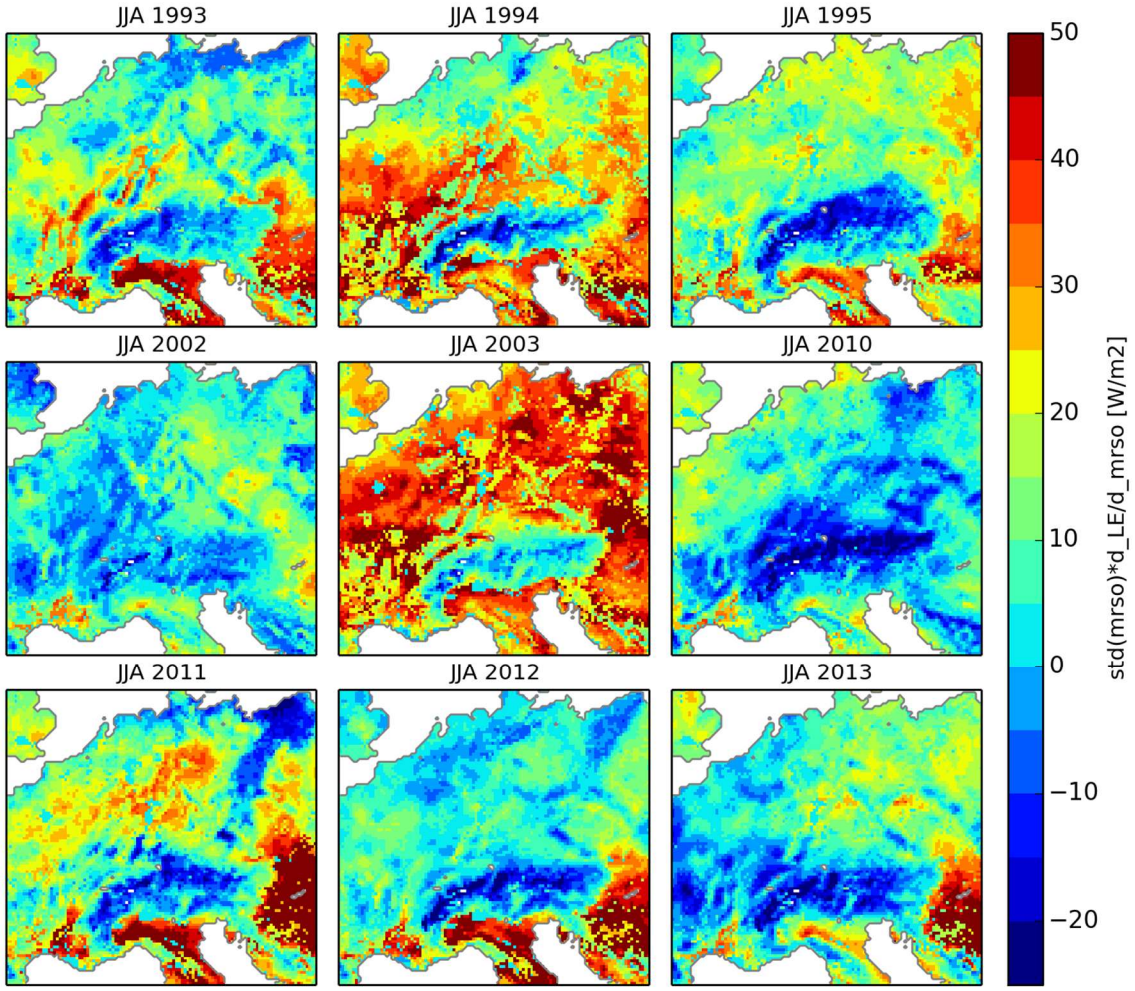

Figure C.0.5: Coupling index $I_{SM,LE}$ for nine individual summer seasons (JJA) 1993-1995, 2002-2003, 2010-2013 in the ERA-Interim driven WRF12 simulation. Red (blue) colours indicates strong (weak) coupling.

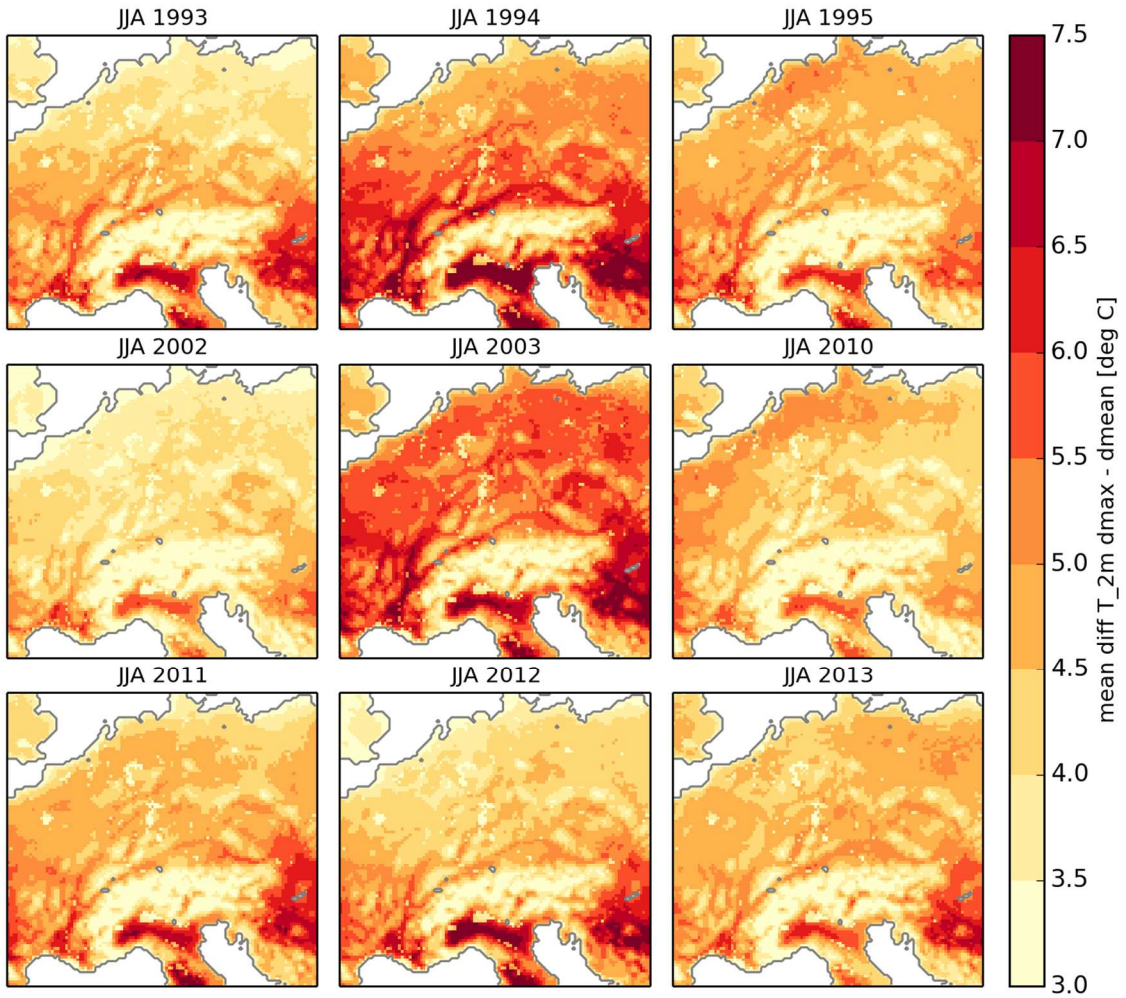

Figure C.0.6: Difference of daily maximum temperature minus mean temperature in summer (JJA) of nine individual years 1993-1995, 2002-2003, 2010-2013 in the ERA-Interim driven WRF12 simulation.

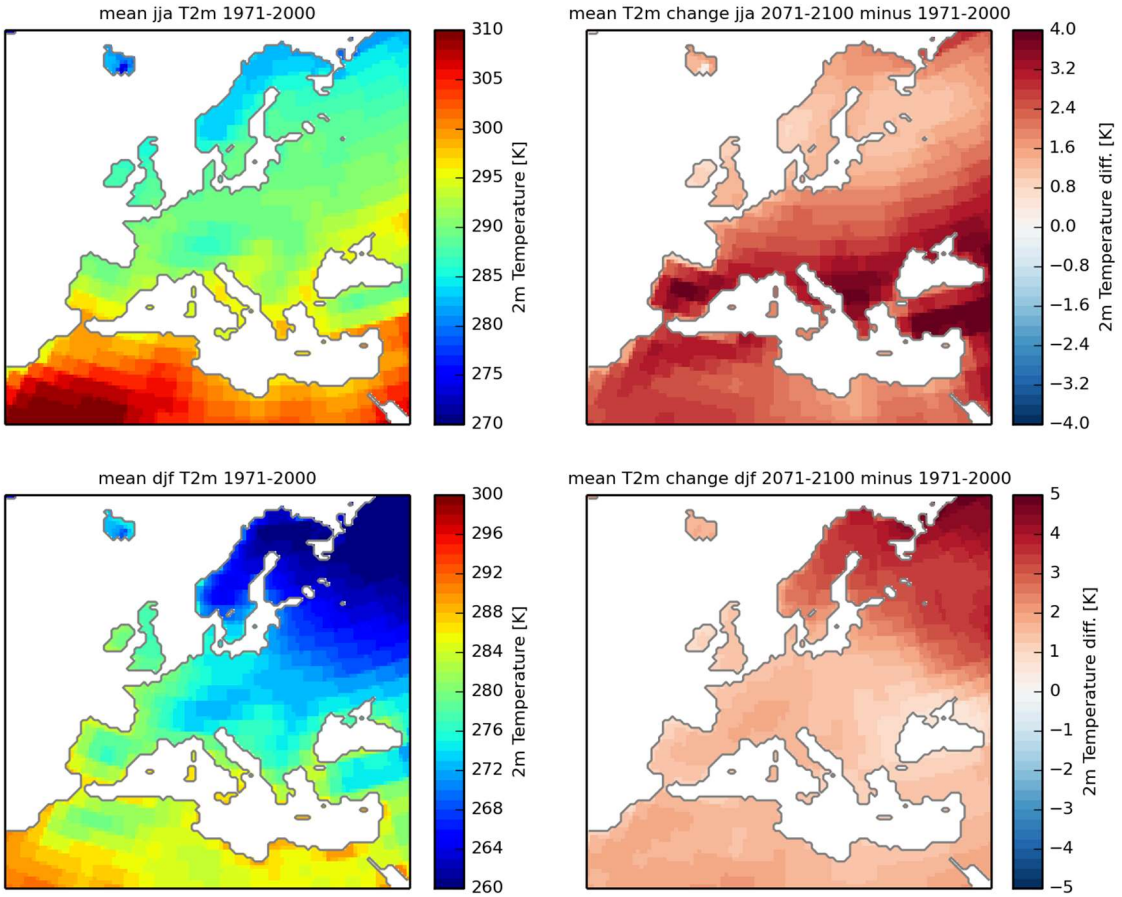

Figure C.0.7: Mean seasonal 2m temperature in the control period (1971-2000, left) and its relative change in the far future (2071-2100, right) in the GCM MPI-ESM-LR simulation in summer (top) and winter (bottom).

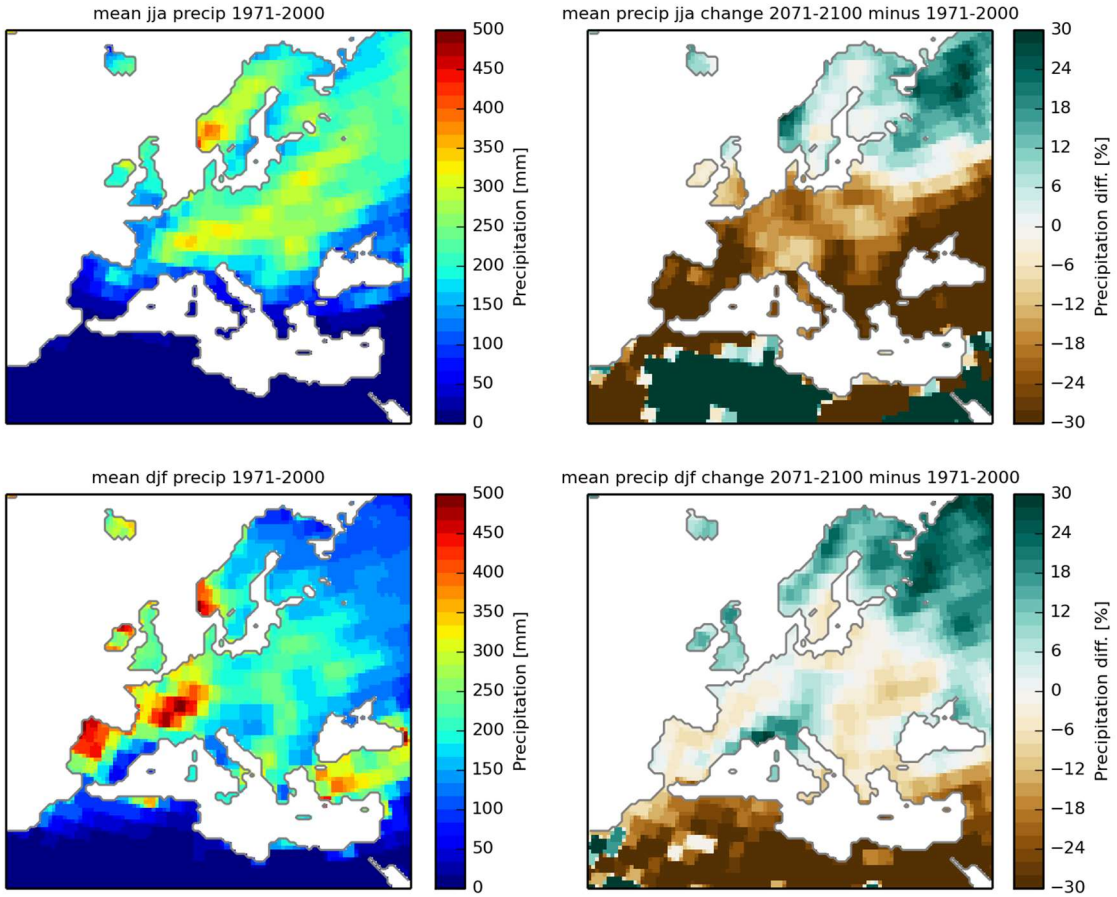

Figure C.0.8: Mean seasonal precipitation sum in the control period (1971-2000, left) and its relative change in the far future (2071-2100, right) in the GCM MPI-ESM-LR simulation in summer (top) and winter (bottom).

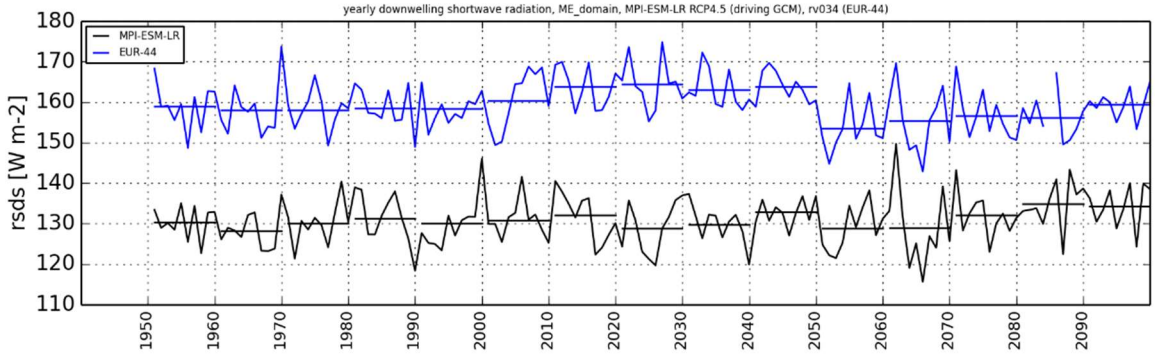

Figure C.0.9: Time series of annual mean downward shortwave radiation (rsds) spatially averaged over the 3kmME domain in MPI-ESM-LR (black) and EUR-44. Horizontal lines indicate decadal means.

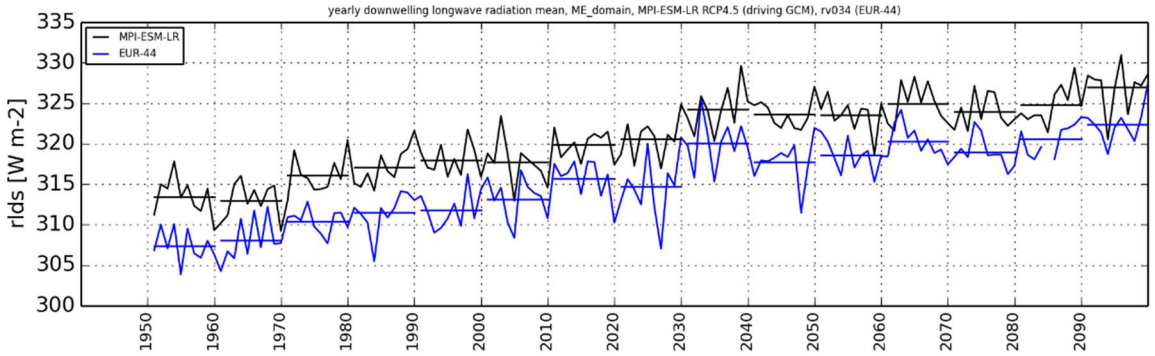

Figure C.0.10: Time series of annual mean downward longwave radiation (rlds) spatially averaged over the 3kmME domain in MPI-ESM-LR (black) and EUR-44. Horizontal lines indicate decadal means.

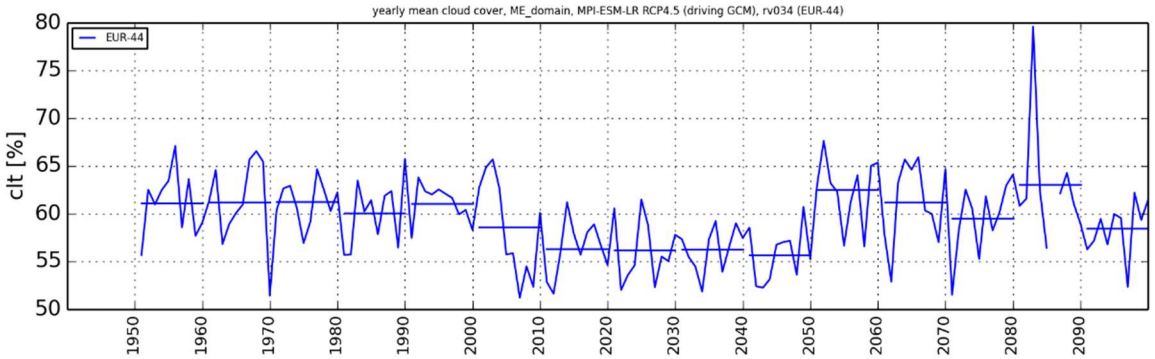

Figure C.0.11.: Time series of annual mean cloud cover (clt) spatially averaged over the 3kmME domain in MPI-ESM-LR (black) and EUR-44. Horizontal lines indicate decadal means.

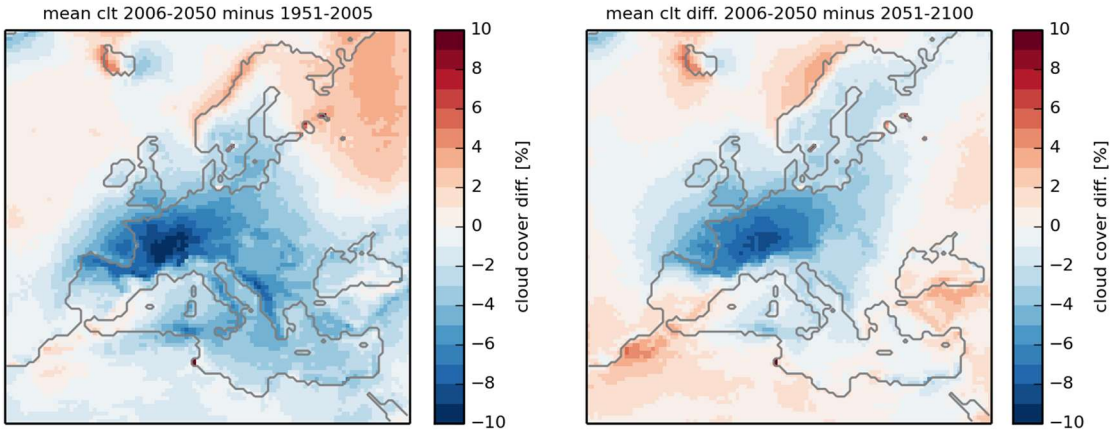

Figure C.0.12: Difference of mean cloud cover in MPI-ESM-LR driven EUR-44 simulation in period 2006-2050 minus 1951-2005 (left) and 2051-2100 (right).

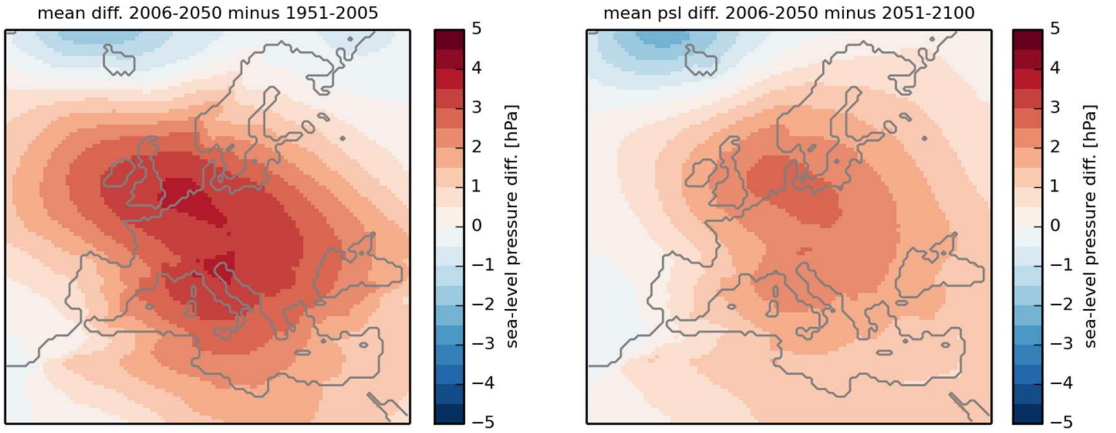

Figure C.0.13: Difference of mean sea-level pressure in MPI-ESM-LR driven EUR-44 simulation in period 2006-2050 minus 1951-2005 (left) and 2051-2100 (right).

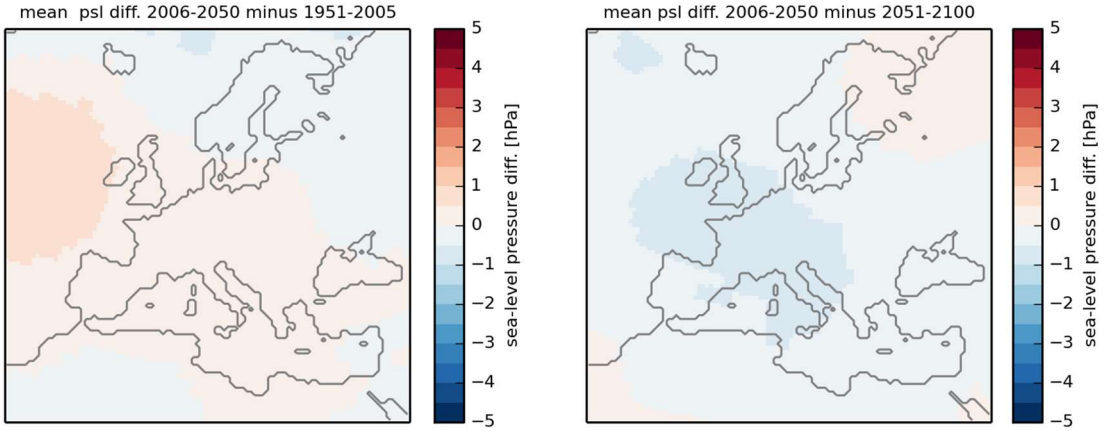

Figure C.0.14: Difference of mean sea-level pressure in MPI-ESM-LR simulation in period 2006-2050 minus 1951-2005 (left) and 2051-2100 (right).

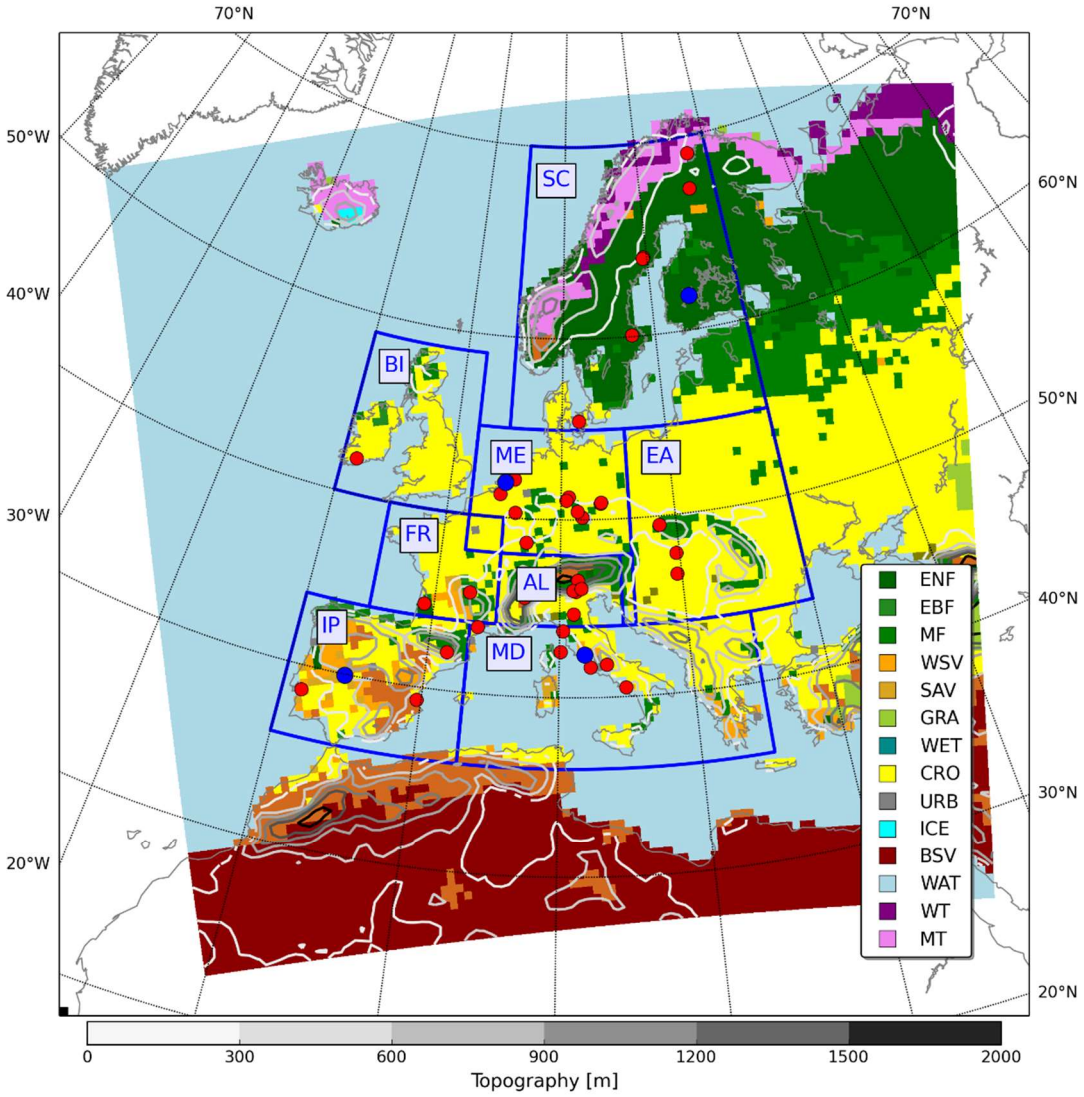

Figure C.0.15: EUR-44 domain. Colors indicate the dominant land use types derived from the MODIS satellite data classification used in the WRF models while white isolines indicate topography (evergreen needleleaf forest ENF, evergreen broadleaf forest EBF, mixed forest MF, wooded savanna WSV, savanna SAV, grasslands GRA, wetlands WET, cropland CRO, urban URB, snow or ice ICE, barely/sparsely vegetated BSV, water WAT, wooded tundra WT, mixed tundra MT). The blue boxes delineate the PRUDENCE analysis regions with their identifiers and dots show the locations of the FLUXNET stations (red: all stations used in the study, blue: stations shown in Figure 3.3).

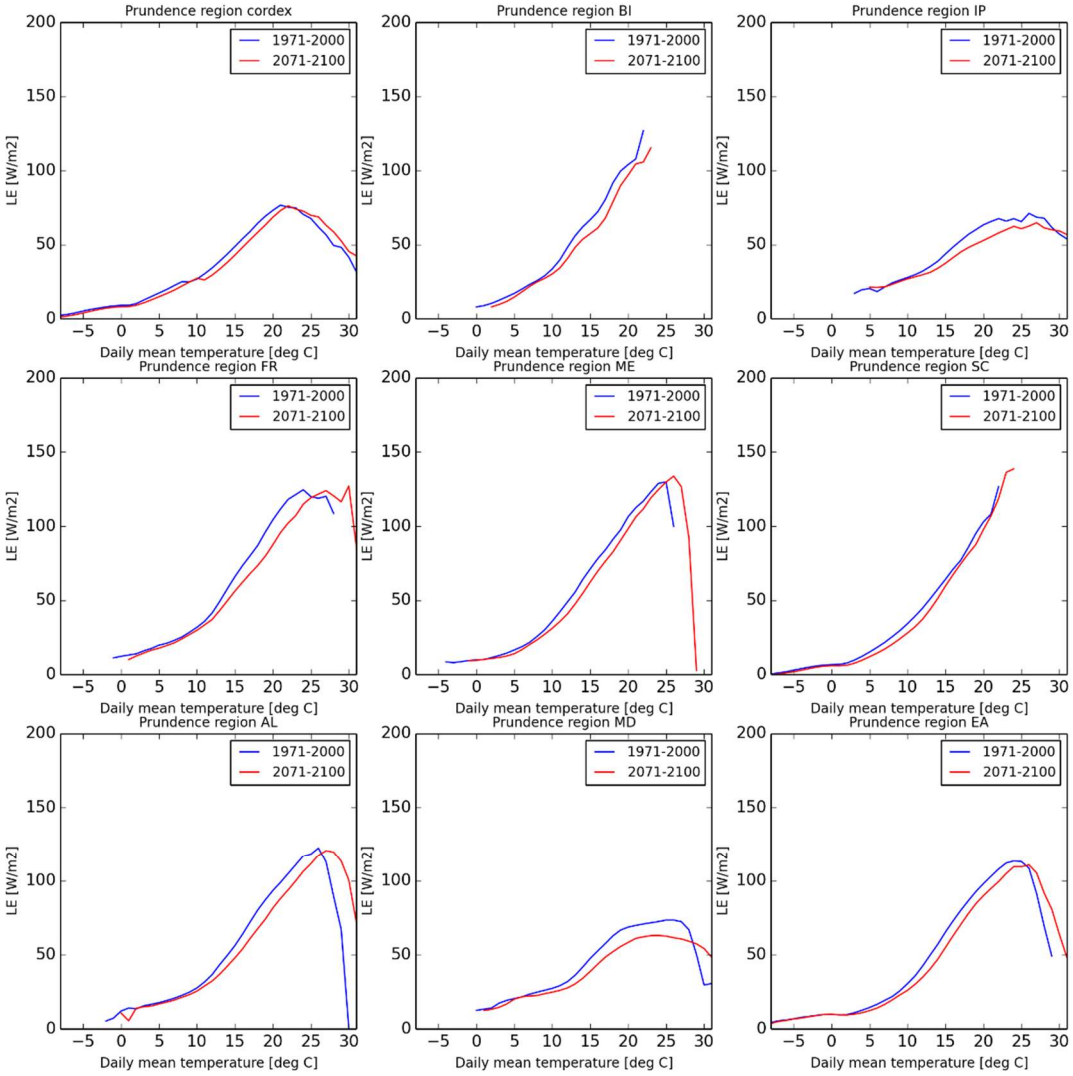

Figure C.0.16: Temperature–latent heat flux (LE) scaling at days with extreme precipitation ($P99_{dmax}$) in the MPI-ESM-LR driven EUR-44 simulation for 1971-2000 (blue) and 2071-2100 (red) averaged over the whole domain (upper left) and individual PRUDENCE regions. For each grid point in the particular analysis region daily maximum 3-hourly precipitation is discretized into one-degree bins of daily mean temperature. For each temperature bin with a sample size larger than 50, the 99^{th} percentile of the precipitation values ($P99_{dmax}$) is calculated and all daily mean latent heat flux values at days with precipitation exceeding $P99_{dmax}$ are selected and averaged over all stations.

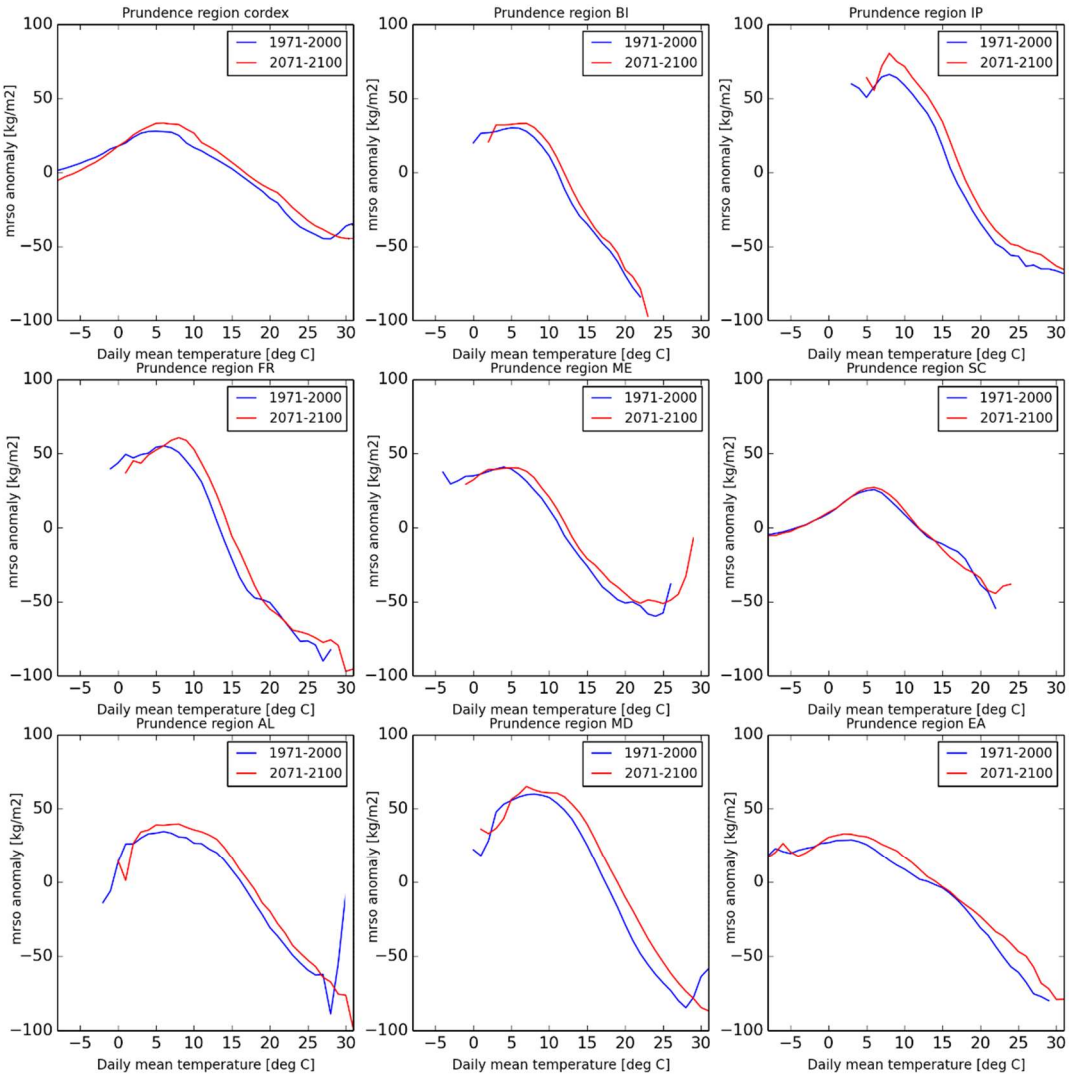

Figure C.0.17: Temperature–soil moisture scaling at days with extreme precipitation ($P99_{dmax}$) in the MPI-ESM-LR driven EUR-44 simulation for 1971-2000 (blue) and 2071-2100 (red) averaged over the whole domain (upper left) and individual PRUDENCE regions. For each grid point in the particular analysis region daily maximum 3-hourly precipitation is discretized into one-degree bins of daily mean temperature. For each temperature bin with a sample size larger than 50, the 99^{th} percentile of the precipitation values ($P99_{dmax}$) is calculated and all morning soil moisture values at days with precipitation exceeding $P99_{dmax}$ are selected and averaged over all stations.

Table C.0.1: EURO-CORDEX RCM simulations used in Chapter 3.

Model ID (Resolution)	Institute	Radiation scheme	Convection scheme	Microphysics scheme	Boundary layer scheme	Land-surface model	Land use
ALADIN (0.44°)	HMS	(Mlawer et al., 1997), (Fouquart and Bonnel, 1980)	(Cuxart et al., 2000), (Bougeault, 1985)	(Smith, 1990), (Ricard and Royer, 1993)	(Troen and Mahrt, 1986)	SURFEX (Masson et al., 2013)	ECOCLIMAP (Champeaux et al., 2005), (Masson et al., 2003)
CLM (0.44°)	CCLM	(Ritter and Geleyn, 1992)	(Tiedtke, 1989)	(Doms et al., 2011), (Baldauf and Schulz, 2004)	(Louis, 1979)	TERRA-ML: (Doms et al., 2011)	GLC2000 (Joint Research Centre, 2003)
HadRM3P (0.44°)	MOHC	(Edwards and Slingo, 1995)	(Gregory and Rowntree, 1990), (Gregory et al., 1997)	(Smith, 1990), (Martin et al., 1994)	(Smith, 1990)	(Essery et al., 2003)	(Hansen et al., 2000)
HIRHAM (0.44°)	DMI	(Morcrette et al., 1986)	(Tiedtke, 1989)	(Lohmann and Roeckner, 1996)	(Louis, 1979)	(Hagemann, 2002)	(Claussen et al., 1994)
RACMO2 (0.44°)	KNMI	(Fouquart and Bonnel, 1980)	(Tiedtke, 1989), (Nordeng, 1994), (Neggers et al., 2009)	(Tiedtke, 1993), (Tompkins et al., 2007), ECMWF-IFS, (Neggers, 2009)	(Lenderink and Holtslag, 2004), (Siebesma et al., 2007)	(Hurk and Viterbo, 2000), (Balsamo et al., 2009)	ECOCLIMAP (Champeaux et al., 2005), (Masson et al., 2003)
RACMO2 (0.11°)	KNMI	same as 0.44°	same as 0.44°	same as 0.44°	same as 0.44°	same as 0.44°	same as 0.44°
RCA4 (0.44°)	SMHI	(Savijärvi, 1990)	(Kain and Fritsch, 1993)	(Rasch and Kristjánsson, 1998)	(Cuxart et al., 2000)	(Samuelsson et al., 2006)	ECOCLIMAP (Champeaux et al., 2005), (Masson et al., 2003)
REMO 2009 (0.44°)	GERICS	(Morcrette et al., 1986)	(Tiedtke, 1989)	(Lohmann and Roeckner, 1996)	(Louis, 1979)	(Hagemann, 2002), (Rechid et al., 2009)	USGS (Hagemann, 2002)
WRF-331A (0.44°)	MIUB	CAM3.: (Collins et al., 2004)	Modified Kain-Fritsch: (Kain, 2004)	WSM 6-class: (Hong and Lim, 2006)	YSU: (Hong et al., 2006)	NOAH: (Ek et al., 2003)	IGBP-MODIS 30''
WRF-331A2 (0.44°)	AUTH	CAM3.: (Collins et al., 2004)	Modified Kain-Fritsch: (Kain, 2004)	WSM 6-class: (Hong and Lim, 2006)	YSU: (Hong et al., 2006)	NOAH: (Ek et al., 2003)	IGBP-MODIS 30''
WRF-331C (0.44°)	BCCR	CAM3.: (Collins et al., 2004)	Modified Kain-Fritsch: (Kain, 2004)	WSM 3-class: (Hong et al., 2004)	YSU: (Hong et al., 2006)	NOAH: (Ek et al., 2003)	IGBP-MODIS 30''
WRF-331D (0.44°)	IDL	RRTMG: (Iacono et al., 2008)	Betts-Miller-Janjic: (Janjić, 1994)	WSM 6-class: (Hong and Lim, 2006)	YSU: (Hong et al., 2006)	NOAH: (Ek et al., 2003)	IGBP-MODIS 30''
WRF-331F (0.11°)	IPSL-INERIS	RRTMG: (Iacono et al., 2008)	(Grell and Dévényi, 2002)	WSM 5-class: (Hong et al., 2004)	YSU: (Hong et al., 2006)	NOAH: (Ek et al., 2003)	USGS Land Use
WRF-331G (0.44°)	UCAN	CAM3.: (Collins et al., 2004)	(Grell and Dévényi, 2002)	WSM 6-class: (Hong and Lim, 2006)	YSU: (Hong et al., 2006)	NOAH: (Ek et al., 2003)	IGBP-MODIS 30''
WRF-331H (0.11°)	UHOH	CAM3.: (Collins et al., 2004)	Modified Kain-Fritsch: (Kain, 2004)	Morrison 2-mom. scheme: (Morrison et al., 2009)	YSU: (Hong et al., 2006)	NOAH: (Ek et al., 2003)	IGBP-MODIS 30''
WRF-341E (0.44°)	NUIM	RRTMG: (Iacono et al., 2008)	Modified Kain-Fritsch: (Kain, 2004)	WSM 6-class: (Hong and Lim, 2006)	YSU: (Hong et al., 2006)	NOAH: (Ek et al., 2003)	IGBP-MODIS 30''

List of abbreviations

AR	Assessment Report
ARW	Advanced Research WRF
BfG	Bundesanstalt für Gewässerkunde (German Federal Institute of Hydrology)
CAPE	Convective Available Potential Energy
C-C	Clausius Clapeyron
CMIP5	Coupled Model Intercomparison Project Phase 5
CORDEX	Coordinated Regional Climate Downscaling Experiment
CPM	Convection-permitting Model
DWD	Deutscher Wetterdienst (German Meteorological Service)
ESD	Empirical Statistical Downscaling
EURO-CORDEX	Coordinated Regional Climate Downscaling Experiment for Europe
EUR-11	RCM simulation on EURO-CORDEX domain with 0.11° grid size
EUR-44	RCM simulation on EURO-CORDEX domain with 0.44° grid size
IPCC	Intergovernmental Panel on Climate Change
LAM	Limited Area Model
LARSIM	Large Area Runoff Simulation Model
LBC	Lateral Boundary Conditions
FLUXNET	Network of flux tower sites
GCM	Global Climate Model
GLACE	Global Land-Atmosphere Coupling Experiment
GLEAM	Global Land Evaporation Amsterdam Model
JSC	Jülich Supercumputing Centre
JUROPA	Supercomputer at JSC
JURECA	Supercomputer at JSC
MPI-ESM-LR	Max Planck Institute for Meteorology Earth System Model
RCM	Regional Climate Model
RCP	Representative Concentration Pathways
WCRP	World Climate Research Program
WPS	WRF Preprocessing System
WRF	Weather Research and Forecasting Model
WRF3	WRF simulation for central Europe with 3 km grid size
WRF3_12	WRF3 interpolated on 12 km grid
WRF12	WRF simulation for central Europe with 12 km grid size

List of figures

[11] Figures 3.1 to 3.12 are in accord with figures in Knist et al. (2017)

[12] Figures 5.2 to 5.5 are in accord with figures in Knist et al. (2018a)

[13] Figures 6.1 to 6.8 are in accord with figures in Knist et al. (2018b)

[14] Figures 7.11 to 7.17 are in accord with figures in Knist et al. (2018a)

Acknowledgments

This work has been funded through a research and development cooperation on hydrometeorology between the Federal Institute of Hydrology (BfG), Koblenz, Germany, and the Meteorological Institute, University of Bonn, Bonn, Germany, through the CRC/TR32 project "Patterns in Soil-Vegetation-Atmosphere Systems: Monitoring, Modelling and Data Assimilation" funded by the German Research Foundation (DFG), and through the EC-funded project eLTER H2020 (GA: 654359 - H2020 INFRAIA call 2014-2015).

The author gratefully acknowledges the computing time granted by the JARA-HPC Vergabegremium and VSR commission on the super-computer JURECA at Forschungszentrum Jülich through compute time project JJSC15 and the support provided by the High-Performance Scientific Computing Center for Terrestrial Systems (HPC-TerrSys) of the Geoverbund ABC/J.

This work used eddy covariance data acquired by the FLUXNET community. I acknowledge the financial support to the eddy covariance data harmonization (www.fluxdata.org). The ERA-Interim data were accessed from http://apps.ecmwf.int/datasets/. The GLEAM data were accessed from www.gleam.eu/#downloads. The underlying RCM data base is available upon request (sknist@uni-bonn.de). The data are archived at the Jülich Supercomputing Centre, Research Centre Jülich, Jülich, Germany.

I thank the coordination and the participating institutes of the EURO-CORDEX initiative for making this study possible.

References

Allen MR, Ingram WJ (2002) Constraints on future changes in climate and the hydrologic cycle. Nature 419:224+. doi: 10.1038/nature01092

Armstrong RL, Brodzik MJ, Knowles K, Savoie M (2005) Global monthly EASE-Grid snow water equivalent climatology. Digit media. doi: http://dx.doi.org/10.5067/KJVERY3MIBPS

Avissar R, Schmidt T (1998) An Evaluation of the Scale at which Ground-Surface Heat Flux Patchiness Affects the Convective Boundary Layer Using Large-Eddy Simulations. J Atmos Sci 55:2666–2689. doi: 10.1175/1520-0469(1998)055<2666:AEOTSA>2.0.CO;2

Baldauf M, Schulz JP (2004) Prognostic precipitation in the Lokal-Modell (LM) of DWD. Cosmo Newsl 4:177–180.

Baldocchi D, Falge E, Gu L, et al (2001) FLUXNET: A New Tool to Study the Temporal and Spatial Variability of Ecosystem-Scale Carbon Dioxide, Water Vapor, and Energy Flux Densities. Bull Am Meteorol Soc 82:2415–2434. doi: 10.1175/1520-0477(2001)082<2415:FANTTS>2.3.CO;2

Balsamo G, Beljaars A, Scipal K, et al (2009) A Revised Hydrology for the ECMWF Model: Verification from Field Site to Terrestrial Water Storage and Impact in the Integrated Forecast System. J Hydrometeorol 10:623–643. doi: 10.1175/2008JHM1068.1

Ban N, Schmidli J, Schaer C bel. (2014) Evaluation of the convection-resolving regional climate modeling approach in decade-long simulations. J Geophys Res Atmos 119:7889–7907. doi: 10.1002/2014JD021478

Ban N, Schmidli J, Schär C (2015) Heavy precipitation in a changing climate: Does short-term summer precipitation increase faster? Geophys Res Lett 42:1165–1172. doi: 10.1002/2014GL062588

Beck HE, van Dijk AIJM, Levizzani V, et al (2016) MSWEP: 3-hourly 0.25° global gridded precipitation (1979–2015) by merging gauge, satellite, and reanalysis data. Hydrol Earth Syst Sci Discuss 1–38. doi: 10.5194/hess-2016-236

Berg P, Moseley C, Haerter JO (2013) Strong increase in convective precipitation in response to higher temperatures. Nat Geosci 6:181–185. doi: 10.1038/ngeo1731

Best MJ, Abramowitz G, Johnson HR, et al (2015) The plumbing of land surface models: benchmarking model performance. J Hydrometeorol 16:1425–1442. doi: 10.1175/JHM-D-14-0158.1

Betts AK, Desjardins R, Beljaars ACM, Tawfik A (2015) Observational study of land-surface-cloud-atmosphere coupling on daily timescales. Front Earth Sci. doi: 10.3389/feart.2015.00013

Betts RA, Cox PM, Lee SE, Woodward FI (1997) Contrasting physiological and structural vegetation feedbacks in climate change simulations. Nature 387:796–799.

Bougeault P (1985) A simple parameterization of the large scale effect of cumulus convection. Mon. Weather Rev. 113:2108–2121.

Brisson E, Van Weverberg K, Demuzere M, et al (2016) How well can a convection-permitting climate model reproduce decadal statistics of precipitation, temperature and cloud characteristics? Clim Dyn 47:3043–3061. doi: 10.1007/s00382-016-3012-z

Brockhaus P, Lüthi D, Schär C (2008) Aspects of the diurnal cycle in a regional climate model. Meteorol Zeitschrift 17:433–443. doi: 10.1127/0941-2948/2008/0316

Casanueva A, Kotlarski S, Herrera S, et al (2015) Daily precipitation statistics in a EURO-CORDEX RCM ensemble: added value of raw and bias-corrected high-resolution simulations. Clim Dyn 1–19. doi: 10.1007/s00382-015-2865-x

Champeaux JL, Masson V, Chauvin F (2005) ECOCLIMAP: a global database of land surface parameters at I km resolution. Meteorol Appl 12:29–32. doi: 10.1017/S1350482705001519

Chen F, Dudhia J (2001) Coupling an Advanced Land Surface–Hydrology Model with the Penn State–NCAR MM5 Modeling System. Part II: Preliminary Model Validation. Mon Weather Rev 129:587–604. doi: 10.1175/1520-0493(2001)129<0587:CAALSH>2.0.CO;2

Christensen JH, Christensen OB (2007) A summary of the PRUDENCE model projections of changes in European climate by the end of this century. Clim Change 81:7–30. doi: 10.1007/s10584-006-9210-7

Claussen M, Lohmann U, Roeckner E, Schulzweida U (1994) A global data set of land-surface parameters.

Collins WD, Rasch PJ, Boville BA, et al (2004) Description of the NCAR community atmosphere model (CAM 3.0).

Coppola E, Sobolowski S, Pichelli E, et al (2017) A first-of-its-kind multi-model convection permitting ensemble for investigating convective phenomena over Europe and the Mediterranean. Submitt to Clim Dyn *:*.

Cuxart J, Bougeault P, Redelsperger J-L (2000) A turbulence scheme allowing for mesoscale and large-eddy simulations. Q J R Meteorol Soc 126:1–30. doi: 10.1002/qj.49712656202

Decker M, Pitman A, Evans J (2015) Diagnosing the seasonal land–atmosphere correspondence over northern Australia: dependence on soil moisture state and correspondence strength definition. 3433–3447. doi: 10.5194/hess-19-3433-2015

Dee DP, Uppala SM, Simmons a. J, et al (2011) The ERA-Interim reanalysis: configuration and performance of the data assimilation system. Q J R Meteorol Soc 137:553–597. doi: 10.1002/qj.828

Dirmeyer P a. (2011) The terrestrial segment of soil moisture-climate coupling. Geophys Res Lett 38:1–5. doi: 10.1029/2011GL048268

Dirmeyer PA, Cash BA, Kinter JL, et al (2012) Simulating the diurnal cycle of rainfall in global climate models: resolution versus parameterization. Clim Dyn 39:399–418. doi: 10.1007/s00382-011-1127-9

Dirmeyer PA, Wang Z, Mbuh MJ, Norton HE (2014) Intensified land surface control on boundary layer growth in a changing climate. Geophys Res Lett 41:1290–1294. doi: 10.1002/2013GL058826

Doms G, Förstner J, Heise E, et al (2011) Consortium for Small-Scale Modelling A Description of the Nonhydrostatic Regional COSMO Model Part II : Physical Parameterization.

Edwards JM, Slingo A (1995) Studies with a flexible new radiation code. I: Choosing a comnfiguration for a large-scale model. Q J R Meteorol Soc 122:689–719. doi: 10.1002/qj.49712253107

Ek MB, Mitchell KE, Lin Y, et al (2003) Implementation of Noah land surface model advances in the National Centers for Environmental Prediction operational mesoscale Eta model. J Geophys Res Atmos. doi: 10.1029/2002JD003296

Essery RLH, Best MJ, Betts R a., et al (2003) Explicit Representation of Subgrid Heterogeneity in a GCM Land Surface Scheme. J Hydrometeorol 4:530–543. doi: 10.1175/1525-7541(2003)004<0530:EROSHI>2.0.CO;2

Fischer EM, Seneviratne SI, Vidale PL, et al (2007) Soil Moisture–Atmosphere Interactions during the 2003 European Summer Heat Wave. J Clim 20:5081–5099. doi: 10.1175/JCLI4288.1

Fosser G, Khodayar S, Berg P (2015) Benefit of convection permitting climate model simulations in the representation of convective precipitation. Clim Dyn 44:45–60. doi: 10.1007/s00382-014-2242-1

Fouquart Y, Bonnel B (1980) Computations of solar heating of the earth's atmosphere- A new parameterization. Beiträge zur Phys der Atmosphäre 53:35–62.

Froidevaux P, Schlemmer L, Schmidli J, et al (2014) Influence of the Background Wind on the Local Soil Moisture–Precipitation Feedback. J Atmos Sci 71:782–799. doi: 10.1175/JAS-D-13-0180.1

García-Díez M (2014) Physical realism, added value and sensitivity to parameterizations of a Regional Climate Model over Europe. Universidad de Cantabria

García-Díez M, Fernández J, Vautard R (2015) An RCM multi-physics ensemble over Europe: multi-variable evaluation to avoid error compensation. Clim Dyn 45:3141–3156. doi: 10.1007/s00382-015-2529-x

Giorgi F (2005) Climate change prediction. Clim Change 73:239–265. doi: 10.1007/s10584-005-6857-4

Giorgi F, Avissar R (1997) Representation of heterogeneity effects in Earth system modeling: Experience from land surface modeling. Rev Geophys 35:413–437. doi: 10.1029/97RG01754

Giorgi F, Jones C, Asrar GR (2009) Addressing climate information needs at the regional level: the CORDEX framework.

Goergen K, Beersma J, Brahmer G, et al (2010) Assessment of climate change impacts on discharge in the Rhine River Basin: results of the RheinBlick2050 project. Internationale Kommission f{ü}r die Hydrologie des Rheingebietes, Lelystad

Gregory D, Kershaw R, Inness PM (1997) Parametrization of momentum transport by convection. II: Tests in single-column and general circulation models. Q J R Meteorol Soc 123:1153–1183. doi: 10.1002/qj.49712354103

Gregory D, Rowntree PR (1990) A Mass Flux Convection Scheme with Representation of Cloud Ensemble Characteristics and Stability-Dependent Closure. Mon. Weather Rev. 118:1483–1506.

Grell GA, Dévényi D (2002) A generalized approach to parameterizing convection combining ensemble and data assimilation techniques. Geophys Res Lett 29:38-1-38–4. doi: 10.1029/2002GL015311

Guillod BP, Orlowsky B, Miralles D, et al (2013) Land surface controls on afternoon precipitation diagnosed from observational data: uncertainties, confounding factors and the possible role of vegetation interception. Atmos Chem Phys Discuss 13:29137–29201. doi: 10.5194/acpd-13-29137-2013

Gutowski JW, Giorgi F, Timbal B, et al (2016) WCRP COordinated Regional Downscaling EXperiment (CORDEX): A diagnostic MIP for CMIP6. Geosci Model Dev 9:4087–4095. doi: 10.5194/gmd-9-4087-2016

Hagemann S (2002) An Improved Land Surface Parameter Dataset for Global and Regional Climate Models. MPI Rep 336:1–21.

Hanel M, Buishand TA (2010) On the value of hourly precipitation extremes in regional climate model simulations. J Hydrol 393:265–273. doi: 10.1016/j.jhydrol.2010.08.024

Hansen MC, Defries RS, Townshend JRG, Sohlberg R (2000) Global land cover classification at 1 km spatial resolution using a classification tree approach.

Hirsch AL, Pitman AJ, Seneviratne SI, et al (2014) Summertime maximum and minimum temperature coupling asymmetry over Australia determined using WRF. Geophys Res Lett 41:1546–1552. doi: 10.1002/2013GL059055

Hirschi M, Mueller B, Dorigo W, Seneviratne SI (2014) Using remotely sensed soil moisture for land–atmosphere coupling diagnostics: The role of surface vs. root-zone soil moisture variability. Remote Sens Environ 154:246–252. doi: 10.1016/j.rse.2014.08.030

Hohenegger C, Brockhaus P, Bretherton CS, Schär C (2009) The Soil Moisture–

Precipitation Feedback in Simulations with Explicit and Parameterized Convection. J Clim 22:5003–5020. doi: 10.1175/2009JCLI2604.1

Hohenegger C, Brockhaus P, Schaer C (2008) Towards climate simulations at cloud-resolving scales. Meteorol ZEITSCHRIFT 17:383–394. doi: 10.1127/0941-2948/2008/0303

Hong S-Y, Dudhia J, Chen S-H (2004) A Revised Approach to Ice Microphysical Processes for the Bulk Parameterization of Clouds and Precipitation. Mon Weather Rev 132:103–120. doi: 10.1175/1520-0493(2004)132<0103:ARATIM>2.0.CO;2

Hong S-Y, Noh Y, Dudhia J (2006) A New Vertical Diffusion Package with an Explicit Treatment of Entrainment Processes. Mon Weather Rev 2318–2341.

Hong S, Lim J (2006) The WRF single-moment 6-class microphysics scheme (WSM6). J. Korean Meteorol. Soc. 42:129–151.

Hurk B Van Den, Viterbo P (2000) Offline validation of the ERA40 surface scheme.

Iacono MJ, Delamere JS, Mlawer EJ, et al (2008) Radiative forcing by long-lived greenhouse gases: Calculations with the AER radiative transfer models. J Geophys Res Atmos 113:2–9. doi: 10.1029/2008JD009944

Ingwersen J, Steffens K, Högy P, et al (2011) Comparison of Noah simulations with eddy covariance and soil water measurements at a winter wheat stand. Agric For Meteorol 151:345–355. doi: 10.1016/j.agrformet.2010.11.010

Jacob D, Petersen J, Eggert B, et al (2013) EURO-CORDEX: new high-resolution climate change projections for European impact research. Reg Environ Chang 14:563–578. doi: 10.1007/s10113-013-0499-2

Jacquemin B, Noilhan J (1990) Sensitivity study and validation of a land surface parameterization using the HAPEX-MOBILHY data set. Boundary-Layer Meteorol 52:93–134. doi: 10.1007/BF00123180

Jaeger EB, Stöckli R, Seneviratne SI (2009) Analysis of planetary boundary layer fluxes and land-atmosphere coupling in the regional climate model CLM. J Geophys Res 114:D17106. doi: 10.1029/2008JD011658

Janjić ZI (1994) The Step-Mountain Eta Coordinate Model: Further Developments of the Convection, Viscous Sublayer, and Turbulence Closure Schemes. Mon. Weather Rev. 122:927–945.

Jones PW (1999) First- and Second-Order Conservative Remapping Schemes for Grids in Spherical Coordinates. Mon Weather Rev 127:2204–2210. doi: 10.1175/1520-0493(1999)127<2204:FASOCR>2.0.CO;2

Kain JS (2004) The Kain–Fritsch Convective Parameterization: An Update. J Appl Meteorol 43:170–181. doi: 10.1175/1520-0450(2004)043<0170:TKCPAU>2.0.CO;2

Kain JS, Fritsch JM (1993) The Representation of Cumulus Convection in Numerical Models. In: Emanuel KA, Raymond DJ (eds). American Meteorological Society,

Boston, MA, pp 165–170

Katragkou E, García-Díez M, Vautard R, et al (2015) Regional climate hindcast simulations within EURO-CORDEX: evaluation of a WRF multi-physics ensemble. Geosci Model Dev 8:603–618. doi: 10.5194/gmd-8-603-2015

Kendon EJ, Roberts NM, Fowler HJ, et al (2014) Heavier summer downpours with climate change revealed by weather forecast resolution model. Nat Clim Chang 4:570–576.

Kendon EJ, Roberts NM, Senior CA, Roberts MJ (2012) Realism of Rainfall in a Very High-Resolution Regional Climate Model. J Clim 25:5791–5806. doi: 10.1175/JCLI-D-11-00562.1

Keune J, Gasper F, Goergen K, et al (2016) Studying the influence of groundwater representations on land surface-atmosphere feedbacks during the European heat wave in 2003. J Geophys Res Atmos 121:301–325. doi: 10.1002/2016JD025426

Knist S, Goergen K, Buonomo E, et al (2017) Land-atmosphere coupling in EURO-CORDEX evaluation experiments. J Geophys Res Atmos 122:79–103. doi: 10.1002/2016JD025476

Knist S, Goergen K, Simmer C (2018a) Evaluation and projected changes of precipitation statistics in convection-permitting WRF climate simulations over Central Europe. Clim Dyn 0:2. doi: 10.1007/s00382-018-4147-x

Knist S, Goergen K, Simmer C (2018b) Effects of land surface inhomogeneity on convection-permitting WRF simulations over Central Europe. Meteorol Atmos Phys submitted:2018.

Knote C, Heinemann GR (2010) Changes in weather extremes: Assessment of return values using high resolution climate simulations at convection-resolving scale. Meteorol Zeitschrift 19:11–23. doi: 10.1127/0941-2948/2010/0424

Koster RD, Sud YC, Guo Z, et al (2006) GLACE: The Global Land–Atmosphere Coupling Experiment. Part I: Overview. J Hydrometeorol 7:590–610. doi: 10.1175/JHM510.1

Kotlarski S, Keuler K, Christensen OB, et al (2014) Regional climate modeling on European scales: a joint standard evaluation of the EURO-CORDEX RCM ensemble. Geosci Model Dev Discuss 7:217–293. doi: 10.5194/gmdd-7-217-2014

Langhans W, Schmidli J, Fuhrer O, et al (2013) Long-term simulations of thermally driven flows and orographic convection at convection-parameterizing and cloud-resolving resolutions. J Appl Meteorol Climatol 52:1490–1510. doi: 10.1175/JAMC-D-12-0167.1

Lenderink G, Holtslag AAM (2004) An updated length-scale formulation for turbulent mixing in clear and cloudy boundary layers. Q J R Meteorol Soc 130:3405–3427. doi: 10.1256/qj.03.117

Lenderink G, van Meijgaard E (2008) Increase in hourly precipitation extremes beyond expectations from temperature changes. Nat Geosci 1:511–514. doi: 10.1038/ngeo262

Leutwyler D, Fuhrer O, Lapillonne X, et al (2016) Towards European-scale convection-resolving climate simulations with GPUs: A study with COSMO 4.19. Geosci Model Dev 9:3393–3412. doi: 10.5194/gmd-9-3393-2016

Liu YY, De Jeu RAM, McCabe MF, et al (2011a) Global long-term passive microwave satellite-based retrievals of vegetation optical depth. Geophys Res Lett 38:1–6. doi: 10.1029/2011GL048684

Liu YY, Parinussa RM, Dorigo W a., et al (2011b) Developing an improved soil moisture dataset by blending passive and active microwave satellite-based retrievals. Hydrol Earth Syst Sci 15:425–436. doi: 10.5194/hess-15-425-2011

Lohmann U, Roeckner E (1996) Design and performance of a new cloud microphysics scheme developed for the ECHAM general circulation model. Clim Dyn 12:557–572. doi: 10.1007/BF00207939

Lorenz R, Pitman AJ, Hirsch AL, Srbinovsky J (2015) Intraseasonal versus Interannual Measures of Land-Atmosphere Coupling Strength in a Global Climate Model: GLACE-1 versus GLACE-CMIP5 Experiments in ACCESS1.3b. J Hydrometeorol 16:2276–2295. doi: 10.1175/JHM-D-14-0206.1

Louis JF (1979) A parametric model of vertical eddy fluxes in the atmosphere. Boundary-Layer Meteorol 17:187–202. doi: 10.1007/BF00117978

Mahrt L, Ek M (1984) The Influence of Atmospheric Stability on Potential Evaporation. J. Clim. Appl. Meteorol. 23:222–234.

Mahrt L, Pan H (1984) A two-layer model of soil hydrology. Boundary-Layer Meteorol 29:1–20. doi: 10.1007/BF00119116

Martens B, Miralles DG, Lievens H, et al (2016) GLEAM v3: satellite-based land evaporation and root-zone soil moisture. Geosci Model Dev Discuss 1–36. doi: 10.5194/gmd-2016-162

Martin GM, Johnson DW, Spice A (1994) The Measurement and Parameterization of Effective Radius of Droplets in Warm Stratocumulus Clouds. J. Atmos. Sci. 51:1823–1842.

Masson V, Champeaux J-L, Chauvin F, et al (2003) a Global Database of Land Surface Parameters At 1Km Resolution in Meteorological and Climate Models. J Clim 16:1261–1282.

Masson V, Le Moigne P, Martin E, et al (2013) The SURFEXv7.2 land and ocean surface platform for coupled or offline simulation of earth surface variables and fluxes. Geosci Model Dev 6:929–960. doi: 10.5194/gmd-6-929-2013

Merrifield AL, Xie SP (2016) Summer U.S. surface air temperature variability: Controlling factors and AMIP simulation biases. J Clim 29:5123–5139. doi:

10.1175/JCLI-D-15-0705.1

Milovac J, Warrach-Sagi K, Behrendt A, et al (2016) Investigation of PBL schemes combining the WRF model simulations with scanning water vapor differential absorption lidar measurements. J Geophys Res Atmos 121:624–649. doi: 10.1002/2015JD023927

Miralles DG, Teuling AJ, van Heerwaarden CC, Vila-Guerau de Arellano J (2014) Mega-heatwave temperatures due to combined soil desiccation and atmospheric heat accumulation. Nat Geosci 7:345–349.

Miralles DG, van den Berg MJ, Teuling a. J, de Jeu R a. M (2012) Soil moisture-temperature coupling: A multiscale observational analysis. Geophys Res Lett 39:n/a-n/a. doi: 10.1029/2012GL053703

Mlawer EJ, Taubman SJ, Brown PD, et al (1997) Radiative transfer for inhomogeneous atmospheres: RRTM, a validated correlated-k model for the longwave. J Geophys Res 102:16663. doi: 10.1029/97JD00237

Morcrette J-J, Smith L, Fouquart Y (1986) Pressure and temperature dependence of the absorption in longwave radiation parametrizations. Beiträge zur Phys der Atmosphäre 59:455–469.

Morrison H, Thompson G, Tatarskii V (2009) Impact of Cloud Microphysics on the Development of Trailing Stratiform Precipitation in a Simulated Squall Line: Comparison of One- and Two-Moment Schemes. Mon Weather Rev 137:991–1007. doi: 10.1175/2008MWR2556.1

Neggers RAJ (2009) A Dual Mass Flux Framework for Boundary Layer Convection. Part II: Clouds. J Atmos Sci 66:1489–1506. doi: 10.1175/2008JAS2636.1

Neggers RAJ, Köhler M, Beljaars ACM (2009) A Dual Mass Flux Framework for Boundary Layer Convection. Part I: Transport. J Atmos Sci 66:1465–1487. doi: 10.1175/2008JAS2635.1

Noilhan J, Planton S (1989) A Simple Parameterization of Land Surface Processes for Meteorological Models. Mon. Weather Rev. 117:536–549.

Nordeng TE (1994) Extended versions of the convection parametrization scheme at ECMWF and their impact upon the mean climate and transient activity of the model in the tropics.

Pan H-L, Mahrt L (1987) Interaction between soil hydrology and boundary-layer development. Boundary-Layer Meteorol 38:185–202. doi: 10.1007/BF00121563

Prein AF, Gobiet A, Suklitsch M, et al (2013) Added value of convection permitting seasonal simulations. Clim Dyn 41:2655–2677. doi: 10.1007/s00382-013-1744-6

Prein AF, Gobiet A, Truhetz H, et al (2016a) Precipitation in the EURO-CORDEX $$0.11^{\circ }$$ 0 . 11 ∘ and $$0.44^{\circ }$$ 0 . 44 ∘ simulations: high resolution, high benefits? Clim Dyn 46:383–412. doi: 10.1007/s00382-015-2589-y

Prein AF, Langhans W, Fosser G, et al (2015) A review on regional convection-permitting climate modeling: Demonstrations, prospects, and challenges. Rev Geophys 53:323–361. doi: 10.1002/2014RG000475

Prein AF, Rasmussen R, Stephens G (2017) Challenges and advances in convection-permitting climate modeling. Bull Am Meteorol Soc 98:1027–1030. doi: 10.1175/BAMS-D-16-0263.1

Prein AF, Rasmussen RM, Ikeda K, et al (2016b) The future intensification of hourly precipitation extremes. Nat Clim Chang 1:1–6. doi: 10.1038/nclimate3168

Rahman M, Sulis M, Kollet SJ (2015) The subsurface–land surface–atmosphere connection under convective conditions. Adv Water Resour 83:240–249. doi: 10.1016/j.advwatres.2015.06.003

Rasch PJ, Kristjánsson JE (1998) A Comparison of the CCM3 Model Climate Using Diagnosed and Predicted Condensate Parameterizations. J Clim 11:1587–1614. doi: 10.1175/1520-0442(1998)011<1587:ACOTCM>2.0.CO;2

Rechid D, Hagemann S, Jacob D (2009) Sensitivity of climate models to seasonal variability of snow-free land surface albedo. Theor Appl Climatol 95:197–221. doi: 10.1007/s00704-007-0371-8

Ricard JL, Royer JF (1993) A statistical cloud scheme for use in an AGCM. Ann Geophys 11:1095–1115.

Ritter B, Geleyn J-F (1992) A Comprehensive Radiation Scheme for Numerical Weather Prediction Models with Potential Applications in Climate Simulations. Mon. Weather Rev. 120:303–325.

Samuelsson P, Gollvik S, Ullerstig A, Smhi (2006) The land-surface scheme of the Rossby Centre regional atmospheric climate model (RCA3). SMHI Meteorol 25.

Santanello J a., Peters-Lidard CD, Kennedy A, Kumar S V. (2013) Diagnosing the Nature of Land–Atmosphere Coupling: A Case Study of Dry/Wet Extremes in the U.S. Southern Great Plains. J Hydrometeorol 14:3–24. doi: 10.1175/JHM-D-12-023.1

Santanello J a., Peters-Lidard CD, Kumar S V., et al (2009) A Modeling and Observational Framework for Diagnosing Local Land–Atmosphere Coupling on Diurnal Time Scales. J Hydrometeorol 10:577–599. doi: 10.1175/2009JHM1066.1

Savijärvi H (1990) Fast Radiation Parameterization Schemes for Mesoscale and Short-Range Forecast Models. J. Appl. Meteorol. 29:437–447.

Schär C, Ban N, Fischer EM, et al (2016) Percentile indices for assessing changes in heavy precipitation events. Clim Change 137:201–216. doi: 10.1007/s10584-016-1669-2

Seneviratne SI, Corti T, Davin EL, et al (2010) Investigating soil moisture–climate interactions in a changing climate: A review. Earth-Science Rev 99:125–161. doi: 10.1016/j.earscirev.2010.02.004

Seneviratne SI, Lüthi D, Litschi M, Schär C (2006) Land-atmosphere coupling and climate change in Europe. Nature 443:205–9. doi: 10.1038/nature05095

Siebesma AP, Soares PMM, Teixeira J (2007) A Combined Eddy-Diffusivity Mass-Flux Approach for the Convective Boundary Layer. J Atmos Sci 64:1230–1248. doi: 10.1175/JAS3888.1

Sippel S, Zscheischler J, Mahecha MD, et al (2016) Refining multi-model projections of temperature extremes by evaluation against land-atmosphere coupling diagnostics. Earth Syst Dynam Discuss 1–24. doi: 10.5194/esd-2016-48, 2016

Skamarock W, Klemp JB, Dudhia J, et al (2008) A Description of the Advanced Research WRF Version 3. NCAR Tech Note. doi: 10.5065/D68S4MVH

Skamarock WC (2004) Evaluating Mesoscale NWP Models Using Kinetic Energy Spectra. Mon Weather Rev 132:3019–3032. doi: 10.1175/MWR2830.1

Smith RNB (1990) A scheme for predicting layer clouds and their water content in a general circulation model. Q J R Meteorol Soc 116:435–460. doi: 10.1002/qj.49711649210

Smith SA, Vosper SB, Field PR (2015) Sensitivity of orographic precipitation enhancement to horizontal resolution in the operational Met Office Weather forecasts. Meteorol Appl 22:14–24. doi: 10.1002/met.1352

Stoy PC, Mauder M, Foken T, et al (2013) A data-driven analysis of energy balance closure across FLUXNET research sites: The role of landscape scale heterogeneity. Agric For Meteorol 171–172:137–152. doi: 10.1016/j.agrformet.2012.11.004

Taylor CM, de Jeu R a M, Guichard F, et al (2012a) Afternoon rain more likely over drier soils. Nature 489:423–6. doi: 10.1038/nature11377

Taylor KE, Stouffer RJ, Meehl GA (2012b) A summary of the CMIP5 experiment design. Bull Am Meteorol Soc 93:485–498. doi: http://dx.doi.org/10.1175/BAMS-D-11-00094.1

Teuling AJ, Seneviratne SI, Stockli R, et al (2010) Contrasting response of European forest and grassland energy exchange to heatwaves. Nat Geosci 3:722–727.

Teuling AJ, Van Loon AF, Seneviratne SI, et al (2013) Evapotranspiration amplifies European summer drought. Geophys Res Lett 40:2071–2075. doi: 10.1002/grl.50495

Tiedtke M (1989) A comprehensive mass flux scheme for cumulus parameterization in large-scale models. Mon. Weather Rev. 117:1179–1800.

Tiedtke M (1993) Representation of Clouds in Large-Scale Models. Mon Weather Rev 121:11:3040–3061.

Tompkins AM, Gierens K, Rädel G (2007) Ice supersaturation in the ECMWF integrated forecast system. Q J R Meteorol Soc 133:53–63. doi: 10.1002/qj.14

Trenberth KE, Dai A, Rasmussen RM, Parsons DB (2003) The changing character of precipitation. Bull Am Meteorol Soc 84:1205–1217+1161. doi: 10.1175/BAMS-84-9-

1205

Troen IB, Mahrt L (1986) A simple model of the atmospheric boundary layer; sensitivity to surface evaporation. Boundary-Layer Meteorol 37:129–148. doi: 10.1007/BF00122760

Van der Linden P, Mitchell J.F.B. E (2009) ENSEMBLES: Climate Change and its Impacts: Summary of research and results from the ENSEMBLES project.

Vautard R, Gobiet A, Jacob D, et al (2013) The simulation of European heat waves from an ensemble of regional climate models within the EURO-CORDEX project. Clim Dyn 41:2555–2575. doi: 10.1007/s00382-013-1714-z

Wagner W, Dorigo W, Jeu R De, et al (2012) Fusion of active and passive microwave observations to create an Essential Climate Variable data record on soil moisture. ISPRS Ann Photogramm Remote Sens Spat Inf Sci I-7:315–321.

Wizemann H, Ingwersen J, Warrach-sagi K, Wulfmeyer V (2015) Three year observations of water vapor and energy fluxes over agricultural crops in two regional climates of Southwest Germany. Meteorol Zeitschrift 24:39–59. doi: 10.1127/metz/2014/0618

BONNER METEOROLOGISCHE ABHANDLUNGEN

Herausgegeben vom Meteorologischen Institut der Universität Bonn durch Prof. Dr. H. FLOHN (Hefte 1-25), Prof. Dr. M. HANTEL (Hefte 26-35), Prof. Dr. H.-D. SCHILLING (Hefte 36-39), Prof. Dr. H. KRAUS (Hefte 40-49), ab Heft 50 durch Prof. Dr. A. HENSE.

Heft 1-63: siehe `http://www.meteo.uni-bonn.de/bibliothek/bma`

64-86: open access, verfügbar unter `https://uni-bn.de/kpSDaQffe1`

Heft 64: ***Michael Weniger***: Stochastic parameterization: a rigorous approach to stochastic three-dimensional primitive equations, 2014, 148 S. + XV.

Heft 65: ***Andreas Röpnack***: Bayesian model verification: predictability of convective conditions based on EPS forecasts and observations, 2014, 152 S. + VI.

Heft 66: ***Thorsten Simon***: Statistical and Dynamical Downscaling of Numerical Climate Simulations: Enhancement and Evaluation for East Asia, 2014, 48 S. + VII. + Anhänge

Heft 67: ***Elham Rahmani***: The Effect of Climate Change on Wheat in Iran, 2014, [erschienen] 2015, 96 S. + XIII.

Heft 68: ***Pablo A. Saavedra Garfias***: Retrieval of Cloud and Rainwater from Ground-Based Passive Microwave Observations with the Multi-frequency Dual-polarized Radiometer ADMIRARI, 2014, [erschienen] 2015, 168 S. + XIII.

Heft 69: ***Christoph Bollmeyer***: A high-resolution regional reanalysis for Europe and Germany - Creation and Verification with a special focus on the moisture budget, 2015, 103 S. + IX.

Heft 70: ***A S M Mostaquimur Rahman***: Influence of subsurface hydrodynamics on the lower atmosphere at the catchment scale, 2015, 98 S. + XVI.

Heft 71: ***Sabrina Wahl***: Uncertainty in mesoscale numerical weather prediction: probabilistic forecasting of precipitation, 2015, 108 S.

Heft 72: ***Markus Übel***: Simulation of mesoscale patterns and diurnal variations of atmospheric CO_2 mixing ratios with the model system TerrSysMP-CO_2, 2015, [erschienen] 2016, 158 S. + II

Heft 73: ***Christian Bernardus Maria Weijenborg***: Characteristics of Potential Vorticity anomalies associated with mesoscale extremes in the extratropical troposphere, 2015, [erschienen] 2016, 151 S. + XI

Heft 74: ***Muhammad Kaleem***: A sensitivity study of decadal climate prediction to aerosol variability using ECHAM6-HAM (GCM), 2016, 98 S. + XII

Heft 75: ***Theresa Bick***: 3D Radar reflectivity assimilation with an ensemble Kalman filter on the convective scale, 2016, [erschienen] 2017, 96 S. + IX

Heft 76: ***Zied Ben Bouallegue***: Verification and post-processing of ensemble weather forecasts for renewable energy applications, 2017, 119 S.

Heft 77: ***Julia Lutz***: Improvements and application of the STatistical Analogue Resampling Scheme STARS, 2016, [erschienen] 2017, 103 S.

Heft 78: ***Benno Michael Thoma***: Palaeoclimate Reconstruction in the Levant and on the Balkans, 2016, [erschienen] 2017, XVI, 266 S.

Heft 79: ***Ieda Pscheidt***: Generating high resolution precipitation conditional on rainfall observations and satellite data, 2017, V, 173 S.

Heft 80: ***Tanja Zerenner***: Atmospheric downscaling using multi-objective genetic programming, 2016, [erschienen] 2017, X, 191 S.

Heft 81: ***Sophie Stolzenberger***: On the probabilistic evaluation of decadal and paleoclimate model predictions, 2017, IV, 122 S.

Heft 82: ***Insa Thiele-Eich***: Flooding in Dhaka, Bangladesh, and the challenge of climate change, 2017, V, 158 S.

Heft 83: ***Liselotte Bach***: Towards a probabilistic regional reanalysis for Europe, 2017 [erschienen] 2018, VI, 114 S.

Heft 84: ***Yen-Sen Lu***: Propagation of land surface model uncertainties in terrestrial system states, 2017, [erschienen] 2018, X, 120 S.

Heft 85: ***Rüdiger Hewer***: Stochastic physical models for wind fields and precipitation extremes, 2018, 99 S.

Heft 86: ***Sebastian Knist***: Land-atmosphere interactions in multiscale regional climate change simulations over Europe, 2018, vii, 147 S.

METEOROLOGISCHES INSTITUT
MATHEMATISCH NATURWISSENSCHAFTLICHE FAKULTÄT
UNIVERSITÄT BONN

Meteorologisches Institut
Universität Bonn